

Advancing electrolysis research from laboratory to application: self-supported sputtered Ir-based catalysts benchmarked in a gas diffusion electrode setup.

Inaugural dissertation
of the Faculty of Science,
University of Bern

presented by

Pablo Collantes Jiménez

from Spain

Supervisor of the doctoral thesis:

Prof. Dr. Matthias Arenz

Department of Chemistry, Biochemistry and Pharmaceutical Sciences

Copyright notice

This following work is licensed under the Creative Commons Attribution-NonCommercial- NoDerivatives 4.0 International License (CC-BY-NC-ND 4.0)
To view a copy of this license, visit <http://creativecommons.org/licenses/by-nc-nd/4.0/> or send a letter to Creative Commons, PO Box 1866, Mountain View, CA 94042, USA.



This license does not apply to Chapter VII. In this last Chapter, the indicated licenses apply individually for the manuscripts appended:

7.1 Manuscript I - Copyright 2022 American Chemical Society

K. Ehelebe, N. Schmitt, G. Sievers, A.W. Jensen, A. Hrnjić, P. Collantes Jiménez, et al. Benchmarking Fuel Cell Electrocatalysts Using Gas Diffusion Electrodes: Inter-lab Comparison and Best Practices. *ACS Energy Lett.* 2022, 7(2):816–26, <https://doi.org/10.1021/acsenerylett.1c02659>

7.2 Manuscript II - Licensed by CC-BY 4.0

P. Collantes Jiménez, G. Sievers, A. Quade, V. Brüser, R.K. Pittkowski, M. Arenz. Gas diffusion electrode activity measurements of iridium-based self-supported catalysts produced by alternated physical vapor deposition. *J Power Sources.* 2023; 569 (April), <https://doi.org/10.1016/j.jpowsour.2023.232990> (Open Access)

To view a copy of this license, visit <http://creativecommons.org/licenses/by/4.0/> or send a letter to Creative Commons, PO Box 1866, Mountain View, CA 94042, USA

7.3 Manuscript III - Licensed by CC-BY 3.0 Unported license

P. Collantes Jiménez, G.K.H. Wiberg, G. Sievers, V. Brüser, M. Arenz. Bridging the gap between basic research and application: a half-cell setup for high current density measurements of Ir-based oxygen evolution reaction catalysts on porous transport electrodes. *J. Mater. Chem. A.* 2023, 11, 20129-20138, <https://doi.org/10.1039/D3TA04136K> (Open Access)

To view a copy of this license, visit <http://creativecommons.org/licenses/by/3.0/> or send a letter to Creative Commons, PO Box 1866, Mountain View, CA 94042, USA.

Original document saved on the web server of the University Library of Bern.

Advancing electrolysis research from laboratory to application: self-supported sputtered Ir-based catalysts benchmarked in a gas diffusion electrode setup.

Inaugural dissertation
of the Faculty of Science,
University of Bern

presented by
Pablo Collantes Jiménez
from Spain

Supervisor of the doctoral thesis:

Prof. Dr. Matthias Arenz

Department of Chemistry, Biochemistry and Pharmaceutical Sciences

Accepted by the Faculty of Science

Bern, 27th of September 2024

The Dean

Prof. Dr. Jean-Louis Reymond

Abstract

Large-scale hydrogen production using renewable sources is a key factor in achieving global decarbonization. To make this a reality, catalysts used for electrolysis need to be highly efficient, scalable, and cost-effective. The presented research focuses on the development of novel self-supported catalysts for electrolysis using sputtering to achieve low loadings and high activity and measuring their performance under more realistic conditions using a gas diffusion electrode setup (GDE setup), accelerating the development stage.

In **Manuscript I**, an inter-lab comparison of the four most relevant GDE setups was used for activity benchmarking of commercial fuel cell catalysts using a unified testing protocol. While small adjustments need to be accounted for every setup, it is shown that standardized testing procedures such as step-galvanostatic activity measurement enable comparable benchmarking results across setups as a function of the catalyst layer quality obtained during the preparation. Furthermore, it becomes apparent that the boundaries for the analysis and interpretation of the activity results are defined by the electrode size and iR-correction accuracy of each system. Ultimately, using this approach mirrors the behavior observed in complex systems better as compared to standard laboratory techniques.

The successfully validated benchmarking method is explored in **Manuscript II** for the development of iridium-based catalysts used for oxygen evolution reaction (OER) in electrolysis. The catalysts are prepared by direct deposition of Ir and Co on a carbon substrate with an alternated magnetron sputtering process resulting in a highly amorphous structure observed by XRD analysis. Following a selective leaching process of the Co in acidic media under controlled potential cycling, the catalyst develops a self-supported metallic Ir structure with enhanced active area. However, a trace amount of Co is retained in the structure, and still detectable by EDX. Then, the highly porous Ir-rich “sponge” catalyst undergoes an electrochemical activation process at a controlled oxidation potential to achieve a higher activity. Using three starting Co ratios to Ir, an 8-fold OER mass activity improvement, compared with a commercial Alfa Aesar IrO_x nanoparticle catalyst, was achieved. The mixed metallic and oxide structure observed by the ex-situ XAS characterization, in combination with the EDX results, suggest a core-shell structure formation associated with a ligand effect and as underlying effects for the increased activity. Ultimately, the combined approach of alternated magnetron sputtering and activity testing in the GDE setup is demonstrated as a viable option to accelerate research toward application stages for OER studies.

Finally, in **Manuscript III**, the limitations of the GDE setup and the substrate materials are addressed enabling characterization conditions and materials that resemble better realistic electrolysis systems. A new version of the test system with an improved electrode assembly and iR-correction accuracy finally allows the study of Ti porous transport electrodes (PTEs) and using liquid water as a reactant. In contrast with the former setup, combining these two factors allows current densities up to 2 A cm⁻² without mass transport limitations and irreversible substrate corrosion. To validate the new PTE setup, we examine the oxygen evolution reaction (OER) performance at room temperature of an IrO_x catalyst with a 0.250 mg_{Ir} cm⁻²_{geo} loading sputtered on a porous transport layer (PTL), achieving approximately 1.56 V_{RHE} at a given geometric current density of 2 A cm⁻². In addition, to demonstrate the feasibility of the new setup for OER activity studies, a 20-hour stability test is conducted, maintaining a current density of 2 A cm⁻² with the previously described IrO_x catalyst. The results show

that the catalyst and the setup exhibit sufficient stability to endure the test, exhibiting only a minimal voltage loss of 20 mV between the initial and end-of-life OER activity protocols. In comparison with the model IrO_x catalyst, the OER potential of Ir-Co catalyst with the same Ir loading reveals a significantly improved OER activity over IrO_x with comparable stability, as demonstrated in a 5-hour stability test. This study further validates the PTE setup as a reliable method for transferring and benchmarking the OER performance and stability of Ir-based catalysts produced by magnetron sputtering into practical applications.

List of Publications

Manuscript I:

K. Ehelebe, N. Schmitt, G. Sievers, A.W. Jensen, A. Hrnjić, P. Collantes Jiménez, et al. Benchmarking Fuel Cell Electrocatalysts Using Gas Diffusion Electrodes: Inter-lab Comparison and Best Practices. *ACS Energy Lett.* **2022**, 7(2):816–26, <https://doi.org/10.1021/acseenergylett.1c02659>

Manuscript II:

P. Collantes Jiménez, G. Sievers, A. Quade, V. Brüser, R.K. Pittkowski, M. Arenz. Gas diffusion electrode activity measurements of iridium-based self-supported catalysts produced by alternated physical vapor deposition. *J Power Sources.* **2023**; 569 (April), <https://doi.org/10.1016/j.jpowsour.2023.232990> (Open Access)

Manuscript III:

P. Collantes Jiménez, G.K.H. Wiberg, G. Sievers, V. Brüser, M. Arenz. Bridging the gap between basic research and application: a half-cell setup for high current density measurements of Ir-based oxygen evolution reaction catalysts on porous transport electrodes. *J. Mater. Chem. A.* **2023**, 11, 20129-20138, <https://doi.org/10.1039/D3TA04136K> (Open Access)

List of Abbreviations

AC/DC	Alternating Current/Direct Current
AEMWE	Anion Exchange Membrane Water Electrolysis
AST	Accelerated Stress Tests
AWE	Alkaline Water Electrolysis
CAPEX	Capital Expenditure
CCM	Catalyst Coated Membrane
CCS	Catalyst Coated Substrate
CE	Counter Electrode
Co	Cobalt
CV	Cyclic voltammogram/voltammetry
DI	De-Ionized
DLR	Deutsches Zentrum für Luft- und Raumfahrt (German Aerospace Center)
ECSA	Electrochemical Surface Area
EDX	Energy-Dispersive X-ray Spectroscopy
GDE	Gas Diffusion Electrode
GDL	Gas Diffusion Layer
GWh	Gigawatt hour
H ₂	Hydrogen molecule
H ₂ O	Water molecule
HClO ₄	Perchloric acid
HER	Hydrogen Evolution Reaction
HHV	High heating value
H _{upd}	Hydrogen underpotential deposition
Ir	Iridium
Ir-SP	Iridium Specific Power density
LHV	Low heating value
MA	Mass Activity
MC	Monte Carlo
MEA	Membrane Electrode Assembly
MMT	Million Metric Tonnes
MPL	Microporous Layer
NZE	Net Zero scenario
O ₂	Oxygen molecule
OER	Oxygen Evolution Reaction
OPEX	Operation Expenditure

V List of Abbreviations

ORR	Oxygen Reduction Reaction
PEEK	Polyether Ether Ketone
PEMFC	Proton Exchange Membrane Fuel Cell
PEMWE	Proton Exchange Membrane Water Electrolysis
Pt	Platinum
PTE	Porous Transport Electrode
PTFE	Polytetrafluoroethylene
PTL	Porous Transport Layer
PVD - MS	Physical Vapor Deposition - Magnetron Sputtering
RDE	Rotating Disk Electrode
RE	Reference Electrode
RF	Radio Frequency
RHE	Reversible Hydrogen Electrode
R_u	Uncompensated resistance
SA	Specific Activity
SDG	Sustainable Development Goals
SE	Secondary Electrons
SEM-EDX	Scanning Electron Microscopy-Energy Dispersive X-ray Spectroscopy
SFC	Electrochemical Scanning Flow Cell
SOWE	Solid Oxide Water Electrolysis
Ti	Titanium
WE	Working Electrode
XAS	X-ray Absorption Spectroscopy
XPS	X-ray Photoelectron Spectroscopy
XRD	X-ray Diffraction

List of Contents

Abstract	I
List of Publications	III
List of Abbreviations	IV
List of Contents	VI
1. Introduction	1
1.1 The role of electrolysis at a global scale	1
1.2 “State of the art” of the studied reactions, catalysts, and experimental setups in PEMWEs	4
1.3 Outline of the thesis	7
2. Experimental methodology	8
2.1 Synthesis and processing of catalysts	8
2.1.1 PVD Magnetron Sputtering	9
2.1.2 Reactor configuration for catalyst deposition	10
2.1.3 Synthesis of self-supported catalysts through acid leaching	12
2.2 Physical characterization of the catalysts	14
2.2.1 Catalyst morphology	15
2.2.2 Chemical composition	20
2.3 The Gas Diffusion Electrode (GDE) setup	26
2.3.1 Self-supported catalyst optimization for OER in the GDE setup	27
2.3.2 Setup development	28
2.4 Electrochemical Characterization and Characterization Techniques	32
2.4.1 Basic operation of the potentiostat	33
2.4.1 Reversible hydrogen electrode (RHE) calibration	35
2.4.2 Acid leaching of Ir-Co catalysts	35
2.4.3 ECSA determination of Ir-based OER catalysts	35
2.4.4 Activation protocol	36
2.4.5 OER activity determination	37
2.4.5 Catalyst stability	38
3. Discussion of the appended manuscripts	40
3.1 Manuscript I:	41
3.1.1 Description:	42
3.1.2 Contribution to the work:	42
3.1.3 Most relevant findings:	43
3.2 Manuscript II:	46
3.2.1 Description	47

VII List of Contents

3.2.2 Contribution to the work.....	47
3.2.3 Most relevant findings.....	48
3.3 Manuscript III:	49
3.3.1 Description:	50
3.3.2 Contribution to the work.....	50
3.3.3 Most relevant findings.....	50
4. Conclusions and perspectives	53
4.1 Conclusions.....	53
4.2 Perspectives.....	55
5. Acknowledgement	58
6. Bibliography.....	59
7. Appended manuscripts	69
7.1 Manuscript I.....	71
7.2 Manuscript II.....	94
7.3 Manuscript III.....	120

1. Introduction

1.1 The role of electrolysis at a global scale

As the global population steadily grows towards an estimated 9 to 11 billion people by 2100¹, the energy demand has been increasing significantly. Already in 2021, the worldwide electricity demand was recorded at 24.7 petawatt-hours (PWh), and it is projected to rise by at least 5.9 PWh by the end of 2030. To put this in perspective, this increase is roughly equivalent to combining the current electricity consumption of both the European Union and the United States²

However, unlike the previous decade, the progress towards achieving energy goals set for 2030 or reaching net-zero emissions by 2050 has been hindered in the last five years. This setback is primarily due to a structural energy crisis exacerbated by geopolitical tensions causing supply shortages and a global health crisis. The slowdown of the economic system and the fragmented supply chains has led to high levels of inflation and instability in stock markets, resulting in a surge in natural gas and crude oil prices not seen since the global financial crisis of 2008³.

A pivotal factor in overcoming this situation and continuing the efforts to fight the over-arching climate crisis lies in the action strategies taken by governments and policymakers. As emphasized in a recent report⁴, a complete restructuring of the energy system is key to achieving the affordable and clean energy goals defined by the Sustainable Development Goal 7 (SDG 7) and the effort to limit global temperature rise to 1.5°C.

While short-term measures like increasing oil and coal-based electricity generation have been adopted in many countries to mitigate the immediate effects of the price increase on consumers, an urgent need for accelerated development of renewable energy technologies is needed to offer long-term alternatives to fossil fuel-based energy production.

Long-term planning encompasses the creation of an electricity network capable of effectively substituting the current system's reliance on coal and natural gas to handle increased energy demand during peak load situations. This new network concept will need to be adaptable to the intermittent production generated by renewable energy sources, where conventional centralized energy production can be combined with bidirectional generation and storage at a smaller scale. The rapid growth in solar power is poised to elevate it to the top position of renewable energy production in terms of total installed power by 2027, closely followed by the development of wind power⁵.

To address the intermittency in energy production from these technologies, storage solutions in the form of batteries and alternative fuels will also need considerable upscaling. Currently, the main support for the growth of renewables is the increase in installed power from batteries, mainly due to their decreased production costs⁶. Reported as 27 GW in 2021, at least a 50-fold increase is expected by 2050 if current policies are applied. However, this factor more than triplicates if a net-zero scenario should be achieved by 2050², which increases concerns about resource availability. On the other hand, even state-of-the-art battery technologies will experience problems with decreased capacities for long-term storage⁷.

To improve this aspect, a further link in the chain of renewables can be added with the incorporation of hydrogen and ammonia as storage⁸⁻¹⁰. Hydrogen holds a particular promise as both an alternative

to replace and blend with the depleting natural gas supply and as a fundamental building block for the transportation sector, the chemical industry, and power generation¹¹. Since hydrogen production can be decentralized, its utilization in stationary applications does not necessitate the immediate construction of a new distribution infrastructure. Still, up to 95% of hydrogen currently produced globally is produced from fossil sources to cover a global demand of 94 million metric tons (MMT) in 2022¹², with high associated carbon emissions.

A positive development of the surge in gas prices in 2021 has been a significant increase in the number of large-scale projects focused on generating hydrogen from renewable sources. In Europe, Spain and Germany are anticipated to take the lead in these developments aiming to reach an installed electrolysis power capacity of 40 GW by the end of 2030 where over 80 terawatt-hours (TWh) of green hydrogen will be required to achieve greenhouse gas-neutral steel production by 2050⁸.

Among the four existing technologies capable of producing low-emission hydrogen through electrolysis, only two are currently at a commercial stage. These are alkaline water electrolysis (AWE) and acidic electrolysis with polymer electrolyte membrane (PEMWEs)¹³.

Alkaline systems have been extensively tested and are currently cheaper on a per-kilowatt basis¹⁴, which makes it attractive for reliable hydrogen production at a MW scale where a steady power supply can be expected, such as in industrial processes. For instance, the HYBRIT project led by the main Swedish companies in the metallurgical and energy sector (SSAB, LKAB, and Vattenfall) aims to replace coal with green hydrogen in the steelmaking process, requiring 4.5 MW of installed power in alkaline electrolysis with an electric consumption of about 50 kWh kgH₂⁻¹, a milestone in the decarbonization strategy of carbon-intensive industries¹⁵.

Nevertheless, intensive research and development efforts towards scalable hydrogen production are focused on PEMWEs, as can be observed from the exponential increase in review papers since 2004¹⁶. This is mainly due to their fast response to load changes in the network, high attainable current densities, and the ability to operate at higher temperatures and pressures^{8,17,18}. As of 2023, a 20 MW PEM system developed by Cummings and Air Liquide in 2021 is the largest PEM system ever developed, capable of delivering 8.4 tons of H₂ daily at 30 bar using renewable electricity with an energy efficiency higher than 51 kWh kgH₂⁻¹. Next-generation systems with a 10-fold increase in power have already been announced for the coming 5 years¹⁹.

Eventually, meeting the ambitious global target of producing 530 MMT of hydrogen by 2050 by scaling up 550 GW of installed electrolysis power in the net-zero-emissions (NZE) scenario will most likely require a combination of both AWE and PEMWE methods^{18,20,21}.

Additionally, it will involve advancing the commercialization of other electrolysis technologies such as the anion exchange electrolysis (AEMWE) and solid oxide water electrolysis (SOWE), which are moving from research into early application stages²²⁻²⁴. A good example of this is the pioneering GrInHy2.0 project developed by Salzgitter AG in cooperation with Sunfire GmbH as part of the SALCOS® program (Salzgitter Low CO₂ Steelmaking) in Germany, where since 2019, 100 tons of hydrogen have been produced using SOWE running at 850 °C, reaching up a 39.7 kWh kgH₂⁻¹ energy efficiency by combining electrical and heat efficiencies.

3 Introduction

The primary obstacle to the widespread advancement of PEMWEs and, more broadly, green hydrogen production, is the elevated levelized cost of hydrogen (LCOH) in Europe. Currently, the price of green hydrogen in Europe averages over \$5 per kilogram, in contrast to the approximately \$1.8 per kilogram for "grey" sources using steam methane reforming and \$2 per kilogram with autothermal reforming with CO₂ capturing²⁵.

The high LCOH of PEMWEs is associated with the use of critical resources in their fabrication increasing the capital expenditures (CAPEX), as well as the operation expenses (OPEX) from running the system on electricity and water. Since the start of the industrialization of PEMWEs in the 1980s beyond military and space applications, the system efficiency and durability have been continuously extended to decrease the use of resources in their development. In the last 20 years, the decreased cost of electricity production and the increased awareness of the climate goals have helped further the development of advanced stack designs and better usage of materials to lower the CAPEX. As a result, a yearly reduction of 4.77 +/- 1.88% was projected in 2020 for the CAPEX in PEMWEs, which doubles the trend reported for AWE systems even though critical resources are not needed in this technology²⁶.

Still, the next generation of PEMWEs will need to enhance their efficiencies by an additional 10% to reach a point where they can provide 80% of the low heating value (LHV), i.e. 41.66 kWh kgH₂⁻¹ energy efficiency, for over 50,000 hours while maintaining lower costs⁸. Achieving this ambitious goal, with a focus on gigawatt-scale production, will require not only cost reductions in the manufacturing of metallic cell components like titanium porous transport layers and bipolar plates but also a substantial reduction in the use of platinum group metal (PGM) catalysts such as platinum (Pt) and iridium (Ir).

Iridium is the state-of-the-art catalyst material used at the anode in PEMWEs to increase the efficiency of the oxygen evolution reaction (OER) at higher voltages. However, it is extremely scarce, with just 7 million tons extracted annually. Furthermore, a 4-fold spike increase in price in 2021 further constrained the scalability of this technology²⁷. Currently, commercial PEMWEs employ very high Ir loadings of 2.5 mg_{Ir} cm⁻²_{geo} in the anode to ensure stability.

As calculated by Gasteiger et al., an Ir-specific power density (Ir-SP) of state-of-the-art PEMWEs is close to 0.5 g_{Ir} kW⁻¹, and considering a 25% of the annual Ir extraction dedicated for electrolysis only, only 20 GW more of installed electrolysis power could be installed by 2030²⁸. Even though 25% is a conservative estimate in 2023, where more than half of Ir is used for electrolysis²⁹, in the proposed example the de-carbonization of the transport sector would not be met even by 2100. Yet, the pathway to the NZE scenario demands a 50-fold reduction in the Ir-SP with equivalent or superior voltage efficiencies. This factor might be even higher since the selected Ir-SP for this example is lower than the average reported values, which range from 0.34 to 2 g_{Ir} kW⁻¹³⁰.

Future catalyst designs aim to improve the Ir-SP by reducing the catalyst loading while keeping a high current density by increasing catalyst utilization. This is achieved by increasing the available area for the reaction and ensuring a sufficient catalyst layer quality by methods that are suitable for industrial upscaling. However, the optimization process should not stop at maximizing the mass activity of the catalyst. Significant performance improvements can also arise from carefully selecting substrates, membranes, and current collectors. These choices can help reduce performance losses due to inefficient transport of water and gas, as well as lower ohmic resistances by engineering interfaces

and electrical connections. Ultimately, to develop a holistic approach to PEMWE development it is necessary to understand the interplay of its elements and underlying processes.

1.2 “State of the art” of the studied reactions, catalysts, and experimental setups in PEMWEs

A PEMWE is an electrochemical conversion device that performs the water-splitting reaction upon the application of an electrical potential. Typical conversion efficiencies are 60%. The reaction can progress more efficiently at elevated temperatures towards 100 °C. A single cell, which is the simplest functional unit, incorporates two electrodes separated by an ion-conducting membrane. This membrane has the capability to separate the reactions on both electrode surfaces by holding the pressure of hydrogen up to several hundred bars, theoretically. However, a trade-off must be considered when determining the membrane thickness, as it impacts both ohmic resistances and gas permeability. Sandwiching the membrane, the anode and cathode electrodes are designed with a porous structure for efficient water and gas distribution to the interface with the membrane, where the catalysts are located. The separate reactions at each electrode can be written as follows:



At the anode site, the OER takes place at the catalyst interface with the membrane, generating oxygen gas and protons from water and electrons, see Eq. 1. The protons travel through the membrane driven by an external electric field and recombine at the cathode in the hydrogen evolution reaction (HER), as described by Eq. 2. In a stack of multiple cells, electrons are transferred through the catalyst to the substrate materials and then pass through the bipolar plates to reach the cathode of the next cell, which is assembled in series.

The fast single-step kinetics of the HER on Pt catalysts at the cathode approaches the reversible thermodynamic potential. By contrast, on the anode side, the OER involves a challenging multi-step reaction pathway characterized by a high kinetic overpotential, which is analogous to the oxygen reduction reaction (ORR) in fuel cells³¹. Despite recent research efforts to introduce non-noble oxides, perovskites, and spinels as catalysts^{32–34}, iridium oxide is still considered the most effective transition metal catalyst to reduce the OER overpotential at high current densities while maintaining stability^{35,36}. Hence, it plays a central role in the ongoing fundamental research aimed at uncovering the OER reaction mechanisms.

Currently, there is an agreement on two main OER mechanisms as a function of the crystallinity and consequently the number of active sites attained during the catalyst preparation method. On the one hand, the OER in crystalline rutile-type IrO₂ progresses by the formation of M-O, M-OH, and M-OOH adsorbate intermediates in a 4-step process. By contrast, amorphous IrO_x has demonstrated a higher activity, attributed to the direct transport of oxygen through lattice vacant and a simplified intermediate route mediated by electrophilic O¹⁻ species³⁷.

Although the scaling relationships of the –OH/–OOH OER intermediates and active sites can serve as useful descriptors to map the activity of different transition metal oxides, relying only on thermodynamic activity trends to find the most optimum catalyst can be misleading as the time-dependent processes are not described³⁸. It has been frequently reported that catalysts showing

excellent OER activities, like ruthenium oxide, tend to undergo extremely rapid dissolution rates at the overpotentials required in realistic operation conditions^{36,39–41}. In this scenario, the catalyst stability is limited to a few hours^{35,42}. The dissolution rates of amorphous iridium oxide also exceed those of its crystalline counterpart, but in comparison to ruthenium oxide, a good balance of activity and stability can be achieved with this material.

Even though Ru and Ir oxides have been successfully implemented in alkaline environments showing high OER activities with moderate stability⁴³, high Ru dissolution rates in acidic media are frequently reported⁴⁴. Hence, even if higher OER activities are reached with Ru oxides, the lack of stability barely justifies the use of PGMs. Instead, the higher stability of IrO_x in comparison with more common metals and oxides e.g. Co, Ni can be leveraged for cost-effective catalyst design using tailored synthesis methods.

There are two approaches to this, which are closely inter-related: the first consists of creating a core-shell structure where IrO_x forms a nanolayer-thick "skin" that wraps the less noble oxide at the core as a result of their surface segregation energy with IrO_x⁴⁵, preserving it stable inside until the IrO_x layer is broken. This arrangement effectively disperses the IrO_x active phase and can even enhance the catalyst's intrinsic activity due to lattice strain⁴⁶ or ligand effects of a modified, more electrophilic Ir-O bond⁴⁷. The second approach to enhancing the OER activity is based on a selective leaching process of a sacrificial template of the less noble element. This results in highly porous nanostructures of mixed metallic oxides which offer increased ECSA and OER activity, thanks to the formation of amorphous IrO_x with a high number of vacant oxygen sites (Ir-X). In this restructuring process, a core-shell structure can be developed to maintain the stability of trace amounts of the non-PGMs⁴⁸.

In summary, catalyst synthesis is a key aspect defining the ultimate performance and lifespan of the catalyst. A separate introduction would be required to address a complete review of catalyst synthesis procedures. Suffice it to say, that they can be divided into three main categories: solid, solution, and vapor-phase synthesis.

Most of today's catalyst synthesis processes reported in literature follow solution phase routes, also called wet-chemistry, which rely upon the use of molecular Ir precursors in liquid solutions to prepare unsupported or supported particles, aiming to optimize the activity and the available electrochemically active surface area (ECSA)³⁷. Adam's fusion can be highlighted among the most common methods to prepare unsupported particles with varying degrees of crystallinity and ECSAs depending on the calcination temperature and time. Nevertheless, this method lacks the control over the particle size and distribution that can be attained by using stabilizers or surfactants in colloidal synthesis. However, the latter is not well suited for industrial production due to the large dependence on chemical solvents and multi-step processes even before fixing on support. Hence, only surfactant-free wet-chemical routes should be considered for upscaling. The fragile nanostructures obtained by any of these methods often need to be fixed to support to increment of their stability. Carbon supports should be avoided since they are not stable under the high potentials and acidic OER environment. Over the last years, the material selection has been narrowed to X-tin oxides, where X represents elements such as antimony, iridium, or fluorine. The method chosen to fix the nanoparticles on the supports and create inks is mostly influenced by any steps that can affect the catalyst structure or the support, as well as the possibility of scaling up the process.

Furthermore, the way the electrode is fabricated is essential in determining how effectively supported nanoparticles serve as catalysts. This involves two primary procedures: catalyst-coated substrate configuration (CCS) or membranes⁴⁹ in the catalyst-coated membrane (CCM) configuration. The state of the art in the industry is CCM production, where the ink is applied by doctor-blading, decal-transfer, spraying, or various printing processes. Each of these methods results in different deposition qualities that can affect the catalyst's performance⁵⁰.

While the wet-chemistry routes can be used to create catalyst nanoparticle formulations based on surface dealloying or core-shell structures via e.g., galvanic replacement, they are generally multi-step processes with a very demanding control of the precursor chemistry. In contrast, direct deposition methods of nanostructured thin film (NSTF) catalysts, e.g., via physical vapor deposition (PVD), single or multi-metallic electrodes can be manufactured in a single step while maintaining precise control over the morphologies, composition, loading, and stoichiometry of the catalyst layer. In particular, magnetron sputtering at high deposition rates and tunable deposition conditions allows reproducible depositions from a wide selection of target materials under clean vacuum conditions that can be readily scaled to the industry. High-performing catalysts for OER created by direct PVD deposition have already been reported in recent studies⁵¹⁻⁵⁴, including an alternated multi-metallic deposition method followed by a selective acid leaching step of the templating element to achieve a highly porous, self-supported Ir nanostructure in CCS configurations⁵⁵.

As much of catalyst development primarily concentrates on enhancing the kinetic activity using simplified experimental setups aided by theoretical models, a crucial step towards their effective integration into larger systems involves the assessment of their stability and degradation pathways.

The current state-of-the-art laboratory method for benchmarking catalyst activity remains the rotating disk electrode (RDE) but is considered too basic for this purpose since it lacks insight into the interfaces, catalyst morphologies, or loadings that can be translated into practical and realistic applications. Specifically, in the RDE setup, the formation of oxygen bubbles adhering to the electrode and artificially creating a deactivation effect can obscure any understanding of actual degradation processes⁵⁶. Other liquid electrolyte methods include the flow cell setup, which is frequently used to measure catalyst degradation by online spectrometry of the dissolved species in accelerated stress tests (ASTs). Nevertheless, direct contact with the acidic electrode already increases the dissolution rates compared to ASTs performed in full-sized membrane electrode assemblies (MEA)^{57,58}. In the latter, these degradation effects can be explored in the actual reaction interfaces formed between the electrode and the membrane, where processing steps such as membrane activation or hot pressing can introduce great changes in conductivity and mass transport properties in operation⁵⁹. However, deriving singular mechanisms at one electrode side can be extremely complex in these systems, which on top of being very material and time-intensive, are not available to every research group. Hence, the exceptionally high activities in RDE stages for newly developed catalysts are not followed up by MEA results due to notable disparities in testing conditions^{60,61}.

To address this development gap between setups, gas diffusion electrode (GDE) half-cell setups have emerged in recent years in fuel cell research as a valuable bridging platform for activity benchmarking. They offer a blend of the swift screening abilities found in three-electrode setups with a more accurate representation of the electrode interfaces interacting with membranes, all while achieving high current densities that are comparable to those seen in MEA systems. Additionally, it introduces the

possibility of studying the half-reaction either in half-CCM and CCS electrode configurations as well as the influence of assembly steps such as hot-pressing in the catalyst activity.

GDE setups have already been validated in research studies related to the oxygen reduction reaction (ORR) in proton exchange membrane fuel cells (PEMFC) ⁶²⁻⁶⁴. Furthermore, they have been extended to explore the oxidation of small organic compounds such as methanol ⁶⁵, ethanol ⁶⁶, formic acid ⁶⁷ and CO₂ reduction ^{68,69} using various cell configurations. The introduction of GDEs for OER studies is a recent development still scarcely reported ^{70,71}, and it has been closely tied to methods that were initially established in the context of the ORR realm for supported catalysts and carbon substrates. In this study, the GDE method is further developed for the OER study of self-supported Ir-based catalysts produced via PVD.

1.3 Outline of the thesis

Firstly, the effectiveness of the GDE method as an electrochemical benchmarking tool is validated by comparing its reproducibility in an array of similar setups. Specifically, an examination is conducted to gauge its utility in benchmarking the activity of ORR in PEMFCs. The primary research question addressed is: "How reproducibly can different GDE half-cell setups assess the ECSA and ORR activity of various PEMFC catalysts following a unified measurement protocol?"

Secondly, an investigation is undertaken into a catalyst development process that combines GDE benchmarking with PVD deposition, focusing specifically on Ir-Co catalysts prepared with varying Co/Ir ratios. The research question posed is: "How do variations in deposition parameters and processing steps for self-supported Ir-Co catalysts impact their electrochemical performance measured by a GDE setup?"

Lastly, a design for the GDE method tailored to assess the OER under realistic operating conditions is proposed, allowing for the benchmarking of materials and operation conditions relevant to PEMWEs. The central research question addressed is: "How can the GDE method be further enhanced to evaluate the performance and stability of self-supported Ir-based catalysts for OER under realistic operating conditions and what insights can be gained regarding catalyst degradation from this approach?"

2. Experimental methodology

This chapter provides a more detailed explanation and commentary on the primary techniques used to generate the outcomes published in the attached manuscripts.

In the first part, the discussion centers around the preparation of the self-supported catalyst layers and the different possibilities presented by the combination of magnetron sputtering with layer processing steps.

Following this, the standard material characterization methods, including SEM-EDX, XPS, XRD, and XAS analysis utilized to support the study of material chemistry and morphology changes are described and reviewed. Additionally, the author's experience with synchrotron analysis is included, along with the opportunities that could be explored further to extract more information at a beamline with this material.

The evolution of the GDE setup for the study of the catalyst-coated substrates from fundamental studies to more realistic conditions in the PTE setup is then traced. In this context, a particular focus is given to the electrode incorporation into the assembly in each of its stages, the interplay of the system elements, and how the setup was used for the electrochemical characterization of the electrochemically active surface area (ECSA), OER activity, and stability. To finalize this part, the interpretation of the measurement results and the limitations of the electrochemical setup are covered.

Most of the experimental work presented in this thesis was accomplished within the context of the BMBF VIP+ 3DNanoMe project at the Leibniz Institute for Plasma Science and Technology (INP) in Greifswald, except for the XAS experiment and analysis included in Manuscript II, which was performed at the Swiss Light Source (SLS) at PSI, Switzerland. Additionally, in-situ XAS measurements performed at the Diamond Light Source in the UK are also discussed and perspectivized.

2.1 Synthesis and processing of catalysts

As described in the Introduction, a bottleneck for upscaling catalyst development is multi-step synthesis processes commonly found in ink formulations for supported catalysts. This approach, which remains today as the commercial standard, requires 1) the development of optimized ink formulations in parallel to 2) suitable deposition methods.

The inclusion of binders to disperse the particles has a proportional increase in the thickness of the catalyst layer. The trend to develop catalyst layers with reduced loadings implies a maximum layer thickness of around 1 μm . Currently, it is a technical challenge to find techniques to disperse the ink over the surface of the substrate homogeneously to create such a thin layer. Hence, the lack of contact sites of the catalyst with the substrate or the membrane can create either electrical conductivity or mass transport limitations¹⁷.

In contrast, plasma-based processes have already been proven as an attractive alternative to perform deposition of highly controlled thin films with a uniform morphology and coverage on multiple substrates. In the realm of catalyst production, plasma physical deposition processes such as physical vapor deposition (PVD). PVD comprises a group of plasma deposition techniques where chemical precursors are not needed. In this approach, a solid material is sublimated in vacuum by the application of a strong electric field and then the vapor is condensed into a thin film.

In particular, magnetron sputtering (PVD-MS) has opened the possibility to produce nanostructures with tunable surface areas both on substrates and membranes allowing us to explore the contact interface properties between elements beyond the limitations imposed by traditional catalyst nanoparticle processes⁷²⁻⁷⁵. PVD-MS allows for generating layers with the same composition of an alloyed target on the substrate and depositing materials that have low or no conductive properties. Most importantly, it is also an excellent choice for industrial-scale production, since larger target sizes can also be adapted to coat multiple substrates simultaneously minimizing processing time and material waste.

2.1.1 PVD Magnetron Sputtering

The basic configuration of a magnetron sputtering system involves a vacuum chamber allocating one or several electrodes, a substrate for deposition, and most importantly a gas that is ionized to form a low-temperature plasma at room temperature. The latter is formed by the application of a high electric field from either a direct current (DC) or a radiofrequency (RF) generator between a negatively charged electrode (cathode) and the positively charged substrate/chamber (anode). The material to be deposited is known as the target and it is situated at the cathode.

A plasma, which is often referred to as the fourth state of matter, is formed when gas is subjected to an intense energy source such as heat or a strong electromagnetic field, causing electrons to detach from their atoms and resulting in a mixture of ions, electrons, and neutral species^{76,77}. Depending on the energy states and the temperature achieved by these species it can be divided into high and low-temperature plasma.

Low-temperature plasmas cover a temperature range spanning from a few hundred to several thousand degrees Celsius. In this state, particles exhibit a broad spectrum of kinetic energies. Upon the application of a strong electric field between the substrate and the target, free electrons are accelerated to energies of a few electron volts (eV), starting the process of ionizing gas atoms within the chamber. Meanwhile, the ionized and neutral species remain at room temperature (RT).

This ionization process proceeds until the breakdown voltage is reached. The optimal breakdown voltage is characteristic for each gas and can be calculated experimentally from Paschen's law by manipulating the distance between the target and substrate and adjusting the gas pressure^{74,76}. At this point, the process progresses to a cascade of ionizations and production of free electrons from the atoms of the gas until the plasma becomes self-sustaining.

As the accelerated positively charged ions hit the target, they create more secondary electrons and displace atoms transferring their momentum, which produces the sputtering. The ratio between the number of emitted atoms to incident ions can be defined as the sputtering yield. The incident ions need to be within a certain energy window for the yield to be optimal. Insufficient energy fails to generate a collision cascade at the target, while excessive energy leads to ion implantation.⁷⁶

A fundamental aspect that enables PVD-MS to be used in practical applications is the use of magnets (magnetrons) at the targets. The perpendicular components of the electric and magnetic effects near the targets cause the electrons to change direction parallel to the target as illustrated in Figure 1. The increased confinement of the electrons in an area parallel to the target produces a more collimated flux of sputtered species and better control over the directionality of the sputtered atoms or ions for the formation of specific nanostructures^{72,78}. The electron-rich region surrounding the target

guarantees a fast plasma ignition and stabilization. At the same time, it increases the ionization rate, allowing sputtering yields that exceed conventional diode sputtering. This unfolds several advantages; the most obvious is the fast production of thicker films or reduced process times.

2.1.2 Reactor configuration for catalyst deposition.

The catalyst film in this work was prepared with a linear PVD-MS reactor (Univex 400, Leybold GmbH, Germany) equipped with two magnetrons and an ion beam installed in the chamber. The substrates, masked to a size of $5 \times 5 \text{ cm}^2$, were mounted on a holder accessible through a load lock at atmospheric pressure. After the quick evacuation of the load lock to a pressure of at least 10^{-4} Pa , a swiveling arm transported the holder into the chamber following a linear trajectory under each of the respective magnetrons. For all catalyst deposition processes, the process chamber was evacuated to a pressure of $1.7 \cdot 10^{-5} \text{ Pa}$. The two-chamber design, see Figure 1, allows a convenient and quick transition between a load lock and the process chamber with minimal interruption.



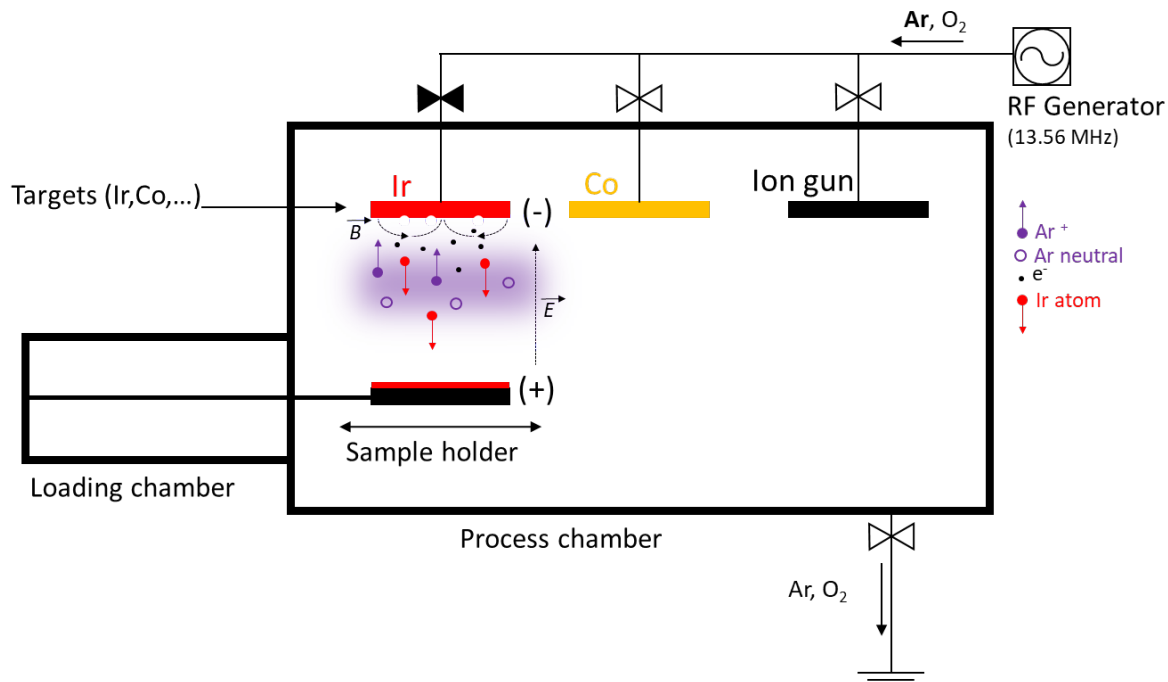


Figure 1. Linear PVD-MS reactor (above) and schematic of the magnetron sputtering process (below). The example shows a metallic deposition of Ir using an Ar plasma in RF mode.

The magnetrons were equipped with pure metallic Ir (99.95%, MaTecK, Germany) and Co (99.95%, Evotec GmbH, Germany) targets with a planar geometry of 177 x 25 x 1.5 mm. The power was delivered with radio frequency (RF) generators (Cito 136, COMET) operated at a driving frequency of 13.56 MHz. Even though a DC configuration is a more economic choice when sputtering conductive target materials, using RF provides some special advantages. The sputtered atoms decreased their energy in inelastic collisions with the ions in the plasma, reaching the substrate with lower energy^{55,75,79}. Additionally, the cooling system employed to refrigerate the magnetrons leads to reduced heat generation, enabling extended deposition durations.

The catalysts produced by PVD-MS for OER in this work can be categorized into two primary groups. This classification is based on either the deposition method or the material chemistry.

From the perspective of the deposition mode, the multi-target configuration can be performed in single or alternated sputtering processes. Alternated sputtering introduces additional process variables to achieve a certain catalyst loading, namely via different the number of cycles per deposition or modifying the ratio between the elements. Combining the deposition of an active and more noble metal with a templating element, the catalyst layer can be processed by leaching to produce a highly porous structure that is beneficial for catalysis, which is further explained in chapter 2.1.3. The relationship between the as-deposited Co:Ir ratios and the correlation with their electrochemical performance was explored in a series of Ir-Co self-supported catalysts for OER featured in Manuscript II.

Adjusting the gas composition of the plasma controls the catalyst chemistry, for example, to produce metallic deposition in pure Ar. In the metallic sputtering configuration of Ir and IrCo, an Ar plasma was ignited at a working pressure of 5 Pa and flushed through the individual magnetron sources at a flow

rate of 100 sccm. In contrast, a mixture of Ar/O₂ was used to create the reactive plasma during the reactive sputtering deposition of the IrO_x catalysts that were used in Manuscript III.

Even though the sputtering process with multiple targets and reaction atmospheres offers great flexibility, not every parameter combination yields attractive catalysts or efficient processes. For example, single depositions of metallic Ir need further processing or activation to form IrO_x and become active for OER. Inner parts of the Ir layer that are inaccessible to chemical and electrochemical activation methods remain metallic. Thus, depositing thicker layers of Ir yields poor catalyst utilization.

In addition, the alternated cycling of the targets and short sputtering times per cycle introduce more complex conditions to maintain a constant sputtering yield, which is desirable to reproducibly achieve specified catalyst loadings and element ratios in a fixed process.

Nevertheless, these options were also explored in the early stages to help the understanding and the direction of the layer deposition development.

2.1.3 Synthesis of self-supported catalysts through acid leaching

The procedure to create self-supported catalysts with high surface area using alternate magnetron sputtering followed by a selective acid leaching step has been described in several previous studies of ORR catalysts such as Pt-Cu⁷⁵, Pt-CoO⁸⁰ as well as with Ir-Co catalysts⁵⁵ for OER.

All these studies share a common procedure to create a heterogeneous bimetallic material where a sacrificial metal is dissolved in an acid solution, leaving a scaffold of the active metal with a highly accessible surface. Unlike the dealloying of bimetallic alloys in homogeneous materials^{81,82}, the initial structure prepared by sputtering is of a heterogeneous and amorphous nature more alike to metallic glasses, exhibiting properties that have piqued scientific curiosity for its catalytic applications since more than 50 years ago⁸³. An interesting aspect is that the deposition parameters can be engineered to present a particular dealloying behavior by changing the ratio between sputtered elements or the number of cycles in the deposition^{55,75,80}. Furthermore, using an RF deposition configuration produces a lower layer density, which allows the leaching agents to reach deeper into the material producing a volumetric effect rather than simply displacing the ad-atoms from the surface.

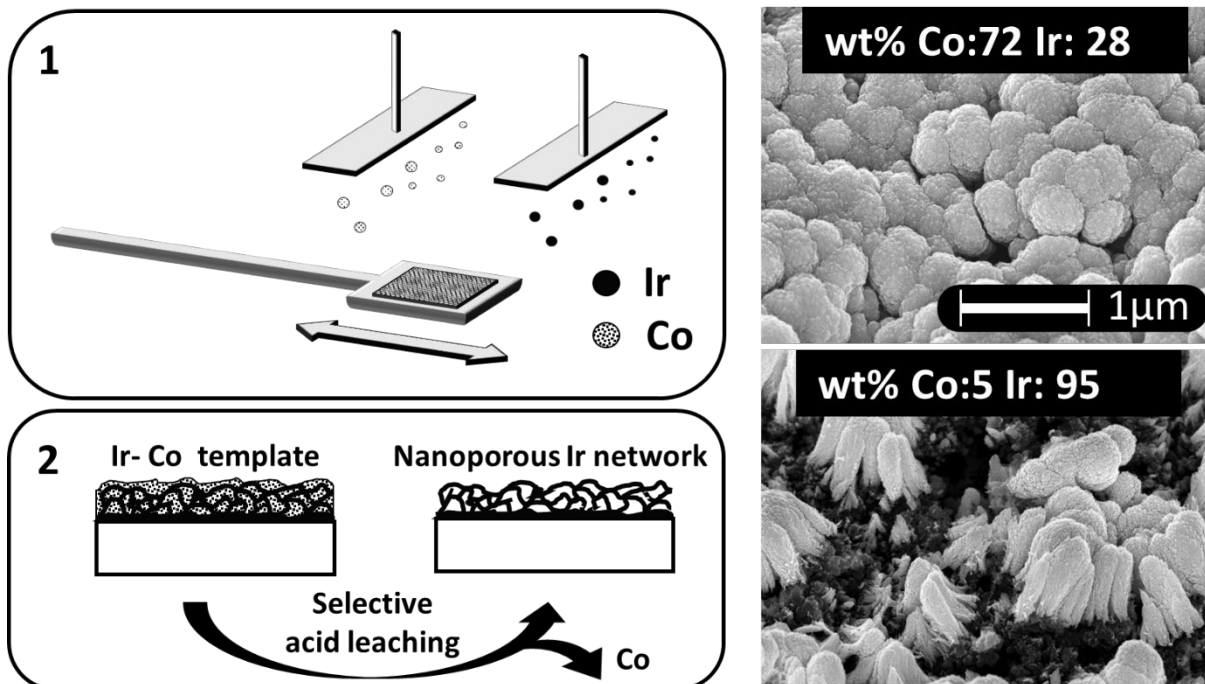


Figure 2. Nanostructure Ir-Co electrode formation by PVD alternated sputtering deposition on a GDL (upper left) followed by a selective leaching step (bottom left). During the acid leaching the initial Co-rich microstructure (upper right) is transformed into scattered clusters of Ir-rich dendrites, leaving parts of the carbon substrate exposed, in black (bottom right).

When the bimetallic layer meets the acid in the absence of potential-controlled conditions, the templating element oxidizes spontaneously in the first few seconds since it is thermodynamically unstable in acidic media. For example, in the leaching of a bimetallic Ir-Co layer in perchloric acid (HClO_4), Co is oxidized to Co^{2+} and complexed in the water into a hexaaquacobalt (II) ion $[\text{Co}(\text{H}_2\text{O})_6]^{2+}$, which gives the solution a characteristic pink hue. Hydrogen is produced in the process, which nucleates in the metal cavities and can be observed from the release of bubbles in the solution. The combination of the mechanical forces created by the gas leaving the structure, the dissolution of the Co-rich domains, and further surface diffusive processes creates the characteristic porous catalyst structure seen in the bottom right of Figure 2.

Aside from the thermodynamic aspects, the leaching is also strongly determined by mass transport factors such as the accessibility of the acid to the substrate surfaces. Unfortunately, the determination of mass transport factors is not as straightforward as in model homogeneous alloys e.g. AgAu where Monte Carlo (MC) simulations have been developed following the spinodal decomposition behavior^{81,84}. Thus, a conventional approach is to perform the leaching under controlled conditions such as in cyclic voltammetry (CV) electrochemical protocols, and characterize the material morphology and chemical composition before and after^{85–87}. The electrochemical leaching procedure is detailed in the chapter 2.4.2.

Since the GDE setup was limited to small electrode areas up to $1 \times 1 \text{ cm}^2$ using the conventional top parts, a special leaching station was designed to perform leaching in the full $5 \times 5 \text{ cm}^2$ as-deposited areas. Taking advantage of the hydrophobic properties of the GDL, the station was designed with a

floating electrode in a pool of HClO_4 1 M to ensure a constant electric field distribution between the catalyst film and the $5 \times 5 \text{ cm}^2$ glassy carbon plate in the bottom acting as a cathode. The gas atmosphere in the closed chamber was controlled during the leaching by purging the air with a continuous Ar flow applied to eliminate the ORR. The catalyst electrode was then contacted from the back with a carbon rod connected to a Pt spring, and the reference was positioned in the special compartment in the frame of the station in contact with the electrolyte pool.

This approach was very successful in reproducing the leaching conditions of Ir-Co layers on GDL substrates obtained in the GDE cell, as could be seen by comparing the CVs in both systems during a deposition.

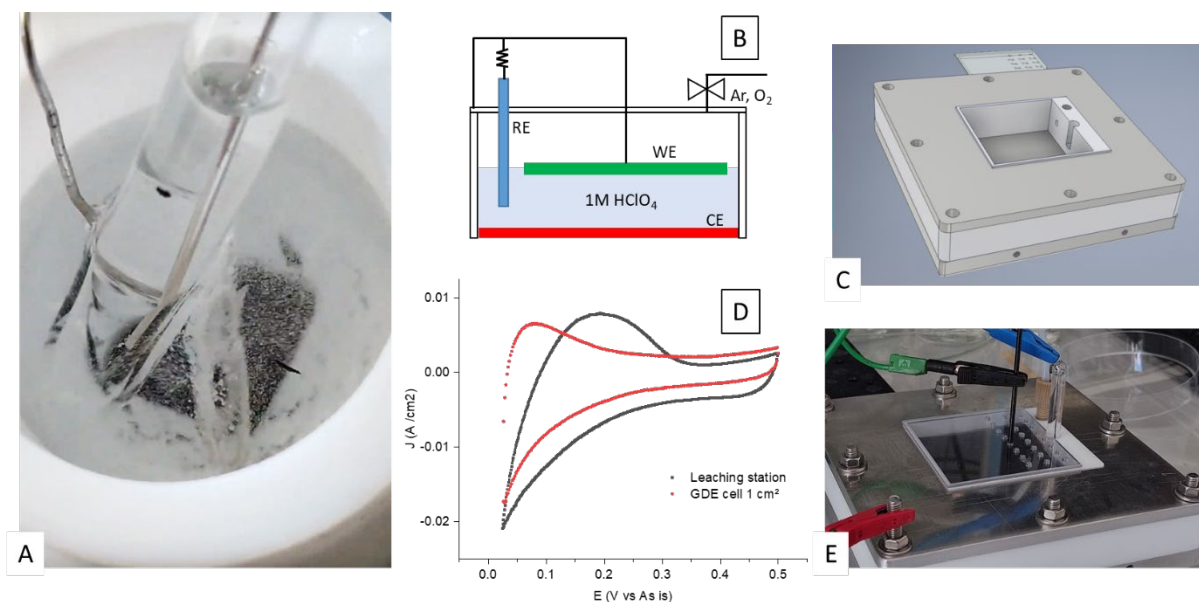


Figure 3. The electrochemically controlled acid leaching process is shown A) in the GDE cell configuration with an area of 1 cm^2 . Alternatively, a B) floating electrode configuration for larger 25 cm^2 areas was proposed and C) designed with the possibility to fix the reference and counter electrodes as well as controlling the gas atmosphere. The final design E) shows the final version of the leaching station, including the contact rod for the WE, the contact of the CE on the top steel plate, the RE notch, and the threaded gas inlet. D) The leaching behavior was comparable in both cells using the same protocol.

However, due to the hydrophilic nature and much denser Ti PTLs, the floating electrode configuration could not be used. Therefore, a chemical leaching process was applied instead, introducing the Ir-Co coated PTLs in a beaker with 1 M HClO_4 for 30 min at room temperature.

2.2 Physical characterization of the catalysts

This chapter outlines the most relevant microscopic and spectroscopic techniques used to extract information regarding the morphology and chemical properties of catalysts and electrodes.

When catalysts are exposed to operating conditions, understanding the dynamic behavior of their surface and chemical composition becomes a complex challenge. Combining electrochemistry with powerful *in-situ* characterization techniques such as X-ray absorption spectroscopy (XAS) can provide a better understanding of how the catalyst is transformed. However, such experiments are often not available at a laboratory scale and require careful planning and result interpretation.

Nevertheless, the combination of non-destructive techniques such as scanning electron microscopy (SEM), energy dispersive X-ray spectroscopy (EDX), X-ray diffraction (XRD), or X-ray photoelectron spectroscopy (XPS) can also provide valuable information to the everyday scientist about the catalyst evolution even in ex-situ conditions if appropriate preparation methods and rigorous analysis are used.

2.2.1 Catalyst morphology

Scanning Electron Microscopy

The working principle of Scanning Electron Microscopy (SEM) is analogous to light optical microscopy, except that the light source is produced from an emitter that releases a beam of electrons when a voltage is applied, which is focused by electromagnetic lenses. Hence, a much higher resolution can be obtained with a SEM due to the smaller interaction distance of electrons with matter. The field emission gun emitter (FEG) and aberration-correction lenses integrated into the SEM model used in this study (JSM 7500F, JEOL) permit to reach a theoretical resolution of less than 2 nm in spot size. At this scale, it is possible to resolve the characteristic morphological features of the catalyst layers and electrode assemblies.

The surface topography information in as-deposited and leached samples was collected through the secondary electron (SE) in-lens detector using a top-down configuration with the samples mounted at a 45° angle. Using a tilted mount gave a better sense of perspective and depth of the thin film structures on the GDLs and Ti PTLs substrates. Since both materials are conductive and the catalyst layers are free of polymer binders, no special preparation was needed for inspection aside from surface cleaning and dehumidification with nitrogen.

Relevant morphological feature samples extend from the mm to nm scale. At low magnifications (25 to 1 k), the surface quality and homogeneity of the as-deposited substrates are visible immediately, see Figure 4. This includes any cracks in the mm range, which are common in carbon MPLs, as well as the topography of fiber or sintered structures in PTLs. Furthermore, the edge quality and deformation can be compared in different materials and thicknesses resulting from the sample extraction.

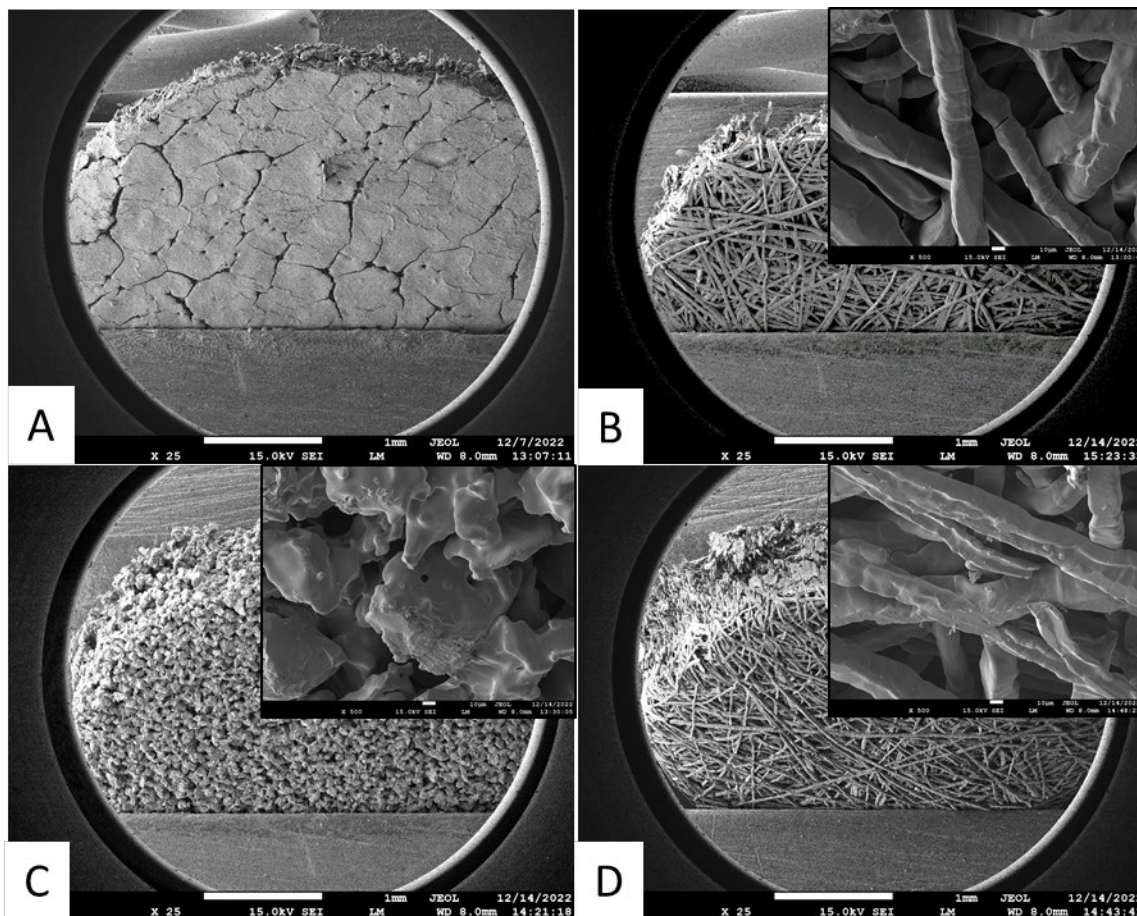


Figure 4. Low-magnification SEM micrographs taken at 25 and 500 magnifications (insets) after sample extraction of A) a GDL with a microporous layer (Sigracet 29BCE, 325 μm thickness), B) A thin Ti fleece PTL (ANKURO Int. GmbH, 0.3 mm thickness), C) a sintered Ti PTL from GKN of 1 mm thickness D) a 1mm-thick Ti PTL with a fiber structure provided by the DLR. The scale bar at the bottom of each image corresponds to 1 mm, and 10 μm in the inset.

Increasing the magnification to 1-10k allows the distinction of the diverse catalyst layer structures between the as-deposited and post-leaching states, as well as the resolution of substrate adhesion in GDLs and PTLs, see Figure 5.

Irrespective of their chemistry and deposition parameters in the as-deposited state, a uniform cauliflower morphology with micrometer-sized features is observed in all sputtered materials on GDLs (Figure 5A-C). On the other hand, the depositions on Ti PTL substrates show morphological differences in particular cases. For example, a continuous IrO_x deposition on Ti PTLs reveals a uniform sub-micrometric platelet structure that fully covers the Ti fibers, see Figure 5D. By contrast, the alternate deposition of Ir-Co on Ti PTLs, see Figure 5C, exhibits similarities in appearance with the GDLs.

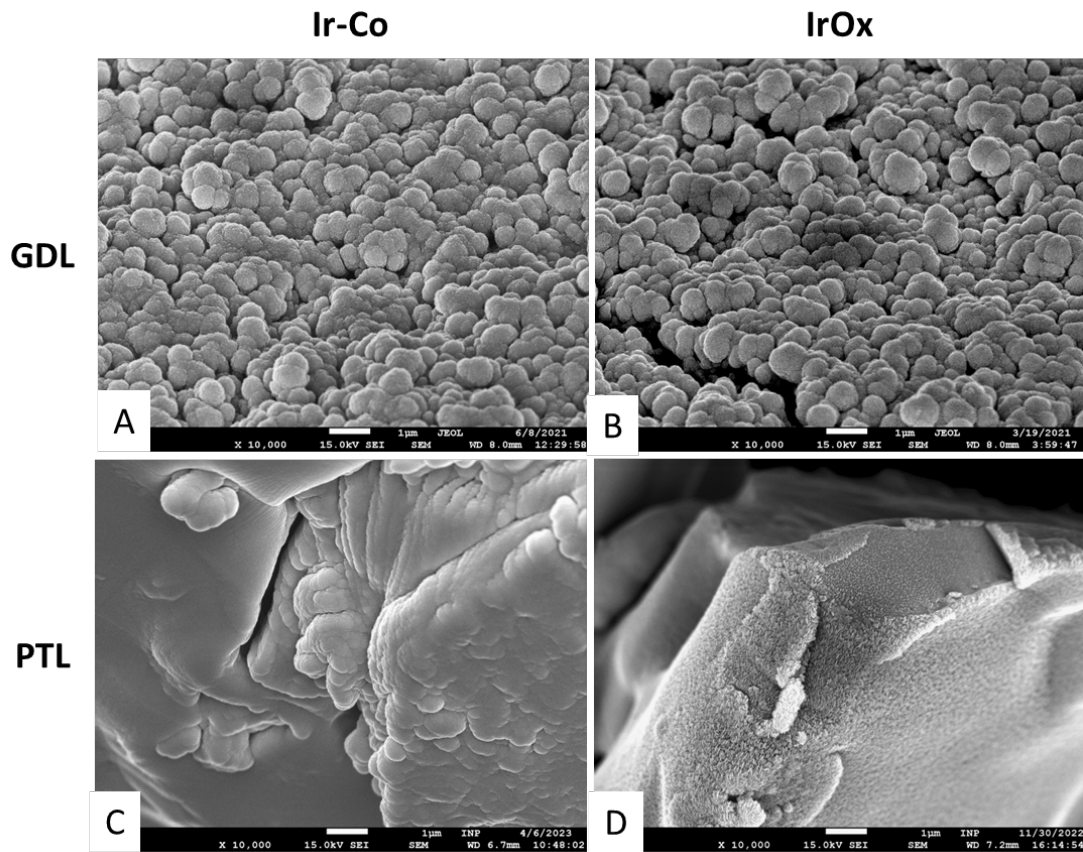


Figure 5. SEM top-down at 10 k magnification of as-deposited catalysts with an equal $0.250 \text{ mg}_{\text{Ir}} \text{ cm}^{-2}_{\text{geo}}$ nominal Ir loading. A) Ir-Co, B) IrO_x, on GDLs, C) Ir-Co, and D) IrO_x deposited on PTLs with a fiber structure, see Figure 4B. The scale bar at the bottom of each image corresponds to 1 μm .

As described in chapter 2.1.3, the leaching process transforms the structure of the bimetallic Ir-Co catalysts dramatically. This is most clearly visible in the depositions onto GDL substrates, where the overall layer thickness decreases, and the initial cauliflower structure evolves to clusters of smaller dendrites as the material is leached.

When the magnification is increased to the practical resolution limit of the instrument at 50k, see Figure 6., the finer details of the catalyst morphology, including nanoscale porosity, are significantly enhanced, and better resolved.

In terms of layer adhesion to the substrate after leaching, the rougher surface of the GDLs provides better anchoring as compared to the smooth untreated Ti fibers in the PTL substrate. Most of the catalyst material remained on the GDL and the areas devoid of material are uniformly distributed, see Figure 6A and B. Conversely, the catalyst layer on the Ti PTL fibers tends to flake and spall off after leaching resulting in the detachment of sizable chunks, see Figures 6C – F.

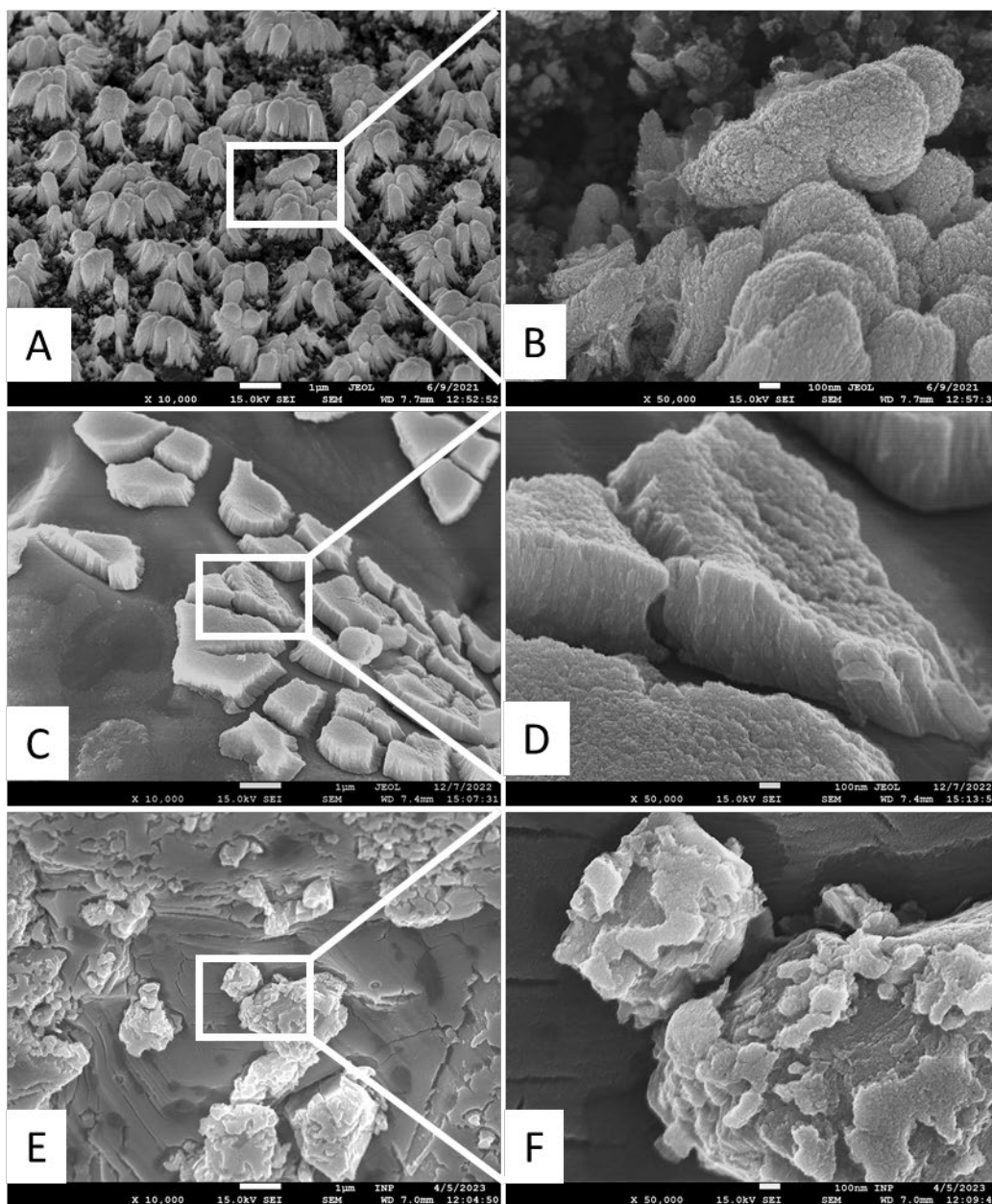


Figure 6. SEM top-down of at 10 k (left column) and 50 k (right column) magnifications for an Ir-Co catalyst with $0.250 \text{ mg}_{\text{Ir}} \text{ cm}^{-2}_{\text{geo}}$ and a Co: Ir ratio of 4 on different substrates and leached under different conditions. In the first row, A) and B) show the catalyst morphology on a GDL substrate after electrochemical leaching in 1 M HClO_4 . The images in the second row, C) and D), were obtained after chemical leaching with HNO_3 on a Ti PTL fleece substrate. Bottom row images, E) and F), were taken after chemical leaching in 1 M HClO_4 on a Ti PTL fleece substrate. The scale bar at the bottom of each image in the left column (A, C, E) corresponds to 1 μm , and 100 nm in the right column (B, D, F).

The previous explanations refer to the top-down configuration for ex-situ analysis in previous steps to the electrochemical characterization. To observe the thickness of the catalyst layer or the interaction between the catalyst and substrate or after hot-pressing the membrane in the half-electrode assembly, cross-sections were prepared.

The procedure to obtain cross-sections with the necessary quality was not straightforward. The first attempt at a cross-section was performed on a sputtered GDL hot pressed with a membrane using a

cryogenic procedure. To obtain the cross-section, the sample was introduced for 15 sec. in a bath of liquid nitrogen and then cut with a scalpel. Even though the process was fast, the results were very far from being satisfactory, see Figure 7A. The surface quality from the scalpel cut was very rough and the catalyst could not be found on the substrate, see Figure B. The sample was also not treated in any other way to increase the conductivity, hence, it continued to warp under observation worsening the image acquisition. This method was eventually discarded since the limited advantages in preparation time did not outweigh the further investment in time to optimize the cutting surface for high-resolution imaging, especially considering that the stiffer Ti PTLs cannot be cut with the scalpel directly. However, this first approximation was very useful in understanding that level of quality was necessary for the section and the behavior of the membrane under the microscope.

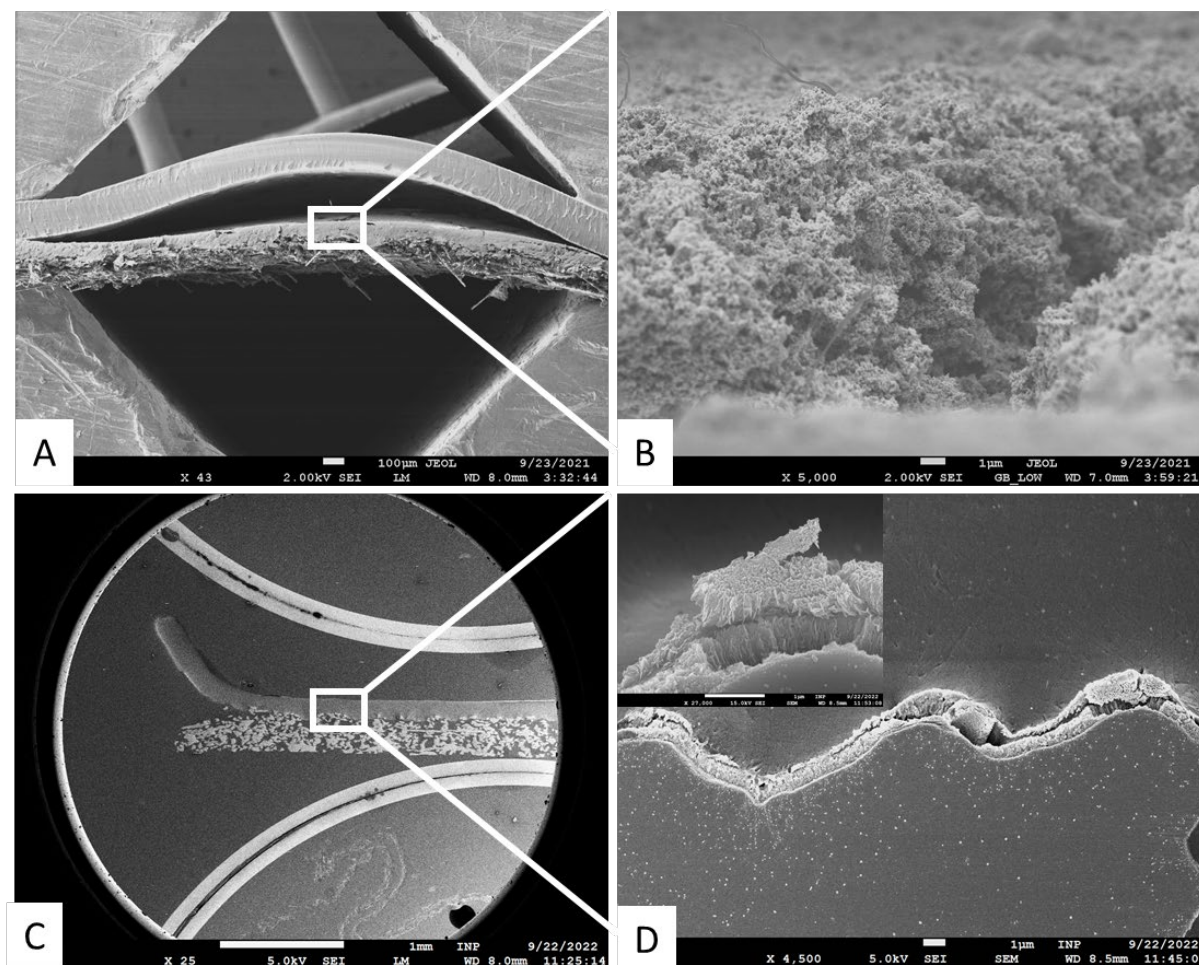


Figure 7. SEM cross-section preparations via A) dipping in liquid nitrogen of a hot-pressed GDE sputtered with Ir, resulting in delamination. B) The GDL layer in this configuration could be seen in the gap formed between both parts. By contrast, C) a hot-pressed PTE held by a metallic spring and embedded in epoxy showed a cleaner view of the D) IrO_x catalyst layer in between the PTL fibers and the membrane, details shown in the inset. The scale bar at the bottom of each image in the left column (A, B) corresponds to 1 mm, and 1 μ m in the right column (B, D).

A much more reliable procedure, albeit involving a longer preparation process, was to mount the electrode assembly into a two-component metallographic resin and then cut and polish it to reveal the interfacial structure, see Figure 7C and D. From the experience with the first attempt, the resin face was sputtered with Au to minimize the charging effects of the Nafion membrane. The results

obtained were greatly improved, as it was possible to see entire sections of the catalyst layer and its thickness with clarity. This technique allowed us to see the improved adhesion after hot-pressing IrO_x on a PTL in Manuscript III.

Despite the improvement obtained with this procedure, further effort was put into obtaining a better surface preparation using a FIB-SEM (Scios 2 HiVac dual beam FIB/SEM system, Thermo Fisher Scientific, Waltham, USA) on a PTL sputtered with an Ir-Co catalyst. In the first attempt with non-optimized parameters, the FIB instrument was able to produce a very acceptable cut of a single fiber in a 200 by 30-micrometer trench without any previous surface preparation, see Figure 8A. However, for further composition analysis, the sample had to be transported to the SEM-EDX instrument, suffering damage in the process as one of the sectioned fibers was missing when the same area was found again, as seen in Figure 8B. The remaining section surface that was left was difficult to be accessible by EDX, which led to shadowing effects. These factors, as well as the fact that complexity that would be added to cut-through assemblies including membranes, decided against using the FIB-SEM for further cross-section preparation.

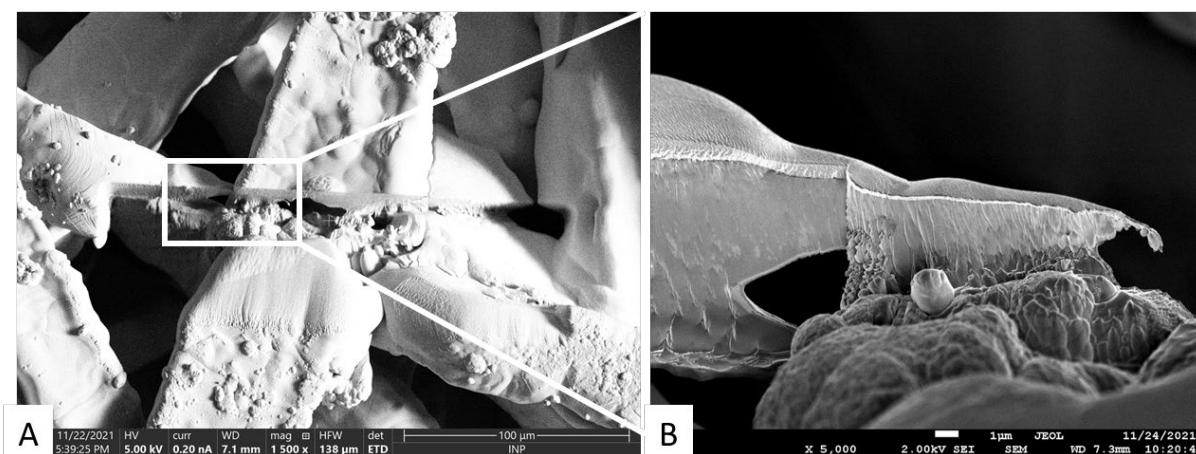


Figure 8. FIB – SEM cross-section of Ir-Co PTL A) as prepared in the instrument. The fiber in the center of the micrograph in A) was lost in the transfer to the B) SEM – EDX instrument.

2.2.2 Chemical composition

Energy-Dispersive X-ray Spectroscopy

The SEM instrument equipped an additional detector (Quantax 200, Bruker) to perform Energy-Dispersive X-ray Spectroscopy (EDX) to complement chemical composition information to the SE micrographs over the same areas. The chemical information is obtained from the characteristic X-ray emission for every element associated with the energy of electrons transitioning between electronic shells (K, L, M) in an atom when excited with sufficiently energetic electrons.

EDX provides the relative composition of several elements at different points, lines, and areas of the sample. The main strength of this technique is the flexibility of analysis of thin films (up to several micrometers, depending on the composition) and bulk materials. This is achieved by tuning the acceleration voltage of the incoming electrons to generate different X-ray interaction volumes and thus giving information about the analysis depth.

21 Experimental methodology

On the one side, for the top-down characterization of thin films, it is desirable to probe relative shallow interaction volumes with low acceleration voltages to obtain information from the film without adding too much substrate as background. However, particularly for films containing heavy elements such as Ir and Co, the acceleration voltages need to be set high enough to produce characteristic x-rays in those elements.

To strike a practical balance between interaction depth and element sensitivity in the sputtered films in this work, an acceleration voltage of 15 keV was selected. This voltage allowed for the identification and differentiation of even thin layers measuring less than a micron in thickness, distinguishing them from the substrate. Moreover, both the Co K α line at 6.924 keV and the Ir L α line at 9.147 keV were successfully obtained with a high signal-to-noise ratio; ensuring reliable and clear measurements according to the capabilities of the analysis instrument, see Figure 9.

Since the same acceleration voltage was also employed during micrograph acquisition, it enabled a seamless switch between the SE and EDX detectors. Aside from increasing the probe current to have a good acquisition rate, eliminating the extra time in fine refocusing adjustments was very effective in decreasing the risk of damage to the analysis area. However, there were certain limitations to this balancing act. Despite using an acceleration voltage of 15 keV, it was not feasible to excite the same energy lines for both Ir and Co. As a result, the precision for precise element quantification was decreased.

In the unleached layers, the ratios between Ir and Co could be reliably determined through point analysis in various areas of the sample, ensuring reproducibility. However, after the leaching process, determining consistent ratios became challenging, as reported in Manuscript II. In certain cases, particularly on untreated PTL substrates, the trace amounts of the remaining layer were extremely challenging to detect, even when using high probe currents, see Figure 9. Consequently, the data were interpreted with even greater caution and emphasis on the qualitative analysis.

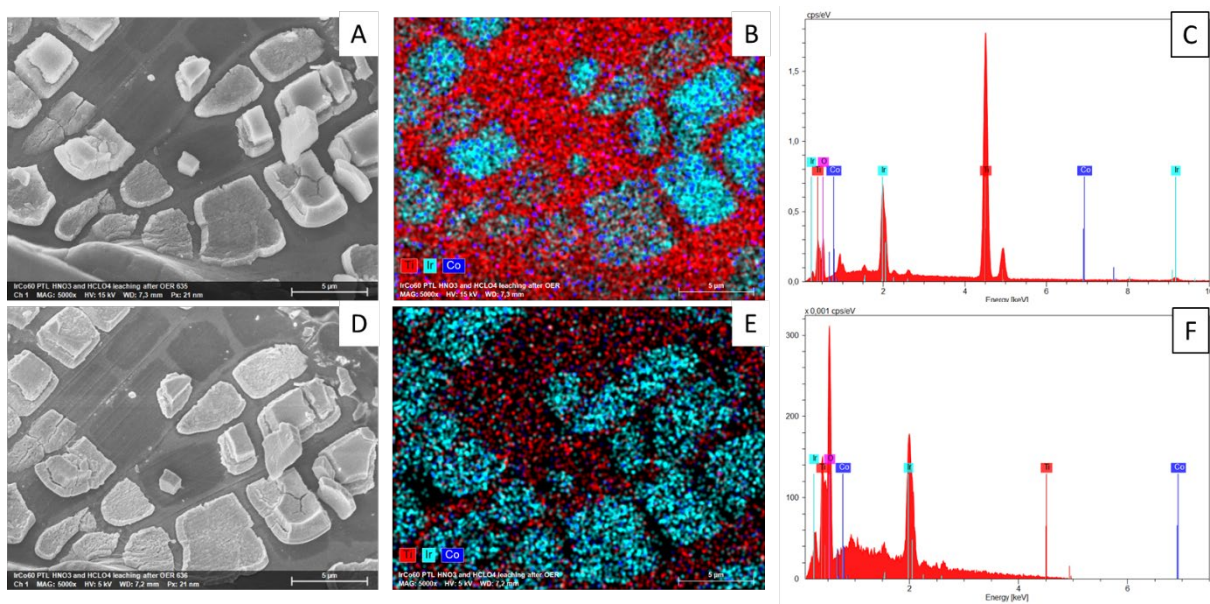


Figure 9. SEM-EDX at 5 k magnification of an Ir-Co catalyst with $0.250 \text{ mg}_{\text{Ir}} \text{ cm}^{-2}_{\text{geo}}$ deposited on a PTL fleece, with a Co: Ir ratio of 4, after being leached chemically on 1 M HNO₃ and 1 M HClO₄. The upper row (A-C) shows the effect of the higher acceleration voltage of 15 keV on the A) detected SEM morphology, B) the distribution of the EDX chemical mapping of Ti, Ir,

and Co, and C) the visible energy lines and counts acquired. As a comparison, the lower row (D-F) was taken at 5 kV, enhancing the D) SEM superficial features, at the cost of a less clear E) EDX mapping and 5 times lower F) count intensity and energy line resolution.

This problem was accentuated even more in the evaluation of cross-sections, where the layers were sometimes damaged by the preparation method. In this configuration, EDX was used only to highlight the chemical contrast between the sandwiched layers rather than to perform any type of quantification, see Figure 10B and D.

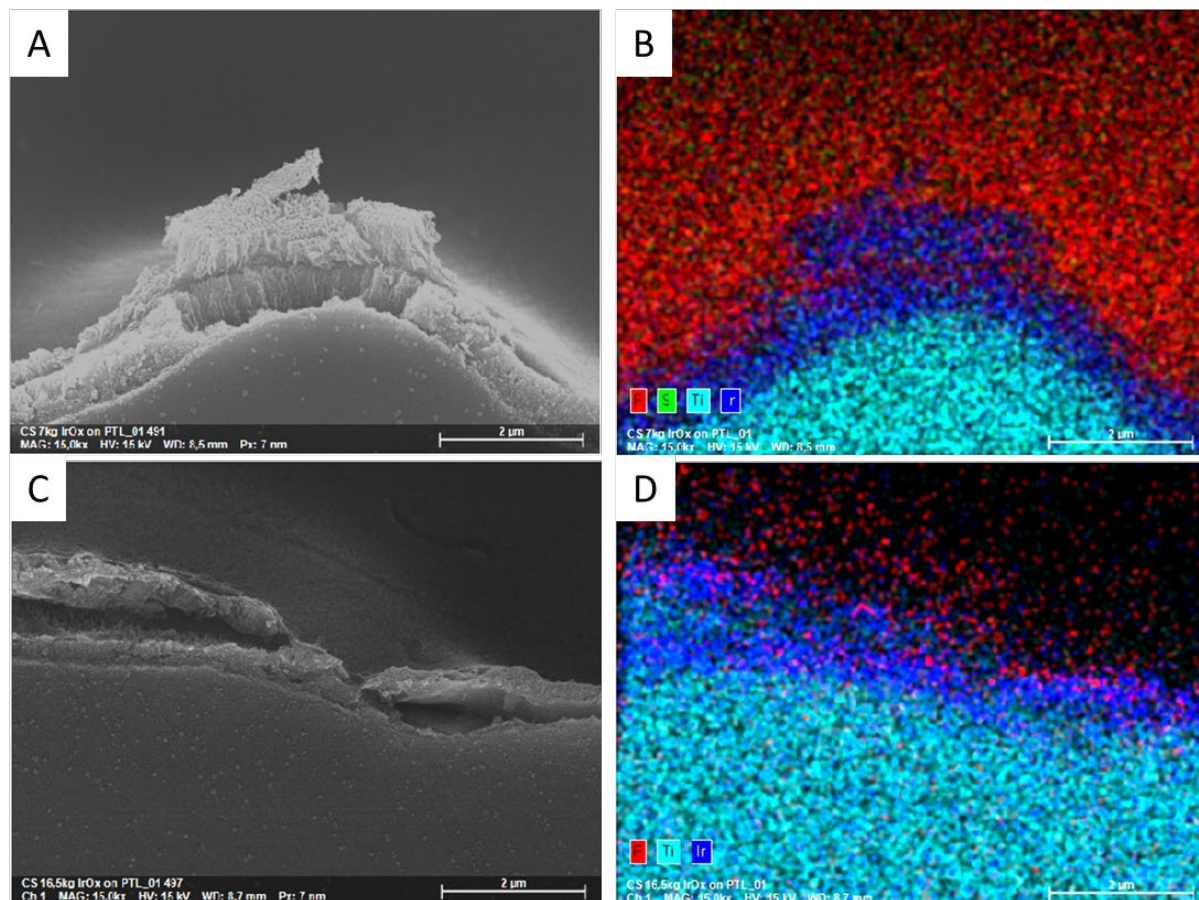


Figure 10. SEM - EDX Cross sections at 15 k magnification of an IrO_x catalyst. The SEM micrographs (A and C) show how the preparation might have affected the quality of the layer, with A) local spallation and C) membrane bending due to charging. Still, a qualitative idea of the element segregation and layer structure can be obtained from the EDX mapping (B and D) of the catalyst layer (Ir in dark blue) deposited on a PTL fleece (Ti in light blue) and hot pressed to a membrane (F colored in red).

X-ray Diffraction

X-ray diffraction (XRD) is a standard technique used in materials science to resolve the crystallographic structure. As stated in the Introduction, changes in phase crystallinity are closely associated with catalytic activity and stability^{55,72,75,79,88,89}.

In Manuscript II, the crystallinity of the Ir-Co catalysts with different Ir to Co ratios on GDLs was investigated *ex-situ* in the as-deposited as well as the after acid-leaching stages with a lab XRD (D8 Advance Diffractometer, Bruker) equipped with a $\text{Cu K}\alpha$ X-ray source.

The samples were extracted from the sputtered GDLs using a round punch of 3 mm in diameter, offering a relatively small analysis volume.

The data acquisition was performed by a laboratory technician using a Bragg-Brentano geometry over a 2 Theta range from 30° to 80° the step width of 0.5°, in 5-second steps. Even though a grazing incidence configuration (GIXRD) would probably have been more indicated for thin films in this type of samples, the amorphous nature of the samples and the increased Ir crystallinity after leaching were identifiable. The post-processing for the evaluation of the diffractograms was performed in the TOPAS software via Diffract Eva (access to databases ICSD and PDF) and Rietveld refinement, which eliminated most of the background noise.

X-ray Photoelectron Spectroscopy

In addition to the surface chemical analysis obtained by EDX, X-ray Photoelectron Spectroscopy (XPS) plays a crucial role in providing valuable insights into the catalyst's elemental surface composition, oxidation states, and chemical bonding by analyzing the photoelectrons emitted upon X-ray irradiation from the few nanometers of the material's surface.

XPS analyses on Ir-Co and IrO_x samples sputtered on GDL substrates were performed by a laboratory scientist following the same sample preparation procedure described for XRD. The spectrometer instrument (Axis Supra, Kratos) equipped a monochromatic AlK α source (1.486 eV) and an X-ray power of 150 W for survey and elemental scans, and 225 W for highly resolved measured spectra, respectively. Charge neutralization was used for all samples. Survey scan analyses were performed with an analysis area of 300 x 700 microns and a pass energy of 160 eV. Core level spectra of all identified elements were acquired at a pass energy of 80 eV, and the highly resolved measured peaks were collected at a pass energy of 10 eV. For these analyses, the instrument was set to the medium magnification lens mode (FOV 2) and by selecting the slot mode providing an analysis area of ~300 μ m.

Spectra were corrected to the main line of the carbon-1s (adventitious carbon) spectrum, which was set to 284.8 eV. Data analysis was performed using CasaXPS (2.3.15) using a Shirley background. Peak fits were achieved using Functional Lorentzian (LF) for the 4f-Peaks and Gaussian-Lorentzian (GL) lineshapes for the satellites as supposed by Freakley et al.⁹⁰

X-ray Absorption Spectroscopy

X-ray Absorption Spectroscopy (XAS) is a technique to examine the local coordination and bonding state of materials by determining the absorption of X-rays as a function of their energy. The measured decrease in X-ray intensity after penetrating a certain distance into the sample correlates with the material-specific linear absorption coefficient $\mu(E)$ that is determined and analyzed. By measuring several absorption edges, the local environment of the different elements contained in the sample can be analyzed.

There are two major regions in the absorption spectra. The first is the X-ray Absorption Near-Edge Structure (XANES), which corresponds to a window of about 50 eV from the detection of the ionization energy of core electrons in the form of a sharp absorption peak or "edge". The magnitude of the "edge" correlates with the oxidation state, which helps to identify the active species e.g. IrO_x involved in catalytic reactions.

The oscillatory tail past the XANES region up to about 1000 eV corresponds to the Extended X-ray Absorption Fine Structure (EXAFS) region. These oscillations are also characteristic of the surrounding atoms and their distances from the central atom since varying distances will result in different backscattering paths and as a result different wave interaction. Using different fitting models for EXAFS interpretation can yield information about the coordination and local structure, which is key to distinguishing activity to ligand and strain effects of multi-element catalysts^{91,92}. In contrast to XPS, XAS is a bulk method, i.e., the spectra display the average of each atom in the beam path.

Ex-situ XAS at the PSI X10DA beamline

Ex-situ XANES and EXAFS measurements were carried out by Adam Clark at the SuperXAS - X10DA beamline of the Swiss Light Source (SLS) at PSI, Switzerland (2.9T superbend source, storage ring current of 400 mA) of three series of Ir-Co catalysts sputtered on GDLs with different Co to Ir ratios after leaching using the floating-electrode configuration described at the end of chapter 2.1.3.

These measurements were conducted on three sets of Ir-Co catalysts deposited on GDLs with a loading of $0.4 \text{ mg}_{\text{Ir}} \text{ cm}^{-2}_{\text{geo}}$ and 4, 2, and 1 Co to Ir nominal ratios. The catalysts were leached using the floating-electrode configuration outlined in chapter 2.1.3. The experimental setup at the beamline consisted of a 2.9T superbend source and a storage ring current of 400 mA.

The leached samples were securely protected using Kapton film and directly mounted into a sample holder for the beamline experiments. The incident beam was collimated using a collimating mirror set at 2.9 mrad (Rh-coated for Ir L_{III}), and it was monochromatized in qexafs mode using a liquid nitrogen-cooled channel-cut Si (111) monochromators⁹³. The beam size on the sample was 1.5mm x 0.4mm (horizontal x vertical). Energy calibration was conducted using a Co reference foil for the Co K-edge position and a Pt reference foil for the Ir L_{III} -edge. XAS detection at the Ir L_{III} -edge was performed in transmission mode using ion chambers with 2 bars of N₂. Co K-edge spectra were collected using a PIPS detector in quick fluorescence mode⁹⁴.

Rebecca Pittkowski processed the data using ProQEXAFS, which involved calibration, interpolation, normalization, and averaging of each sample (with a measurement time of 300 seconds)⁹⁵. The averaged XAS spectra were further analyzed using the DEMETER software package. The raw spectra were aligned to a metal reference foil in terms of energy, corrected for background, and normalized based on the edge step. The energy units (eV) were converted to photoelectron wave number (k) units (\AA^{-1}), and the resulting $\chi(k)$ functions of the XAS spectra were weighted with k^2 and then Fourier transformed to obtain pseudo-radial structure functions.

The fits to the EXAFS spectra were carried out using ARTEMIS, a component of the DEMETER software package based on IFFEFIT⁹⁶. Reference XAS spectra of pure metal foils were utilized to estimate the amplitude reduction factors. For the Ir L_{III} -edge data, the fitting was performed in R-space with weights of k^2 and k^3 . The Fourier transform was applied within a k -range of 3-15 (\AA^{-1}), while the fit window was set within an R-range of 1.2-3.0 \AA . Similarly, for the Co K-edge data, the fitting was done in R-space with a weight of k^3 . The Fourier transform was performed within a k -range of 3-11 (\AA^{-1}), and the fit window was defined within an R-range of 1.15-3 \AA .

The metal-oxygen scattering path was assumed to have an ideal six-fold (octahedral) coordination, while the metal-metal scattering paths were based on a 12-fold coordination. To simplify the fitting

process for the Co K-edge EXAFS, the estimated values obtained from the respective fits of the Ir L_{III} -edge data were utilized and kept constant for the M-O and Co-Ir scattering paths.

In-situ XAS at the Diamond B18 beamline

To obtain more information from the formation of the local structural arrangements of the catalytically active iridium as well as the influence of cobalt as a secondary element under operating conditions, *in-situ* XANES and EXAFS were performed using an electrochemical flow cell configuration⁹⁷ at the Diamond B18 beamline. The measuring team sent to the beamline was formed by Jochen Klein and Sonja Blaseio from TU Braunschweig, who performed the XAS measurements; and me, who prepared the samples for the *in-situ* electrochemistry.

Aside from preparing a new batch of Ir-Co samples in the same way as for the XAS analysis at the PSI, a set of as-deposited samples was included. Furthermore, metallic Ir and IrO_x samples sputtered with a $0.4 \text{ mg}_{\text{Ir}} \text{ cm}^{-2}_{\text{geo}}$ on GDL substrates were provided as references.

Due to the configuration of the beam monochromators, it was not possible to measure Ir and Co together. Hence, X-ray absorption spectra were collected on the Ir L_{III} -edges of all Ir-Co leached samples *ex-situ* and *in situ*. Additionally, X-ray absorption spectra were collected of the *ex-situ* samples at the Co K-edge.

In the first place, *ex-situ* X-ray absorption spectra were collected at the Ir L_{III} -edge detectors for both the as-deposited and leached Ir-Co samples.

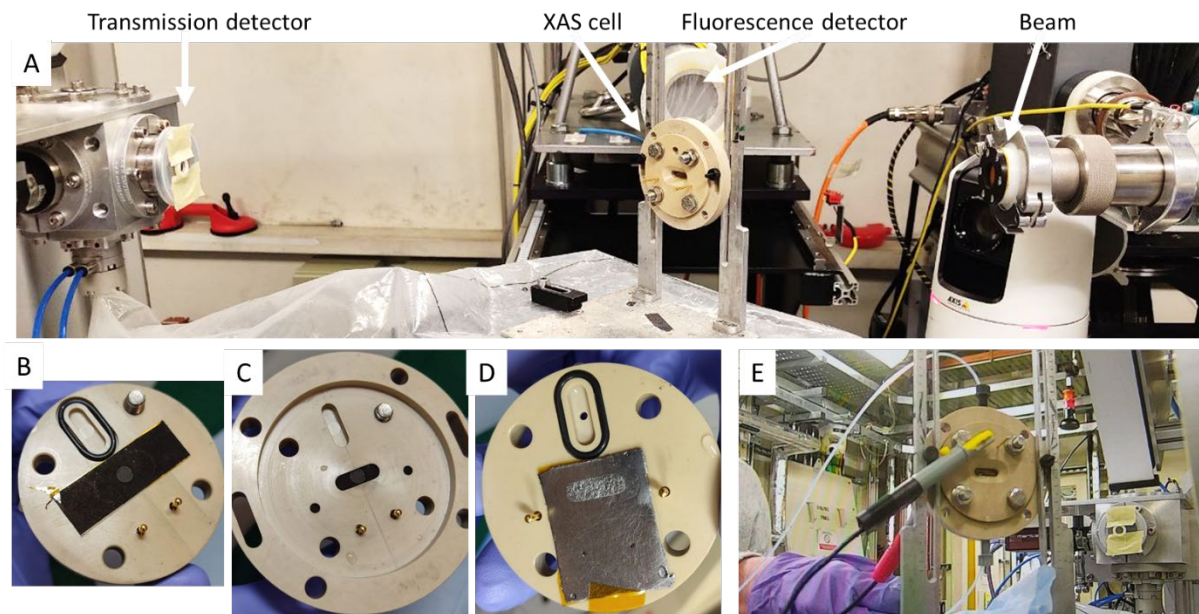


Figure 11. Beamline setup for *in-situ* XAS in the B18 beamline in Diamond A) Detectors and the cell configuration. Assembly of the B) sample embedded in carbon paper with Kapton backing as working electrode, C) cell separating element, and D) graphite cathode below the sealed reference electrode chamber. The assembled cell with the tubing for continuous flow of electrolytes can be seen in E).

Using the same beamline configuration, the three leached series with different Ir: Co ratios were mounted into the electrochemical flow-cell setup, see Figure 11. The samples were inserted first into a GDL backing taped with Kapton from the backside to electrolyte permeation and leakage and then

aligned with the analysis window in the center of the cell. To reduce the measurement noise and contact problems during the measurement, no membranes were used in the assembly.

In this setup, the X-ray absorption spectra of the Ir LIII-edge were collected *in situ*. The samples in the series were studied under an open circuit potentially and then under increasing oxidation currents (10; 100 and 250 mA/cm²). The chemical states and the local structure were studied with XANES and EXAFS respectively.

After the beam configurations were changed to measure Co, we intended to gather *in-situ* measurements on the same samples on the cobalt K-edge. Unfortunately, due to the constant flushing of the electrolyte over the surface of the electrode, the remaining Co content after the previous *in-situ* Ir-edge measurements was deemed too low to produce an acceptable signal in a reasonable measurement time. Hence, the Co edges could only be measured *ex-situ* in as-deposited and leached samples.

2.3 The Gas Diffusion Electrode (GDE) setup

To this day, the most conventional methods to benchmark catalyst activity for PEM fuel cells and electrolyzers remain the thin-film rotating disk electrode (TF-RDE), mainly for fundamental studies⁹⁸⁻¹⁰¹, and the membrane electrode assembly (MEA), which integrates the basic elements of a single-cell system.

Undoubtedly, MEA measurements provide the most comprehensive approach for investigating catalyst activity and degradation in PEMWE or PEMFC systems. In this setup, the performance of complete electrode assemblies with large electrode areas and thicknesses can be evaluated under realistic conditions, while maintaining meticulous control over reaction parameters like temperature, pressure, and reactant flow^{28,57,102,103}.

On the other hand, breaking down the influence of each element and specifically processes at the electrode interfaces from the overall system performance poses a significant challenge, which often requires extensive experience to achieve solid benchmarking conditions. Therefore, obtaining the full picture is a resource and cost-intensive process, not only in materials and instruments but also in human capital and time. Furthermore, to benchmark catalyst activity, RDE measurements can capture pure kinetic data.

Due to its relatively quick operation and cross-comparability, the TF-RDE has succeeded for many years in the research community as the preferred laboratory-scale method to extract catalyst activity. However, it's widely acknowledged that the idealized conditions found in RDE setups limit the comparability to the realistic operational conditions observed at the reaction interface within full membrane electrode assembly (MEA) systems. This discrepancy arises primarily due to artifacts identified in the measurements, reactant supply, the limited substrate options, and the restriction to use low catalyst loadings and current densities^{61,69,98,99,104,105}.

Fortunately, the recently introduced gas diffusion electrode (GDE) technique has helped greatly to bridge many of these limitations from traditional lab testing to industrial applications. Same as the TF-RDE, the GDE setup is a three-electrode setup designed for small electrode sizes, which can be easily assembled to produce multiple measurements in a short time.

However, the GDE permits the assessment of half-reactions by featuring realistic electrode structures and higher loadings that result from thicker layers. In this regard, the transfer of the reacting species is produced through the pore structure defined by the substrate and the catalyst deposition, permitting to study of different characteristic mass transport accurately. Furthermore, a membrane can be hot-pressed on the test electrode creating a triple-phase boundary analogously to MEA configurations. These conditions offer a true insight into the mass activities of the catalyst by factoring in the electrochemical active area and the specific activity recorded in the reaction surfaces.

The GDE technique has already been established for ORR conditions for PEMFCs^{62–64,79} using supported catalysts on carbon substrates and also introduced to OER studies^{70,71}.

A crucial focus of this work has been to develop and create a novel GDE setup aimed at evaluating self-supported catalysts used in water electrolysis under realistic conditions. Combining the GDE setup characterization and the PVD-MS catalyst manufacturing approaches allows for making better use of the resources by deriving the relationship existing between catalyst design and performance.

The process of expanding the capabilities of the original setup went beyond simply interpreting the electrochemical processes occurring within the system. It also involved comprehending the mechanical interactions influenced by the geometry of elements in the cell element and optimizing the measurement parameters to attain realistic operation conditions. The continuous setup optimization permitted to differentiate between artifacts and noise from valuable information related to the physical and chemical processes taking place in the system.

2.3.1 Self-supported catalyst optimization for OER in the GDE setup.

The introduction of the GDE setup for PEM electrolysis in acidic media has been only reported in a handful of studies^{70,71}. Furthermore, its application with self-supported catalysts had never been explored previously and hence required its own optimization path.

The starting basic half-cell GDE configuration was first introduced by Wiberg et al. (2015)⁶⁶ featuring a lower cell made of stainless steel with a circular flow field extruded \varnothing 3 mm inside and a Teflon top compartment with a single chamber. The reader is referred to Manuscript II for a visual understanding of the details of the original cell design and the changes that were introduced in the GDE into the cell to accomplish OER studies with in PTL substrates. Although the initial OER investigations on the GDE cell using carbon substrates did not require a special cell design, it was necessary to optimize two aspects.

First, the contact assembly was updated with a \varnothing 20 mm Teflon ring with a \varnothing 3 mm Ti PTL mesh inset. The Teflon washer provided a better sealing than the carbon paper and the PTL mesh improved the pressure distribution in all parts of the catalyst and hence guaranteed a stable electrical contact, which is especially relevant in an open cell setup where pressure is only applied from one side. Additionally, the inset also served as a guide to provide a reproducible sample positioning at the center of the cell. Underneath, a \varnothing 20 mm GDL without an MPL was used as a spacer to close the cell.

Second, a new pressing procedure was designed to form the GDE. The conventional cold-pressing procedure was not successful in creating a lasting contact between the membrane and the sputtered carbon substrates, which unlike the catalyst layers in previous studies did not include any binder in their composition. Therefore, the GDE assembly experienced delamination during the measurement

leading to poor activities and generally poor reproducibility. Hence, a hot-pressing step was necessary to infiltrate the Nafion from the membrane into the catalyst layer and create a much larger contact interface that could anchor the assembly together.

In this procedure, a custom hot-pressing station developed in the laboratory was utilized. This station employed a modified soldering iron to generate the necessary heat and featured a small vertical lever press equipped with adjustable weights to control pressure levels. To conduct the hot pressing, the soldering iron was set to a temperature of 130 °C, with the hot tip's temperature being monitored using a type J thermocouple. Before pressing, the GDEs were placed on the hot end of the setup 15 minutes in advance to ensure a uniform temperature distribution. Following this preheating step, the GDEs were subjected to a pressure of 84 bar for 60 seconds. This pressing process aimed to establish a strong interfacial contact between the coated substrates and the Nafion 117 membrane (183 μm thickness, Fuel Cell Store). The Nafion membrane was activated following the method described by Schröder et al. (2021)⁷⁰.

The hot-pressed GDE could then be placed into the cell over the contact assembly and tightened with a clamp. Next, the top chamber was filled with 1M HClO₄ as the supporting electrolyte, and the RHE and Pt wire used as CE were carefully positioned in their respective frits. Notably, the entire assembly process for a single test could be accomplished within 15 minutes.

2.3.2 Setup development

Initially, the GDE setup was used for OER studies using the same assembly configuration as in ORR investigations, where only GDLs and backing materials were utilized. However, there is a fundamental difference hindering this concept. In the case of ORR, even under high current densities, the cell potential window under normal operation ($0.4 < V_{\text{RHE}} < 1$) does not trigger the degradation of carbon material. This absence of degradation is crucial, as carbon degradation could otherwise lead to increased permeability electrolyte and flooding issues as it for long been reported in fuel cell start-up/shut-down situations under hydrogen starvation conditions¹⁰⁶. Indeed, when comparing the OER activity of Ir-Co catalysts on carbon substrates in Manuscript II, irreversible carbon degradation triggered at $> 1.6 V_{\text{RHE}}$ drastically limited the achievable current density range of the measurements. Therefore, approaching MEA-like conditions required changing the substrates to Ti PTLs, where the native TiO₂ oxide formed under acidic conditions offers much better protection against the high OER potentials.

Towards reliable activity measurements

The adoption of PTL substrates was the starting point of a series of modifications including a tighter, carbon-free assembly; newly designed cell elements for an improved iR-correction, and an updated water supply system using a peristaltic pump. The collective outcome of these changes resulted in the updated experimental setup, referred to as the PTE setup, exemplified in Manuscript III.

Initially, the adoption of Ti PTL substrates posed challenges in their processing. Unlike the soft GDLs, punching through the 0.4 mm Ti sheet caused deformation to the Titanium fibers, see Figure 12A and B. On the other hand, processing the material using laser cutting offered better results, see Figure 12C and D. However, using the latter method for every sample could question the PTE setup as a lab-scale technique for accelerated and economical testing.

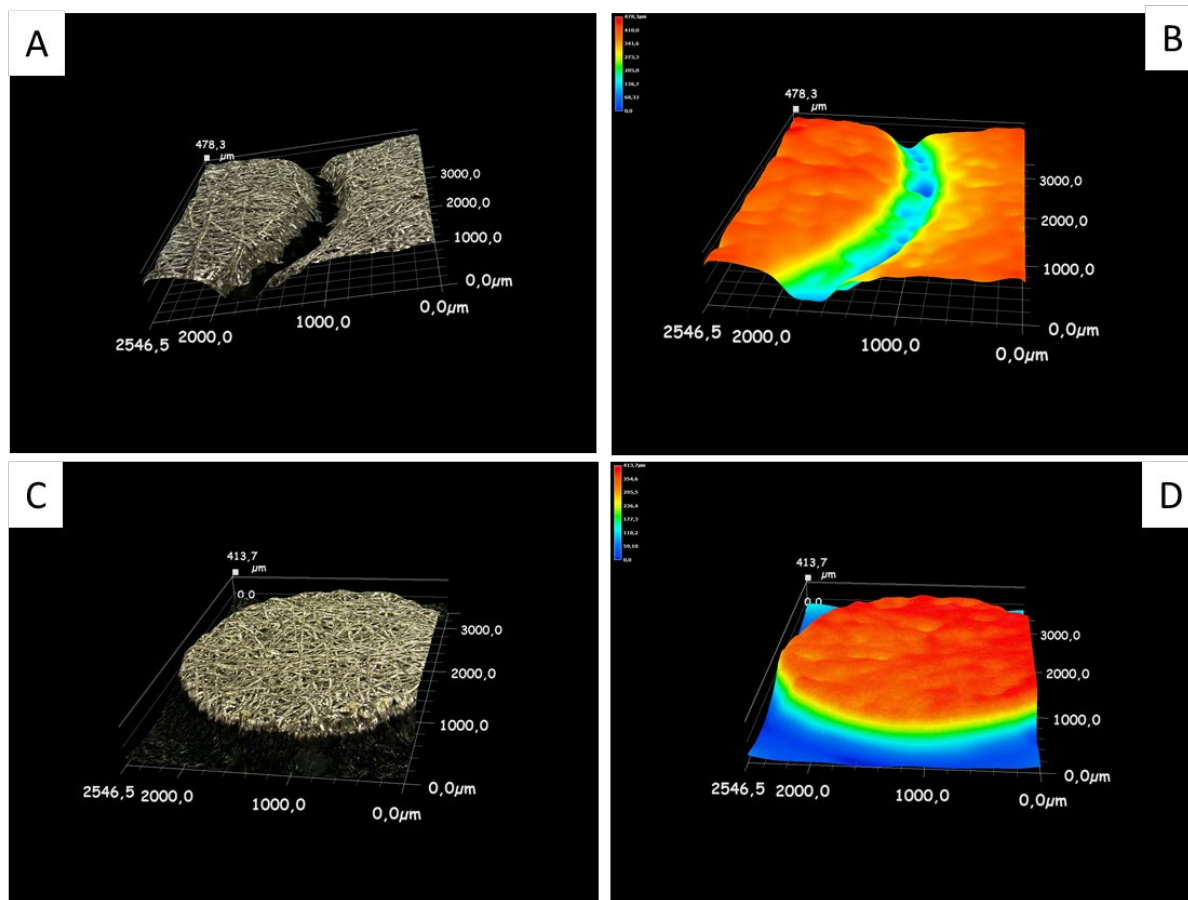


Figure 12. Confocal microscope images (A, C) and height map contours (B, D) from Ti felt PTL blanks of 3 mm in diameter were extracted by two different methods: hand punching in the upper row, and laser cutting in the bottom row.

The solution was to increase the punched-out areas from \varnothing 3 mm to \varnothing 5 mm. With a 277% increased area, the relationship between edge deformation and flatter, undamaged area in the middle of the samples was relatively small.

The larger electrode area is also signified using high currents, which could create a larger error in the measured potential considering the high measured high-frequency resistance (HFR) measured by the RHE. A newly designed top-cell made of PEEK addressed this problem with the incorporation of a Luggin capillary in a separate chamber ending directly on the membrane. In this way, the HFR measurement was reduced by 90% from the previous single-chamber configuration. The choice of PEEK over Teflon also prevented the bubbles from forming at the CE to stay at the bottom of the aperture creating a massive cell resistance.

Since the primary focus in Manuscript III was placed on the development of the PTE setup for extended current density studies, the catalyst material variables and preparation processes were minimized by using a sputtered IrO_x catalyst with 0.250 mg_{Ir} cm⁻²_{geo} on a PTL. Aside from the change in substrate materials from GDEs to PTEs, the influence of the hot-pressing method and the reactant supply of the high current density were also studied in the new setup.

The reactant supply was benchmarked using the parameters used for the former GDE configuration, i.e. using humidified O₂ gas at 100 sccm, and comparing it to using DI water supplied by a peristaltic pump (Ismatec Reglo Quick) into the cell at 40 ml min⁻¹ from an open reservoir.

The hot-pressing procedure in this study was performed at a temperature of 125 °C and for one minute. At first, the PTEs were hot-pressed with the membrane with a 7 kg weight as described in the former study in Manuscript II. As described in Manuscript III, the resulting contact pressure was only around 30 bar in the bigger electrode area, which showed low reproducibility and worse activity performances.

Hence, increasing the weight from 7 to 16.7 kg weight was needed to scale the 84-bar pressure to the bigger electrode area. The relatively thicker Nafion 117 membrane allowed very high pressures to produce a good electrode contact consistently without any pinholes. It should be noted that from the literature, the trends in pressure values in CCM configurations tend to be smaller in the range of 30 to 50 bar, as thinner membranes with lower ohmic resistances offer a better voltage efficiency²⁸.

In summary, achieving a larger current density reproducibly without mass-transport limitations in the PTE setup was only possible by combining a suitable hot-pressing method and using water as a reactant.

Considerations about stability measurements in the PTE configuration

While the PTE setup was soon ready to perform reproducible activity measurements, finding the right configuration for longer stability measurements at high current densities was not straightforward. The main challenge was to maintain good contact with the cell elements during the length of the measurement and find an optimal water flow to limit mass transport from bubble evolution at high current densities, which produces an unstable voltage signal.

Initially, it was assumed that mass transport limitations would decrease by increasing the flow until a constant stream of oxygen bubbles and water could be observed at the outlet. To observe the effect of different water flow rates on the stability of the measured potential was determined. A 10-minute run at operational currents of 2 A cm⁻² was conducted on an IrO_x catalyst deposited on a PTL fleece. The water was pumped from an open reservoir inside a double-sleeved glass insulation chamber into the cell through 6 mm thick flexible silicone tubing (Tygon R-3603, outer Ø 4.8 mm, wall thickness 1.6 mm). Three different water feed rates were chosen for the peristaltic pump: the pump was initially set at 40 ml min⁻¹, and then two additional values were tested, one set 100% higher and the other set 50% lower than the initial setting, see Figure 13A.

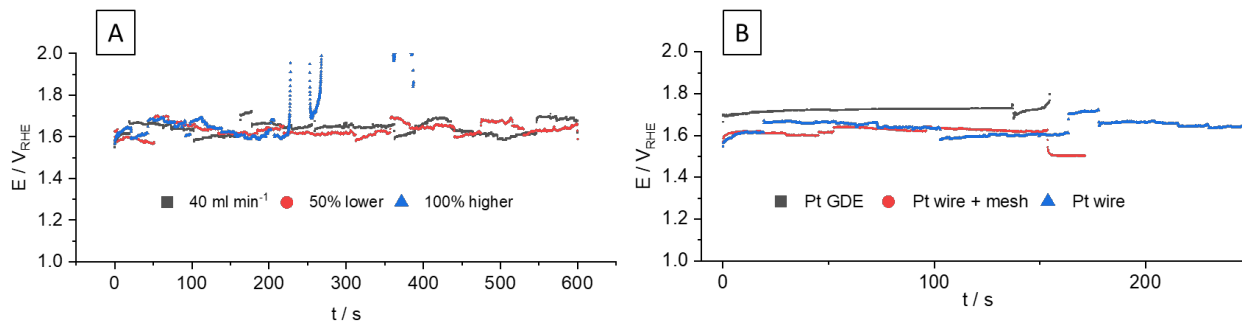


Figure 13. Voltage steadiness in the PTL setup at 2 A cm⁻² of an IrO_x catalyst of 0.250 mg_{Ir} cm⁻²_{geo} deposited on a PTL fleece. A) Influence of flow rate of water and B) Area and type of counter electrode.

Even though the higher flow rates influenced the ratio of liquid water to bubbles at the outlet, it did not greatly influence the potential stability during the activity measurements. The pulsed pump operation from the peristaltic mechanism was also not detectable in the voltage signal.

A further attempt was performed to investigate the origin of the voltage instability and bubble evolution as a function of different conditions in the CE chamber, see Figure 13B. In this case, the flow rate was fixed to 40 ml min^{-1} , and three CE configurations were explored: a normal Pt wire, a Pt wire with a finer coiling and larger area, and finally a Pt GDE hot-pressed in a single step with the membrane and anode PTE and contacted from the back with a carbon rod to avoid having electrolyte in the chamber. The increased surface area of the Pt showed only a small positive effect on the voltage stability. On the other hand, the voltage stability was greatly increased with the Pt-coated GDL configuration.

Since the bubbles were only avoided by eliminating the electrolyte from the experiment, it can be deduced that voltage instability is mainly produced due to oxygen bubbles in the electrolyte in the CE chamber nucleating over the membrane once the entire electrolyte volume is saturated. However, using a Pt-coated GDE as a CE is, in practice, preparing a small MEA with all associated difficulties: difficult alignment and hot-pressing preparation, contact issues and sealing problems with the reference electrode chamber, possible contamination (illustrated by the larger overpotential in Figure 13B) and in summary, sacrificing the simple operation and potential for diagnostic from the open configuration in the half-cell.

In the former experiments, it was detected that feeding water into the cell with the peristaltic pump increased the pressures between the inlet and outlet over time, pushing the PTE and the assembly through the aperture. The separation of the assembly elements resulted in increasingly worse electrical contact and decreased cell tightness. Ultimately, the increased pressure produced sudden failures due to water and electrolytes flooding the inner cell assembly or snapping off the tubing connections, as was the case while using higher flow rates (in blue) in Figure 13A.

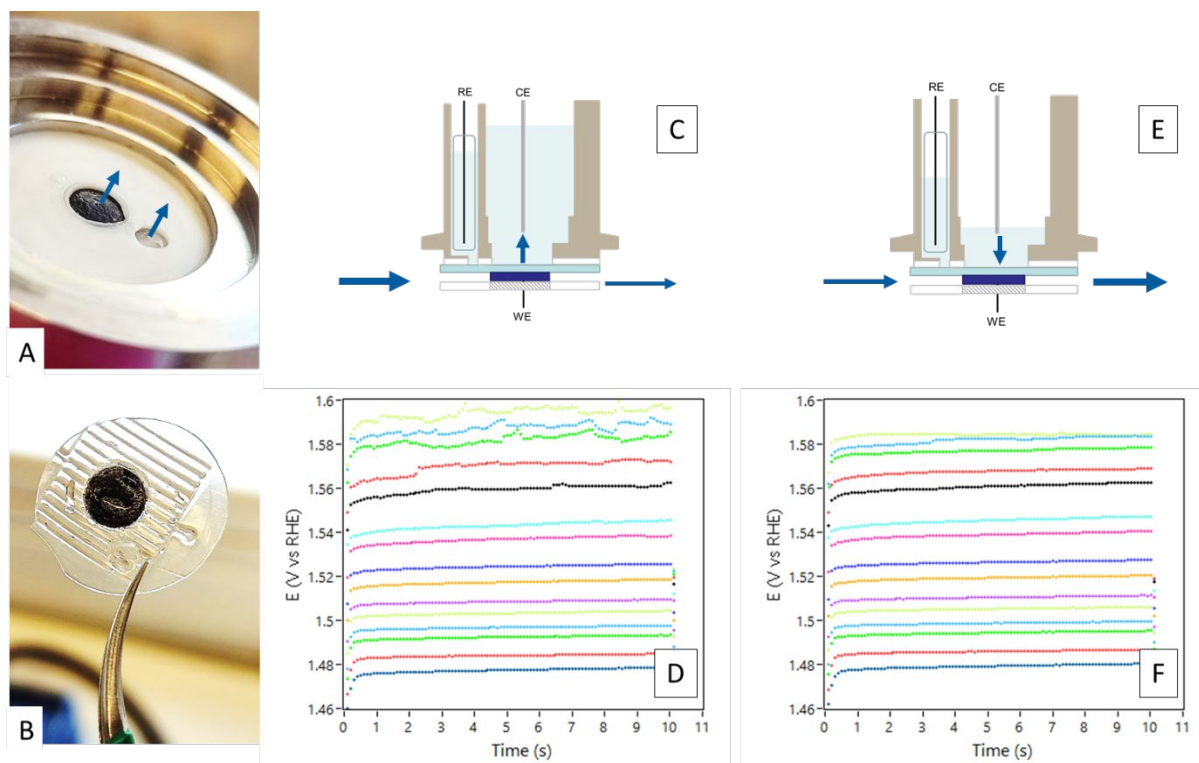


Figure 14. Improvements in the steadiness of the working electrode potential by changing the pump configuration. A) The pressure (represented in blue arrows) is introduced by the water as it is being “pushed” from the pump through the cell. B) While the outer membrane parts are tightly formed in the assembly, the upward force from water and the evolving gas can deform and detach the membrane from the substrate. Using the C) “push” configuration, the D) voltage steadiness at high current densities is resented. On the other hand, E) drawing the water from the reservoir into the cell creates a downward force on the membrane, helping bubble removal, and F) increasing the voltage stability.

A small advancement in maintaining a steady measured potential was achieved by reversing the pump configuration, see Figure 14. Instead of pushing water through the cell (Figure 14C), water was drawn from the reservoir at the same flow rate (Figure 14E), which helped reduce contact problems by creating instead a downward force that compressed all the elements together (Figure 14F). Moreover, the negative pressure ensured that the connections between the tubes remained closed while under compression. This configuration also allowed us to assess the assembly's tightness by directly observing the electrolyte level within the upper cell or the emergence of air bubbles from the outlet while the cell was not subject to any load. A quick appearance of air bubbles at the outlet and a rapid decline in electrolyte level due to the suction force from the pump evidenced that the cell was untight. A further advancement in the steadiness of the measured potential was reached by carefully adjusting the probing aperture of the Luggin in the top cell on an area of the membrane that would not deform under pressure.

2.4 Electrochemical Characterization and Characterization Techniques

All the electrochemical measurements were performed using a potentiostat (ECi-211, Nordic Electrochemistry ApS, Denmark).

Other than the experiments performed in Manuscript I, which were aimed at comparing the ORR activity and ECSA across different GDE setup configurations, the rest of the measurements included in publications II and III were performed on Ir-based catalysts with OER in focus. In Manuscript II, the

development of the metallic Ir-Co catalyst structure connected with the Co: Ir ratio was investigated in the GDE setup. Here, specific protocols were designed for the leaching of the Co, activation, ECSA, and OER activity determination. With the development of the PTE setup, stability protocols could be introduced into this configuration using IrO_x, as well as recording the degradation from the loss of OER activity and CVs included in Manuscript III.

2.4.1 Basic operation of the potentiostat

At the heart of all electrochemical measurements lies the potentiostat. Although more detailed explanations can be sourced from various references, it's crucial to grasp several fundamental concepts linked to potentiostat instrumentation to effectively configure electrochemical measurements and understand the limitations of the instrument. In the terminology used by Nordic EC for its potentiostats, these are the *current mode*, *current range*, and *control speed*.

Physically, the potentiostat records a voltage signal $U_{measured}$ when the current i_{WE} applied travels through an internal resistor $R_{measure}$, see equation 3. The different *current modes* refer to measurement resistors of varying magnitudes which apply independent conversion factors to transform current into voltage. In a later stage, the signal can be amplified, which is done by selecting the *current range*.

$$U_{measured} = Amplification \times R_{measure} \times i_{WE} \quad (3)$$

As it is stated in equation 4, the working electrode potential U_{WE} in a three-electrode setup is obtained by measuring the potential against the reference electrode. The iR-free potential can be obtained by subtracting the voltage drop through the solution resistance R_{sol} from the measured potential $U_{measured}$. This resistance can be recorded continuously with a small AC signal with a varying amplitude that is proportional to the current range. Changing the amplitude of the signal allows it to be strong enough to be detected, but not so high that it disturbs the applied current during the measurement.

$$U_{WE} = U_{measured} - i_{WE} * R_{sol} \quad (4)$$

One should also realize that changing the current mode could affect the R_{sol} compensation, as the $U_{measured}/i_{WE}$ the conversion factor for each resistor might be different.

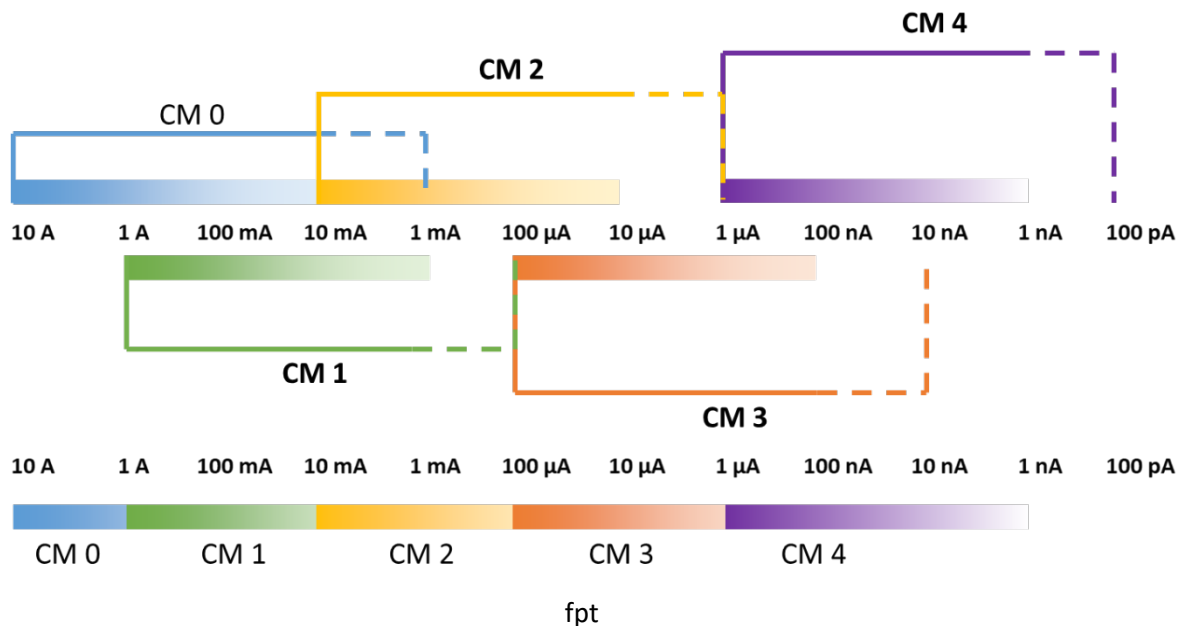


Figure 15. A schematic view of the current coverage scale from the ECi-211 potentiostat. The resistors controlling the current modes (CM) are represented in different colors and their current range is symbolized by the straight connectors. The saturation gradient represents the loss of measurement signal quality due to signal amplification.

As seen in Figure 15, the highest quality of the $U_{measured}$ potential signal is obtained with the minimum amplification. However, not all current ranges can be always selected due to the restrictions set by the current mode. Hence, it is important to find the correct current mode and current range combination for a specific measurement.

When we need the potentiostat to set a particular U_{WE} electrode potential, the *current speed* becomes important. This parameter refers to the agility of the potentiostat to perform the feedback loop to approximate the $U_{measured}$ to U_{WE} using a proportional integrative derivative (PID) controller. The components respond differently to time, which means that the frequency of the control loop can regulate the stability of the system at the cost of less responsiveness to follow the process. In a practical sense, a slower *control speed* is preferred for fast-changing processes, involving perhaps bubble evolution in a reaction. Effectively, the potentiostat reacts more sluggishly to the changes in the system. On the other hand, a faster control can make the measurement more stable in processes where small changes need to be adjusted quickly, such as in the CV using a Luggin capillary with a very low R_{sol} .

Aside from the electrical measurements, the used potentiostat collects and transmits electrical signals to other units responsible for controlling the experimental conditions, such as the switch between Ar and O₂ gas during the measurement process. As the setup evolved, a Pt100 resistor sensor was integrated to enable temperature readings in the stainless-steel bottom cell section. Additionally, the drivers were upgraded to regulate the speed of a peristaltic pump as part of the measurement protocol.

2.4.1 Reversible hydrogen electrode (RHE) calibration

Preparing the RHE was the starting point and the common denominator to all electrochemical measurements performed through the three Manuscripts. This choice was made due to its simplicity and ease of use.

The RHE consists of a glass borosilicate capillary with a Pt wire open to one side, which can be easily cleaned in an acid bath and boiled in water to strip away any metal and organic contamination. Once cleaned, it is prepared by driving the HER in situ with the supporting electrolyte, eliminating the need for salt bridges that could otherwise contaminate the electrolyte. Furthermore, the RHE remains pH-independent during the Oxygen Evolution Reaction (OER) as the pH corresponds to the solution, the same electrolyte is used. However, the open configuration could also allow oxygen from the air or foreign Co ion contamination from leaching residues to enter the capillary over time and shift its potential. The latter problem was solved after placing the RHE in a glass frit in the PTFE mono-compartment in the GDE setup and was neither detected when the RHE was in a separated compartment using the PEEK top in the PTE setup.

To prevent any false potential reading due to potential shifts, the RHE was prepared in a separate cell with a Pt GDE and an H₂-saturated electrolyte of the same molar concentration as the test cell, e.g. 1 M HClO₄. Cycling in a small potential window of -0.005 to 0.005 V with a 100 mV s⁻¹ sweep rate, the current behaves approximately linearly with the potential, allowing us to find the true V_{RHE} electrode potential at the intersection of zero current. The acceptable range for initial RHE values was defined as ± 0.003 V_{RHE}. In case of a larger deviation, the RHE was remade, and the calibration procedure was repeated to avoid systematic potential deviation errors. A large deviation can happen due to oxygen residuals in the gas atmosphere of the RHE.

2.4.2 Acid leaching of Ir-Co catalysts

Ir-Co catalysts prepared on GDLs described in Manuscript II were leached electrochemically in the GDE and the leaching station in 1 M HClO₄. The catalysts were submitted to a CV protocol using HClO₄ 1M reported by Jensen et al.⁵⁵. Leaching took place in a humidified Ar atmosphere with a flow rate of 100 sccm. The leaching process occurred within a potential range of 0.05 to 0.5 V_{RHE}, utilizing a scanning rate of 100 mV s⁻¹ for a total of 30 cycles. The final CVs were typically stable.

The selected potential window and the de-oxygenated atmosphere ensured that Ir remained in a metallic state, which is necessary for the quantification of the electrochemically active surface area (ECSA) using the hydrogen underpotential deposition (H_{upd}). After leaching, the electrolyte was exchanged into the top compartment to avoid Co contamination of the RHE and CE electrodes.

2.4.3 ECSA determination of Ir-based OER catalysts

Before obtaining the H_{upd} of Ir-Co catalysts in a metallic state, the GDEs were cycled 30 times between 0.025 to 1.2 V_{RHE} at a scan rate of 100 mV s⁻¹ while purging the cell with humidified Ar to clean the surface of any impurities and saturate the atmosphere with Ar to see the H_{upd} region. It should be noted that ECSA characterization by the H_{upd} method does not apply to sputtered IrO_x catalysts as the surface is already oxidized.

The hydrogen underpotential deposition H_{upd} was quantified from the integrated area in a window of 0.025 to 0.25 V_{RHE} of the last anodic scan over a linear baseline constructed from two current values

measured at larger potentials between 0.4 to 0.5 V_{RHE} in a capacitive-only window as shown by Inaba *et al.*¹⁰⁷

To determine the electrochemically active surface area (ECSA) of the catalyst, a fixed conversion coefficient of 176 μC cm⁻², as referenced by Jensen *et al.*⁵⁵, was applied to calculate the ECSA using the following formula:

$$ECSA [m^2 g^{-1}] = \frac{QH_{upd}}{L_{Ir} \times 176 \mu C cm^{-2}} \quad (5)$$

The changes in the H_{upd} area and the double layer capacity before and after OER activity and stability measurements provided a better understanding of the catalyst's behavior and performance over time. Averaging the charge from the CV area could help to distinguish between activation processes and loss of ECSA due to degradation. The degradation of the catalyst would be indicated by a decrease in the total charge area in the CV, both in the double layer capacity decreased along with the H_{upd}. On the other hand, a decrease in the H_{upd} in favor of an increase of the double layer capacity in larger potentials of 1 to 1.2 V_{RHE} would suggest an increase in total capacity and an activation process of the catalyst.

2.4.4 Activation protocol

All sputtered catalysts, especially the Ir-Co catalysts, were susceptible to undergo a structural and chemical transformation that led to an enhancement in their OER activity. This process, known as activation, involves the development of chemically active phases which are typically Ir oxides and hydroxides in a dynamic process. To achieve this, the catalyst must be exposed to controlled oxidation conditions where the active phases can be formed avoiding degradation as much as possible in the process.

There are different advantages to performing this under potential or galvanostatic control in the potentiostat. Under current control, the current is set between the WE and CE, and the potential is recorded between the WE and RE. However, as it was mentioned before in chapter 2.3, the highest current densities in GDEs were limited to hundredths of mA cm⁻² since the process was limited by carbon degradation. This effect was visible in the exponential increase in the overpotential per step after reaching a certain potential, where the irreversible degradation process was accelerated. Using current control, there is a risk of trespassing the stable potential window of the electrode.

Potentiostatic protocols are a more conservative choice, as they prevent any corrosion processes above the selected potential to be produced. In turn, any increase in uncompensated resistance leads to a diminished amount of current applied to the electrode, limiting the application of the current by the most resistive component in the electrode. A further improvement to this method is the application of iR-compensated potentials during the measurement, which is a feature made possible by the application of AC to in-situ compensate for the iR drop configuration. Only then, the potential applied is at all times as close as possible to the real potential at the electrode surface. Hence, the activation currents are generally more stable during the process.

The Activation step used in Manuscript II for Ir-Co catalysts on GDLs was designed after this principle, applying 1.70 V_{RHE} for 20 min. in an Ar atmosphere with an iR-compensation set to 95%.

2.4.5 OER activity determination

Aside from characterizing the activation and degradation effects by CV, OER activity measurements were recorded using a step galvanostatic protocol in the GDE and the PTE setup.

The initial parameters in the protocol for the GDE setup studies were transferred from the former OER studies in the GDE setup from Schröder et al.⁷⁰, such as using humidified gas as a reactant in a limited range of current densities. The OER activity protocol in the GDE setup in Manuscript II started at 0.25 mA cm^{-2} and was limited to current densities up to 250 mA cm^{-2} where mass-transport effects were already noticeable. This represents 1 to $1000 \text{ A g}^{-1}_{\text{Ir}}$ in terms of mass current density for the three Ir-Co series of equal loading ($0.25 \text{ mg}_{\text{Ir}} \text{ cm}^{-2}_{\text{geo}}$). In this range, a total of 15 data points were collected through sequential 5-minute current steps spanning over two different current modes to avoid using strong current amplification. The data points were collected in narrower intervals in the initial activation range and were progressively spaced as the current densities increased, and the last 30 seconds were integrated to obtain the potential at every specified current density.

The introduction of the PTE setup to explore realistic Ti PTL substrates allowed to extend mass transport-free OER currents by a factor of 8 up to 2 A cm^{-2} ($8 \text{ k A g}^{-1}_{\text{Ir}}$), feeding DI-water from a reservoir into the cell at 40 ml min^{-1} . As the focus of the protocol shifted towards larger current densities, 6 additional current steps were added, and the step length was reduced to 10 s. By choosing a shorter step length, a stable signal was achieved despite the rapid bubble evolution at elevated current densities. Comparing 10 and 30 s step lengths revealed that integrating the potential over the final second of a 10-second step yielded comparable results to the last five seconds of the 30-second step, which shows that a steady state could be achieved relatively fast, see Figure 16A.

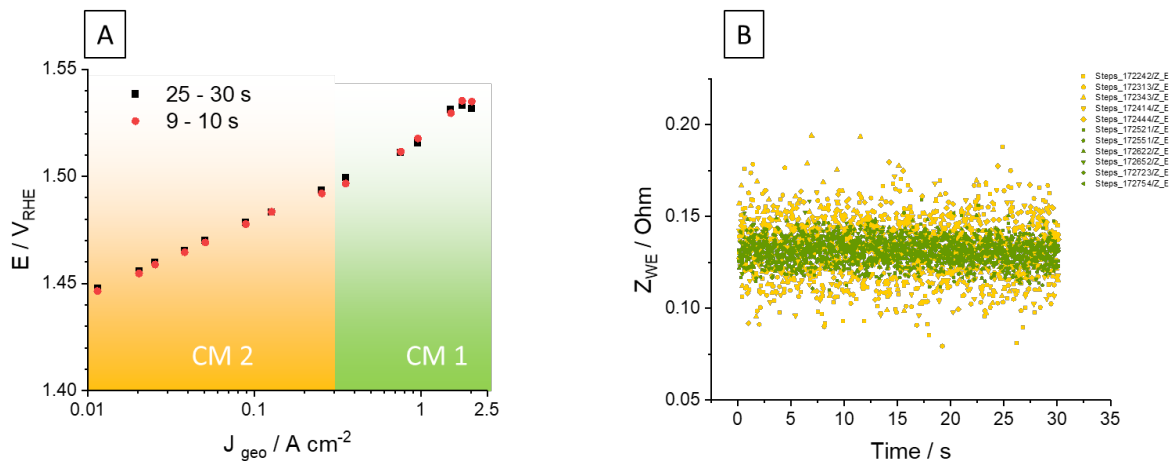


Figure 16. A. OER potential stability is compared between two different integration ranges for every step in the same protocol, with the indicated current modes (CM) used for the respective steps. B. The impedance signal collected in the steps at the lower current mode (orange) was more scattered than the ones at high current densities in the higher current mode (green).

In the GDE setup, the Tafel slope was obtained in a reduced interval in the kinetic-dominated region from 2.5 to 25 mA cm^{-2} where mass transport limitations were negligible. The enhancements made in the PTE setup in terms of precise iR -correction in combination with the better mass transports achieved in the electrodes allowed for Tafel extrapolation up to high current densities.

iR – correction

In both GDE and PTE setups, an AC signal with a frequency of 5 kHz and small amplitudes (max. 10% of the applied current) was applied to the DC currents to obtain the HFR throughout the length of this step. As discussed by Schmitt et al. (2022) in the context of ORR measurements in GDEs at high current densities¹⁰⁸, online-HFR measurement can provide a more accurate post-correction of the measured potentials in comparison with doing EIS every step, as the shorter steps minimized the possible artifacts like bubble evolution or temperature changes during measurements. However, this method delivers an overall value of uncompensated resistance, which in this frequency range is assumed to be equal to the HFR, i.e. the pure sum of ohmic contributions. In practice, the quality HFR signal collected must be interpreted carefully.

First, the HFR signal-to-noise ratio collected in the low current region is very low even if high AC amplitudes are used and should not be considered absolute. Fortunately, as the currents increase to magnitudes where the correction error becomes more relevant, so does the HFR signal-to-noise ratio, see Figure 16B.

Second, as previously mentioned, the recorded impedance recorded at this single frequency is assumed to be mostly dominated by uncompensated ohmic resistance contributions. That is, the sum of interfacial resistances from the RE up to the clamping position of the WE, as well as the bulk resistance of the membrane, catalyst, and all assembly elements including the cell body. As observed by Zheng W. (2023), a post-correction of the uncompensated resistance gives a value close to the intrinsic activity of the catalyst¹⁰⁹. However, to make the previous assumption, the phase value of the impedance should always be very small, close to zero. Nevertheless, it is not uncommon to observe increased phase values during the measurement, corresponding to capacitive contributions that increase the overall resistance value and draw overcorrection errors.

Phase variations in the measured impedance during the protocol might introduce *iR* post-correction errors by including capacitive or inductive contributions. These variations become more evident when switching the measured resistor by changing the *current mode* due to their calibration parameters. However, a more significant influence on the stability of the measured impedance lies in the quality of the cell assembly and the contact areas. Therefore, it is critical to maintain the cell contact surfaces free of any rust or debris, position the inner cell elements in a reproducible manner, and keep a constant clamping pressure when tightening the cell parts together.

2.4.5 Catalyst stability

Literature shows that the most challenging conditions for maintaining anode catalyst stability in PEMWEs occur during continuous high-current density tests for extended duration.^{104,110–112}

As introduced in chapter 2.3.2, stability measurements featured in Manuscript III at high current densities were first introduced with the PTE setup on an IrO_x sputtered catalyst with a 0.25 mg_{Ir} cm⁻²_{geo} loading to avoid introducing further material-related experimental variables such as leaching and activation.

The suggested stability protocol involved the application of a constant current density of 2 A cm⁻² in a 20 h continuous operation separated into 4 blocks of 5 hours. Online measurement of the high-frequency resistance (HFR) was conducted using a 5 kHz AC signal with a 5-mV amplitude. This

approach enabled the continuous assessment of cell resistance while causing minimal disruption to the measurement process.

Liquid DI water was recirculated at RT during the measurement pushing it from a reservoir in a 1.5 L laboratory flask into the cell at 40 ml min^{-1} with a peristaltic pump. CVs and the OER activity up to 2 A cm^{-2} were recorded before and after the stability test to assess the performance losses.

Eventually, this stability protocol on the PTE setup was also demonstrated for Ir-Co catalysts.

3. Discussion of the appended manuscripts

In this chapter, the manuscripts in which I was involved are presented. My specific contributions are indicated for each manuscript, encompassing activities ranging from conceptualizing, performing, and analyzing the experiments to the drafting of the manuscript.

In the discussion parts, the key findings are summarized and elaborated by incorporating insights from discussions in group presentations and conducting an in-depth analysis of experiments. This approach aims to offer readers a more comprehensive understanding of the topic at hand.

The appended manuscripts are presented in the following order:

Manuscript I consolidates the Gas Diffusion Electrode testing technique concerning its application for studying fuel cell catalysts. The technique addresses the need within the electrocatalysis community to bridge RDE and MEA measurements and provides transferrable insights at a research laboratory scale. In the manuscript an interlaboratory comparison is conducted and best practices are presented.

Manuscript II focuses on the integration of the Gas Diffusion Electrode technique for water electrolysis investigations using cutting-edge catalyst materials. It outlines an accelerated catalyst development cycle by combining this benchmarking technique with catalyst production methods using physical vapor deposition.

Manuscript III extends the application of the Gas Diffusion Electrode technique for water electrolysis investigations by introducing a Porous Transport Electrode configuration. These studies expand the capabilities of our setup to perform investigations of Ir-based catalysts on application-ready substrate materials at high current densities.

3.1 Manuscript I:

K. Ehelebe, N. Schmitt, G. Sievers , A.W. Jensen, A. Hrnjić, P. Collantes Jiménez, et al.

Benchmarking Fuel Cell Electrocatalysts Using Gas Diffusion Electrodes: Inter-lab Comparison and Best Practices.

ACS Energy Lett. **2022**, 7(2):816–26,

<https://doi.org/10.1021/acsenergylett.1c02659>

3.1.1 Description:

In recent years, extensive fundamental research has focused on developing catalysts for PEMFCs by RDE measurements. These efforts have led to the discovery of several promising catalyst materials. However, a notable challenge has emerged when translating these findings into technologically relevant conditions; particularly within the context of MEA tests, where noticeably less favorable performances have been observed.

RDE measurements are a fast and cost-efficient way to investigate the intrinsic activity of catalysts. MEA tests, on the other hand, are crucial for understanding the complex interactions among various components within the catalyst film, such as support and ionomer, as well as cell components such as the catalyst film, membrane, and porous transport layer. However, the effort and expenses required to set up and carry out MEA tests are considerable, requiring significant amounts of materials and time. These resource-intensive factors impede scientific progress. Furthermore, the task of comprehending electrode processes is inhibited by the fact that many factors contribute to the observed performance. Finally, comparing different MEA studies is hindered by differences in electrode processing and the applied operating conditions.

To facilitate the transition of new materials from their testing in research laboratories to industrial applications, it is essential to develop a robust testing platform at the laboratory level that allows the performance assessment of catalyst layers that can be as approximate as possible to MEA tests. For this purpose, several types of GDE half-cell setups have been introduced in recent years. They are intended as a “bridging tool from research to application”, combining a simple operation and cross-comparability ascribed to the RDE methodology with the more representative environment of full-scale systems investigated in single-cell MEAs.

However, to date, there has been a lack of consistency in the reported activity data obtained with the various GDE setups due to variations in the experimental protocols. The primary objective of this study was to establish a uniform measurement protocol for electrochemical and electrocatalytic characterization of materials across different laboratories, akin to previous work concerned with the RDE technique^{101,113–115}.

In particular, the study aimed to compare the obtained values for ECSA and the ORR activity when using different GDE setups, however, the same catalyst layer and experimental protocol. This study was conducted with three different GDE half-cell designs with varying geometric areas of the working electrode, i.e. GDE-L= 2.01 cm², GDL-M= 0.385 cm², and GDE-S= 0.0707 cm² (∅ 3 mm). In addition, measurements with a modified floating electrode setup (MFE) with a geometric working electrode area of 0.0316 cm² (∅ 2 mm) were also performed and compared against the other setups.

3.1.2 Contribution to the work:

I performed the electrochemical measurements on the commercially available Pt/C (HiSPEC® 4000) and PtCo/C (Umicore Elyst) materials prepared at the Helmholtz-Institute Erlangen-Nürnberg (HI-ERN) using the GDE setup configuration developed at the University of Copenhagen^{64,66}, denominated GDE-S in the study. Initially, I performed ECSA determination for both catalysts using H_{upd}. I received a protocol for the ORR activity determination using a step-galvanostatic control alternated with EIS steps for iR post-correction. I modified and optimized this measurement protocol for its application in my GDE setup. Aside from recording the ORR activity with the proposed step-galvanostatic

protocol, the evolution of the ORR activity under non-steady conditions was studied using cyclic voltammetry and amperometry on the Pt/C GDEs (HiSPEC4000). Finally, I contributed to reviewing the first draft written by K. Ehelebe along with the rest of the authors.

The ORR catalysts examined in this study included 1) A commercial Pt/C GDE (40 wt % Pt on Vulcan, FuelCellsEtc) 2) A self-sprayed Pt/C GDE (HiSPEC4000, 40 wt % Pt on Vulcan, Johnson Matthey), and 3) A self-spray-coated PtCo/C GDE (Elyst 0690, 30 wt % PtCo on high surface area carbon, Umicore).

3.1.3 Most relevant findings:

The research underscores the significance of maintaining the catalyst layer quality and using a unified benchmarking protocol to achieve comparable measurements with different setups. The different capabilities of used GDE designs are interpreted based on their respective electrode sizes.

Catalyst layer quality and GDE reproducibility:

An initial inter-lab comparison was established using the commercial Pt/C GDE used as a benchmark. Even though the ORR-specific activity obtained was in good agreement for all setups and the literature values from RDE studies, a trend for lower performance was seen in the setup designs with smaller electrode areas. This effect was attributed to a higher representation of catalyst layer defects in systems using smaller electrode areas, highlighting the importance of homogeneous catalyst layer quality in ORR activity and ECSA measurement reproducibility and independent of the setup configuration used.

The comparison was extended to the self-spray-coated Pt/C GDE (HiSPEC4000) and PtCo/C GDE (Elyst 0690), both with 3 times lower loading (0.1 Pt cm^{-2}) as compared to the commercial Pt/C GDE. In this comparison, the ORR activity and ECSA values measured using H_{upd} and CO-stripping were compared for both catalysts in all cell configurations. The ECSA of Pt/C HiSPEC4000 showed comparable values using both techniques on every cell setup, as well as the specific ORR activity. A SEM cross-section from this catalyst evidenced a homogeneous layer quality, which affirms the previous statement about the cross-comparability of results.

On the other hand, the ECSA collected by CO-stripping on the PtCo/C Elyst 0690 catalyst was consistently higher in every setup compared to using H_{upd} . The higher ECSA values obtained through CO-stripping could indicate that this method captures the active area of catalysts with a greater roughness factor with better accuracy, as it was observed for Pt-alloys in RDE¹¹⁶ and MEA¹¹⁷ configurations. Furthermore, the ORR-specific activity was substantially less comparable and showed a similar trend as for the commercial Pt/C catalyst, where larger electrode areas resulted in a higher performance. The discrepancies of ECSA and ORR activities between the setups observed for the PtCo/C Elyst 0690 catalyst were mainly attributed to the layer inhomogeneities due to the increased porosity of the high-surface-area carbon support material, as well as a non-optimized spraying deposition method. By using drop-casting instead of spraying for the catalyst preparation, an increased comparability of the ORR activities was achieved. Further differences related to activation processes in microporous catalysts were also acknowledged, but not explored in the scope of the study.

To finalize the comparison between catalysts, the ORR activity for every catalyst was benchmarked in the GDE-L setup configuration. Interestingly, the ORR performance trend of commercial Pt/C > self-spray-coated Pt/C > PtCo/C at low current densities up to $0.75 \text{ A}_{\text{geo}} \text{ cm}^{-2}$ was reversed at higher

currents, situating self-spray-coated Pt/C > commercial Pt/C > PtCo/C. This can be understood by analyzing the influence of mass transport on the observed reaction rate by determining the Tafel slope. Ultimately, these results show that GDEs provide a distinct view into the higher current range processes mirroring MEA conditions which cannot be extrapolated from RDE measurements.

The role of the GDE design in the electrochemical measurements

To achieve true electrode potential measurements, it is crucial to measure the uncompensated resistance (R_u) as precisely as possible. This is a setup-dependent variable that is typically scaled with the electrode area, where R_u is most affected by measurement artifacts in large electrode areas. It was demonstrated that the current densities achieved by scanning the potential over time are limited by R_u compensation errors and the difficulty of achieving a steady state even at low scanning rates. Scanning the current over time instead, known as chronoamperometry (CA), eliminates the error introduced by R_u compensation. Nevertheless, the dynamic nature of CA results in hysteresis between cycles that difficult the obtention of a reproducible voltage measurement difficult. Hence, the best practice to measure catalyst activity is to use a step-galvanostatic protocol, where the voltage is recorded in steady-state conditions. To achieve this, the measurement steps should be long enough to achieve the desired steady state, and measurement artifacts should not affect the averaged potential. Most importantly, R_u should be measured as precisely as possible to avoid large iR post-correction errors.

To correctly represent the ECSA measurements of Pt-alloy catalysts, CO-stripping should be chosen over H_{upd} when possible. In cases where H_{upd} is used, an integration baseline that follows the double layer capacity should be used with carbon supports with high surface area in RDE studies, as well as a reduced Ar flow to avoid shifts in the hydrogen reduction peak to more positive potentials, common in MEA studies.

Although all half-cell setups can produce comparable results using the same electrochemical protocol, their intrinsic differences from the different electrode areas and how they affect the iR correction need to be accounted for in the study design and result interpretation. From my perspective, the advantages of the setups with a smaller area are as follows.

In the first place, fewer catalyst and electrolyte volume is needed, reducing the costs per measurement. In turn, the molarity may be increased to raise the conductivity. In this study, the electrolyte molarity in the GDE-S setup was doubled to 2 M to reach 2 A cm^{-2} and obtain comparable results to the other GDE setups. On the other hand, a larger molarity could increase the risk of contamination, which is not so much of a problem in larger setups.

Additionally, using smaller currents simplifies the necessary control equipment e.g. for impedance spectroscopy, as compared to the comparable current densities in large areas. In particular, the measurement control of the iR -drop at large current densities is not so crucial due to the low absolute current. To illustrate this, the GDL-L had an iR drop of over 2 V at high current densities whereas the GDL-S was only about 1 V. However, a too-small electrode size can restrict the current density range due to very high internal resistance. This was the reason why the extremely small electrode size of the MFE setup had a restricted current density range of 0.5 A cm^{-2} , in contrast to the 2 A cm^{-2} attained by the other GDE designs.

In the third place, less heating and bubbles are produced when using a smaller CE, minimizing measurement artifacts. On the other side, the measurement stability at high current densities is reduced if the bubbles cover the whole electrode surface, which is a consideration to improve the setup design.

Finally, the smaller electrode areas used in GDEs give a much more sensitive electrochemical insight into the inhomogeneities of the catalyst layer as in systems using large areas. However, the smaller the electrode size, the larger the number of experiments to understand the average values of inhomogeneous catalysts, as well as the effort to maintain a high measurement reproducibility.

3.2 Manuscript II:

P. Collantes Jiménez, G. Sievers , A. Quade, V. Brüser, R.K. Pittkowski, M. Arenz.

Gas diffusion electrode activity measurements of iridium-based self-supported catalysts produced by alternated physical vapor deposition.

J Power Sources. **2023**; 569 (April).

<https://doi.org/10.1016/j.jpowsour.2023.232990> (Open Access)

3.2.1 Description

The scarce supply of Ir necessitates alternative approaches for designing more active catalysts with minimal resource usage in water electrolysis. PEMWEs are being explored for energy storage solutions and industrial hydrogen demand. As global hydrogen demand is expected to increase significantly, electrolysis capacity needs to be expanded.

In numerous scenarios requiring scalability, elevated current densities, and swift adaptation to changing loads, PEMWEs hold the upper hand compared to alkaline electrolyzers. Nonetheless, PEMWEs depend on costly PGMs, notably the scarce Pt for the cathode and the even rarer Ir to facilitate the OER at the anode.

Despite the strong efforts to reduce PGM usage by developing PGM-free catalysts with more abundant metals, Ir-based catalysts are presently regarded as the standard anode material option in commercial PEMWEs. Hence, it is important to consider alternative ways to increase the effective use of Ir and reduce its loading. The studied Ir-based catalyst features an enhanced ECSA due to its self-supported porous nanostructure. This process includes an alternated PVD magnetron sputtering procedure, which defines composition and morphology, followed by a selective leaching step to create the self-supported structure.

After demonstrating the viability of this method with Ir-Co catalysts in RDE studies⁵⁵, this research now shifts its focus to the electrochemical assessment using a GDE setup of three series of Ir-Co catalysts with a loading of $0.250 \text{ mg}_{\text{Ir}} \text{ cm}^{-2}_{\text{geo}}$ and different nominal Co: Ir (1,2 and 4) weight ratios. By optimizing the deposition parameters, a 10-fold improvement in OER performance was achieved compared to a commercial IrO_x particle catalyst of a higher loading tested in a comparable GDE setup.

3.2.2 Contribution to the work

In this work, I performed the electrochemical measurements and material characterization on three series of self-supported Ir-Co catalysts starting with a similar GDE setup configuration for OER studies as seen in the study from J. Schröder. G. Sievers performed the bimetallic catalyst deposition.

The self-supported structure was created in an acid-leaching process using a floating electrode cell configuration of my design. Then, I adapted the half-cell assembly to include a hot-pressing step to preserve good contact between all elements in the half-cell GDE assemblies, as well as incorporating better sealing elements. To measure the OER activity, I adapted the step-galvanostatic protocol proposed by J. Schröder and extended the upper limit of the current density range from 150 up to 1000 $\text{mA mg}_{\text{Ir}}^{-1}$.

I performed the SEM and EDX characterization and result interpretation in all bimetallic catalysts series. I also prepared the samples for the XAS performed at the PSI SuperXAS beamline X10DA. The results were measured by A. Clark and interpreted by R. Pittkowsky. A. Quade analyzed the samples I submitted for XPS analysis. Last, the samples I sent for XRD were measured by A. Albrecht, our lab technician.

I wrote the first draft, and after internal review from G. Sievers, M. Arenz, and R.K. Pittkowsky, it was approved by all co-authors.

3.2.3 Most relevant findings

This study design highlights the flexibility of the PVD + GDE method combination to fast-track the catalyst development process: The GDE cell shows the potential to bridge the gap between research and application for next-generation water-splitting catalysts.

Self-supported catalyst processing

The Co: Ir ratio detected by EDX in the as-deposited state ($\text{Ir}_{28}\text{Co}_{72}$, $\text{Ir}_{45}\text{Co}_{55}$, $\text{Ir}_{75}\text{Co}_{25}$) followed the same trend established in the nominal ratios (4,2,1), albeit not identically. The three series of Ir-Co catalysts displayed similar microstructural features and compositional and high homogeneity as observed by the SEM – EDX. XRD analysis indicated a highly amorphous catalyst phase structure.

After acid leaching of the Co in acid media, the morphology and the chemical distribution of Co and Ir in the layer were drastically transformed. Newly formed Ir-rich dendritic structures alternated with depleted areas on the carbon substrate could be observed by SEM–EDX. However, the morphology of these structures was not much alike the preparations obtained in glassy carbon in a former study by Jensen et al.⁵⁵. Nonetheless, a slight increase in Ir (111) crystallinity was detected by XRD as reported by the latter.

Even though Co was largely removed by the leaching process, EDX analysis showed Co contents up to 10 wt. % normalized with Ir. A further look into the local structure of Ir and Co after leaching using ex-situ XAS revealed a local Ir–Co coordination that followed the EDX data. Additionally, a mixed oxide and metallic character was observed, which was also observed by partial Ir oxidation states from the XPS analysis. Interpreting this information together with previous studies on Co stability in acidic media indicates the formation of a core-shell structure where part of the Co could have remained protected by an Ir layer formed during the surface restructuring process.

Electrochemical characterization in the GDE setup

The three series of Ir-Co catalysts experienced a positive influence of temperature increase and dynamic surface activation due to the oxidation of metallic Ir on catalyst activity. Interestingly, the ECSA and OER mass activities scaled with as-deposited Co content, following the sequence $\text{Ir}_{28}\text{Co}_{72} > \text{Ir}_{45}\text{Co}_{55} > \text{Ir}_{75}\text{Co}_{25}$ with a top oxygen evolution performance measured in terms of mass activity over ten times higher compared to a commercial IrO_x nanoparticle catalyst in a similar setup. The same ECSA and OER activity trend was observed in the results measured at 30 and 60 °C.

While the complex mechanisms behind Co content influence and electrochemical performance are not fully explained by measurement results., the remaining Co suggests a positive effect on specific activity attributed to higher dispersion and ligand effect, supported by Co leaching and the XAS data.

Ultimately, it was shown that the PVD catalysts could be measured with good reproducibility in the GDE setup. This could be attributed to several factors: first, a robust leaching process in the floating electrode (FE), which provided a controlled gas atmosphere and electrode potential conditions. In second place, is an optimized hot-pressing preparation process to form the GDE. Lastly, a steady process control in the catalyst deposition step as well as maintaining a consistent protocol for electrochemical characterization.

3.3 Manuscript III:

P. Collantes Jiménez, G.K.H. Wiberg, G. Sievers, V. Brüser, M. Arenz.

Bridging the gap between basic research and application: a half-cell setup for high current density measurements of Ir-based oxygen evolution reaction catalysts on porous transport electrodes.

J. Mater. Chem. A. **2023**, 11, 20129-20138

<https://doi.org/10.1039/D3TA04136K> (Open Access)

3.3.1 Description:

Bridging catalyst research and development to applications in PEMWEs requires testing at high current densities. While traditional lab techniques such as RDE continue to be used extensively to report catalyst activity and stability, this technique has been now proven to have intrinsic limitations in representing realistic catalyst morphologies and operating conditions. Hence, the only alternative to observe the real performance of the new materials is to perform membrane electrode assembly MEA tests. However, this technique presents many challenges for widespread research development. First, the data obtained requires a complex analysis to discern the influence of individual electrode processes on the overall performance. Additionally, the elevated expenses related to materials, setup instrumentation, and extensive optimization limit the accessibility of this technique to many research groups.

GDE half-cell setups offer a more accurate representation of individual electrode reactions and have been successfully implemented in ORR studies in comparable conditions to MEAs. First attempts to investigate the oxygen evolution reaction OER in GDE setups with Ir-based nanoparticle catalysts have reported comparable performances in the kinetic region to former RDE studies. Using the GDE setup, our previous study demonstrated a 10-fold increase in activity in a novel series of self-supported Ir-Co catalysts created via PVD in comparison to that of IrO_x nanoparticle catalysts measured under similar conditions¹¹⁸.

However, the corrosion and flooding issues at OER potentials brought by using carbon as the substrate have previously restricted until now the characterization to low current densities. This work expands the GDE setup to technologically relevant operation conditions at current densities of $>2 \text{ A cm}^{-2}_{\text{geo}}$ by introducing small but important changes in the cell configuration to allow accurate and reproducible measurement of PVD sputtered catalysts on Ti PTEs using liquid water. The optimized PTE setup was used to benchmark the OER activity and stability of self-supported IrO_x and Ir-Co catalysts, extracting information about catalyst degradation in realistic OER conditions for the first time in this configuration.

3.3.2 Contribution to the work

I performed the electrochemical activity and stability measurements of the electrode assemblies as well as the material characterization using SEM. G. Sievers performed the IrO_x and Ir-Co catalyst deposition on GDL and Ti PTL substrates. G. Sievers and G.K.H. Wiberg introduced the idea of the Luggin capillary ending on the membrane, from which I created a top-cell design used in the PTE setup configuration. The activity protocol was extended from our former study in GDE configuration, extending the upper limit of the current density range by an order of magnitude from 250 up to 2000 mA cm⁻²_{geo}. I wrote the first draft, and after an internal review from G. Sievers, M. Arenz, and G.K.H. Wiberg, it was adapted and approved by all co-authors.

3.3.3 Most relevant findings

This study proposes a new design of GDE setup, denominated the PTE setup, compatible with realistic electrode materials and able to reach realistic operation conditions. This setup fundamentally improved the OER activity and stability determination of state-the-art self-supported catalysts.

Creating functional OER electrodes

In the context of the self-supported catalysts embedded in GDEs discussed in Manuscript II, a crucial aspect for maintaining assembly stability during measurements was the integration of a hot-pressing stage. This procedure effectively countered membrane detachment due to significant bubble formation, an issue encountered with the cold-pressed method.

Despite this, the promising performances reported for these catalysts in the former GDE setup were still limited by mass transport limitations due to the corrosion of carbon substrates in OER potentials already at current densities of $100 \text{ mA cm}^{-2}_{\text{geo}}$. Consequently, the switch to Ti PTEs in the PTE setup became necessary to eliminate carbon degradation sources and fully leverage the potential of self-supported catalysts. To facilitate the processing of these electrodes and achieve more reproducible results, the electrode area was increased, and the hot-pressing procedure was optimized to achieve a strong contact.

Setup enhancements

As observed in Manuscript I, larger electrode areas require more precise management of uncompensated resistance at larger current densities. To tackle this issue in the PTE setup, a new cell top was designed featuring a separated chamber for the reference electrode with the Luggin capillary directly connected to the membrane. By doing this, the resistance was reduced by 90%, and voltage fluctuations due to shifts in electrode positioning were minimized. A second chamber was designated to allocate the counter electrode. The upper compartment was constructed using PEEK, a more hydrophobic material than Teflon, which was essential to manage the massive bubble formation at high current densities and prevent blockages of the electrolyte path to the counter electrode.

Aside, a key element to achieving higher current densities with optimized PTEs was the addition of liquid water as a reactant supply. A rectangular flow field pattern was used in the bottom cell to achieve more even water flow and minimize membrane deformation. Transitioning from humidified gas to liquid water required some minor assembly modifications using Teflon rings to provide better sealing and prevent water leakages.

Electrochemical characterization in the PTE setup

A comparison was conducted to evaluate the OER activity between the GDE setup and the PTE setup. This was benchmarked against a sputtered IrO_x self-supported catalyst on both carbon GDEs and titanium PTEs while considering variations in hot-pressing and reactant supply conditions. The results indicated that the most favorable OER performance was achieved by combining PTEs with liquid water under the optimal hot-pressing parameters, as it was recently reported by Geuß et al.¹¹⁹.

For benchmarking purposes, a stability test was conducted on the IrO_x material applying a constant current of $2 \text{ A cm}^{-2}_{\text{geo}}$ for 20 hours at room temperature. Aside from some artifacts found in the measurement related to the electrolyte consumption, the catalyst showed remarkable stability. The degradation during the measurement was interpreted from the OER activity decrease and the flattening of CV features between the beginning and end of the stability test. In comparison, an Ir-Co self-supported catalyst had similar stability during the first 5 hours of measurement at the same current density, but at harsher temperature conditions.

The results in this new setup indicate that self-supported Ir-Co catalysts are viable catalysts for further development in single cells.

4. Conclusions and perspectives

4.1 Conclusions

This thesis primarily explores two concurrently developed ideas. On one side, it delves into the creation and enhancement of self-supported Ir-based OER catalysts created by plasma synthesis. Complementary, it focuses on adapting and optimizing the GDE setup as a measurement tool within this context, demonstrating its potential as a laboratory method capable of studying the catalyst performance and stability under realistic conditions.

As a frame to this development, the intrinsic capabilities of the GDE setup for catalyst benchmarking are compared in different GDE configurations in the context of ORR studies. It is shown that reproducible measurements can be obtained across every GDE design despite their intrinsic limitations when a unified benchmarking protocol is used. The further use of the GDE setup in OER studies focuses on developing Ir-Co self-supported catalysts with adjustable properties through a process combining an alternating magnetron-sputtering step of Ir and Co followed by selective Co leaching. This study sparked the development of a new version of the gas diffusion electrode setup, denominated the PTE setup. In this optimized version, the OER activity and stability studies of the self-supported catalysts can be characterized using more realistic electrode materials and operational conditions.

In the first place, an inter-lab comparison of four GDE designs was conducted to evaluate the reproducibility of ORR activity and ECSA measurements (Manuscript I). This was explored with three types of Pt-based particle catalysts deposited on carbon: a commercial and a self-sprayed Pt/C and a self-sprayed Pt-Co alloy. The limitations to cross-comparability are discussed in terms of material processing, i.e. achieving a homogeneous catalyst layer quality; and best measurement practices i.e., using unified test protocols with the highest possible iR -correction accuracy.

From the material processing perspective, the commercial Pt/C and self-sprayed Pt/C catalysts demonstrated notably similar specific activity in all setups, with the self-sprayed variant exhibiting relatively superior layer quality. However, the self-sprayed PtCo/C alloy catalyst exhibited significantly more limited measurement reproducibility and cross-comparability. Leaving aside the possible activation effects of the nanostructured layer of this catalyst, the origin of this discrepancy was determined to be the lower layer quality from the manufacturing process. Indeed, higher performance was obtained when using optimized drop-casting deposition parameters.

Concerning the choice of best measurement practices, a further comparison between $H_{up,d}$ and CO-stripping as ECSA determination techniques showed that CO-stripping tends to give higher surface area estimates. This suggests that CO-stripping could offer a more accurate determination of ECSA in catalysts with rougher morphologies. Regarding the protocol for ORR activity determination, it is shown that a steady-state protocol with galvanostatic control and iR post-correction is far more stable and reproducible across setups as opposed to scanning techniques of the potential or the current. Ultimately, the accuracy of the R_u determination in the different designs becomes the crucial step for the correct determination of the electrode potential during the measurement, especially at high current densities where the error can be in the same order of magnitude as the potential it is measured. This correction error is minimized in the GDE setups using smaller electrodes, as the absolute currents are scaled accordingly. However, the smaller electrodes provide a larger resistance,

which in some cases (i.e., the MFE setup) can limit the achievable performance compared to larger designs. Aside, other setup differences must be considered for interpreting results. Smaller setups minimize the artifacts introduced by heating and excessive bubble formation and reduce the cost of materials and instruments for measuring low currents. However, with these setups, it is paramount to control the iR correction and perform multiple measurements to average the effect of catalyst layer inhomogeneities.

Ultimately, this study emphasizes the importance of maintaining quality in catalyst layers and using best-practice methods to achieve reliable measurements across various setups, particularly considering the effects introduced by their electrode sizes.

With regard to the development of the Ir-Co catalysts, the evolution of the OER activity and ECSA of three series of Ir-based self-supported catalysts produced by PVD was benchmarked in the GDE setup (Manuscript II) and compared to a commercial catalyst. After an alternated magnetron sputtering process to produce three catalysts series with different Co:Ir ratios, an electrochemically controlled Co de-alloying acid leaching treatment was used to selective remove the Co, which has a scaffolding effect on the catalyst structure.

As a result, the nanoporous layer developed a slight increase of the crystallinity and an Ir-rich dendritic cluster morphology, which interestingly, differed from the former morphologies observed on glassy carbon from earlier studies. This effect could be ascribed to the irregular substrate topography and the increased thickness catalyst layer achieved with the $0.250 \text{ mg}_{\text{Ir}} \text{ cm}^{-2}_{\text{geo}}$ loading.

Further CV and OER activity measurements revealed a dynamic surface activation process with a positive impact on catalyst performance, especially at increased temperatures. In this regard, the higher the Co content was initially sputtered in the catalyst, the higher the measured ECSA and OER activity. An exceptional 10-fold increase in OER mass activity was reported for the highest Co-containing series compared to the commercial IrO_x-supported catalyst, underlining the potential of the plasma processing and GDE development cycle to fast-track catalyst development.

As it was shown in a previous study with a similar material⁵⁵, XPS and EDX analysis showed that Co could still be found in trace amounts even after the acid-leaching process. This surprising finding could be explained by the formation of an Ir-shell structure protecting the Co remained in the core from contact with the acid. Indeed, the correlation between the specific activity and the Ir-Co bonding from the XAS coordination data after leaching could indicate that the residual amount of Co might have a positive effect on the catalyst activity beyond simply acting as a templating agent to increase the catalyst surface area. Nevertheless, a mechanistic explanation to demonstrate this hypothetical ligand effect lies outside the purpose of the study.

Finally, the benchmarking capabilities of the GDE setup were expanded and optimized for its use with Ir-based sputtered PTEs, allowing for the first time to obtain kinetic-dominated current densities up to $2 \text{ A cm}^{-2}_{\text{geo}}$ without diffusion limitations (Manuscript III). As demonstrated with a sputtered IrO_x and an Ir-Co nanostructured catalyst with low loadings ($0.250 \text{ mg}_{\text{Ir}} \text{ cm}^{-2}_{\text{geo}}$), the new PTE setup is mature for OER and stability measurements at application-relevant conditions, which particularly for the nanostructured Ir-Co catalyst have even shown very promising results. This reconfigured setup serves as a valuable tool for bridging the gap between laboratory research and industrial settings, potentially accelerating the development of self-supported Ir-based catalysts toward more complex systems.

The most decisive step toward achieving stable electrodes at OER potentials involved replacing carbon with Ti in the electrode preparation process. Due to the stiffness of the Ti fibers within the PTLs, a more careful approach was required for sample extraction and the application of hot-pressing procedures, as detailed in Manuscript II. By increasing the electrode area to offset the surface inhomogeneity after punching and adjusting the pressure accordingly, good contact was still achieved between the membrane and the PTEs.

Subsequently, several enhancements were made to the PTE setup to improve *iR*-correction and incorporate liquid water as a reactant. This modified configuration, featuring an IrO_x catalyst on a PTE, demonstrated the clear advantages of GDEs. It enabled the achievement of current densities of 2 A cm⁻² without encountering mass transport issues—a critical context in which to evaluate catalyst stability. Indeed, the IrO_x catalyst proved itself as a reliable benchmark for stability at 30 °C in a 20-hour stability measurement at high current density.

Furthermore, the Ir-Co catalyst exhibited comparable stability at the same current densities and even at higher temperatures, as seen in a five-hour stability measurement. Considering the increasing popularity of direct-deposition methods for nanostructured catalyst development in PEM electrolysis, which are primarily found in academic research contexts, the PTE setup can expedite the benchmarking and selection process before standard MEA testing.

4.2 Perspectives

As it can be deduced from SEM microscopy and CV features, the preparation of the high porosity self-supported Ir-Co structures with high ECSAs in this study is not achieved without losing a large amount of Ir in the acid-leaching process. As seen both in GDL and PTL substrates, large areas are stripped away from the coating, which under the aggressive leaching conditions proves to have an insufficient adhesion. Hence, it is fundamental to find better ways to improve the layer adhesion to the substrate as well as find a reproducible manner to dissolve the templating element in the leaching process without damaging the structure.

To this extent, the use of surface pre-treatments becomes extremely important for catalyst-coated substrates. The incorporation of surface roughening steps in an inert atmosphere can help to achieve better layer adhesion. Furthermore, the substrate can be functionalized with thin sputtered interlayers of high conductivity before the catalyst deposition as shown by Liu et al.⁵³, increasing the conductivity and protecting the substrate against oxidation in the few microns away from the anode catalyst-membrane interface where the potentials are highest in operation¹²⁰. As it has been demonstrated in previous work^{55,74,88,121}, magnetron sputtering provides a perfect environment to integrate these processes directly in catalyst manufacturing under very controlled conditions. Earlier attempts of this procedure in PTE configurations, which have not been included in this thesis since they are being studied within an industrial context, show a very positive evolution in the catalyst activity and stability.

On the other hand, exploring the origin of the activation effects reported for the different series of Ir-Co catalysts on GDEs poses a significant challenge. While the Ir-Co bond length from the ex-situ XAS analysis of the leached samples suggested the influence of a ligand effect between these two elements and the formation of a core-shell structure, supported by the specific activity and the EDX,

this hypothesis is supported by the previously observed behavior in similar systems and cannot be entirely confirmed from the gathered data. Ideally, the *in-operando* XAS study attempted at the B18 Diamond beamline would have provided valuable insight into the evolution of the core-shell formation in the leached catalysts. However, after this experiment, it could only be affirmed that: 1) the mixed contributions of Ir and residual Co to the local coordination after the EXAFS fitting indicate the formation of an alloy and that 2) the oxide content detected by XANES increased in the mixed metallic structure as a function of the applied oxidative current. The main limitations found were that neither the trace Co content that remains in the catalyst layer after leaching nor the carbon substrates exhibit sufficient stability under OER conditions to make definite estimations. This problem is accentuated by the mechanics of the XAS flow cell design, where the catalyst is continuously exposed to electrolyte convection, accelerating its degradation. Even after long analysis times to improve measurement quality, it was hard to discern whether cobalt was still present at the high current densities related to the oxygen evolution reaction. The reason is that the data could be fitted with different structural models both including and excluding cobalt. As cobalt is the minority element after acid leaching, the data collected from the Ir L_{III}-edge alone does not provide conclusive evidence for the presence or absence of cobalt in the nanostructured iridium networks under operating conditions.

There are multiple ways to address this limitation, starting by proposing a XAS study of the evolution of the structural features of Ir-Co *in operando* conditions with surface-treated PTEs, where the catalyst layer and substrates could remain stable at higher current densities. Nevertheless, this would require further development of the cell configuration for synchrotron studies to guarantee the sealing integrity during the experiment. Even then, it would only be possible to measure the absorption in fluorescence configuration since the X-ray transmission would be blocked by the high absorption of the Ti substrates. Therefore, it would make sense to combine the analysis of the site coordination with other microscopy analysis methods such as high-angle annular dark field scanning TEM (HAADF-STEM)^{122,123} and electron energy loss spectroscopy (EELS)¹²⁴, which can strengthen the confidence in the hypothesis about the formation of core-shell particle formation of the catalyst.

Time efficiency is also an essential matter at large-scale facilities, which requires careful sample pre-selection. Concerning this point, the task that was set out in this thesis to find a reliable platform for benchmarking the OER activity of the self-supported catalysts was achieved with the development of the GDE setup into the PTE configuration. Furthermore, the same system was shown to be compatible with stability studies that exceed any of its class. This was however not achieved without limitations, which could be overcome by optimizing the sealing system. Mitigating the uneven pressure distribution within the central assembly is challenging due to the constraints posed by the open cell configuration, even with precise clamp tightening. Moreover, pressure distribution shifts along the outer circumference are accentuated by the disparity between the smaller circumference of the cell bottom part and the clamp's inner diameter, resulting in pressure variations attributed to the slight play between the components. Hence, a sensible step towards stability measurements would be to redesign the clamping mechanism. With this improvement, OER faradaic efficiencies and element dissolution as stability metrics could be obtained from the outlet stream, which could then be represented by a stability number like in Cherevko's group¹⁰⁴.

The very recent introduction of more GDE configurations for OER studies, such as the configuration used by Geuß et al. in Cherevko's group¹¹⁹, together with the urgent lack of standardized protocols for OER studies¹²⁵ indicates that an inter-lab comparison for GDEs in OER conditions also needs to be

established. The validation of GDE setups brings an interesting opportunity for the development of ultra-low loading catalysts, which are currently almost exclusively benchmarked in aqueous systems such as RDE or flow cell designs before jumping to MEA setups^{126,127}. The higher resolution of GDE configurations on catalyst layer quality due to their electrode size and precise electrode potential measurement could help to create faster statistics for catalyst development and integration in larger systems.

Another consideration from the PTE setup to bring conditions closer to MEA development is the ability to perform measurements with higher cathode pressures. The ability of the PTE setup to separate reaction gases while being able to perform the reaction with small electrode sizes means that this system could be safer to operate even at high pressures. A pressurized version of the original GDE setup has already been achieved for fuel cell studies and it could serve as an example for the PTE setup¹²⁸.

Last, but perhaps most important, is to address the matter of sustainability. Since the development of OER catalysts based on critical raw materials takes a central role in this work, it would be essential to explore further the possible pathways of catalyst recycling. This is especially important in the context of the described manufacturing process of the Ir-rich template through acid leaching. As previously discussed, a significant amount of both Co (as a templating element) and Ir is dissolved in this operation. While Ir thrifting and reclamation were not covered in this work, it is possible to take reference from recent studies that have already incorporated this aspect from the manufacturing process⁵⁴.

5. Acknowledgment

I would like to start by giving my greatest appreciation to my supervisor Matthias Arenz for guiding me through this journey with his incredible patience, understanding and support. Whatever the challenge, you have always taken the time to help me and adapt to my learning process, breaking the complexities into easier tasks and turning my anxiety into concrete actions, plans and results. For that alone, I could not have imagined a better mentor to develop this project. I remain very much part of your group in my heart, and I hope that we can maintain close contact to each other.

Gustav, you are my closest partner in this story, teaching me with the example and counseling me in my brightest and darkest moments. Yet, you have pushed me to the end beyond my many fears (as you like to say, "Just do it!"), and I have been lifted by your infinite enthusiasm, patience, and humor. I am glad that we have built a friendship transcending our work together. I hope your projects, especially the catalyst development, will be successful, and that you have a bright future ahead of you.

I also would like to colleagues in Greifswald, both inside and outside the lab (and two very special people now in Austria and Switzerland). You know who you are, and rather than a list of names, I would rather use this space to say what you have meant to me. Life in Greifswald can be gritty, dark, or lonely. Yet, having you by my side turned it to be one of the most colorful periods of my life, filled with shared happiness, new hobbies, and good moments. I cannot thank you enough for all you have given me, and I miss you all every day.

My group members in Bern have also a special place here because even though a great of our contact has been through our Zoom meetings, I feel very close to you. I am happy to see how your projects evolve, the interesting discussions and helpful remarks that we have shared, and especially the privilege of meeting you for some days in person – I had a great time with you!

Wiebke, I would like to give you a special acknowledgment here, since I feel that you have been the real driving force for me to even start a PhD. Your incredible do-mentality, charisma - and over everything, love - is at the backbone of my work. Thank you for everything.

Last but not least, I want to thank my parents for their continuous moral support, which has been essential to me not only to accomplish this work but also to the path that has taken me to it and beyond.

I acknowledge the use of the language model Chat GPT v3.5 by Open AI to improve the writing style in short sections of the document.

6. Bibliography

- (1) Ritchie, H.; Rodés-Guirao, L.; Mathieu, E.; Gerber, M.; Ortiz-Ospina, E.; Hasell, J.; Roser, M. Population Growth. *Our World in Data* **2023**.
- (2) IEA. *World Energy Outlook 2022*. <https://www.iea.org/reports/world-energy-outlook-2022>,
- (3) Trading Economics. *1990-2022 Natural Gas Historical Price Chart*. <https://tradingeconomics.com/commodity/natural-gas>.
- (4) IEA; IRENA; UNSD; World Bank; WHO. *Tracking SDG 7: The Energy Progress Report*. <https://www.irena.org/Publications/2023/Jun/Tracking-SDG7-2023>.
- (5) IEA - International Energy Agency. *Renewables 2022, IEA, Paris. Analysis Forecast to 2027*. **2022**, 158.
- (6) Dunn, B.; Kamath, H.; Tarascon, J.-M. Electrical Energy Storage for the Grid: A Battery of Choices. *Science* **2011**, 334 (6058), 928–935.
- (7) Wadia, C.; Albertus, P.; Srinivasan, V. Resource Constraints on the Battery Energy Storage Potential for Grid and Transportation Applications. *Journal of Power Sources* **2011**, 196 (3), 1593–1598.
- (8) IRENA. *Green Hydrogen Cost Reduction*; 2020.
- (9) García, P.; Torreglosa, J. P.; Fernández, L. M.; Jurado, F. Improving Long-Term Operation of Power Sources in off-Grid Hybrid Systems Based on Renewable Energy, Hydrogen and Battery. *Journal of Power Sources* **2014**, 265, 149–159.
- (10) Chalk, S. G.; Miller, J. F. Key Challenges and Recent Progress in Batteries, Fuel Cells, and Hydrogen Storage for Clean Energy Systems. *Journal of Power Sources* **2006**, 159 (1), 73–80.
- (11) Otto, M.; Chagoya, K. L.; Blair, R. G.; Hick, S. M.; Kapat, J. S. Optimal Hydrogen Carrier: Holistic Evaluation of Hydrogen Storage and Transportation Concepts for Power Generation, Aviation, and Transportation. *Journal of Energy Storage* **2022**, 55, 105714.
- (12) IEA - International Energy Agency. *Global Hydrogen Review 2022*.
- (13) Chatenet, M.; Pollet, B. G.; Dekel, D. R.; Dionigi, F.; Deseure, J.; Millet, P.; Braatz, R. D.; Bazant, M. Z.; Eikerling, M.; Staffell, I.; others. Water Electrolysis: From Textbook Knowledge to the Latest Scientific Strategies and Industrial Developments. *Chemical Society Reviews* **2022**, 51 (11), 4583–4762.
- (14) Saba, S. M.; Müller, M.; Robinius, M.; Stolten, D. The Investment Costs of Electrolysis – A Comparison of Cost Studies from the Past 30 Years. *International Journal of Hydrogen Energy* **2018**, 43 (3), 1209–1223. <https://doi.org/10.1016/j.ijhydene.2017.11.115>.
- (15) Pei, M.; Petäjäniemi, M.; Regnell, A.; Wijk, O. Toward a Fossil Free Future with HYBRIT: Development of Iron and Steelmaking Technology in Sweden and Finland. *Metals* **2020**, 10 (7), 972.
- (16) Makhsoos, A.; Kandidayeni, M.; Pollet, B. G.; Boulon, L. A Perspective on Increasing the Efficiency of Proton Exchange Membrane Water Electrolyzers— a Review. *International Journal of Hydrogen Energy* **2023**, 48 (41), 15341–15370. <https://doi.org/10.1016/j.ijhydene.2023.01.048>.
- (17) Pham, C. V.; Escalera-López, D.; Mayrhofer, K.; Cherevko, S.; Thiele, S. Essentials of High Performance Water Electrolyzers – From Catalyst Layer Materials to Electrode Engineering. *Advanced Energy Materials* **2021**, 11 (44). <https://doi.org/10.1002/aenm.202101998>.
- (18) Net Zero by 2050 - A Roadmap for the Global Energy Sector. *IEA* **2021**, IEA, Paris.
- (19) Keddar, M.; Zhang, Z.; Periasamy, C.; Doumbia, M. L. Power Quality Improvement for 20 MW PEM Water Electrolysis System. *International Journal of Hydrogen Energy* **2022**, 47 (95), 40184–40195. <https://doi.org/10.1016/j.ijhydene.2022.08.073>.
- (20) KPMG Advisory N.V. *How to Evaluate the Cost of the Green Hydrogen Business Case?*; 2022.

-
- (21) IEA - International Energy Agency. *Tracking Clean Energy Progress 2023*; 2023.
- (22) Xu, Q.; Zhang, L.; Zhang, J.; Wang, J.; Hu, Y.; Jiang, H.; Li, C. Anion Exchange Membrane Water Electrolyzer: Electrode Design, Lab-Scaled Testing System and Performance Evaluation. *EnergyChem* **2022**, 100087.
- (23) Pandiyan, A.; Uthayakumar, A.; Subrayan, R.; Cha, S. W.; Krishna Moorthy, S. B. Review of Solid Oxide Electrolysis Cells: A Clean Energy Strategy for Hydrogen Generation. *Nanomaterials and Energy* **2019**, 8 (1), 2–22.
- (24) Atanasiu, M.; Aguilo-Rullan, A.; Dirmiki, D.; Tsimis, D.; Kontonasiou, E. (Invited) The Status of SOFC and SOEC R&D in the Clean Hydrogen Partnership. *ECS Trans.* **2023**, 111 (6), 15. <https://doi.org/10.1149/11106.0015ecst>.
- (25) LBST. *Hydrogen Council - Path to Hydrogen Competitiveness: A Cost Perspective*; 2020.
- (26) Glenk, G.; Reichelstein, S. Economics of Converting Renewable Power to Hydrogen. *Nature Energy* **2019**, 4 (3), 216–222. <https://doi.org/10.1038/s41560-019-0326-1>.
- (27) Johnson Matthey 2022. *PGM management*. <https://matthey.com/products-and-markets/pgms-and-circularity/pgm-management> (accessed 2022-06-28).
- (28) Bernt, M.; Siebel, A.; Gasteiger, H. A. Analysis of Voltage Losses in PEM Water Electrolyzers with Low Platinum Group Metal Loadings. *Journal of The Electrochemical Society* **2018**, 165 (5), F305–F314. <https://doi.org/10.1149/2.0641805jes>.
- (29) Matthey, J. *PGM Market Report*; 2023.
- (30) Clapp, M.; Zalitis, C. M.; Ryan, M. Perspectives on Current and Future Iridium Demand and Iridium Oxide Catalysts for PEM Water Electrolysis. *Catalysis Today* **2023**, 420, 114140. <https://doi.org/10.1016/j.cattod.2023.114140>.
- (31) Suermann, M.; Schmidt, T. J.; Büchi, F. N. Comparing the Kinetic Activation Energy of the Oxygen Evolution and Reduction Reactions. *Electrochimica Acta* **2018**, 281, 466–471. <https://doi.org/10.1016/j.electacta.2018.05.150>.
- (32) Vazhayil, A.; Vazhayal, L.; Thomas, J.; C, S. A.; Thomas, N. A Comprehensive Review on the Recent Developments in Transition Metal-Based Electrocatalysts for Oxygen Evolution Reaction. *Applied Surface Science Advances* **2021**, 6, 100184. <https://doi.org/10.1016/j.apsadv.2021.100184>.
- (33) Hong, W. T.; Risch, M.; Stoerzinger, K. A.; Grimaud, A.; Suntivich, J.; Shao-Horn, Y. Toward the Rational Design of Non-Precious Transition Metal Oxides for Oxygen Electrocatalysis. *Energy and Environmental Science* **2015**, 8 (5), 1404–1427. <https://doi.org/10.1039/c4ee03869j>.
- (34) He, Y.; Kang, Z.; Li, J.; Li, Y.; Tian, X. Recent Progress of Manganese Dioxide Based Electrocatalysts for the Oxygen Evolution Reaction. *Industrial Chemistry & Materials* **2023**, 1 (3), 312–331. <https://doi.org/10.1039/D3IM00034F>.
- (35) McCrory, C. C. L.; Jung, S.; Ferrer, I. M.; Chatman, S. M.; Peters, J. C.; Jaramillo, T. F. Benchmarking Hydrogen Evolving Reaction and Oxygen Evolving Reaction Electrocatalysts for Solar Water Splitting Devices. *J. Am. Chem. Soc.* **2015**, 137 (13), 4347–4357. <https://doi.org/10.1021/ja510442p>.
- (36) Reier, T.; Oezaslan, M.; Strasser, P. Electrocatalytic Oxygen Evolution Reaction (OER) on Ru, Ir, and Pt Catalysts: A Comparative Study of Nanoparticles and Bulk Materials. *ACS Catalysis* **2012**, 2 (8), 1765–1772. <https://doi.org/10.1021/cs3003098>.
- (37) Dhawan, H.; Secanell, M.; Semagina, N. State-of-the-Art Iridium-Based Catalysts for Acidic Water Electrolysis: A Minireview of Wet-Chemistry Synthesis Methods: Preparation Routes for Active and Durable Iridium Catalysts. *Johnson Matthey Technology Review* **2021**, 65 (2), 247–262. <https://doi.org/10.1595/205651321x16049404388783>.

- (38) Exner, K. S. Design Criteria for Oxygen Evolution Electrocatalysts from First Principles: Introduction of a Unifying Material-Screening Approach. *ACS Applied Energy Materials* **2019**, *2* (11), 7991–8001. <https://doi.org/10.1021/acsaem.9b01480>.
- (39) Geiger, S.; Kasian, O.; Shrestha, B. R.; Mingers, A. M.; Mayrhofer, K. J. J.; Cherevko, S. Activity and Stability of Electrochemically and Thermally Treated Iridium for the Oxygen Evolution Reaction. *Journal of The Electrochemical Society* **2016**, *163* (11), F3132. <https://doi.org/10.1149/2.0181611jes>.
- (40) Paoli, E. A.; Masini, F.; Frydendal, R.; Deiana, D.; Schlaup, C.; Malizia, M.; Hansen, T. W.; Horch, S.; Stephens, I. E. L.; Chorkendorff, I. Oxygen Evolution on Well-Characterized Mass-Selected Ru and RuO₂ Nanoparticles. *Chem. Sci.* **2015**, *6* (1), 190–196. <https://doi.org/10.1039/C4SC02685C>.
- (41) Rao, R. R.; Kolb, M. J.; Halck, N. B.; Pedersen, A. F.; Mehta, A.; You, H.; Stoerzinger, K. A.; Feng, Z.; Hansen, H. A.; Zhou, H.; Giordano, L.; Rossmesl, J.; Vegge, T.; Chorkendorff, I.; Stephens, I. E. L.; Shao-Horn, Y. Towards Identifying the Active Sites on RuO₂(110) in Catalyzing Oxygen Evolution. *Energy and Environmental Science* **2017**, *10* (12), 2626–2637. <https://doi.org/10.1039/c7ee02307c>.
- (42) Escudero-Escribano, M.; Pedersen, A. F.; Paoli, E. A.; Frydendal, R.; Friebel, D.; Malacrida, P.; Rossmesl, J.; Stephens, I. E. L.; Chorkendorff, I. Importance of Surface IrO_x in Stabilizing RuO₂ for Oxygen Evolution. *J. Phys. Chem. B* **2018**, *122* (2), 947–955. <https://doi.org/10.1021/acs.jpcc.7b07047>.
- (43) Roy, C.; Rao, R. R.; Stoerzinger, K. A.; Hwang, J.; Rossmesl, J.; Chorkendorff, I.; Shao-Horn, Y.; Stephens, I. E. L. Trends in Activity and Dissolution on RuO₂ under Oxygen Evolution Conditions: Particles versus Well-Defined Extended Surfaces. *ACS Energy Letters* **2018**, *3* (9), 2045–2051. <https://doi.org/10.1021/acsenerylett.8b01178>.
- (44) Ying, J.; Chen, J.-B.; Xiao, Y.-X.; Torresi, S. I. C. de; Ozoemena, K. I.; Yang, X.-Y. Recent Advances in Ru-Based Electrocatalysts for Oxygen Evolution Reaction. *J. Mater. Chem. A* **2023**, *11* (4), 1634–1650. <https://doi.org/10.1039/D2TA07196G>.
- (45) Danilovic, N.; Subbaraman, R.; Chang, K. C.; Chang, S. H.; Kang, Y.; Snyder, J.; Paulikas, A. P.; Strmcnik, D.; Kim, Y. T.; Myers, D.; Stamenkovic, V. R.; Markovic, N. M. Using Surface Segregation To Design Stable Ru-Ir Oxides for the Oxygen Evolution Reaction in Acidic Environments. *Angewandte Chemie International Edition* **2014**, *53* (51), 14016–14021. <https://doi.org/10.1002/anie.201406455>.
- (46) Strasser, P.; Koh, S.; Anniyev, T.; Greeley, J.; More, K.; Yu, C.; Liu, Z.; Kaya, S.; Nordlund, D.; Ogasawara, H.; others. Lattice-Strain Control of the Activity in Dealloyed Core–Shell Fuel Cell Catalysts. *Nature chemistry* **2010**, *2* (6), 454–460.
- (47) Bligaard, T.; Nørskov, J. K. Ligand Effects in Heterogeneous Catalysis and Electrochemistry. *Electrochimica Acta* **2007**, *52* (18), 5512–5516. <https://doi.org/10.1016/j.electacta.2007.02.041>.
- (48) Strickler, A. L.; Flores, R. A.; King, L. A.; Nørskov, J. K.; Bajdich, M.; Jaramillo, T. F. Systematic Investigation of Iridium-Based Bimetallic Thin Film Catalysts for the Oxygen Evolution Reaction in Acidic Media. *ACS Applied Materials and Interfaces* **2019**, *11* (37), 34059–34066. <https://doi.org/10.1021/acsaami.9b13697>.
- (49) Klingele, M.; Breitwieser, M.; Zengerle, R.; Thiele, S. Direct Deposition of Proton Exchange Membranes Enabling High Performance Hydrogen Fuel Cells. *J. Mater. Chem. A* **2015**, *3* (21), 11239–11245. <https://doi.org/10.1039/C5TA01341K>.
- (50) Geiger, S.; Kasian, O.; Mingers, A. M.; Nicley, S. S.; Haenen, K.; Mayrhofer, K. J. J.; Cherevko, S. Catalyst Stability Benchmarking for the Oxygen Evolution Reaction: The Importance of Backing

- Electrode Material and Dissolution in Accelerated Aging Studies. *ChemSusChem* **2017**, *10* (21), 4140–4143. <https://doi.org/10.1002/cssc.201701523>.
- (51) Liu, C.; Wippermann, K.; Rasinski, M.; Suo, Y.; Shviro, M.; Carmo, M.; Lehnert, W. Constructing a Multifunctional Interface between Membrane and Porous Transport Layer for Water Electrolyzers. *ACS Applied Materials and Interfaces* **2021**, *13* (14), 16182–16196. <https://doi.org/10.1021/acsami.0c20690>.
- (52) Liu, C.; Carmo, M.; Bender, G.; Everwand, A.; Lickert, T.; Young, J. L.; Smolinka, T.; Stolten, D.; Lehnert, W. Performance Enhancement of PEM Electrolyzers through Iridium-Coated Titanium Porous Transport Layers. *Electrochemistry Communications* **2018**, *97* (September), 96–99. <https://doi.org/10.1016/j.elecom.2018.10.021>.
- (53) Liu, C.; Shviro, M.; Gago, A. S.; Zaccarine, S. F.; Bender, G.; Gazdzicki, P.; Morawietz, T.; Biswas, I.; Rasinski, M.; Everwand, A.; Schierholz, R.; Pfeilsticker, J.; Müller, M.; Lopes, P. P.; Eichel, R.; Pivovar, B.; Pylypenko, S.; Friedrich, K. A.; Lehnert, W.; Carmo, M. Exploring the Interface of Skin-Layered Titanium Fibers for Electrochemical Water Splitting. *Advanced Energy Materials* **2021**, *11* (8), 2002926. <https://doi.org/10.1002/aenm.202002926>.
- (54) Lee, J. K.; Anderson, G.; Tricker, A. W.; Babbe, F.; Madan, A.; Cullen, D. A.; Arregui-Mena, J. D.; Danilovic, N.; Mukundan, R.; Weber, A. Z.; Peng, X. Ionomer-Free and Recyclable Porous-Transport Electrode for High-Performing Proton-Exchange-Membrane Water Electrolysis. *Nat Commun* **2023**, *14* (1), 4592. <https://doi.org/10.1038/s41467-023-40375-x>.
- (55) Jensen, A. W.; Sievers, G. W.; Jensen, K. D.; Quinson, J.; Arminio-Ravelo, J. A.; Brüser, V.; Arenz, M.; Escudero-Escribano, M. Self-Supported Nanostructured Iridium-Based Networks as Highly Active Electrocatalysts for Oxygen Evolution in Acidic Media. *J. Mater. Chem. A* **2020**, *8* (3), 1066–1071. <https://doi.org/10.1039/C9TA12796H>.
- (56) El-Sayed, H. A.; Weiß, A.; Olbrich, L. F.; Putro, G. P.; Gasteiger, H. A. OER Catalyst Stability Investigation Using RDE Technique: A Stability Measure or an Artifact? *Journal of The Electrochemical Society* **2019**, *166* (8), F458–F464. <https://doi.org/10.1149/2.0301908jes>.
- (57) Martens, S.; Asen, L.; Ercolano, G.; Dionigi, F.; Zalitis, C.; Hawkins, A.; Martinez Bonastre, A.; Seidl, L.; Knoll, A. C.; Sharman, J.; Strasser, P.; Jones, D.; Schneider, O. A Comparison of Rotating Disc Electrode, Floating Electrode Technique and Membrane Electrode Assembly Measurements for Catalyst Testing. *Journal of Power Sources* **2018**, *392*, 274–284. <https://doi.org/10.1016/j.jpowsour.2018.04.084>.
- (58) Milosevic, M.; Böhm, T.; Körner, A.; Bierling, M.; Winkelmann, L.; Ehelebe, K.; Hutzler, A.; Suermann, M.; Thiele, S.; Cherevko, S. In Search of Lost Iridium: Quantification of Anode Catalyst Layer Dissolution in Proton Exchange Membrane Water Electrolyzers. *ACS Energy Lett.* **2023**, *8* (6), 2682–2688. <https://doi.org/10.1021/acsenergylett.3c00193>.
- (59) Jung, H.-Y.; Kim, J. W. Role of the Glass Transition Temperature of Nafion 117 Membrane in the Preparation of the Membrane Electrode Assembly in a Direct Methanol Fuel Cell (DMFC). *International Journal of Hydrogen Energy* **2012**, *37* (17), 12580–12585. <https://doi.org/10.1016/j.ijhydene.2012.05.121>.
- (60) Alia, S. M.; Ha, M.-A.; Anderson, G. C.; Ngo, C.; Pylypenko, S.; Larsen, R. E. The Roles of Oxide Growth and Sub-Surface Facets in Oxygen Evolution Activity of Iridium and Its Impact on Electrolysis. *Journal of The Electrochemical Society* **2019**, *166* (15), F1243–F1252. <https://doi.org/10.1149/2.0771915jes>.
- (61) Fathi Tovini, M.; Hartig-Weiß, A.; Gasteiger, H. A.; El-Sayed, H. A. The Discrepancy in Oxygen Evolution Reaction Catalyst Lifetime Explained: RDE vs MEA - Dynamicity within the Catalyst Layer Matters. *Journal of The Electrochemical Society* **2021**, *168* (1), 014512. <https://doi.org/10.1149/1945-7111/abdcc9>.

- (62) Ehelebe, K.; Seeberger, D.; Paul, M. T. Y.; Thiele, S.; Mayrhofer, K. J. J.; Cherevko, S. Evaluating Electrocatalysts at Relevant Currents in a Half-Cell: The Impact of Pt Loading on Oxygen Reduction Reaction. *Journal of The Electrochemical Society* **2019**, *166* (16), F1259–F1268. <https://doi.org/10.1149/2.0911915jes>.
- (63) Ehelebe, K.; Schmitt, N.; Sievers, G.; Jensen, A. W.; Hrnjić, A.; Collantes Jiménez, P.; Kaiser, P.; Geuß, M.; Ku, Y. P.; Jovanović, P.; Mayrhofer, K. J. J.; Etzold, B.; Hodnik, N.; Escudero-Escribano, M.; Arenz, M.; Cherevko, S. Benchmarking Fuel Cell Electrocatalysts Using Gas Diffusion Electrodes: Inter-Lab Comparison and Best Practices. *ACS Energy Letters* **2022**, *7* (2), 816–826. <https://doi.org/10.1021/acscenergylett.1c02659>.
- (64) Inaba, M.; Jensen, A. W.; Sievers, G. W.; Escudero-Escribano, M.; Zana, A.; Arenz, M. Benchmarking High Surface Area Electrocatalysts in a Gas Diffusion Electrode: Measurement of Oxygen Reduction Activities under Realistic Conditions. *Energy and Environmental Science* **2018**, *11* (4), 988–994. <https://doi.org/10.1039/c8ee00019k>.
- (65) Zhang, D.; Du, J.; Quinson, J.; Arenz, M. On the Electro-Oxidation of Small Organic Molecules: Towards a Fuel Cell Catalyst Testing Platform Based on Gas Diffusion Electrode Setups. *Journal of Power Sources* **2022**, *522*, 230979. <https://doi.org/10.1016/j.jpowsour.2022.230979>.
- (66) Wiberg, G. K. H.; Fleige, M.; Arenz, M. Gas Diffusion Electrode Setup for Catalyst Testing in Concentrated Phosphoric Acid at Elevated Temperatures. *Review of Scientific Instruments* **2015**, *86* (2). <https://doi.org/10.1063/1.4908169>.
- (67) Du, J.; Quinson, J.; Zhang, D.; Wang, B.; Wiberg, G. K. H.; Pittkowski, R. K.; Schröder, J.; Simonsen, S. B.; Kirkensgaard, J. J. K.; Li, Y.; Reichenberger, S.; Barcikowski, S.; Jensen, K. M. Ø.; Arenz, M. Nanocomposite Concept for Electrochemical *In Situ* Preparation of Pt–Au Alloy Nanoparticles for Formic Acid Oxidation. *JACS Au* **2022**, *2* (7), 1757–1768. <https://doi.org/10.1021/jacsau.2c00335>.
- (68) Alinejad, S.; Inaba, M.; Schröder, J.; Du, J.; Quinson, J.; Zana, A.; Arenz, M. Testing Fuel Cell Catalysts under More Realistic Reaction Conditions: Accelerated Stress Tests in a Gas Diffusion Electrode Setup. *J. Phys. Energy* **2020**, *2* (2), 024003. <https://doi.org/10.1088/2515-7655/ab67e2>.
- (69) Nösberger, S.; Du, J.; Quinson, J.; Berner, E.; Zana, A.; Wiberg, G. K. H.; Arenz, M. The Gas Diffusion Electrode Setup as a Testing Platform for Evaluating Fuel Cell Catalysts: A Comparative RDE-GDE Study. *Electrochemical Science Advances* **2023**, *3* (1), 1–12. <https://doi.org/10.1002/elsa.202100190>.
- (70) Schröder, J.; Mints, V. A.; Bornet, A.; Berner, E.; Fathi Tovini, M.; Quinson, J.; Wiberg, G. K. H.; Bizzotto, F.; El-Sayed, H. A.; Arenz, M. The Gas Diffusion Electrode Setup as Straightforward Testing Device for Proton Exchange Membrane Water Electrolyzer Catalysts. *JACS Au* **2021**, *1* (3), 247–251. <https://doi.org/10.1021/jacsau.1c00015>.
- (71) Bornet, A.; Pittkowski, R.; Nielsen, T. M.; Berner, E.; Maletzko, A.; Schröder, J.; Quinson, J.; Melke, J.; Jensen, K. M. Ø.; Arenz, M. Influence of Temperature on the Performance of Carbon- and ATO-Supported Oxygen Evolution Reaction Catalysts in a Gas Diffusion Electrode Setup. *ACS Catalysis* **2023**, *13* (11), 7568–7577. <https://doi.org/10.1021/acscatal.3c01193>.
- (72) Kúš, P.; Ostroverkh, A.; Khalakhan, I.; Fiala, R.; Kosto, Y.; Šmíd, B.; Lobko, Y.; Yakovlev, Y.; Nováková, J.; Matolínová, I.; Matolín, V. Magnetron Sputtered Thin-Film Vertically Segmented Pt-Ir Catalyst Supported on TiC for Anode Side of Proton Exchange Membrane Unitized Regenerative Fuel Cells. *International Journal of Hydrogen Energy* **2019**, *44* (31), 16087–16098. <https://doi.org/10.1016/j.ijhydene.2019.04.216>.
- (73) Liang, J.; Liu, Q.; Li, T.; Luo, Y.; Lu, S.; Shi, X.; Zhang, F.; Asiri, A. M.; Sun, X. Magnetron Sputtering Enabled Sustainable Synthesis of Nanomaterials for Energy Electrocatalysis. *Green Chemistry* **2021**, *23* (8), 2834–2867. <https://doi.org/10.1039/d0gc03994b>.

- (74) Nefedkin, S. I.; Klimova, M. A.; Ryabukhin, A. V.; Chizhov, A. V.; Levin, I. I. Fabrication of Catalytic Compositions for Electrodes of Fuel Cells and Water Electrolyzers with Proton-Exchange Membrane by Magnetron Sputtering of Composite Targets. *Nanobiotechnology Reports* **2021**, *16* (4), 516–524. <https://doi.org/10.1134/S2635167621040078>.
- (75) Sievers, G. W.; Bowen, J. R.; Brüser, V.; Arenz, M. Support-Free Nanostructured Pt–Cu Electrocatalyst for the Oxygen Reduction Reaction Prepared by Alternating Magnetron Sputtering. *Journal of Power Sources* **2019**, *413* (December 2018), 432–440. <https://doi.org/10.1016/j.jpowsour.2018.12.044>.
- (76) Bräuer, G. Magnetron Sputtering. *Comprehensive Materials Processing* **2014**, *4*, 57–73. <https://doi.org/10.1016/B978-0-08-096532-1.00403-9>.
- (77) Setsuhara, Y. *Plasma Sources in Thin Film Deposition*; Elsevier, 2014; Vol. 4. <https://doi.org/10.1016/B978-0-08-096532-1.00415-5>.
- (78) López-Fernández, E.; Gil-Rostra, J.; Espinós, J. P.; González-Elipe, A. R.; de Lucas Consuegra, A.; Yubero, F. Chemistry and Electrocatalytic Activity of Nanostructured Nickel Electrodes for Water Electrolysis. *ACS Catal.* **2020**, *10* (11), 6159–6170. <https://doi.org/10.1021/acscatal.0c00856>.
- (79) Sievers, G. W.; Jensen, A. W.; Brüser, V.; Arenz, M.; Escudero-Escribano, M. Sputtered Platinum Thin-Films for Oxygen Reduction in Gas Diffusion Electrodes: A Model System for Studies under Realistic Reaction Conditions. *Surfaces* **2019**, *2* (2), 336–348. <https://doi.org/10.3390/surfaces2020025>.
- (80) Sievers, G. W.; Jensen, A. W.; Quinson, J.; Zana, A.; Bizzotto, F.; Oezaslan, M.; Dworzak, A.; Kirkensgaard, J. J. K. K.; Smits huysen, T. E. L. L.; Kadkhodazadeh, S.; Juelsholt, M.; Jensen, K. M. Ø. Ø.; Anklam, K.; Wan, H.; Schäfer, J.; Čépe, K.; Escudero-Escribano, M.; Rossmeisl, J.; Quade, A.; Brüser, V.; Arenz, M. Self-Supported Pt–CoO Networks Combining High Specific Activity with High Surface Area for Oxygen Reduction. *Nature Materials* **2021**, *20* (2), 208–213. <https://doi.org/10.1038/s41563-020-0775-8>.
- (81) Erlebacher, J.; Aziz, M. J.; Karma, A.; Dimitrov, N.; Sieradzki, K. Evolution of Nanoporosity in Dealloying. *Nature* **2001**, *410* (6827), 450–453. <https://doi.org/10.1038/35068529>.
- (82) Parida, S.; Kramer, D.; Volkert, C. A.; Rösner, H.; Erlebacher, J.; Weissmüller, J. Volume Change during the Formation of Nanoporous Gold by Dealloying. *Physical Review Letters* **2006**, *97* (3), 4–7. <https://doi.org/10.1103/PhysRevLett.97.035504>.
- (83) Baiker, A. Metallic Glasses in Heterogeneous Catalysis. *Faraday Discuss. Chem. Soc.* **1989**, *87* (0), 239–251. <https://doi.org/10.1039/DC9898700239>.
- (84) Gößler, M.; Hengge, E.; Bogar, M.; Albu, M.; Knez, D.; Amenitsch, H.; Würschum, R. In Situ Study of Nanoporosity Evolution during Dealloying AgAu and CoPd by Grazing-Incidence Small-Angle X-Ray Scattering. *The Journal of Physical Chemistry C* **2022**, *126* (8), 4037–4047. <https://doi.org/10.1021/acs.jpcc.1c09592>.
- (85) Strasser, P.; Koh, S.; Greeley, J. Voltammetric Surface Dealloying of Pt Bimetallic Nanoparticles: An Experimental and DFT Computational Analysis. *Physical Chemistry Chemical Physics* **2008**, *10* (25), 3670–3683.
- (86) Koh, S.; Strasser, P. Electrocatalysis on Bimetallic Surfaces: Modifying Catalytic Reactivity for Oxygen Reduction by Voltammetric Surface Dealloying. *Journal of the American Chemical Society* **2007**, *129* (42), 12624–12625. <https://doi.org/10.1021/ja0742784>.
- (87) Oezaslan, M.; Heggen, M.; Strasser, P. Size-Dependent Morphology of Dealloyed Bimetallic Catalysts: Linking the Nano to the Macro Scale. *J. Am. Chem. Soc.* **2012**, *134* (1), 514–524. <https://doi.org/10.1021/ja2088162>.

- (88) Slavcheva, E.; Radev, I.; Bliznakov, S.; Topalov, G.; Andreev, P.; Budevski, E. Sputtered Iridium Oxide Films as Electrocatalysts for Water Splitting via PEM Electrolysis. *Electrochimica Acta* **2007**, *52* (12), 3889–3894. <https://doi.org/10.1016/j.electacta.2006.11.005>.
- (89) Hu, W.; Zhong, H.; Liang, W.; Chen, S. Ir-Surface Enriched Porous Ir-Co Oxide Hierarchical Architecture for High Performance Water Oxidation in Acidic Media. *ACS Applied Materials and Interfaces* **2014**, *6* (15), 12729–12736. <https://doi.org/10.1021/am5027192>.
- (90) Freakley, S. J.; Ruiz-Esquius, J.; Morgan, D. J. The X-Ray Photoelectron Spectra of Ir, IrO₂ and IrCl₃ Revisited. *Surface and Interface Analysis* **2017**, *49* (8), 794–799. <https://doi.org/10.1002/SIA.6225>.
- (91) Ma, L.; Luo, X.; Kropf, A. J.; Wen, J.; Wang, X.; Lee, S.; Myers, D. J.; Miller, D.; Wu, T.; Lu, J.; others. Insight into the Catalytic Mechanism of Bimetallic Platinum–Copper Core–Shell Nanostructures for Nonaqueous Oxygen Evolution Reactions. *Nano Letters* **2016**, *16* (1), 781–785.
- (92) Wang, C.; Zhai, P.; Xia, M.; Wu, Y.; Zhang, B.; Li, Z.; Ran, L.; Gao, J.; Zhang, X.; Fan, Z.; others. Engineering Lattice Oxygen Activation of Iridium Clusters Stabilized on Amorphous Bimetal Borides Array for Oxygen Evolution Reaction. *Angewandte Chemie International Edition* **2021**, *60* (52), 27126–27134.
- (93) Müller, O.; Nachtegaal, M.; Just, J.; Lützenkirchen-Hecht, D.; Frahm, R. Quick-EXAFS Setup at the SuperXAS Beamline for in Situ X-Ray Absorption Spectroscopy with 10 Ms Time Resolution. *urn:issn:1600-5775* **2016**, *23* (1), 260–266. <https://doi.org/10.1107/S1600577515018007>.
- (94) Clark, A. H.; Steiger, P.; Bornmann, B.; Hitz, S.; Frahm, R.; Ferri, D.; Nachtegaal, M. Fluorescence-Detected Quick-Scanning X-Ray Absorption Spectroscopy. *urn:issn:1600-5775* **2020**, *27* (3), 681–688. <https://doi.org/10.1107/S1600577520002350>.
- (95) Clark, A. H.; Imbao, J.; Frahm, R.; Nachtegaal, M. ProQEXAFS: A Highly Optimized Parallelized Rapid Processing Software for QEXAFS Data. *urn:issn:1600-5775* **2020**, *27* (2), 551–557. <https://doi.org/10.1107/S1600577519017053>.
- (96) Ravel, B.; Newville, M. ATHENA, ARTEMIS, HEPHAESTUS: Data Analysis for X-Ray Absorption Spectroscopy Using IFEFFIT. *urn:issn:0909-0495* **2005**, *12* (4), 537–541. <https://doi.org/10.1107/S0909049505012719>.
- (97) Binninger, T.; Fabbri, E.; Patru, A.; Garganourakis, M.; Han, J.; Abbott, D. F.; Sereda, O.; Kötz, R.; Menzel, A.; Nachtegaal, M.; Schmidt, T. J. Electrochemical Flow-Cell Setup for In Situ X-Ray Investigations. *J. Electrochem. Soc.* **2016**, *163* (10), H906. <https://doi.org/10.1149/2.0201610jes>.
- (98) Hartig-Weiss, A.; Tovini, M. F.; Gasteiger, H. A.; El-Sayed, H. A. OER Catalyst Durability Tests Using the Rotating Disk Electrode Technique: The Reason Why This Leads to Erroneous Conclusions. *ACS Applied Energy Materials* **2020**, *3* (11), 10323–10327. <https://doi.org/10.1021/acsaem.0c01944>.
- (99) Lazaridis, T.; Stühmeier, B. M.; Gasteiger, H. A.; El-Sayed, H. A. Capabilities and Limitations of Rotating Disk Electrodes versus Membrane Electrode Assemblies in the Investigation of Electrocatalysts. *Nature Catalysis* **2022**, *5* (May). <https://doi.org/10.1038/s41929-022-00776-5>.
- (100) Wiberg, G.; Mayhofer, K.; Arenz, M. Investigation of the Oxygen Reduction Activity of Non-Platinum Catalysts - a RDE Methodology. *ECS Trans.* **2009**, *19* (31), 37. <https://doi.org/10.1149/1.3271360>.
- (101) Kocha, S. S.; Shinozaki, K.; Zack, J. W.; Myers, D. J.; Kariuki, N. N.; Nowicki, T.; Stamenkovic, V.; Kang, Y.; Li, D.; Papageorgopoulos, D. Best Practices and Testing Protocols for Benchmarking ORR Activities of Fuel Cell Electrocatalysts Using Rotating Disk Electrode. *Electrocatalysis* **2017**, *8* (4), 366–374. <https://doi.org/10.1007/s12678-017-0378-6>.

- (102) Siracusano, S.; Van Dijk, N.; Backhouse, R.; Merlo, L.; Baglio, V.; Aricò, A. S. Degradation Issues of PEM Electrolysis MEAs. *Renewable Energy* **2018**, *123*, 52–57. <https://doi.org/10.1016/j.renene.2018.02.024>.
- (103) Therdthianwong, A.; Manomayidthikarn, P.; Therdthianwong, S. Investigation of Membrane Electrode Assembly (MEA) Hot-Pressing Parameters for Proton Exchange Membrane Fuel Cell. *Energy* **2007**, *32* (12), 2401–2411. <https://doi.org/10.1016/j.energy.2007.07.005>.
- (104) Geiger, S.; Kasian, O.; Ledendecker, M.; Pizzutilo, E.; Mingers, A. M.; Fu, W. T.; Diaz-Morales, O.; Li, Z.; Oellers, T.; Fruchter, L.; Ludwig, A.; Mayrhofer, K. J. J.; Koper, M. T. M.; Cherevko, S. The Stability Number as a Metric for Electrocatalyst Stability Benchmarking. *Nature Catalysis* **2018**, *1* (7), 508–515. <https://doi.org/10.1038/s41929-018-0085-6>.
- (105) Liu, M.; Zhao, Z.; Duan, X.; Huang, Y. Nanoscale Structure Design for High-Performance Pt-Based ORR Catalysts. *Advanced Materials* **2019**, *31* (6), 1802234. <https://doi.org/10.1002/adma.201802234>.
- (106) Gu, W.; Carter, R. N.; Yu, P. T.; Gasteiger, H. A. Start/Stop and Local H₂ Starvation Mechanisms of Carbon Corrosion: Model vs. Experiment. *ECS Trans.* **2007**, *11* (1), 963. <https://doi.org/10.1149/1.2781008>.
- (107) Inaba, M.; Quinson, J.; Bucher, J. R.; Arenz, M. On the Preparation and Testing of Fuel Cell Catalysts Using the Thin Film Rotating Disk Electrode Method. *JoVE (Journal of Visualized Experiments)* **2018**, No. 133, e57105.
- (108) Schmitt, N.; Schmidt, M.; Mueller, J. E.; Schmidt, L.; Etzold, B. J. M. How to Maximize Geometric Current Density in Testing of Fuel Cell Catalysts by Using Gas Diffusion Electrode Half-Cell Setups. *Electrochemistry Communications* **2022**, *141*, 107362. <https://doi.org/10.1016/J.ELECOM.2022.107362>.
- (109) Zheng, W. IR Compensation for Electrocatalysis Studies: Considerations and Recommendations. *ACS Energy Letters* **2023**, 1952–1958. <https://doi.org/10.1021/acsenergylett.3c00366>.
- (110) Weiß, A.; Siebel, A.; Bernt, M.; Shen, T.-H.; Tileli, V.; Gasteiger, H. A. Impact of Intermittent Operation on Lifetime and Performance of a PEM Water Electrolyzer. *Journal of The Electrochemical Society* **2019**, *166* (8), F487–F497. <https://doi.org/10.1149/2.0421908jes>.
- (111) Aßmann, P.; Gago, A. S.; Gazdzicki, P.; Friedrich, K. A.; Wark, M. Toward Developing Accelerated Stress Tests for Proton Exchange Membrane Electrolyzers. *Current Opinion in Electrochemistry* **2020**, *21* (March), 225–233. <https://doi.org/10.1016/j.coelec.2020.02.024>.
- (112) Rakousky, C.; Keeley, G. P.; Wippermann, K.; Carmo, M.; Stolten, D. The Stability Challenge on the Pathway to High-Current-Density Polymer Electrolyte Membrane Water Electrolyzers. *Electrochimica Acta* **2018**, *278*, 324–331. <https://doi.org/10.1016/j.electacta.2018.04.154>.
- (113) Gasteiger, H. A.; Kocha, S. S.; Sompalli, B.; Wagner, F. T. Activity Benchmarks and Requirements for Pt, Pt-Alloy, and Non-Pt Oxygen Reduction Catalysts for PEMFCs. *Applied Catalysis B: Environmental* **2005**, *56* (1–2), 9–35.
- (114) Shinozaki, K.; Zack, J. W.; Richards, R. M.; Pivovar, B. S.; Kocha, S. S. Oxygen Reduction Reaction Measurements on Platinum Electrocatalysts Utilizing Rotating Disk Electrode Technique: I. Impact of Impurities, Measurement Protocols and Applied Corrections. *Journal of The Electrochemical Society* **2015**, *162* (10), F1144.
- (115) Mayrhofer, K. J. J.; Strmcnik, D.; Blizanac, B. B.; Stamenkovic, V.; Arenz, M.; Markovic, N. M. Measurement of Oxygen Reduction Activities via the Rotating Disc Electrode Method: From Pt Model Surfaces to Carbon-Supported High Surface Area Catalysts. *Electrochimica Acta* **2008**, *53* (7), 3181–3188. <https://doi.org/10.1016/j.electacta.2007.11.057>.
- (116) van der Vliet, D. F.; Wang, C.; Li, D.; Paulikas, A. P.; Greeley, J.; Rankin, R. B.; Strmcnik, D.; Tripkovic, D.; Markovic, N. M.; Stamenkovic, V. R. Unique Electrochemical Adsorption

- Properties of Pt-Skin Surfaces. *Angewandte Chemie International Edition* **2012**, *51* (13), 3139–3142. <https://doi.org/10.1002/anie.201107668>.
- (117) Garrick, T. R.; Moylan, T. E.; Carpenter, M. K.; Kongkanand, A. Editors' Choice—Electrochemically Active Surface Area Measurement of Aged Pt Alloy Catalysts in PEM Fuel Cells by CO Stripping. *J. Electrochem. Soc.* **2017**, *164* (2), F55–F59. <https://doi.org/10.1149/2.0381702jes>.
- (118) Collantes Jiménez, P.; Sievers, G.; Quade, A.; Brüser, V.; Pittkowski, R. K.; Arenz, M. Gas Diffusion Electrode Activity Measurements of Iridium-Based Self-Supported Catalysts Produced by Alternated Physical Vapour Deposition. *Journal of Power Sources* **2023**, *569* (April). <https://doi.org/10.1016/j.jpowsour.2023.232990>.
- (119) Geuß, M.; Milosevic, M.; Bierling, M.; Lötttert, L.; Abbas, D.; Escalera, D.; Lloret, V.; Ehelebe, K.; Mayrhofer, K. J. J.; Thiele, S.; Cherevko, S. Investigation of Iridium-Based OER Catalyst Layers in a GDE Half-Cell Setup: Opportunities and Challenges. *J. Electrochem. Soc.* **2023**. <https://doi.org/10.1149/1945-7111/ad07ac>.
- (120) Becker, H.; Dickinson, E. J. F.; Lu, X.; Bexell, U.; Proch, S.; Moffatt, C.; Stenström, M.; Smith, G.; Hinds, G. Assessing Potential Profiles in Water Electrolysers to Minimise Titanium Use. *Energy Environ. Sci.* **2022**, *15* (6), 2508–2518. <https://doi.org/10.1039/D2EE00876A>.
- (121) Spöri, C.; Briois, P.; Nong, H. N.; Reier, T.; Billard, A.; Köhl, S.; Teschner, D.; Strasser, P. Experimental Activity Descriptors for Iridium-Based Catalysts for the Electrochemical Oxygen Evolution Reaction (OER). *ACS Catalysis* **2019**, *9* (8), 6653–6663. <https://doi.org/10.1021/acscatal.9b00648>.
- (122) Liu, D.; Lu, S.; Xue, Y.; Guan, Z.; Fang, J.; Zhu, W.; Zhuang, Z. One-Pot Synthesis of IrNi@Ir Core-Shell Nanoparticles as Highly Active Hydrogen Oxidation Reaction Electrocatalyst in Alkaline Electrolyte. *Nano Energy* **2019**, *59*, 26–32. <https://doi.org/10.1016/j.nanoen.2019.01.070>.
- (123) Hoffmeister, D.; Finger, S.; Fiedler, L.; Ma, T.-C.; Körner, A.; Zlatar, M.; Fritsch, B.; Witte-Bodnar, K.; Carl, S.; Götz, A.; Zubiri, B. A.; Will, J.; Spiecker, E.; Cherevko, S.; Freiberg, A. T. S.; Mayrhofer, K. J. J.; Thiele, S.; Hutzler, A.; Pham, C. V. Scalable Synthesis of TiO₂@IrO_x Core-Shell Catalyst for Proton Exchange Membrane Water Electrolysis with Low Iridium Loading. ChemRxiv March 13, 2024. <https://doi.org/10.26434/chemrxiv-2024-kld98>.
- (124) Jovanović, P.; Hodnik, N.; Ruiz-Zepeda, F.; Arčon, I.; Jozinović, B.; Zorko, M.; Bele, M.; Šala, M.; Šelih, V. S.; Hočevar, S.; Gaberšček, M. Electrochemical Dissolution of Iridium and Iridium Oxide Particles in Acidic Media: Transmission Electron Microscopy, Electrochemical Flow Cell Coupled to Inductively Coupled Plasma Mass Spectrometry, and X-Ray Absorption Spectroscopy Study. *Journal of the American Chemical Society* **2017**, *139* (36), 12837–12846. <https://doi.org/10.1021/jacs.7b08071>.
- (125) Risch, M. Reporting Activities for the Oxygen Evolution Reaction. *Commun Chem* **2023**, *6* (1), 1–5. <https://doi.org/10.1038/s42004-023-01024-y>.
- (126) Murawski, J.; Scott, S.; Rao, R.; Rigg, K.; Zalitis, C.; Stevens, J.; Sharman, J.; Hinds, G.; Stephens, I. E. L. Benchmarking Stability of IrO_x in Acidic Media under O₂ Evolution Conditions: A Review. *Johnson Matthey Technology Review* **2023**. <https://doi.org/10.1595/205651323X16848455435118>.
- (127) Zlatar, M.; Escalera-López, D.; Rodríguez, M. G.; Hrbek, T.; Götz, C.; Mary Joy, R.; Savan, A.; Tran, H. P.; Nong, H. N.; Pobedinskas, P.; Briega-Martos, V.; Hutzler, A.; Böhm, T.; Haenen, K.; Ludwig, A.; Khalakhan, I.; Strasser, P.; Cherevko, S. Standardizing OER Electrocatalyst Benchmarking in Aqueous Electrolytes: Comprehensive Guidelines for Accelerated Stress Tests and Backing Electrodes. *ACS Catal.* **2023**, *13* (23), 15375–15392. <https://doi.org/10.1021/acscatal.3c03880>.

- (128) Wiberg, G. K. H.; Nösberger, S.; Arenz, M. Evolution of a GDE Setup: Beyond Ambient Conditions. *Current Opinion in Electrochemistry* **2022**, *36* (Current Opinion in Electrochemistry), 101129. <https://doi.org/10.1016/j.coelec.2022.101129>.

7. Appended manuscripts

The following chapter includes the three manuscripts discussed in the chapter three along with their supporting information.

7.1 Manuscript I:

K. Ehelebe, N. Schmitt, G. Sievers , A.W. Jensen, A. Hrnjić, P. Collantes Jiménez, et al.

Benchmarking Fuel Cell Electrocatalysts Using Gas Diffusion Electrodes: Inter-lab Comparison and Best Practices.

The published paper is reprinted with permission from *ACS Energy Lett.* **2022**, 7(2):816–26. Copyright 2022 American Chemical Society.

ACS Energy Lett. **2022**, 7(2):816–26,

<https://doi.org/10.1021/acsenergylett.1c02659>

Benchmarking Fuel Cell Electrocatalysts Using Gas Diffusion Electrodes: Inter-lab Comparison and Best Practices

Cite This: *ACS Energy Lett.* 2022, 7, 816–826

Read Online

ACCESS |



Metrics & More



Article Recommendations



Supporting Information

Due to hydrogen's excellent energy density, proton exchange membrane fuel cells (PEMFCs) are very promising to power CO₂-free long-distance and heavy-duty transport. However, high loadings of scarce and expensive Pt group metals (PGMs) are still needed at the cathode to overcome its sluggish oxygen reduction reaction (ORR) kinetics. Replacement or reduction of the noble metal content is obligatory to achieve cost-effective and broadly implemented fuel cell applications. Tremendous effort has been made to optimize the intrinsic activity of PGM catalyst materials mainly by alloying (especially with Co or Ni) or changing the shape and morphology of nanoparticles.^{1–3} Additionally, electrocatalysts based on non-PGM materials have been introduced as Earth-abundant and cheap alternatives.^{3,4} Nevertheless, the extremely promising activities of all these materials achieved in an ideal rotating disk electrode (RDE) environment cannot (yet) be transferred to technologically relevant membrane electrode assemblies (MEAs).^{5–8}

The discrepancies between ORR performance measured in RDE and MEA systems can mainly be ascribed to the different electrolytes (liquid vs solid)⁷ and a non-optimal catalyst layer composition. The latter is a delicate interplay between catalyst, catalyst support, and ionomer, which significantly affects the mass transport of ORR educts and products. It therefore holds huge potential to significantly improve catalyst layer performance in MEAs.^{2,9–11} The catalyst layer composition has to be optimized for each individual catalyst system.¹² Yet, the effects of catalyst layer parameters on the ORR performance cannot be assessed with the RDE technique due to its limitation to low current densities and the idealized catalyst layers on a solid substrate.¹³ Thus, MEA experiments have to be employed for catalyst layer optimization. However, such investigations are time-consuming and expensive (large quantities of catalyst needed, extended test equipment) and do not allow segregated investigation of either the cathode or anode catalyst layer. Furthermore, comparison of different MEA studies can be challenging due to varying processing and operating conditions.

Therefore, techniques combining the advantages of RDE, namely simplicity, rapidity, and comparability, with the realistic operating ranges of MEA are urgently required to retrieve the potential of catalyst layer optimization.^{5,14} Gas diffusion electrode (GDE)^{15–17} or floating electrode (FE)^{18–20} half-

cell setups have recently been introduced as such tools to bridge the existing gap between fundamental and applied fuel cell catalyst research (see Figure 1).

With these advanced half-cell techniques, it is possible to evaluate catalyst layer performance at realistic current densities and potential ranges without systematic mass-transport limitations. Thereby they open up the possibility to couple the electrochemical characteristics to advanced external analytics, such as identical location transmission electron microscopy (IL-TEM),^{20–22} small-angle X-ray scattering (SAXS),^{23,24} operando X-ray and neutron imaging,²⁵ Fourier-transform infrared spectroscopy,²⁶ and online mass spectrometry.^{27,28} Coupling of electrochemical measurements with these external analytics is extremely challenging in MEA setups. Hence, GDE half-cell setups enable dedicated insights into catalyst layer stability and selectivity phenomena under relevant mass transport conditions.

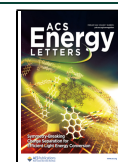
So far, comparison of activity data from different GDE setups is still challenging, mainly because different electrochemical protocols are used^{17,29} (see Figure S1). In RDE research this challenge was met by establishing best practices for catalyst benchmarking.^{13,30–34} In the present work, different commercially available Pt-based catalysts are compared in four different setups and laboratories to show that comparable ORR activity testing with GDE half-cell setups is possible if specific protocols are followed and homogeneous catalyst layers are used. From this inter-lab comparison, we propose best practices for catalyst layer benchmarking at relevant current densities along with advantages and limitations of the different GDE half-cell designs.

1. Inter-lab Comparison with Pt-Based Gas Diffusion Electrodes. Four different setups, displayed in Figure 2, have been used for the inter-lab comparison: (A) the GDE setup developed at the Helmholtz-Institute Erlangen-Nürnberg (GDE-L),¹⁷ (B) a commercial GDE cell from Gaskatel, adapted at TU Darmstadt (GDE-M), (C) the GDE half-cell

Received: December 6, 2021

Accepted: January 11, 2022

Published: January 24, 2022



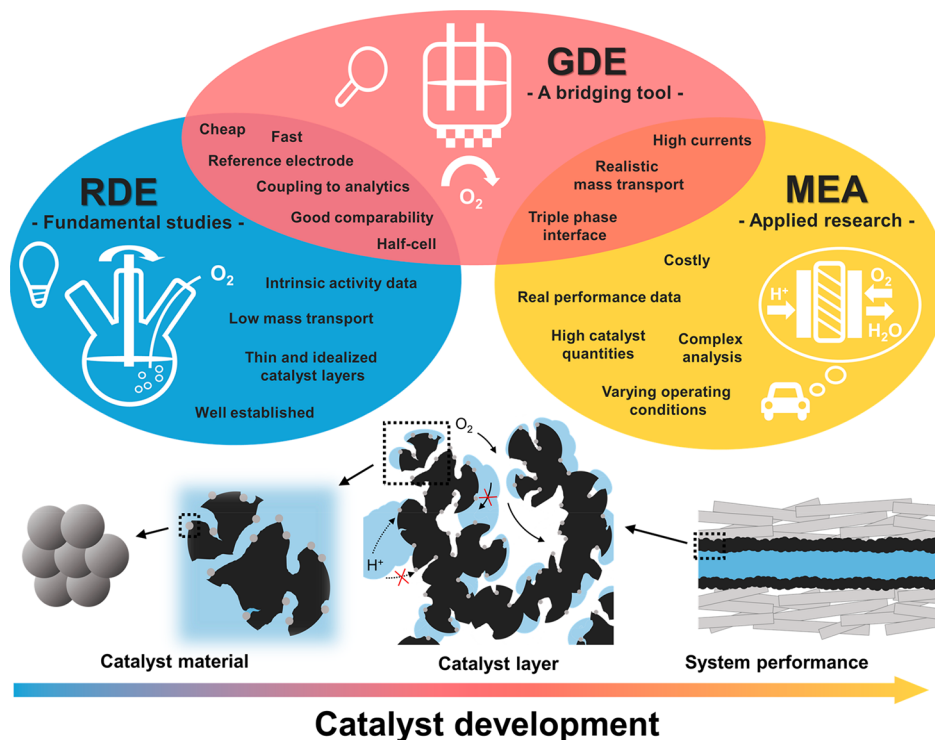


Figure 1. Comparison of different levels of electrochemical catalyst (layer) evaluation.

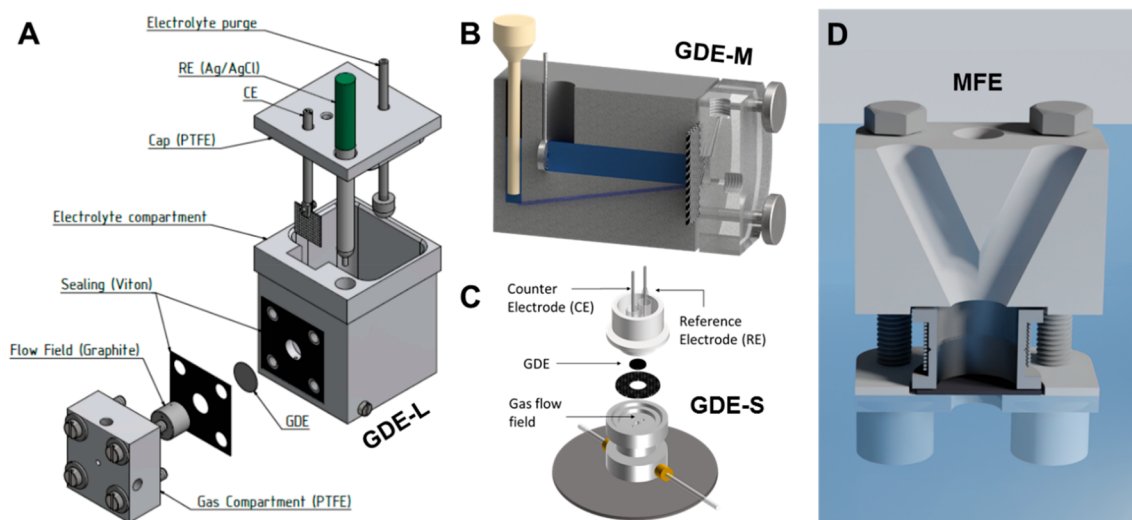


Figure 2. Different GDE half-cell setups used for the inter-lab comparison. (A) GDE setup developed at the Helmholtz-Institute Erlangen-Nürnberg¹⁷ (GDE-L). Reprinted with permission from ref 17. Copyright IOP Publishing, 2019. (B) Commercial GDE cell from Gaskatel adapted at TU Darmstadt (GDE-M). (C) GDE cell developed by the group of Arenz et al.¹⁶ used in the University of Copenhagen and Leibniz Institute for Plasma Science and Technology (GDE-S). (D) Modified floating electrode (MFE) setup developed at the National Institute of Chemistry in Ljubljana.²⁰

developed by the group of Arenz et al.¹⁶ at the University of Copenhagen and Leibniz Institute for Plasma Science and Technology (GDE-S), and (D) the modified floating electrode (MFE) setup developed at the National Institute of Chemistry in Ljubljana.²⁰ The abbreviations for the different GDE cells were chosen according to their geometric working electrode area: L = large ($S_{\text{geo,L}} = 2.01 \text{ cm}^2$), M = medium ($S_{\text{geo,M}} = 0.385 \text{ cm}^2$), and S = small ($S_{\text{geo,S}} = 0.0707 \text{ cm}^2$). Further information about the setups and experimental details can be retrieved from Table S1.

To evaluate GDEs in terms of their ORR activity, the following metrics are determined: (i) electrochemically active surface area (ECSA) via hydrogen desorption and CO-stripping charge and (ii) polarization curve in O_2 via galvanostatic steps with in situ impedance spectroscopy at each step (GEIS), as presented in previous works.^{15,17} The precise electrochemical protocol can be found in Table S2. The setups used for this study (except the MFE) have recently been contrasted in a literature review.²⁹ However, in the compiled literature, different catalysts, catalyst layer manufacturing methods, and electrochemical protocols have been

utilized, complicating a meaningful comparison. Therefore, in the present inter-lab comparison, we test the same three commercially available catalysts with all half-cell setups: (a) a commercial Pt/C GDE (40 wt % Pt on Vulcan, FuelCellsEtc), (b) a self-spray-coated Pt/C GDE (HiSPEC4000, 40 wt % Pt on Vulcan, Johnson Matthey), and (c) a self-spray-coated PtCo/C GDE (Elyst 0690, 30 wt % PtCo on high surface area carbon, Umicore). The results enable an extensive comparison of the four different setups and allow us to set a benchmark for catalyst activity evaluation in GDE half-cells.

1.1. Commercial Pt/C GDEs. As a starting point and a suitable benchmark for future GDE half-cell designs, the same commercially available Pt/C GDE as in the previous work from Pinaud et al.¹⁵ was used. The results are displayed in Figure 3.

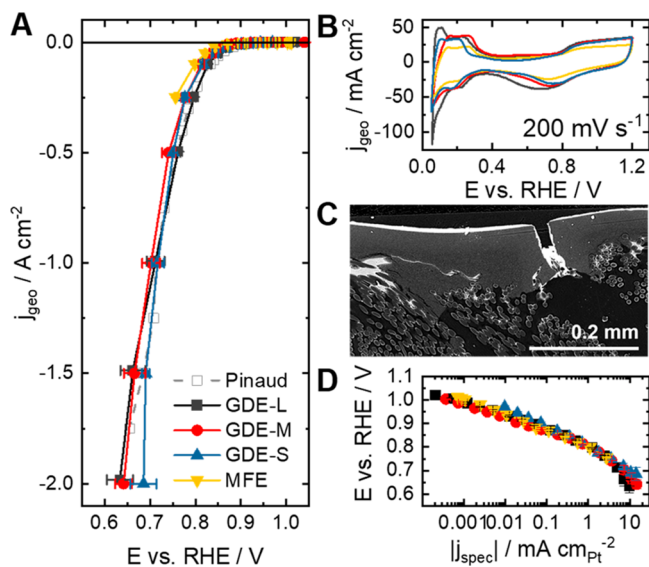


Figure 3. Interlab comparison of a commercial Pt/C GDE (0.3 mg_{Pt} cm⁻², FuelCellsEtc). (A) Polarization curves in O₂. Data from Pinaud et al. extracted from ref 15. (B) CVs in Ar. (C) SEM cross-sectional image of GDE. (D) Tafel plot of polarization curve normalized to specific surface area determined via H_{upd}. Experiments conducted in 1.0 M HClO₄ (except GDE-S: 2 M HClO₄).

First of all, we observe that comparable polarization curves in O₂ up to -2 A cm^{-2} without systematic mass transport limitations can be reached in all setups (Figure 3A). Only exception is the MFE, where current densities are limited to maximum -0.5 A cm^{-2} . This limitation is consistent also throughout the following comparisons and will be further discussed in section 3. In general, the results are also in good agreement with formerly reported GDE half-cell data from Pinaud et al.¹⁵ using similar commercial samples. All this suggests that the previously detected differences when measuring ORR performance in various GDE setups^{17,29} (see also Figure S1) are caused not by the differences in GDE half-cell setup designs but rather by the different electrochemical protocols and catalysts (or catalyst layers) used in previous experiments.

Despite generally good comparability, it can be seen that, in the MFE setup, slightly lower ORR performance is measured. At the same time, a lower active surface area is determined (Figure 3B), which explains the lower absolute ORR currents. The differences in the amount of active Pt sites and absolute

ORR performance can be attributed to the inhomogeneity of the commercial catalyst layers (Figure 3C and Figure S2). They exhibit huge cracks in the catalyst layer and the microporous layer and an uneven catalyst layer thickness in general. However, when the activity is normalized to the specific Pt surface area determined via H_{upd}, the results for all four setups exhibit very good reproducibility (Figure 3D). This proves that, with the same electrochemical protocol, similar absolute ORR performances can be measured in different GDE half-cell setups. However, for reproducible half-cell testing, it is very important to use homogeneous catalyst layers and analyze several repeats and their standard deviation, especially if setups with small geometric surface areas are used (see section 3 for further discussion). The catalyst layer quality of the tested commercial samples is not satisfactory for an adequate comparison. Therefore, as a next step, self-sprayed Pt/C GDEs are evaluated in the four different setups.

1.2. Spray-Coated Pt/C GDEs. To extend the comparison, CO-stripping is measured additionally to determine the electrochemically active Pt surface area via CO desorption charge. The results from the four different laboratories are displayed in Figure 4.

As for the previously tested GDEs, the spray-coated samples exhibit comparable polarization curves in O₂ for all four setups (see Figure 4A). However, in contrast to commercial samples, also the cyclic voltammograms (CVs) obtained in Ar environment are almost identical (see Figure 4B), resulting in very comparable ECSAs determined via H_{upd} (Figure 4C). As previously demonstrated in RDE^{35,36} and MEA³⁷ experiments, for pure Pt catalysts, CO-stripping experiments result in similar ECSA values, obtained as the integration of the H_{upd} region (average ECSA values between all setups: ECSA_{H_{upd}} = $46.9 \pm 3.4 \text{ m}^2 \text{ g}_{\text{Pt}}^{-1} \sim \text{ECSA}_{\text{CO}} = 46.8 \pm 2.5 \text{ m}^2 \text{ g}_{\text{Pt}}^{-1}$). The similarities of both the ECSA and polarization curves also lead to well-comparable ORR performances normalized to specific Pt surface area.

The demonstrated comparability between the results obtained in four different laboratories with four different setups shows again that it is possible to obtain well-comparable performance data for ORR catalyst layers when the same electrochemical protocol and homogeneous catalyst layers are used. The SEM cross sections (Figure 4E and Figure S2) show that sufficiently homogeneous catalyst layers can be obtained using ultrasonic spray-coating. To extend the scope of this work beyond pure Pt/C catalysts solely, additionally a GDE with a commercial PtCo/C catalyst was spray-coated and tested.

1.3. Spray-Coated PtCo/C GDEs. The performances measured in the different setups for the spray-coated PtCo/C GDEs are compared in Figure 5. Already from the polarization curves in O₂ (Figure 5A), it becomes obvious that, in this case, comparability between the results from different setups is limited. It can generally be seen that, in the GDE half-cell with a bigger geometric surface area (GDE-L, S_{geo} = 2.01 cm²), a significantly better performance can be measured, compared to the GDE half-cells with smaller geometric working electrode areas (GDE-M, GDE-S, MFE). Besides the polarization curves, also the CVs in Ar exhibit different shapes (Figure S3A). This also leads to different ECSA values obtained (Figure 5B). By comparing the ECSA values, however, one fact is consistent: As demonstrated in RDE³⁵ and MEA³⁷ research, for PtCo-alloys, the ECSA

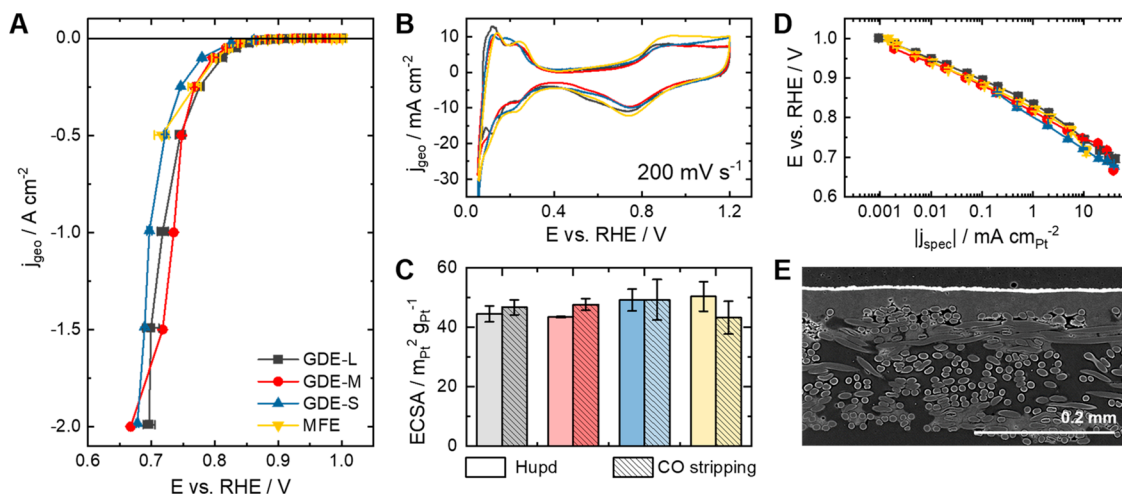


Figure 4. Inter-lab comparison of spray-coated Pt/C GDEs ($0.1 \text{ mg}_{\text{Pt}} \text{ cm}^{-2}$, HiSPEC4000). Experiments conducted in 1.0 M HClO_4 (except GDE-S: 2 M HClO_4). (A) Polarization curves in O_2 . (B) CVs in Ar. (C) Electrochemically active surface areas determined via H_{upd} and CO-stripping. (D) Tafel plot of polarization curves normalized to specific surface area determined via CO-stripping. For panels B, C, and D, the color code is similar to that in panel A. (E) SEM cross-sectional image of the GDE.

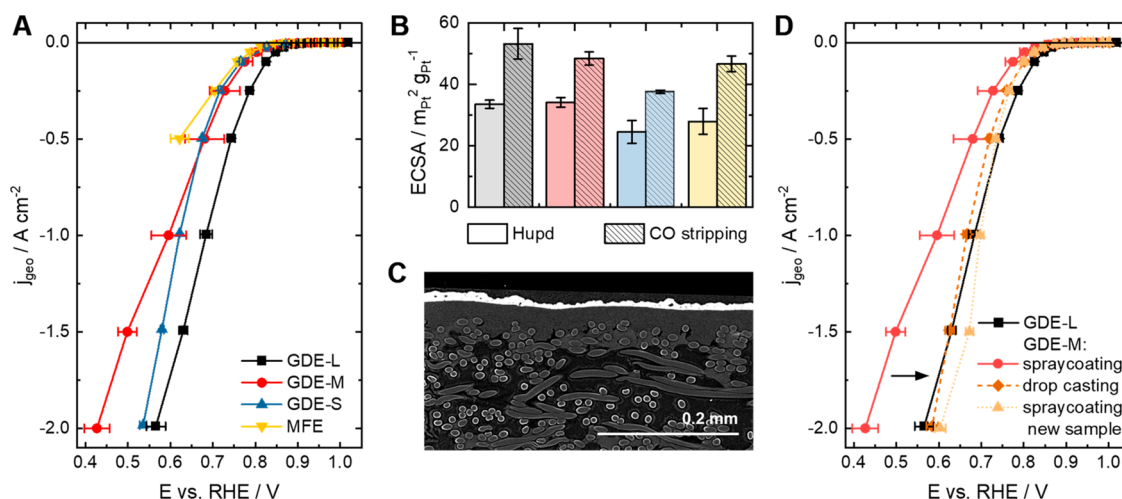


Figure 5. Inter-lab comparison of spray-coated PtCo/C GDEs ($0.1 \text{ mg}_{\text{Pt}} \text{ cm}^{-2}$, Elyst0690). (A) Polarization curves in O_2 . (B) Electrochemically active surface areas (ECSAs) determined via H_{upd} and CO-stripping. Color code is similar to that in panel A. (C) SEM cross-sectional image of the GDE. (D) Polarization curves in O_2 measured with GDE-L and GDE-M in comparison with distinct sample preparation methods and different spots of the original sample measured in GDE-M. Experiments conducted in 1.0 M HClO_4 (except GDE-S: 2 M HClO_4).

determined via CO-stripping is significantly higher compared to the value obtained by H_{upd} . This emphasizes that, if possible, CO-stripping should be used for correct determination of the ECSA of Pt-alloy catalysts.

Nevertheless, the question remains about the origin of the discrepancies between the results obtained with different setups. There are three major hypotheses, which are discussed more in detail in section 2.3 of the SI: The first is poisoning with leached Co species in the electrolyte, which, however, was ruled out in further experiments (see Figure S4A). The second is catalyst layer inhomogeneity. The PtCo/C catalyst is based on a high surface area carbon support, which exhibits a substantially larger porosity than the HiSPEC4000, with its Vulcan carbon support.¹² These different carbon supports also behave differently when an ink is formed for the spray-coating process.³⁸ For the sake of comparability, the same ink composition that was previously optimized for the HiSPEC4000 catalyst was used to spray-coat both the Pt/C

and PtCo/C catalyst layers. The utilization of this non-optimized ink recipe for the high-surface-area PtCo/C catalyst apparently resulted in a rather inhomogeneous catalyst layer (see Figure 5C and Figure S2) and hence the measured discrepancies in electrochemical performance. To elucidate this hypothesis further, a drop-casting approach using a PTFE mask to control the coated area was applied, aiming at catalyst layers with precise catalyst loading control also for low geometric surface areas. Using this approach, also small geometric surface area analogues (here GDE-M) gave polarization curves in O_2 (see Figure 5D) and ECSA values (see Figure S4C,D) comparable to those obtained with the large geometric surface area cell design (GDE-L). Additionally, another small sample from a different part of the formerly spray-coated GDE sheet ($5 \times 8 \text{ cm}$) was taken and tested with GDE-M, also leading to more comparable results (see Figure 5D and Figure S4). This indicates that the spray-coating process over a large surface area with a non-optimized ink led

to significant inhomogeneities in the GDE catalyst layers and therefore discrepancies in the electrochemical performance.

Finally, also a missing activation procedure³⁹ for the microporous PtCo/C catalyst might cause differences between the various setups. Especially microporous catalysts usually require some sort of pre-activation, as a certain amount of water, which is produced during the ORR, is needed to enable proton transport toward the catalyst nanoparticles in the pores. The various cell designs, with their different geometries (working electrode area, shape of flow field, etc.), could affect the optimal activation procedure in various manners. Additionally, we observed that the duration between catalyst layer manufacturing and testing might affect ORR performance measurements. This could be related to an unfavorable drying of the Nafion in the layer. To elucidate this extremely complex field exceeds the scope of this work. Therefore, a dedicated systematic study is required to understand the impact of catalyst layer (de)activation on comparable benchmarking with GDE half-cell setups.

In general, we can conclude that, with the similar electrochemical protocol and using homogeneous catalyst layers, the absolute performance of ORR catalyst layers can be evaluated reproducibly, even if different setup designs are used. This is a significant achievement compared to thin-film RDE studies, where even several years after the introduction of the concept,⁴⁰ significant differences in absolute activity were obtained although the same cell design was used.¹³ However, inhomogeneous catalyst layers can lead to severe discrepancies, especially when small geometric surface area setups are used. Lastly, the testing of Pt-alloy and microporous catalysts might need a further activation procedure, which should be investigated separately. In the next parts we will first compare the performance of the different catalysts before we derive some best practices for comparable GDE half-cell testing and give an overview over the advantages and limitations of the different electrochemical half-cell setups.

1.4. Comparison of the Different Catalyst Layers. Once it was shown that comparable measurements are possible between different setups, also the ORR performance of the three tested catalyst layers was to be compared. We must note that, for the inter-lab comparison, only widely commercially available catalysts have been chosen to create a benchmark, which could easily be reproduced by researchers all over the world. However, all three catalyst systems are fairly different. The manufacturing process of the commercially obtained GDEs is unknown. The only parameters which can be derived from the manufacturer are the loading of $0.3 \text{ mg}_{\text{Pt}} \text{ cm}^{-2}$ and the catalyst specification (40 wt % Pt on Vulcan). For the self-sprayed Pt/C reference, a commercial catalyst with similar Pt content and carbon support was selected (HiSPEC4000, 40 wt % Pt on Vulcan). The ink formulation and ionomer-to-carbon (I/C) ratio were previously optimized for this catalyst to obtain optimal ORR performance data.¹⁷ Therefore, in comparison to the commercial GDEs, mainly catalyst layer parameters (manufacturing method, loading, I/C ratio etc.) differ.

For the commercial PtCo/C GDEs, catalyst layer parameters similar to those for the HiSPEC4000 are used. However, also here various parameters differ from the HiSPEC4000 Pt/C catalyst (PtCo alloy, Pt density, high surface area carbon support). High surface area catalyst supports typically require a higher I/C ratio for optimal ORR performance.¹² In addition, also the metal-to-carbon ratio might influence the optimal I/C

ratio.⁴¹ Therefore, the chosen I/C ratio of 0.7 is probably not optimal for the commercial PtCo/C catalyst powder. Due to all these differences, an intrinsic comparison between the different catalyst layers is difficult with the commercially available catalysts. Nevertheless, some basic derivations can be made when comparing the ORR performance data in Figure 6. For the sake of simplicity, only the results from one setup (GDE-L) are displayed.

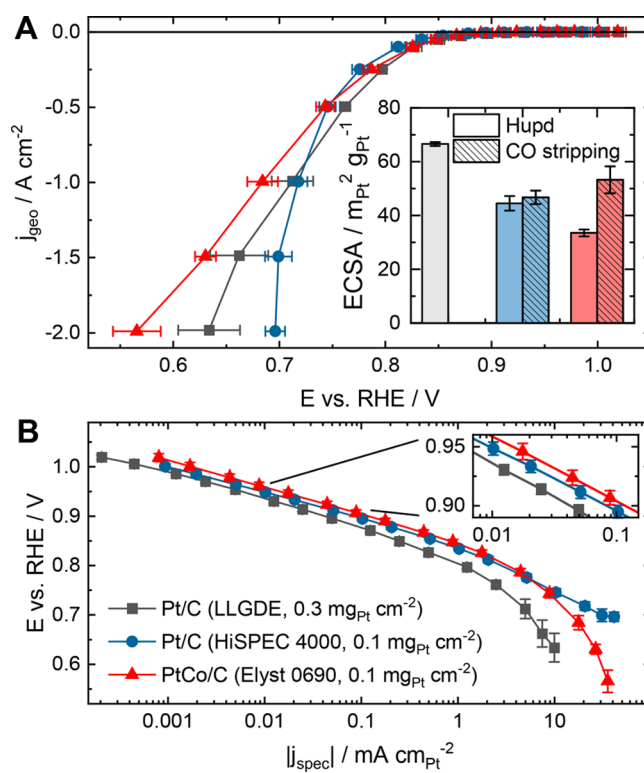


Figure 6. Comparison of the different tested GDEs (GDE-L data). (A) Polarization curves in O₂ and ECSA (inset). (B) Tafel plot of polarization curves normalized to specific surface area.

The polarization curves in O₂ (Figure 6A) reveal that the commercial Pt/C GDE (LLGDE, black) exhibits the best performance, with respect to geometric electrode area, in the low current region, followed by the self-sprayed PtCo/C GDE (red). This is expected, as the commercial LLGDE has a 3-fold higher catalyst loading compared to the other samples and PtCo/C catalysts are known to exhibit higher intrinsic activity than Pt/C catalysts¹⁴ (see also Figure 6B inset). At high currents, however, the self-sprayed HiSPEC4000 Pt/C catalyst (blue) outperforms both other GDEs, although it exhibits the lowest ECSA (Figure 6A inset). This illustrates the importance of mass-transport limitations through non-optimal catalyst layers, which can clearly be seen in the Tafel plots (Figure 6B) as a drop in potential at high current regime. In contrast to the self-sprayed HiSPEC4000 Pt/C GDE, a clear decay in the slope can be observed for both the commercial Pt/C GDE and the spray-coated PtCo/C. The superior performance of the self-sprayed HiSPEC4000 Pt/C GDE can be explained by an optimal mass-transport behavior due to the optimized catalyst layer parameters for the Vulcan carbon support.

The fact that the spray-coated HiSPEC4000 Pt/C GDE outperforms the commercial GDE, although a significantly lower loading is used, stresses the importance of catalyst layer

Table 1. Summary of Best Practices for Benchmarking Oxygen Reduction Reaction Catalysts in a Gas Diffusion Electrode Half-Cell Setup

	Best Practices
Sample preparation	<ul style="list-style-type: none"> Homogeneous catalyst layers are prerequisite. Minimize time between sample preparation and electrochemical measurements to avoid undesired catalyst layer deactivation. For Pt-alloys: Pre-leaching and exchanging electrolyte after cleaning cycles are recommended. For microporous catalyst support: Electrochemical activation protocol might be needed to ensure sufficient humidification of pores.
Electrochemical evaluation^a	<ul style="list-style-type: none"> ORR polarization curve: Precise <i>iR</i>-correction is crucial. Therefore, galvanostatic steps with impedance spectroscopy to determine uncompensated resistance (R_u) at each step should be used instead of scanning techniques. ECSA: CO-stripping is mandatory for Pt-alloy catalysts and should generally be used if possible. If H_{upd} is used, the correct determination of the baseline and the lower potential limit need to be considered. The flow from the back of the GDE should be minimized.

^aDetailed recommended electrochemical protocol can be found in Table S2.

parameters to ORR performance. It can also be seen that data that could also be gathered with RDE, such as activity at 0.9 V vs RHE and ECSA (in both, the self-sprayed HiSPEC4000 Pt/C GDEs show the lowest values), do not automatically allow projections about the performance at higher current regions. Therefore, GDE half-cell setups can be a very valuable tool for optimizing catalyst layer parameters in a fast and straightforward manner, as it was already shown in literature that they can mimic MEA performance well.^{15–17}

2. Best Practices for Comparable GDE Half-Cell Testing. In the present work, we demonstrated the feasibility of obtaining comparable results with very different GDE setups. However, certain best practices in sample preparation and the electrochemical protocol need to be considered. They are summarized in Table 1 and will be discussed below.

2.1. Sample Preparation and Quality Control. To enable comparable testing, homogeneous catalyst layers are prerequisites that should be controlled using SEM cross-sectional imaging and/or optical microscopy. Especially for the use of GDE setups with very small geometric surface areas, optimized manufacturing procedures might need to be applied. Using small samples from a catalyst film prepared by vacuum filtration⁴² has been shown to lead to reproducible results in degradation studies.²² Furthermore, analyzing several repeats using new catalyst films is highly recommended to validate reproducibility. For future work, it is recommended to minimize the time between sample preparation and electrochemical measurements, as storage in ambient conditions might affect ORR performance measurements. When measuring Pt-alloy samples, the electrolyte should be exchanged after cleaning cycles to avoid any cross contamination. Additionally, it could be beneficial to pre-leach Pt-alloy samples chemically to avoid uncontrolled leaching of less noble elements, which could also lead to differences in nanoparticle structures.⁴³ Especially for microporous catalyst supports, specific activation procedures might be necessary. However, developing suitable activation procedures for GDE half-cells still requires further dedicated investigations.

2.2. Electrochemical Protocol. In the following, we discuss strategies for correct determination of polarization curves in O₂ and the ECSA. The differences between the various setups are not considered here but will be discussed in the following section. First of all, it has to be stated that, due to the high reaction rates, the uncompensated resistance between working and reference electrode introduces the largest uncertainty to the activity determination. Therefore, a precise *iR* post-correction or in situ compensation is crucial for measuring polarization curves in GDE half-cell setups. In some setups, the

iR drop exceeds 2 V at currents as high as -2 A cm^{-2} (Figure 7A). Despite this huge *iR* drop, we show with the present work

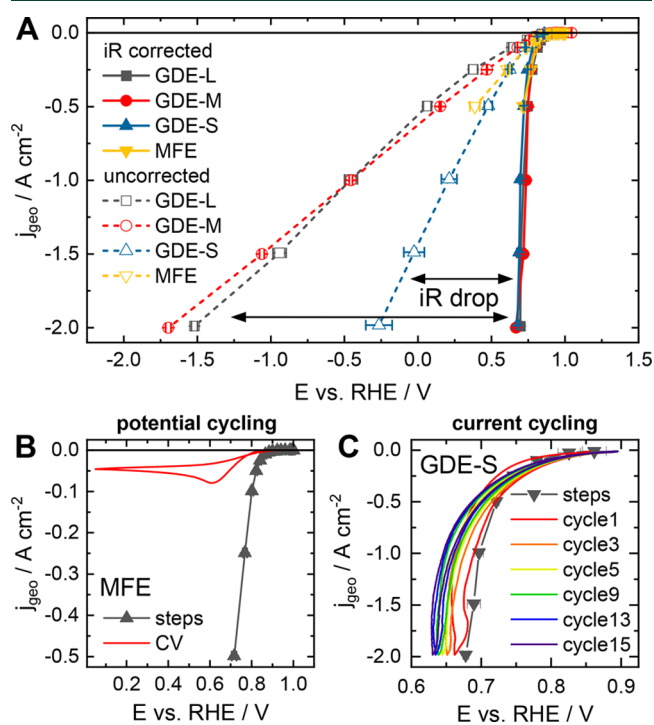


Figure 7. Best practice considerations for GDE half-cell measurements. (A) Comparison of polarization curves measured in O₂ with galvanostatic steps with and without *iR* correction. (B) Comparison of polarization curves in O₂ obtained with galvanostatic steps and cyclic voltammetry (MFE setup, 20 mV s⁻¹). (C) Comparison of polarization curves in O₂ obtained with galvanostatic steps and cyclic amperometry (GDE-S setup, scan rate 10 mA s⁻¹ = 141 mA cm⁻² s⁻¹). All polarization curves were measured for spray-coated Pt/C GDEs (0.1 mg_{Pt} cm⁻², HiSPEC4000). Experiments were conducted in 1.0 M HClO₄ (except GDE-S: 2 M HClO₄).

that, with galvanostatic steps and impedance spectroscopy at each step, comparable measurements between different setups are possible. To make sure that *iR* correction is done as accurately as possible, impedance spectroscopy should be measured at each step, as the uncompensated resistance can change during measurements (see Figure S5A), probably due to a local temperature increase or bubble formation in the electrolyte from the counter electrode reaction. This fluctuation of uncompensated resistance within measurements

is differently pronounced, depending on the setup used (see Figure S5B), which will be further discussed in the following section.

In previous literature, cyclic voltammetry (CV) in O₂ has regularly been used to evaluate catalyst performance also at higher current densities. Here we show that, using those CV measurements, no reliable results can be obtained (Figure 7B), likely due to non-steady-state conditions during cycling and insufficient *iR* compensation. Furthermore, the scan rate effect on ORR, where faster scans exhibit larger activities, has to be considered,⁴⁴ especially as *iR* post-correction leads to current-dependent scan rates.⁴⁵ Another scanning technique is cyclic amperometry. Thereby, a certain current range (not potential) is scanned. The measured potentials are post-corrected for the *iR* drop, with the high-frequency resistance simultaneously measured at 5 kHz. The results obtained with this technique are closer to the data measured with galvanostatic steps compared to the CV results (Figure 7C). However, still significant differences between subsequent cycles and stationary measurements can be observed. Therefore, we suggest using galvanostatic steps with impedance spectroscopy at each current step to determine reliable performance curves with GDE half-cells and strongly recommend not using CV for ORR activity determination at higher current densities. Cyclic amperometry could be an alternative, but further optimization and deeper investigations in technique development are still needed. In general, if scanning techniques are employed, they should be compared to a polarization curve using steps at least once to see the systematic error of the measurements.

Also when determining the ECSA, several best practices should be followed. In general, it has to be stated that the determination of ECSA via CO-stripping is more reliable compared to the H_{upd} method. Therefore, CO-stripping should be preferred for reliable determination of ECSA for Pt-based catalyst layers. For testing Pt-alloys it becomes mandatory to use CO-stripping, as the actual active surface area is drastically underestimated with the H_{upd} technique (see Figure 5B) due to electronic effects, as already known from RDE³⁵ and MEA³⁷ experiments. However, for pure Pt catalysts it is also possible to determine the ECSA with H_{upd}. This could be more convenient as not in all laboratories safe access to CO is possible.

If H_{upd} is used for ECSA determination, certain effects should be considered. First, the choice of baseline for the integration of the hydrogen desorption charge significantly affects the ECSA determination via H_{upd}. Due to high surface area carbon supports used in catalyst powders, no horizontal baseline should be applied for the integration, but rather a slightly tilted baseline following the double layer region or the shape of the CV with adsorbed CO (see Figure S6) as discussed in RDE literature.³² Second, the flow from the back of the GDE should be decreased to a minimum as high Ar flows shift the onset of hydrogen evolution to more positive potentials and hence lead to an underestimation of the ECSA (see Figure S7A). This effect is well known from MEA literature.^{46,47} However, a complete reduction of flow is not possible for all GDE half-cell designs, as undesired ambient air can enter the cell when the Ar flow is stopped, leading to a significant shift of the CV toward negative currents in the low current regime. Lastly, when no or only a low flow is applied, also the determination of an appropriate lower potential limit affects the ECSA determination (Figure S7B). If the lower potential limit is chosen too high, the H_{upd} region is cut,

leading to an underestimation of ECSA. If lower potential limit is chosen too low, H₂ is produced excessively at low potentials, generating an H₂ oxidation peak on the positive going scan. This hydrogen oxidation peak overlays with the hydrogen desorption region, leading to an overestimation of the ECSA. Therefore, a suitable intermediate lower potential limit should be chosen. All these considerations show, that reliable ECSA determination via H_{upd} in GDE half-cell setups is not trivial. Hence, if possible we suggest to use CO-stripping as a more robust method for ECSA determination not only for Pt-alloys but also for pure Pt catalysts.

One additional comment should be given about the electrolyte concentration of choice: Pinaud et al.¹⁵ investigated the impact of different electrolyte concentrations on the measured ORR performance and found that the optimal electrolyte concentration is an interplay between sufficient conductivity to allow high current densities and undesired contamination or perchlorate anion adsorption⁴⁸ from the electrolyte. They recommended to choose the lowest electrolyte concentration possible to still achieve high current densities: 1 M HClO₄ in their case, which we followed in the present work. However, with the GDE-S setup utilized in this study 2 M HClO₄ were needed to achieve sufficient conductivity and to hold the applied potentiostat potential in an adequate range. The experiments with the different electrolytes still lead to comparable results. Therefore, we can conclude that both 1 and 2 M HClO₄ can be used as electrolytes for comparable ORR catalyst testing in GDE half-cell setups.

3. Advantages and Limitations of the Different GDE Half-Cell Designs. In the present work, we have compared different GDE half-cell designs (for details see Table S1) with similar catalyst layers for the first time. In this section, we elaborate on the limitations and advantages of each design, which are summarized in Table 2.

The most obvious difference is the limitation of MFE to currents below -0.5 A cm^{-2} . Due to high internal resistance between working, reference, and counter electrodes, higher currents could not be applied with the utilized setup. However, in the future, this could be overcome by decreasing the distance between working and counter as well as working and reference electrodes. In contrast, when using the GDE-S setup, difficulties arose at low current densities. This could be in part due to the chosen activation procedure in combination with differences in the age of the catalyst layer (time delay between preparation of the catalyst layer and its measurement). Using not freshly prepared catalyst layers, the activation procedure might not have been sufficient for full humidification in the catalyst layer at low current densities. Further optimization of the activation procedure would have been needed to fully resolve this issue. As this was not the main focus of the present work and would have hampered the comparability between measurements in the different designs, only current densities $>10 \text{ mA cm}^{-2}$ were measured in the GDE-S setup for this comparison. Additionally, with the GDE-S setup, 2 M instead of 1 M HClO₄ had to be used, to hold the applied electrode potential in an adequate range and be able to perform reliable measurements up to -2 A cm^{-2} .

Besides these limitations, the various designs reveal different advantages and disadvantages when comparing their performance. Most of these differences are based on the various geometric working electrode areas determined by the different cell designs. With roughly 2 cm^2 the GDE-L cell design shows

Table 2. Comparison of the Advantages of Gas Diffusion Electrode Half-Cell Designs with Different Working Electrode Areas

	large working electrode area designs	small working electrode area designs
Advantages	<ul style="list-style-type: none"> • Robust in testing also non-ideal catalyst layers 	<ul style="list-style-type: none"> • Less catalyst material needed • Less sophisticated potentiostats required: no boosters needed and exact determination of uncompensated resistance (R_u) not as crucial
Should be considered	<ul style="list-style-type: none"> • Sophisticated potentiostats needed for R_u determination (fluctuation of R_u at elevated currents and current boosters needed) 	<ul style="list-style-type: none"> • Very sensitive to catalyst layer inhomogeneities • Higher cell resistances might lead to limitations • Exact determination of catalyst loading of small samples necessary

the far largest geometric surface area, which is almost approaching the area used in small MEA testing (5 cm^2). In the other designs significantly smaller geometric surface areas are used (GDE-M: 0.385 cm^2 , GDE-S: 0.0707 cm^2 , and MFE: 0.0316 cm^2 , see Table S1), which are approximately in the range of geometric working electrode areas used for RDE measurements. These smaller geometric working electrode areas imply several advantages. For such designs, less catalyst material for electrode preparation is needed, which can be very beneficial when newly developed catalysts shall be tested at relevant current densities. Additionally, due to the small areas, also significantly lower absolute currents have to be applied to achieve similar current densities. Hence, no extra potentiostat booster devices are needed, and undesired side effects at high currents, such as electrolyte heating or excessive formation of bubbles at the counter electrode (depending on its size), are less pronounced during measurements at high current densities. In larger surface area cells, these side effects lead to relatively large shifts in uncompensated resistance during the measurements, which significantly affect iR post-correction (see Figure S8B). In small cells (with smaller absolute currents), iR post-correction is less sensitive to absolute errors in determining the uncompensated resistance. Therefore, when using a design with large geometric surface area, a more sophisticated determination of the uncompensated resistance is required. However, when discussing the impact of iR correction, it also has to be considered that, in the designs with small geometric working electrode area, the absolute values for the uncompensated resistance were more than 1 order of magnitude higher compared to those with the higher area cell (see Figure S8A). Hence, in all GDE half-cell designs (with exception of MFE), in total a similar iR drop has to be post-corrected when measuring ORR performance curves (see Figure 7A, considering that the data from the GDE-S setup was obtained with 2 M instead of 1 M HClO_4).

In short, it can be presumed that, in larger electrode area cells, the critical factor which determines the accuracy of the measurement cells is the ability to accurately determine a low uncompensated resistance. For smaller electrode area cells, efforts to minimize the cell resistance (by increasing electrolyte concentration and decreasing distance between electrodes) are crucial. Regardless of the different effects of the current and the uncompensated resistance on the performed measurements, we prove here that comparable ORR testing throughout all setups is possible when a suitable electrochemical protocol is chosen.

From the comparison with the inhomogeneous catalyst layers, another effect of the working electrode size on the GDE half-cell measurements has become apparent: Commonly used GDE preparation methods for fuel cell testing are often developed to fabricate large electrode areas. Yet, inhomogeneities in the catalyst layer cannot always be prevented in

research laboratories. Those inhomogeneities affect the individual performance curves in cell designs with small geometric working electrode areas. Cell designs with a larger working electrode area are more robust in this regard, as inhomogeneities are averaged out. Hence, with such large working electrode area cells, a single measurement represents a good overview of the average activity of the electrode sample fabricated with similar electrode preparation methods as for MEA testing. For the use of GDE cell designs with small geometric surface areas, catalyst layer quality control and repeated measurements of different electrode samples from a catalyst layer are required. The standard deviation of the obtained activities then displays inhomogeneities in the catalyst layer.

When measuring with small electrode area designs, three more factors should be considered: (i) the relative error increases when determining the exact catalyst loading of small samples; (ii) the higher cell resistance leads to a less “sharp” response of the H_{upd} features around the lower potential limit (see Figure 3B and Figure 4B); and (iii) due to the small electrolyte volume, effective removal of bubbles formed at the counter electrode needs to be ensured.

Generally, we can state that reliable and comparable measurements are possible with all tested setups. Due to the outlined advantages and limitations in the designs, larger or smaller areas for the working electrode may be chosen based on the specific goals of the investigations. Designs with a small working electrode do not require a large amount of catalyst and in some sense are closer to fundamental RDE measurements, whereas designs with a large working electrode require more powerful electrochemical equipment and are closer to MEA measurements. In all cases, it should be kept in mind that the measurements display the properties of the catalyst layers, and not necessarily the intrinsic performance of the respective catalyst. Therefore, on the one hand, adequate catalyst layer manufacturing is essential for reliable GDE half-cell testing. On the other hand, exactly this significant impact of the catalyst layer parameters on the performance can be investigated explicitly when potentiostat, half-cell design, and electrochemical protocol are carefully chosen and tuned.

In summary, we can conclude that both FE and GDE half-cell setups are promising techniques to investigate the impact of catalyst layer properties on the ORR performance. The current inter-lab comparison with three different Pt-based GDEs revealed that good comparability can be achieved between different setups and laboratories if two factors are considered: (i) a similar electrochemical protocol with galvanostatic steps and iR correction at each step should be utilized, and (ii) a homogeneous catalyst layer needs to be fabricated for the wide range of different geometric surface areas. Non-homogeneous catalyst layers can lead to problems in comparability of individual measurements, especially when

very small geometric surface area setups are used. Also, the testing of Pt-alloy and microporous catalysts might need a further activation procedure, which should be investigated separately. The derived best practices from this work set the basis for efficient and comparable electrochemical evaluation of catalyst layers in GDE half-cell setups at technologically relevant current densities, which will be a cornerstone for rapid catalyst introduction and catalyst layer optimization in the future. With further developments such as the addition of a membrane to the catalyst layer or measurements at elevated temperatures,¹⁶ realistic fuel cell conditions can be further approached. Additionally, the different GDE half-cell designs can be coupled to external in situ online mass spectrometry^{26,28} or ex situ analytics (such as SAXS²³ or IL-TEM^{21,22}), enabling unique insights into the effect of catalyst layer properties on stability and selectivity. As the utilization of GDE half-cell setups is not limited to fuel cell reactions, this will be of high priority for both understanding the stability of catalysts in real electrochemical energy conversion devices⁴⁹ and the scale-up of electrochemical synthesis reactions.⁵⁰ Both topics will be crucial for a transition toward a climate-neutral society.

Konrad Ehelebe  orcid.org/0000-0001-9441-5642

Nicolai Schmitt  orcid.org/0000-0001-8668-288X

Gustav Sievers

Anders W. Jensen

Armin Hrnjić

Pablo Collantes Jiménez  orcid.org/0000-0003-3381-154X

Pascal Kaiser  orcid.org/0000-0002-8438-8238

Moritz Geuß  orcid.org/0000-0003-3287-088X


Yu-Ping Ku  orcid.org/0000-0003-4234-3135

Primož Jovanovič  orcid.org/0000-0003-2477-3895

Karl J. J. Mayrhofer  orcid.org/0000-0002-4248-0431

Bastian Etzold  orcid.org/0000-0001-6530-4978

Nejc Hodnik  orcid.org/0000-0002-7113-9769

María Escudero-Escribano  orcid.org/0000-0002-6432-3015

Matthias Arenz  orcid.org/0000-0001-9765-4315

Serhiy Cherevko  orcid.org/0000-0002-7188-4857

■ ASSOCIATED CONTENT

SI Supporting Information

The Supporting Information is available free of charge at <https://pubs.acs.org/doi/10.1021/acseenergylett.1c02659>.

Experimental details (including Tables S1 and S2), cross-sectional SEM images and supplementary figures (Figures S1–S8) and discussion for the PtCo/C comparison, the best practice procedure, and the comparison between different cell designs (PDF)

■ AUTHOR INFORMATION

Complete contact information is available at:

<https://pubs.acs.org/doi/10.1021/acseenergylett.1c02659>

Author Contributions

K.E., N.S., G.S., A.W.J., and A.H. conceived and planned the experiments. K.E., N.S., G.S., A.W.J., A.H., P.C.J., M.G., and Y.-P.K. carried out the experiments. K.E., N.S., and M.G. contributed to sample preparation. P.K. provided SEM images. K.E. analyzed and summarized the data. K.E., N.S., G.S., A.W.J., A.H., and S.C. contributed to the interpretation of the results. K.E. took the lead in writing the manuscript. All

authors provided critical feedback and helped shape the research, analysis, and manuscript.

Notes

The authors declare no competing financial interest.

Views expressed in this Energy Focus are those of the authors and not necessarily the views of the ACS.

■ ACKNOWLEDGMENTS

K.E. acknowledges the Heinrich Böll Foundation for financial support. K.E., M.G., Y.-P.K., P.K., and S.C. acknowledge funding by the German Federal Ministry for Economic Affairs and Energy (BMWi) within the projects 03ETB027A and 03EI3029AN.S. N.S. and B.E. acknowledge funding from the European Research Council (ERC) under the European Union's Horizon 2020 research and innovation program (grant agreement no. 681719). A.W.J., M.E.-E., and M.A. acknowledge the Danish National Research Foundation for the Center for High Entropy Alloy Catalysis (CHEAC), DNRF-149. M.A. acknowledges the Swiss National Science Foundation (SNSF) via project no. 200021_184742. A.H., P.J., and N.H. acknowledge the Slovenian research agency (ARRS) program P2-0393, the projects NC-0006, NC-0007, and NC-0016, and funding from the European Research Council (ERC) under the European Union's Horizon 2020 research and innovation program (grant agreement no. 852208).

■ REFERENCES

- (1) Chen, C.; Kang, Y.; Huo, Z.; Zhu, Z.; Huang, W.; Xin, H. L.; Snyder, J. D.; Li, D.; Herron, J. A.; Mavrikakis, M.; Chi, M.; More, K. L.; Li, Y.; Markovic, N. M.; Somorjai, G. A.; Yang, P.; Stamenkovic, V. R. Highly Crystalline Multimetallic Nanoframes with Three-Dimensional Electrocatalytic Surfaces. *Science* **2014**, *343* (6177), 1339–1343.
- (2) Banham, D.; Ye, S. Current Status and Future Development of Catalyst Materials and Catalyst Layers for Proton Exchange Membrane Fuel Cells: An Industrial Perspective. *ACS Energy Lett.* **2017**, *2* (3), 629–638.
- (3) Wang, X.; Li, Z.; Qu, Y.; Yuan, T.; Wang, W.; Wu, Y.; Li, Y. Review of Metal Catalysts for Oxygen Reduction Reaction: From Nanoscale Engineering to Atomic Design. *Chem.* **2019**, *5* (6), 1486–1511.
- (4) Martinez, U.; Komini Babu, S.; Holby, E. F.; Chung, H. T.; Yin, X.; Zelenay, P. Progress in the Development of Fe-Based PGM-Free Electrocatalysts for the Oxygen Reduction Reaction. *Adv. Mater.* **2019**, *31* (31), 1806545.
- (5) Stephens, I. E. L.; Rossmeisl, J.; Chorkendorff, I. Toward sustainable fuel cells. *Science* **2016**, *354* (6318), 1378–1379.
- (6) Pan, L.; Ott, S.; Dionigi, F.; Strasser, P. Current challenges related to the deployment of shape-controlled Pt alloy oxygen reduction reaction nanocatalysts into low Pt-loaded cathode layers of proton exchange membrane fuel cells. *Curr. Opin. Electrochem.* **2019**, *18*, 61–71.
- (7) Ly, A.; Asset, T.; Atanassov, P. Integrating nanostructured Pt-based electrocatalysts in proton exchange membrane fuel cells. *J. Power Sources* **2020**, *478*, 228516.
- (8) Kodama, K.; Nagai, T.; Kuwaki, A.; Jinnouchi, R.; Morimoto, Y. Challenges in applying highly active Pt-based nanostructured catalysts for oxygen reduction reactions to fuel cell vehicles. *Nat. Nanotechnol.* **2021**, *16* (2), 140–147.
- (9) Kongkanand, A.; Mathias, M. F. The Priority and Challenge of High-Power Performance of Low-Platinum Proton-Exchange Membrane Fuel Cells. *J. Phys. Chem. Lett.* **2016**, *7* (7), 1127–1137.
- (10) Yarlagadda, V.; Carpenter, M. K.; Moylan, T. E.; Kukreja, R. S.; Koestner, R.; Gu, W.; Thompson, L.; Kongkanand, A. Boosting Fuel

Cell Performance with Accessible Carbon Mesopores. *ACS Energy Lett.* **2018**, *3* (3), 618–621.

(11) Yoshizumi, T.; Kubo, H.; Okumura, M. Development of High-Performance FC Stack for the New MIRAI. *SAE WCX Digital Summit 2021*, DOI: 10.4271/2021-01-0740.

(12) Kobayashi, A.; Fujii, T.; Harada, C.; Yasumoto, E.; Takeda, K.; Kakinuma, K.; Uchida, M. Effect of Pt and Ionomer Distribution on Polymer Electrolyte Fuel Cell Performance and Durability. *ACS Applied Energy Materials* **2021**, *4* (3), 2307–2317.

(13) Gasteiger, H. A.; Kocha, S. S.; Sompalli, B.; Wagner, F. T. Activity benchmarks and requirements for Pt, Pt-alloy, and non-Pt oxygen reduction catalysts for PEMFCs. *Applied Catalysis B: Environmental* **2005**, *56* (1–2), 9–35.

(14) Escudero-Escribano, M.; Jensen, K. D.; Jensen, A. W. Recent advances in bimetallic electrocatalysts for oxygen reduction: design principles, structure-function relations and active phase elucidation. *Curr. Opin. Electrochem.* **2018**, *8*, 135–146.

(15) Pinaud, B. A.; Bonakdarpour, A.; Daniel, L.; Sharman, J.; Wilkinson, D. P. Key Considerations for High Current Fuel Cell Catalyst Testing in an Electrochemical Half-Cell. *J. Electrochem. Soc.* **2017**, *164* (4), F321–F327.

(16) Inaba, M.; Jensen, A. W.; Sievers, G. W.; Escudero-Escribano, M.; Zana, A.; Arenz, M. Benchmarking high surface area electrocatalysts in a gas diffusion electrode: measurement of oxygen reduction activities under realistic conditions. *Energy Environ. Sci.* **2018**, *11* (4), 988–994.

(17) Ehelebe, K.; Seeberger, D.; Paul, M. T. Y.; Thiele, S.; Mayrhofer, K. J. J.; Cherevko, S. Evaluating Electrocatalysts at Relevant Currents in a Half-Cell: The Impact of Pt Loading on Oxygen Reduction Reaction. *J. Electrochem. Soc.* **2019**, *166* (16), F1259–F1268.

(18) Zalitis, C. M.; Kramer, D.; Kucernak, A. R. Electrocatalytic performance of fuel cell reactions at low catalyst loading and high mass transport. *Phys. Chem. Chem. Phys.* **2013**, *15* (12), 4329–4340.

(19) Lin, X.; Zalitis, C. M.; Sharman, J.; Kucernak, A. Electrocatalyst Performance at the Gas/Electrolyte Interface under High-Mass-Transport Conditions: Optimization of the “Floating Electrode” Method. *ACS Appl. Mater. Interfaces* **2020**, *12* (42), 47467–47481.

(20) Hrnjić, A.; Ruiz-Zepeda, F.; Gaberscek, M.; Bele, M.; Suhadolnik, L.; Hodnik, N.; Jovanovič, P. Modified Floating Electrode Apparatus for Advanced Characterization of Oxygen Reduction Reaction Electrocatalysts. *J. Electrochem. Soc.* **2020**, *167*, 166501.

(21) Hrnjić, A.; Kamšek, A. R.; Pavličič, A.; Šala, M.; Bele, M.; Moriau, L.; Gatalo, M.; Ruiz-Zepeda, F.; Jovanovič, P.; Hodnik, N. Observing, tracking and analysing electrochemically induced atomic-scale structural changes of an individual Pt-Co nanoparticle as a fuel cell electrocatalyst by combining modified floating electrode and identical location electron microscopy. *Electrochim. Acta* **2021**, *388*, 138513.

(22) Alinejad, S.; Inaba, M.; Schröder, J.; Du, J.; Quinson, J.; Zana, A.; Arenz, M. Testing fuel cell catalysts under more realistic reaction conditions: accelerated stress tests in a gas diffusion electrode setup. *J. Phys.: Energy* **2020**, *2*, No. 024003.

(23) Schröder, J.; Quinson, J.; Mathiesen, J. K.; Kirkensgaard, J. J. K.; Alinejad, S.; Mints, V. A.; Jensen, K.; Arenz, M. A New Approach to Probe the Degradation of Fuel Cell Catalysts under Realistic Conditions: Combining Tests in a Gas Diffusion Electrode Setup with Small Angle X-ray Scattering. *J. Electrochem. Soc.* **2020**, *167*, 134515.

(24) Alinejad, S.; Quinson, J.; Schröder, J.; Kirkensgaard, J. J. K.; Arenz, M. Carbon-Supported Platinum Electrocatalysts Probed in a Gas Diffusion Setup with Alkaline Environment: How Particle Size and Mesoscopic Environment Influence the Degradation Mechanism. *ACS Catal.* **2020**, *10* (21), 13040–13049.

(25) Gebhard, M.; Paulisch, M.; Hilger, A.; Franzen, D.; Ellendorff, B.; Turek, T.; Manke, I.; Roth, C. Design of an In-Operando Cell for X-Ray and Neutron Imaging of Oxygen-Depolarized Cathodes in Chlor-Alkali Electrolysis. *Materials* **2019**, *12* (8), 1275.

(26) Zhang, G.; Kucernak, A. Gas Accessible Membrane Electrode (GAME): A Versatile Platform for Elucidating Electrocatalytic

Processes Using Real-Time and in Situ Hyphenated Electrochemical Techniques. *ACS Catal.* **2020**, *10* (17), 9684–9693.

(27) Hasa, B.; Jouny, M.; Ko, B. H.; Xu, B.; Jiao, F. Flow Electrolyzer Mass Spectrometry with a Gas Diffusion Electrode Design. *Angew. Chem., Int. Ed.* **2021**, *60* (6), 3277–3282.

(28) Ehelebe, K.; Knöppel, J.; Bierling, M.; Mayerhöfer, B.; Böhm, T.; Kulyk, N.; Thiele, S.; Mayrhofer, K. J. J.; Cherevko, S. Platinum Dissolution in Realistic Fuel Cell Catalyst Layers. *Angew. Chem., Int. Ed.* **2021**, *60* (16), 8882–8888.

(29) Loukrakpam, R.; Ferreira Gomes, B.; Kottakkat, T.; Roth, C. A bird's eye perspective of the measurement of oxygen reduction reaction in gas diffusion electrode half-cell set-ups for Pt electrocatalysts in acidic media. *Journal of Physics: Materials* **2021**, *4*, No. 044004.

(30) Shinozaki, K.; Zack, J. W.; Pylypenko, S.; Pivovar, B. S.; Kocha, S. S. Oxygen Reduction Reaction Measurements on Platinum Electrocatalysts Utilizing Rotating Disk Electrode Technique: II. Influence of Ink Formulation, Catalyst Layer Uniformity and Thickness. *J. Electrochem. Soc.* **2015**, *162* (12), F1384–F1396.

(31) Shinozaki, K.; Zack, J. W.; Richards, R. M.; Pivovar, B. S.; Kocha, S. S. Oxygen Reduction Reaction Measurements on Platinum Electrocatalysts Utilizing Rotating Disk Electrode Technique: I. Impact of Impurities, Measurement Protocols and Applied Corrections. *J. Electrochem. Soc.* **2015**, *162* (10), F1144–F1158.

(32) Mayrhofer, K. J. J.; Strmcnik, D.; Blizanac, B. B.; Stamenkovic, V.; Arenz, M.; Markovic, N. M. Measurement of oxygen reduction activities via the rotating disc electrode method: From Pt model surfaces to carbon-supported high surface area catalysts. *Electrochim. Acta* **2008**, *53* (7), 3181–3188.

(33) Kocha, S. S.; Shinozaki, K.; Zack, J. W.; Myers, D. J.; Kariuki, N. N.; Nowicki, T.; Stamenkovic, V.; Kang, Y.; Li, D.; Papageorgopoulos, D. Best Practices and Testing Protocols for Benchmarking ORR Activities of Fuel Cell Electrocatalysts Using Rotating Disk Electrode. *Electrocatalysis* **2017**, *8* (4), 366–374.

(34) Inaba, M.; Quinson, J.; Bucher, J. R.; Arenz, M. On the Preparation and Testing of Fuel Cell Catalysts Using the Thin Film Rotating Disk Electrode Method. *JoVE* **2018**, No. 133, e57105.

(35) van der Vliet, D. F.; Wang, C.; Li, D.; Paulikas, A. P.; Greeley, J.; Rankin, R. B.; Strmcnik, D.; Tripkovic, D.; Markovic, N. M.; Stamenkovic, V. R. Unique Electrochemical Adsorption Properties of Pt-Skin Surfaces. *Angew. Chem., Int. Ed.* **2012**, *51* (13), 3139–3142.

(36) Shao, M.; Odell, J. H.; Choi, S.-I.; Xia, Y. Electrochemical surface area measurements of platinum- and palladium-based nanoparticles. *Electrochem. Commun.* **2013**, *31*, 46–48.

(37) Garrick, T. R.; Moylan, T. E.; Carpenter, M. K.; Kongkanand, A. Editors' Choice—Electrochemically Active Surface Area Measurement of Aged Pt Alloy Catalysts in PEM Fuel Cells by CO Stripping. *J. Electrochem. Soc.* **2017**, *164* (2), F55–F59.

(38) Khandavalli, S.; Park, J. H.; Kariuki, N. N.; Myers, D. J.; Stickel, J. J.; Hurst, K.; Neyerlin, K. C.; Ulsh, M.; Mauger, S. A. Rheological Investigation on the Microstructure of Fuel Cell Catalyst Inks. *ACS Appl. Mater. Interfaces* **2018**, *10* (50), 43610–43622.

(39) Christmann, K.; Friedrich, K. A.; Zamel, N. Activation mechanisms in the catalyst coated membrane of PEM fuel cells. *Prog. Energy Combust. Sci.* **2021**, *85*, 100924.

(40) Schmidt, T. J.; Gasteiger, H. A.; Stäb, G. D.; Urban, P. M.; Kolb, D. M.; Behm, R. J. Characterization of High-Surface-Area Electrocatalysts Using a Rotating Disk Electrode Configuration. *J. Electrochem. Soc.* **1998**, *145* (7), 2354–2358.

(41) Nösberger, S.; Du, J.; Quinson, J.; Berner, E.; Zana, A.; Wiberg, G. K. H.; Arenz, M. The Gas diffusion electrode setup as a testing platform for evaluating fuel cell catalysts: a comparative RDE-GDE study. *ChemRxiv Preprint* **2021**, DOI: 10.33774/chemrxiv-2021-mqltk.

(42) Yarlagadda, V.; McKinney, S. E.; Keary, C. L.; Thompson, L.; Zulevi, B.; Kongkanand, A. Preparation of PEMFC Electrodes from Milligram-Amounts of Catalyst Powder. *J. Electrochem. Soc.* **2017**, *164* (7), F845–F849.

(43) Moriau, L. J.; Hrnjić, A.; Pavlišić, A.; Kamšek, A. R.; Petek, U.; Ruiz-Zepeda, F.; Sala, M.; Pavko, L.; Šelih, V. S.; Bele, M.; Jovanovič, P.; Gatalo, M.; Hodnik, N. Resolving the nanoparticles' structure-property relationships at the atomic level: a study of Pt-based electrocatalysts. *iScience* **2021**, *24* (2), 102102.

(44) Hodnik, N.; Baldizzone, C.; Cherevko, S.; Zeradjanin, A.; Mayrhofer, K. J. J. The Effect of the Voltage Scan Rate on the Determination of the Oxygen Reduction Activity of Pt/C Fuel Cell Catalyst. *Electrocatalysis* **2015**, *6* (3), 237–241.

(45) Wiberg, G. K. The development of a state-of-the-art experimental setup demonstrated by the investigation of fuel cell reactions in alkaline electrolyte. Ph.D. Thesis, Technische Universität München, 2010.

(46) Carter, R. N.; Kocha, S. S.; Wagner, F.; Fay, M.; Gasteiger, H. A. Artifacts in Measuring Electrode Catalyst Area of Fuel Cells through Cyclic Voltammetry. *ECS Trans.* **2007**, *11* (1), 403–410.

(47) Schneider, I. A.; Kramer, D.; Wokaun, A.; Scherer, G. G. Effect of inert gas flow on hydrogen underpotential deposition measurements in polymer electrolyte fuel cells. *Electrochem. Commun.* **2007**, *9* (7), 1607–1612.

(48) Attard, G. A.; Brew, A.; Hunter, K.; Sharman, J.; Wright, E. Specific adsorption of perchlorate anions on Pt{hkl} single crystal electrodes. *Phys. Chem. Chem. Phys.* **2014**, *16* (27), 13689–13698.

(49) Ehelebe, K.; Escalera-López, D.; Cherevko, S. Limitations of aqueous model systems in the stability assessment of electrocatalysts for oxygen reactions in fuel cell and electrolyzers. *Curr. Opin. Electrochem.* **2021**, *29*, 100832.

(50) Higgins, D.; Hahn, C.; Xiang, C.; Jaramillo, T. F.; Weber, A. Z. Gas-Diffusion Electrodes for Carbon Dioxide Reduction: A New Paradigm. *ACS Energy Lett.* **2019**, *4* (1), 317–324.

- Supporting Information -

Benchmarking fuel cell electrocatalysts using gas diffusion electrodes: Inter-lab comparison and best practices

Konrad Ehelebe^{a,b,*}, *Nicolai Schmitt*^c, *Gustav Sievers*^d, *Anders W. Jensen*^e, *Armin Hrnjić*^{f,g},
Pablo Collantes Jiménez^d, *Pascal Kaiser*^{a,b}, *Moritz Geuß*^{a,b}, *Yu-Ping Ku*^{a,b}, *Primož Jovanovič*^f, *Karl J.J. Mayrhofer*^{a,b}, *Bastian Etzold*^c, *Nejc Hodnik*^{f,g}, *María Escudero-Escribano*^e, *Matthias Arenz*^h, *Serhiy Cherevko*^{a,*}

^a Helmholtz-Institute Erlangen-Nürnberg for Renewable Energy (IEK-11),
Forschungszentrum Jülich GmbH, Cauerstr. 1, 91058 Erlangen, Germany

^b Department of Chemical and Biological Engineering, Friedrich-Alexander University
Erlangen-Nürnberg, Cauerstr. 1, 91058 Erlangen, Germany

^c Department of Chemistry, Technical University of Darmstadt, Ernst-Berl-Institut für
Technische und Makromolekulare Chemie, Alarich-Weiss-Str. 8, 64287 Darmstadt, Germany

^d Leibniz Institute for Plasma Science and Technology, Felix-Hausdorff-Str. 2, 17489
Greifswald, Germany

^e Department of Chemistry, Center for High Entropy Alloy Catalysis, University of
Copenhagen, Universitetsparken 5, 2100 Copenhagen, Denmark

^f Department of Materials Chemistry, National Institute of Chemistry, Hajdrihova 19,
Ljubljana SI-1000, Slovenia

^g University of Nova Gorica, Vipavska 13, 5000 Nova Gorica, Slovenia

^h Department of Chemistry, Biochemistry and Pharmaceutical Sciences, University of Bern,
Freiestrasse 3, 3012 Bern, Switzerland

^z Corresponding Authors: k.ehelebe@fz-juelich.de, s.cherevko@fz-juelich.de

Table of Content

1. Experimental Details	2
1.1 Electrode manufacturing.	2
1.2 Electrochemical setups	3
1.3 Electrochemical protocol.....	4
2. Supplementary Data	5
2.1 Comparison of previously reported GDE half-cell data.....	5
2.2 Cross sectional SEM images of tested GDE samples	6
2.3 Discussion about discrepancies obtained testing PtCo/C samples	7
2.4 Details on best practice procedure.....	10
2.5 Details on the comparison between GDE cell designs	11
References	12

1. Experimental Details

1.1 Electrode manufacturing.

For the first experimental comparison commercial Pt/C GDEs were used ($0.3 \text{ mg}_{\text{Pt}} \text{ cm}^{-2}$, 40 % Pt on Vulcan, FuelCellsEtc). For other experiments, GDEs have been prepared in-house using an ultrasonic spray coater (Biofluidix) and commercial Pt/C or PtCo/C catalyst (Pt/C: HiSPEC4000, 40 wt% Pt on Vulcan, Johnson Matthey; PtCo/C: Elyst 0690, 30 wt% PtCo on Carbon black, Umicore). The ink for the GDE fabrication consisted of a total 1 wt% solids in a solvent mixture of 20 wt% isopropylalcohol (IPA) in H_2O . The solid fraction was composed of 70 % catalyst powder and 30 wt% ionomer (Nafion D520; Dupont) resulting in a gravimetric ionomer to carbon ratio of about 0.7. The ink was homogenised for 20 min at 60 W and 0°C with an ultrasonic horn (Hielscher). GDE sheets (5 x 8 cm) were fabricated by applying the catalyst ink onto a Freudenberg H23C8 gas diffusion media (230 μm thick) with the ultrasonic spray coater on a heated stage at 85°C . The loading was determined by weighing (Sartorius Cubis®, 0.001 mg) the samples before and after the catalyst ink spray deposition.

1.2 Electrochemical setups

Table S1. Experimental details for inter-lab comparison.

	GDE-L	GDE-M	GDE-S	MFE
Setup	GDE half-cell introduced in Ref. ¹	Commercial GDE cell from Gaskatel	GDE cell introduced in Ref. ²	Modified Floating Electrode setup introduced in Ref. ³
Laboratory	Helmholtz-Institute Erlangen Nürnberg (HIERN)	TU Darmstadt	Leibniz Institute for Plasma Science (INP) and Technology and University of Copenhagen	National Institute of Chemistry Ljubljana
WE geometric area	2.01 cm ² (ø 16 mm)	Reduced to 0.385 cm ² (ø 7 mm) with sealing (Normal area = 3 cm ²)	0.0707cm ² (ø 3 mm)	0.0316 cm ² (ø 2 mm)
CE	Ir/Ta Mixed metal oxide mesh on Ti	PtIr wire	Pt wire/Pt mesh	Pt mesh (GoodFellow 50 × 50 mm)
RE	Ag/AgCl (Metrohm)	RHE (Hydroflex Gaskatel)	RHE (stationary)	RHE (HydroFlex, Gaskatel)
Electrolyte	1 M HClO ₄ (~ 200 ml, Suprapure, 70 %, Merck)	1 M HClO ₄ (25 ml, ROTIPURAN@Ultra 70 %, Carl-Roth)	2 M HClO ₄ (4 ml, Suprapure, 70 %, Merck)	1 M HClO ₄ (20 ml, ROTIPURAN@Supra, 70 %, Carl Roth)
Flow field	parallel flow field from graphite	No flow field	Stainless steel flow field (ø 3 mm, 0.5 mm extrusion in cell body)	No flow field
Gases	Ar, O ₂ , H ₂ (all 99.998 %), CO (99.997 %; all gases Air Liquide)	CO, O ₂ , H ₂ (all 99.999 %, Air Liquide), N ₂ (cold evaporated)	Ar (99.999 %, Air Liquide), O ₂ (99.999 %, Air Liquide), CO (99.97 %, Air Liquide)	Ar, O ₂ (99,999 %, Messer), CO (99.997 %, Air Liquide)
Potentiostat	Biologic VSP-300 with 2 x 2A-booster	Ivium Octostat 5000	Nordic Electrochemistry ECi-211	Biologic SP-200

1.3 Electrochemical protocol

Table S2. Electrochemical protocol used for evaluation of ORR electrocatalysts.

Step	Electrochemical Technique	Parameters
0	RE potential determination	Open circuit potential (OCP) Gas purge (Flow rate) Time H ₂ (250 ml min ⁻¹) ~ 10 min
1	Electrochemical cleaning	Cyclic voltammograms (CV) Gas purge (Flow rate) Potential limits Scan rate Number of cycles Ar (300 ml min ⁻¹), humidified ⁽¹⁾ 0.05 – 1.2 V vs. RHE 200 mV s ⁻¹ ~ 30 - 50 (until CV is stable)
2	ECSA determination (H _{upd})	CV Gas purge (Flow rate) Potential limits Scan rate Number of cycles iR-compensation Ar (0 ml min ⁻¹ , if possible), humidified ⁽¹⁾ 0.05 – 1.2 V vs. RHE 50/100/200 mV s ⁻¹ 3 each 95 % in-situ correction + 5 % post-corr.
3	Oxide reduction	Chronoamperometry (CA) Gas purge (Flow rate) Potential Time Ar (0 ml min ⁻¹), humidified ⁽¹⁾ 0.1 V vs. RHE 5 min
4	Polarization curve (O ₂)	OCP Gas purge (Flow rate) Time O ₂ (250 ml min ⁻¹), humidified ⁽¹⁾ 10 min
		Galvanostatic steps coupled with impedance spectroscopy (GEIS) Gas purge (Flow rate) Current steps (hold time) EIS frequency range EIS amplitude iR-compensation O ₂ (250 ml min ⁻¹ , ambient pressure) - 0.05/-0.1 mA cm ⁻² (90 s), -0.25/-0.5 mA cm ⁻² (60 s), -1/-2.5 mA, -5/-10 mA cm ⁻² (30 s), -25/-50/-100/-250 mA cm ⁻² (5s) -0.5/-1.0/-1.5/-2.0 A cm ⁻² (5s) f= 200 kHz – 10 Hz 10 % of current (min. 5 mA cm ⁻²) 100 % post-correction
5	ECSA determination (CO-stripping)	CA Gas purge (Flow rate) Potential Time CO (100 ml min ⁻¹) 0.1 V vs. RHE 2 min
		CV Gas purge (Flow rate) Potential Scan rate Number of cycles iR-compensation Ar (500 ml min ⁻¹) 0.1 V vs. RHE ~20 min, Ar (0 ml min ⁻¹), humidified ⁽¹⁾ 0.1 – 1.2 V vs. RHE 200 mV s ⁻¹ 3 95 % in-situ correction + 5 % post-corr.

⁽¹⁾In MFE setup non-humidified O₂ was used. However, in preliminary experiments we found that humidification does not affect the measurements at room temperature.

For calculation of the electrochemically active surface area (ECSA) the following constants have been used: hydrogen desorption (H_{upd}, 210 μC cm_{Pt}⁻²) and CO-stripping charge

($420 \mu\text{C cm}_{\text{Pt}}^{-2}$). All experiments are repeated at least twice and conducted at ambient temperature.

2. Supplementary Data

2.1 Comparison of previously reported GDE half-cell data

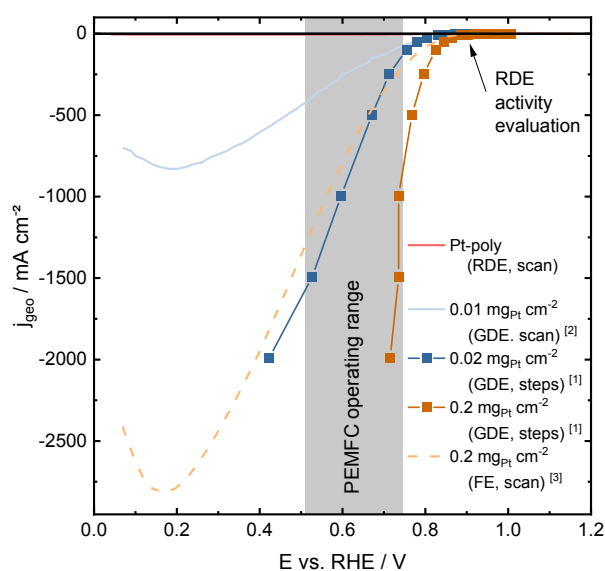


Figure S1. Comparison of different GDE half-cell data previously published. Blue: Low Pt/C loading GDEs, Orange: High loading Pt/C GDEs. Significant differences in the measured activities can be observed when galvanostatic steps (intense colour points) or scanning techniques (pale coloured lines) are used. Scanning techniques result in significantly lower performance measured in relevant potential ranges. However, it has to be considered that also different catalyst systems were used, which could also lead to different results. Therefore, a systematic comparison is needed. Data reprinted from Inaba et al. ², Ehelebe et al. ¹ and Hrnjic et al. ³

2.2 Cross sectional SEM images of tested GDE samples

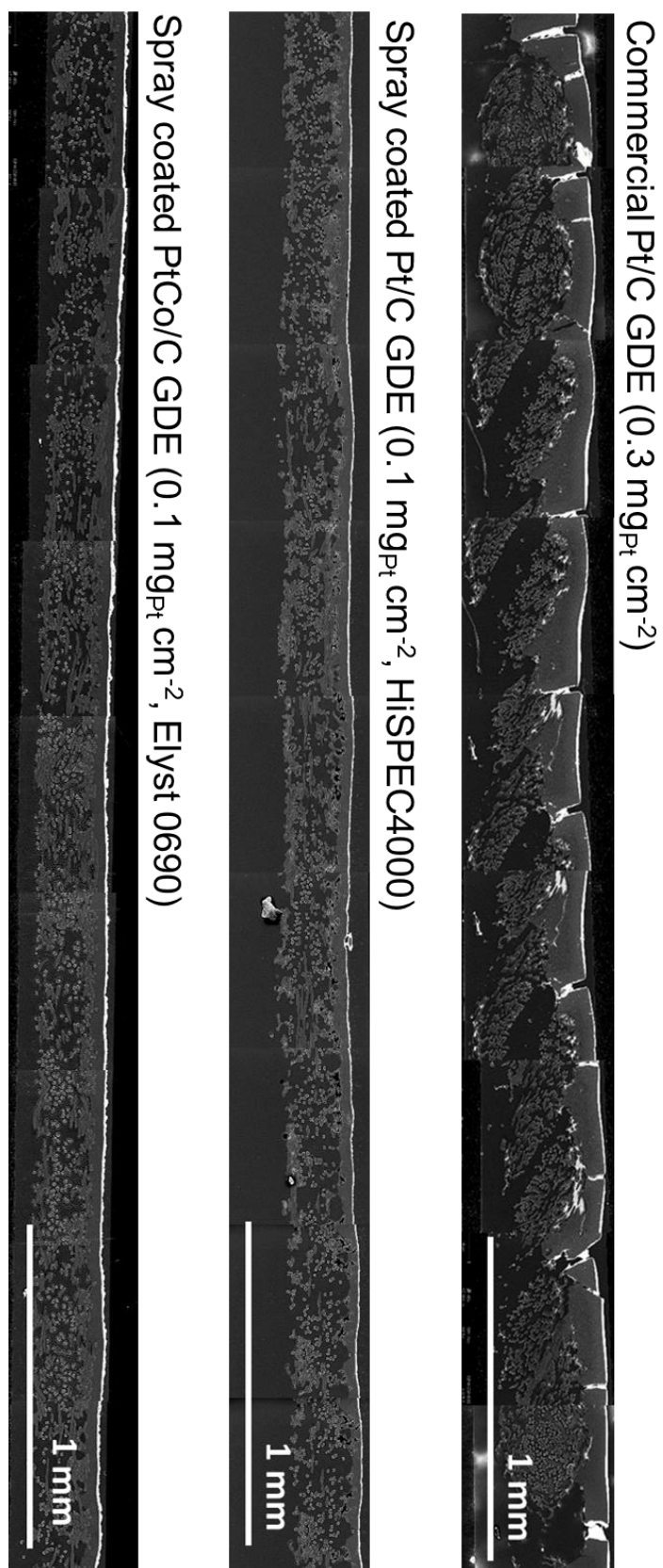


Figure S2. SEM cross-sectional images of the tested catalyst layers. To achieve an overview over a wide range of the catalyst layer, several SEM images are stringed together.

2.3 Discussion about discrepancies obtained testing PtCo/C samples

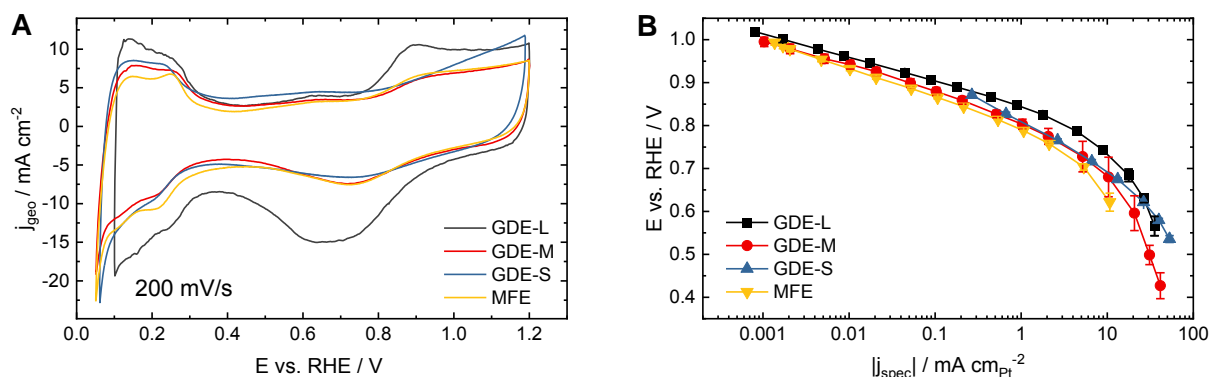


Figure S3. Inter-lab comparison of spray coated PtCo/C GDEs (0.1 mgPt cm⁻², Elyst0690). A: CVs in Ar, B: Tafel-plot normalized to specific surface area determined via CO-stripping.

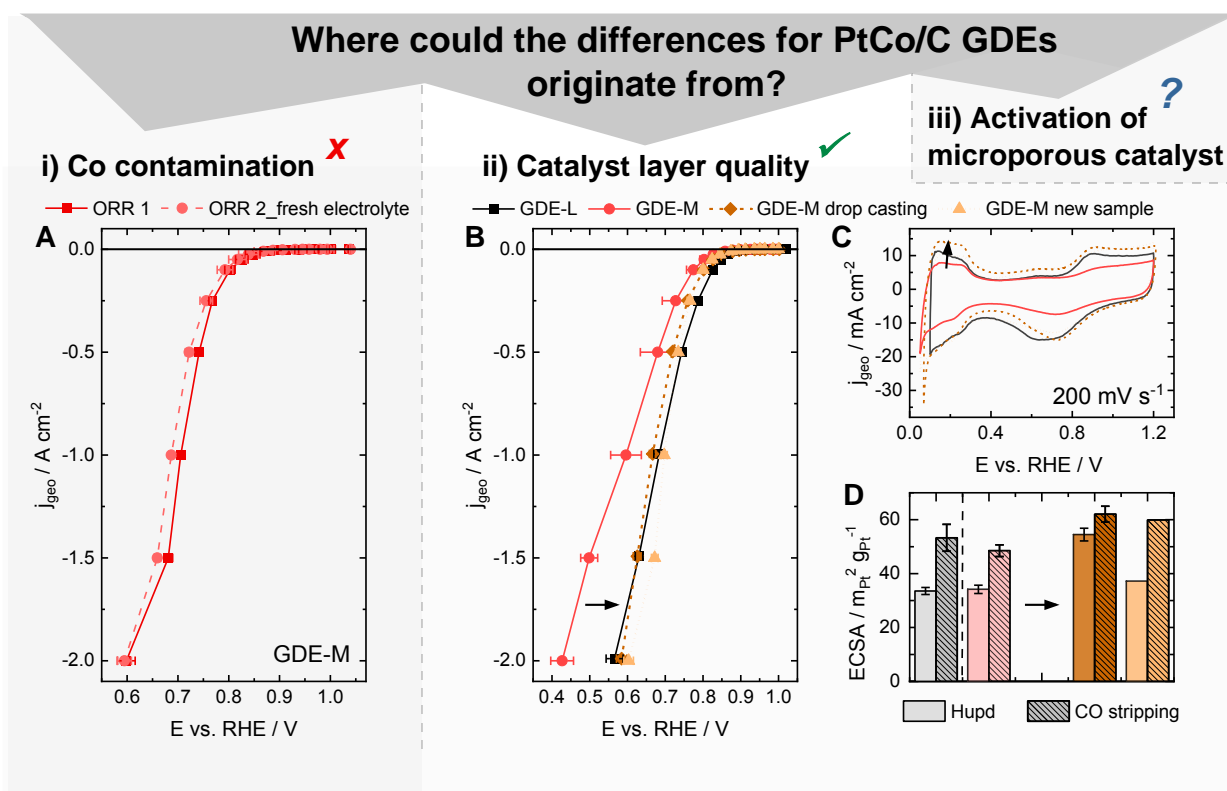


Figure S4. Three hypotheses to explain the measured differences for spray coated PtCo/C GDEs (Co contamination, catalyst layer quality and activation of microporous layer). A: Effect of Co contamination. Consecutive polarization curves in O₂ with same electrolyte from cleaning cycles and fresh electrolyte. B: Polarization curves in O₂ measured with GDE-L and GDE-M in comparison with distinct sample preparation methods and different spot of the original sample measured in GDE-M. C: CVs in Ar, respectively. D: Electrochemically active surface area determined via Hupd and CO-stripping.

Significant discrepancies have been observed when comparing the PtCo/C catalysts in different laboratories and with different setups. There are three major hypotheses where these discrepancies could originate from. Firstly, the discrepancies could be due to poisoning with

leached Co species in the electrolyte. During cleaning cycles or leaving the working electrode at open circuit potential Co species are leached out of the catalyst.⁴ Due to different electrolyte volumes of the various setups, also the Co concentration in the electrolyte would be different, leading to a different amount of contamination. This hypothesis, however is not very likely as a poisoning effect should be most apparent in the very low current regions of the polarization curves. Yet, in this region the Tafel-plots with Pt surface area normalized specific current densities exhibit quite similar activities (see Figure S3B). Further tests also exhibit no significant change in polarization curve, when the electrolyte is exchanged between activation cycles and ORR measurements (see Figure S4A). However, despite not being the main reason for the discrepancies, for future work it is still recommended to exchange the electrolyte after cleaning cycles when measuring Pt-alloy samples to avoid any cross contamination. Additionally, it could be beneficial to pre-leach Pt-alloy samples chemically and control the electrode potential throughout the whole experiment (also during filling the cell with electrolyte) to avoid uncontrolled Co leaching processes, which can also result in differences in nanoparticle structures.⁵

Another reason for the discrepancies obtained could be catalyst layer inhomogeneity and ageing. As already discussed, a homogeneous catalyst layer is prerequisite for comparable GDE testing, especially when designs with very small geometric surface areas are used. SEM cross-sectional images show that compared to the Pt/C GDEs the PtCo/C samples exhibit larger inhomogeneities (see Figure S2). Although there are no visible cracks as in the commercial sample, still significant differences in catalyst layer thickness and an increased roughness of the catalyst layer surface can be observed. Those differences in catalyst layer quality can be ascribed to the structural differences between the commercial PtCo/C catalyst from Umicore and the previously tested HiSPEC catalyst, which are discussed in detail in section 1.4 of the main text. In the PtCo/C case, a high surface area carbon support is used, which exhibits a significantly higher porosity than the HiSPEC4000 with its Vulcan carbon support.⁶ The different carbon supports also behave differently when an ink is formed for the spray coating process.⁷ For the sake of comparability, here the same ink composition – which was previously optimized for the HiSPEC4000 catalyst – is utilized for spray coating both Pt/C and PtCo/C catalyst layer. The utilization of this non-optimized ink recipe for the high-surface area PtCo/C catalyst might therefore be the reason for an inhomogeneous catalyst layer and hence the measured discrepancies in electrochemical performance. To elucidate this hypothesis further, a drop casting approach using a PTFE mask to control the coated area was applied aiming at

catalyst layers with precise catalyst loading control also for low geometric surface areas. Using this approach, also small geometric surface area analogues (here GDE-M) gave comparable polarization curves in O₂ compared to with respect to large geometric surface area analogues (GDE-L, see Figure S4B). Also the shape of the CVs in Ar environment is more similar to the one measured with the GDE-L cell, even exhibiting higher ECSA values (see Figure S4C & D). Additionally, another small sample from a different part of the formerly spray coated GDE sheet (5 x 8 cm) was taken and tested with GDE-M, also leading to more comparable results (see Figure S4B, C & D). This indicates, that the spray coating process over a large surface area (5 x 8 cm) with a non-optimized ink led to significant inhomogeneities in the GDE catalyst layers and therefore discrepancies in the electrochemical performance.

Finally, also a missing activation procedure for the microporous PtCo/C catalyst might cause differences between the various setups. Especially microporous catalysts usually require some sort of pre-activation as a certain amount of water, which is produced during ORR, is needed to enable proton transport towards the catalyst nanoparticles in the pores. In a floating electrode setup using extremely thin catalyst layers, it was recently shown that ORR performance is significantly affected by preceding activation procedure.⁸ This effect might even be more pronounced in thicker catalyst layers as tested in the half-cell setups here. The different cell designs, with their different geometries (geometric surface area, shape of flow field etc.) could impact the optimal activation procedure in various manners. For more insights on activation mechanisms in catalyst layers, the readers are referred to an extensive recent review.⁹ Additionally, we observed that when catalyst layers are stored in air, performance and reproducibility deteriorate. This might be related to an unfavourable drying of the Nafion in the layer. Therefore, also the duration between catalyst layer manufacturing and testing might affect ORR performance measurements.

2.4 Details on best practice procedure

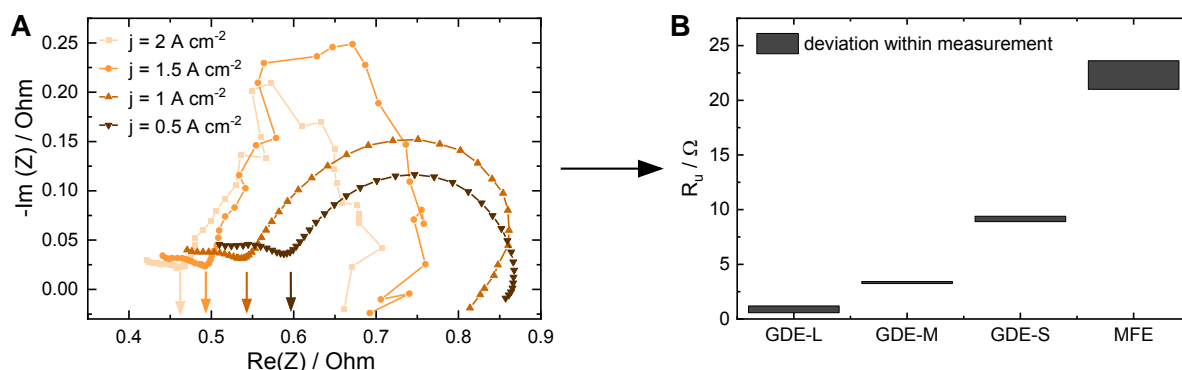


Figure S5. Importance of determining the uncompensated resistance (R_u) at each current step. A: Nyquist plot for different currents in the GDE-L setup. It can be seen, that R_u decreases with increasing current density. B: Comparison of R_u changes within one polarization curve measurement.

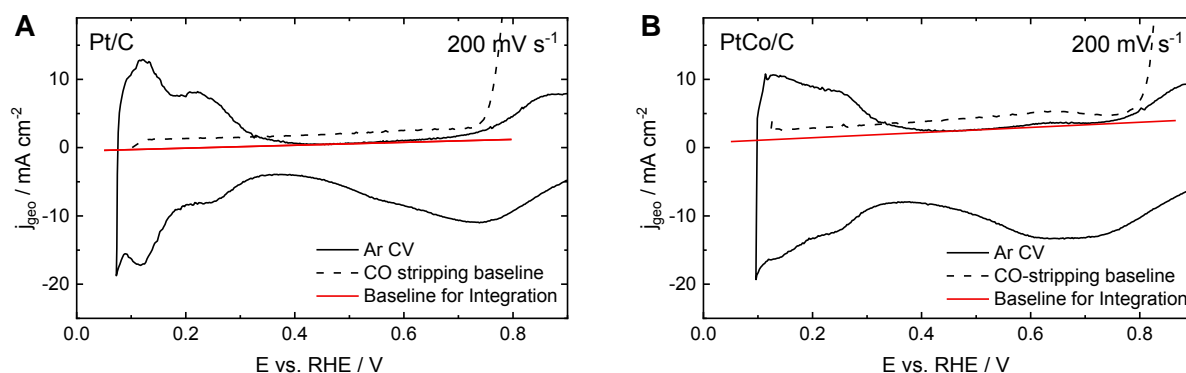


Figure S6. Guideline on choosing the correct baseline for ECSA determination via H_{upd} (data from GDE-L) on the example of a Pt/C (A) and PtCo/C (B) GDE. No straight line should be chosen due to the high surface area carbon support. The baseline should rather be adjusted to the double layer region. It should be parallel to the CV with CO adsorbed on the Pt surface. Due to some undesired O_2 in all GDE half-cell setups, it is necessary to shift the baseline according to the double layer region. Following this guideline, similar ECSA values as with CO stripping can be obtained for Pt/C GDEs.

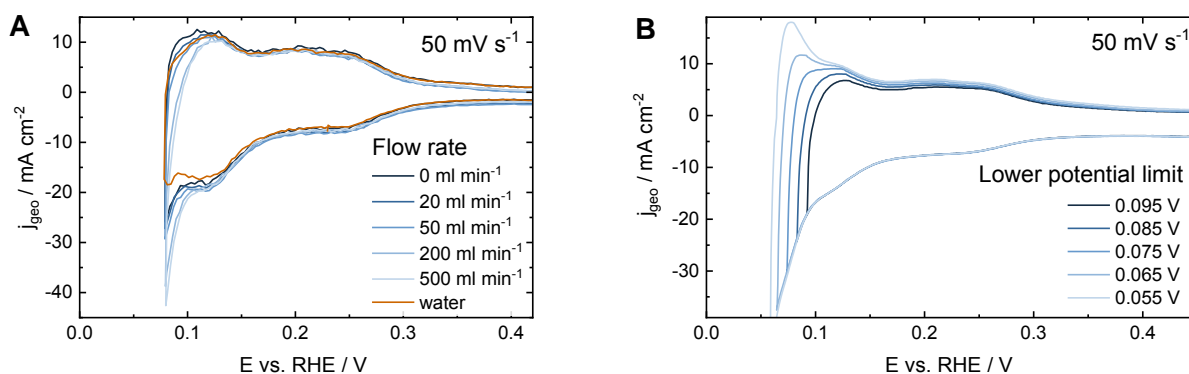


Figure S7. Parameters affecting the ECSA determination via H_{upd} method. A: Impact of the back gas flow on H_{upd} region of Ar CVs. Spray coated Pt/C GDEs ($0.4 \text{ mg}_{Pt} \text{ cm}^{-2}$, HiSPEC4000). B: Impact of the lower potential limit on H_{upd} region of CVs obtained in Ar environment without back flow (commercial GDE, $0.3 \text{ mg}_{Pt} \text{ cm}^{-2}$). Here an adequate lower potential limit would be around 0.075 V vs. RHE.

2.5 Details on the comparison between GDE cell designs

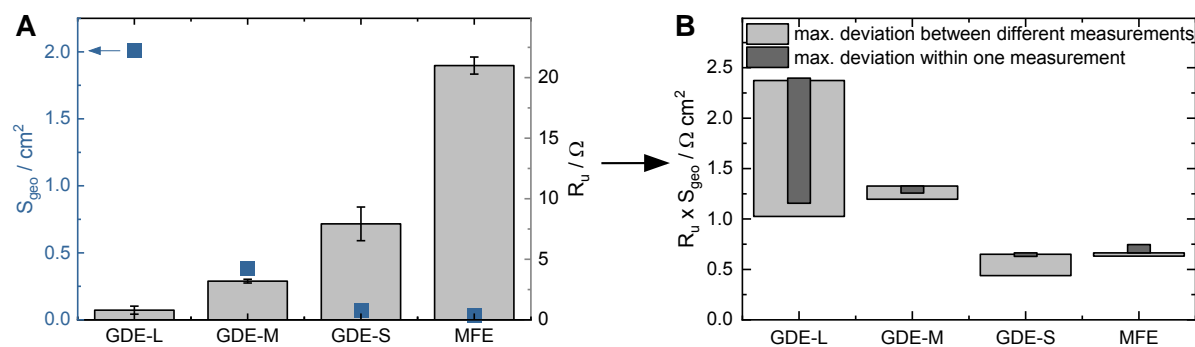


Figure S8. Impact of the geometric surface area (S_{geo}) and the uncompensated resistance (R_u) on the iR-drop. A: Comparison of S_{geo} (blue) and R_u for the different setups. B: The product of S_{geo} and R_u is proportional to the iR-drop in each cell. It can be seen that the fluctuations of the R_u affect the iR-drop significantly for the bigger area cell (GDE-L). Therefore, especially in this cell, correct R_u determination at each step is extremely important.

References

1. Ehelebe, K.; Seeberger, D.; Paul, M. T. Y.; Thiele, S.; Mayrhofer, K. J. J.; Cherevko, S., Evaluating Electrocatalysts at Relevant Currents in a Half-Cell: The Impact of Pt Loading on Oxygen Reduction Reaction. *J. Electrochem. Soc.* **2019**, *166* (16), F1259-F1268.
2. Inaba, M.; Jensen, A. W.; Sievers, G. W.; Escudero-Escribano, M.; Zana, A.; Arenz, M., Benchmarking high surface area electrocatalysts in a gas diffusion electrode: measurement of oxygen reduction activities under realistic conditions. *Energy Environ. Sci.* **2018**, *11* (4), 988-994.
3. Hrnjić, A.; Ruiz-Zepeda, F.; Gaberscek, M.; Bele, M.; Suhadolnik, L.; Hodnik, N.; Jovanovič, P., Modified Floating Electrode Apparatus for Advanced Characterization of Oxygen Reduction Reaction Electrocatalysts. *J. Electrochem. Soc.* **2020**, *167*, 166501.
4. Ahluwalia, R. K.; Papadias, D. D.; Kariuki, N. N.; Peng, J.-K.; Wang, X.; Tsai, Y.; Graczyk, D. G.; Myers, D. J., Potential Dependence of Pt and Co Dissolution from Platinum-Cobalt Alloy PEFC Catalysts Using Time-Resolved Measurements. *J. Electrochem. Soc.* **2018**, *165* (6), F3024-F3035.
5. Gatalo, M.; Jovanovič, P.; Petek, U.; Šala, M.; Šelih, V. S.; Ruiz-Zepeda, F.; Bele, M.; Hodnik, N.; Gaberšček, M., Comparison of Pt–Cu/C with Benchmark Pt–Co/C: Metal Dissolution and Their Surface Interactions. *ACS Applied Energy Materials* **2019**, *2* (5), 3131-3141.
6. Kobayashi, A.; Fujii, T.; Harada, C.; Yasumoto, E.; Takeda, K.; Kakinuma, K.; Uchida, M., Effect of Pt and Ionomer Distribution on Polymer Electrolyte Fuel Cell Performance and Durability. *ACS Applied Energy Materials* **2021**, *4* (3), 2307-2317.
7. Khandavalli, S.; Park, J. H.; Kariuki, N. N.; Myers, D. J.; Stickel, J. J.; Hurst, K.; Neyerlin, K. C.; Ulsh, M.; Mauger, S. A., Rheological Investigation on the Microstructure of Fuel Cell Catalyst Inks. *ACS Appl. Mater. Interfaces* **2018**, *10* (50), 43610-43622.
8. Lin, X.; Zalitis, C. M.; Sharman, J.; Kucernak, A. R. J., Electrocatalyst performance at the gas/electrolyte interface under high mass transport conditions: optimization of the “floating electrode” method. *ACS Appl. Mater. Interfaces* **2020**.
9. Christmann, K.; Friedrich, K. A.; Zamel, N., Activation mechanisms in the catalyst coated membrane of PEM fuel cells. *Prog. Energy Combust. Sci.* **2021**, *85*, 100924.

7.2 Manuscript II:

P. Collantes Jiménez, G. Sievers , A. Quade, V. Brüser, R.K. Pittkowski, M. Arenz.

Gas diffusion electrode activity measurements of iridium-based self-supported catalysts produced by alternated physical vapor deposition.

The published paper is reprinted with permission from *J Power Sources*. **2023**; 569 (April).

J Power Sources. **2023**; 569 (April).

<https://doi.org/10.1016/j.jpowsour.2023.232990> (Open Access)



Gas diffusion electrode activity measurements of iridium-based self-supported catalysts produced by alternated physical vapour deposition

Pablo Collantes Jiménez^a, Gustav Sievers^{a, **}, Antje Quade^a, Volker Brüser^a, Rebecca Katharina Pittkowski^{b, ***}, Matthias Arenz^{c, *}

^a Leibniz Institute for Plasma Science and Technology, Felix-Hausdorff-Strasse 2, 17489, Greifswald, Germany

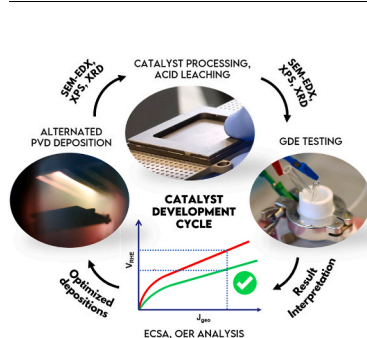
^b Department of Chemistry, University of Copenhagen, Universitetsparken 5, 2100 Copenhagen, Denmark

^c Department of Chemistry, Biochemistry and Pharmaceutical Sciences, University of Bern, Freiestrasse 3, CH-3012, Bern, Switzerland

HIGHLIGHTS

- Electrochemical active surface area and oxygen evolution reaction mass activities scaled with as-deposited Co content.
- Remaining Co suggests a positive effect on the specific activity.
- Accelerated development of oxygen evolution reaction electrode production method and testing demonstrated.

GRAPHICAL ABSTRACT



ARTICLE INFO

Keywords:

PEM Water electrolysis
Oxygen evolution reaction
Physical vapour deposition
Gas diffusion electrodes
Self-supported catalysts

ABSTRACT

The scarce supply of Ir used to catalyze the sluggish oxygen evolution reaction in acidic water electrolysis calls for unconventional approaches to design more active catalysts with minimal resource usage for their commercial scaling. Industrial-ready production methods and laboratory scale tests that can reflect the catalyst behaviour realistically need to be included in this process. In this work, we benchmarked three series of self-supported Ir–Co catalysts with low Ir loading produced by physical vapour deposition under relevant current densities in a gas diffusion electrode setup. It was seen that after selective acid leaching of the Co, a nanoporous structure with a high electrochemically active surface area and a mixed oxide and metallic character was formed. Depending on the initial Co:Ir deposition ratio over ten times higher oxygen evolution mass activities could be reached as compared to a commercial, unsupported IrOx nanoparticle catalyst used as a benchmark in the same setup configuration. The presented integrative catalyst design and testing strategy will help to facilitate bridging the gap between research and application for the early introduction of next-generation catalysts for water splitting.

* Corresponding author.

** Corresponding author.

*** Corresponding author.

E-mail addresses: sievers@inp-greifswald.de (G. Sievers), rebecca.pittkowski@chem.ku.dk (R.K. Pittkowski), matthias.arenz@unibe.ch (M. Arenz).

<https://doi.org/10.1016/j.jpowsour.2023.232990>

Received 22 January 2023; Received in revised form 11 March 2023; Accepted 20 March 2023

Available online 5 April 2023

0378-7753/© 2023 The Authors. Published by Elsevier B.V. This is an open access article under the CC BY license (<http://creativecommons.org/licenses/by/4.0/>).

1. Introduction

Recently, there has been a widespread development of materials and techniques to buffer the intermittent renewable energy supply via diverse applications such as supercapacitors [1–3] and lithium-ion batteries [4,5]. In addition, hydrogen production via proton exchange membrane water electrolysis cells (PEMWEs) stands in the focus of current academic and industrial research. Aside from energy storage for the grid, heat or mobility, PEMWEs can also be a key element in industrial markets that demand hydrogen, such as the ammonia chemical industry, chemical stock synthesis or fuel synthesis (power-to-x) [6]. According to the International Energy Agency (IEA), global demand for hydrogen was estimated at 87 million metric tonnes (MMT) year in 2020 and is forecasted to increase by 13 MM T/year until reaching 528 MMT in 2050 [7]. To reach a net-zero emission scenario in 2050 without further investment in fossil-fuel-based carbon capture, utilization and storage (CCUS) an extra 190 MT of hydrogen power produced by water electrolysis would be necessary to provide 2000 GW of net capacity. To put this development into perspective, by the year 2030 a target for 40 GW in electrolysis capacity should be reached according to the European Green Deal, with an associated cost of EUR 20 to 40 billion without accounting for the electricity costs [8]. While commercial alkaline electrolyzer systems are currently more economical at a lower price per kilowatt [9], PEMWEs have experienced a greater cost reduction due to R&D efforts. The interest in PEMWE development stems from their ability to provide higher current densities and to work at higher temperatures and pressure as compared to alkaline electrolyzers, which makes them a more interesting option for industrial scaling [10]. However, their most challenging limitation is the requirement of Platinum Group Metals (PGMs) such as Ir and Pt to improve the slow electrode reaction kinetics under harsh acidic conditions and high potentials. In particular, the oxygen evolution reaction (OER) occurs in a multi-step reaction that is favoured on the active sites of Ir-based oxide catalysts [11]. While Ru-based oxides have shown higher activity than IrO₂ for the OER, the latter sustains the most balanced equilibrium between high activity and durability in the acidic environment [12]. Since PEMWEs should withstand periods of >50 k operating hours under high current densities and transients without showing significant degradation, the choices are further narrowed. Unfortunately, the supply of Ir and Pt is very limited and costly. Just in the first quarter of 2021, the price per ton of Iridium increased sharply by four times, which is the highest price increase registered in the last 20 years [13]. Hence, to upscale the PEMWE production the capital expenditure (CAPEX) cost including noble metal cost has to decrease. To establish Ir catalysts as a commercially viable and scalable option in PEMWEs, the catalyst loading needs to be reduced while maximizing the catalytic activity. For maintaining a high catalytic activity with low loadings, the electrochemically active surface area (ECSA) should be as high as possible. A common strategy to reduce the catalyst loading is to develop alloys with synergistic effects that increase the intrinsic activity [14] as is observed when combining Ir with Cu, Co, or Ni [15,16] or forming core-shell structures [17] that benefit from an Ir-rich surface [18–20]. Another approach is to develop completely PGM-free catalysts based on alloys of more abundant metals, i.e., Co, Ni, Fe or Mo derived from metal-organic frameworks (MOF) [21–24]. However, the most known commercial catalysts are still unsupported, Ir-based nanoparticles. Several synthesis approaches have been tested to produce nanoparticles with different characteristics [25]. It is not possible to support the nanoparticles on carbon to increase the surface area, as the carbon degrades. This has the disadvantage that the ECSA of Iridium black is small compared to Pt/C catalysts used in fuel cell systems [11,26–28]. Recently developed self-supported catalyst nanostructured catalysts present a possible solution to this problem since the catalyst is applied on the substrate (e.g., a gas diffusion electrode) directly without using binder materials. With this approach, it already has been shown that microstructure tuning and modulation of the catalysts' electronic structure with heteroatoms can

produce highly active and stable catalysts [29–32]. However, multi-step processes are often used at the lab scale to synthesize catalyst particles and coatings, which can impose limitations in the industrial scaling. On the other hand, physical vapour deposition (PVD) is a well-known technique in the industry. The plasma process yields homogenous composition in the layers and allows flexible operative conditions such as the direct deposition of oxides or control of the morphology modifying, e.g., the sputtering angle or chamber pressure [33]. In recent studies, PVD has been used to produce highly active self-supported catalysts with tunable morphologies using a co-sputtered templating metal [11,34,35]. High ECSAs are achieved by selective dissolution of the templating metal in an acid-leaching processing step, which creates an interconnected network of the active metal. Several publications concerning this method report large ECSAs and activities [11,34,35]. On the other hand, the high catalyst performance observed with traditional academic testing techniques such as the thin-film rotating disk electrode (TF-RDE) hardly ever translates to real operation conditions seen on full membrane electrode assembly (MEA) systems [36]. The step from lab testing to an industrial application is thus very wide. Testing in a liquid acidic environment under mass transport limited conditions does not describe accurately those of a Membrane-Electrode-Assembly. Furthermore, it has been discussed that the degradation trials on OER could have been systematically misinterpreted [37–40]. Due to the method limitations, the oxygen evolved during the reaction is trapped close to the surface of the catalyst causing early failure during the test, while the catalyst features remain unchanged [39]. Gas diffusion electrode (GDE) setups have been introduced as a bridging tool as they include realistic constraints (real catalyst loadings, membrane layer, gas diffusion/porous transport layers, three-phase boundary) while keeping the fast screening capabilities of the TF-RDE and retaining the ability to measure the potential drop of the anode in a three-electrode setup. While initially designed for oxygen reduction reaction (ORR) studies [41–43], an increasing number of publications with GDE setups in different configurations also prove its flexibility to explore different reactions such as the OER [25]. It is expected that this technique becomes a standard in the electrochemical community and is used more systematically to develop catalyst layers in a fast and cost-effective manner before applying MEA tests [44]. In the present study, we use a GDE setup modified to accommodate electrolysis conditions to perform an electrochemical characterization of the OER in three series of IrCo catalysts produced by PVD with different sputtering Co:Ir ratios. In particular, we aim to study the influence of the deposition parameters on the reaction performance. To that end, we use morphological and chemical characterization techniques (SEM-EDS, XAS, XRD, XPS) to follow the development of the catalyst during different steps in the material preparation (magnetron sputtering followed by acid leaching). The features observed (mesoporosity, chemical distribution, crystallinity) are further discussed alongside the electrochemical characterization of the ECSA of the catalyst by cyclic voltammetry (CV) and OER mass activity. Our findings indicate a direct relationship between the deposition parameters and the electrochemical results. Furthermore, this study underlines the interesting synergy of the PVD with the GDE method to fast-track catalyst film optimization for industrial applications.

2. Experimental section

2.1. Materials, chemicals, gases

De-ionized ultrapure water (resistivity >18.2 MΩ cm, total organic carbon (TOC) < 5 ppb) from an Aquinity P –10² system (Membrapure, Germany) was used for electrolyte preparation and the cleaning of the GDE half-cell. Carbon gas diffusion layers (GDL) with a microporous layer (MPL) (Sigracet 29BCE, 325 μm thick, Fuel Cell Store) served as a substrate for the sputtering of the catalyst film. A polytetrafluoroethylene (PTFE) disk (Bola, 0.12 mm thickness), a GDL without an MPL

(Freudenberg H23, 210 μm thick, Fuel Cell Store), a porous transport layer (PTL) (ANKURO Int. GmbH, 0.3 mm thickness, 50% open porosity), and a Nafion membrane (Nafion 117, 183 μm thick, Chemours, Wilmington, DE, USA) were used for the cell assembly (see Fig. 1). As a counter electrode (CE) a platinum wire of 0.5 mm diameter (99.99%, Junker Edelmetalle GmbH) was used, which was folded several times at one side to increase the active surface area. Another Pt wire was used to manufacture a hydrogen reference electrode (RE) using a borosilicate glass capillary of 40 mm in length and 6 mm in diameter. Additionally, self-manufactured borosilicate glass frits (6 mm internal diameter, 20 mm length) were used to hold the RE during the electrochemical measurements. Perchloric acid (70% HClO_4 , Suprapur, Merck) was used for electrolyte preparation. O_2 (99.999%, Air Liquide) and Ar (99.999%, Air Liquide) were used for magnetron sputtering, acid leaching, and electrochemical measurements.

2.2. Catalyst synthesis - preparation of the Ir-Co network

To prepare the self-supported nanoporous catalyst film, a linear sputtering magnetron reactor (Univex 400, Leybold GmbH, Germany) was used. The process chamber was evacuated to a pressure of $1.7 \cdot 10^{-5}$ Pa. The film substrate (GDL) was placed on a holder in a load lock at atmospheric pressure and then evacuated to a base pressure of at least 10^{-4} Pa. From there, a swivelling arm allowed the holder to enter the process chamber with minimal interruption. During the deposition, an Ar plasma was ignited at the magnetron electrode at a working pressure of 5 Pa and flushed through the individual magnetron sources at a flow rate of 100 sccm. For the $\text{Ir}_x\text{Co}_{1-x}$ film deposition, two magnetrons were equipped with planar targets of Co (99.95%, Evotec GmbH, Germany) and Ir (99.95%, MaTeck, Germany) of $177 \times 25 \times 1.5$ mm located at the upper part of the chamber. The RF generators (Cito 136, COMET) operated at a driving frequency of 13.56 MHz. Further information about the sample preparation process and the reactor configuration can be found in the SI. A mask of $5 \text{ cm} \times 5 \text{ cm}$ on the substrate holder limited the sputtered area during the deposition. The sample was allowed to oscillate in a linear trajectory between the two respective magnetrons. The sputtering was initiated when the sample reached the position below each magnetron. At that point, the sample holder was programmed to oscillate with an amplitude of 1 mm to increase the homogeneity of the deposition. The holder reached an acceleration of 100 mm s^{-2} and a maximum linear velocity of 50 mm s^{-1} . The RF power was chosen as 225 W for Co and 50 W for Ir. The alternating sputtering process was performed for 500 cycles in all series, modifying the deposition time to achieve three different element ratios as seen in Table 1. The average deposition time was 4–5 h. Before the

Table 1

Material parameters during the magnetron sputtering process.

Series By element wt.% (EDX)	Sputtering time (s)	Number of cycles	Loading Ir ^a (mg cm^{-2})	Gas atmosphere	Substrate type
$\text{Ir}_{28}\text{Co}_{72}$	Ir: 3 Co: 6	500	0.250	Ar 100%	GDL 29BCE
$\text{Ir}_{45}\text{Co}_{55}$	Ir: 3 Co: 3	500	0.250	Ar 100%	GDL 29BCE
$\text{Ir}_{75}\text{Co}_{25}$	Ir: 3 Co: 1	500	0.250	Ar 100%	GDL 29BCE

^a Theoretical loading calculated by mass gravimetry.

measurements, a calibration of the sputtering process was performed where Ir was sputtered continuously for 20 min on a substrate. The final Ir loading was measured by mass gravimetry, and the thickness homogeneity was verified using a profilometer (Alpha Step D-600, KLA). Assuming a linear dependency of loading with the sputtering time, three series were produced with a nominal Ir loading of 0.250 mg cm^{-2} and different Co:Ir deposition time ratios. The resulting Co:Ir ratios were determined experimentally by EDX on the as-prepared samples (Table 1).

As part of the Ir-Co catalyst film preparation, the samples were leached after the deposition in 1 M HClO_4 to create a nanoporous self-supported Ir structure by selectively dissolving the Co under potential-controlled conditions according to the method developed by Sievers et al. [11]. The individual steps of the acid leaching procedure are summarized in Table 2 and described more in detail within the Result and Discussion section. Once the samples were leached, they were cleaned in distilled water and left to dry in air before further manipulation.

2.3. Gas diffusion electrode setup

The GDE was prepared using a Nafion membrane (Nafion 117, 183 μm thick, Fuel Cell Store) hot pressed to the sputtered gas diffusion layer (GDL). In this study, the Nafion membrane was activated as described by Schröder et al. [25]. A concentric circular steel punch (BOEHM, Germany) was used to cut small disks from the GDL and the assembly material. First, a disk of $\varnothing 3$ mm was cut from the sputtered GDL. Using an in-house built hot press (Fig. S1) with a modified soldering iron and 6 kg steel weights, a $\varnothing 10$ mm Nafion membrane was hot pressed on top of the catalyst layer at 120°C using 84 kg cm^{-2} for 30 s.

As indicated in Fig. 1, a $\varnothing 20$ mm Gas Diffusion Layer (GDL) without

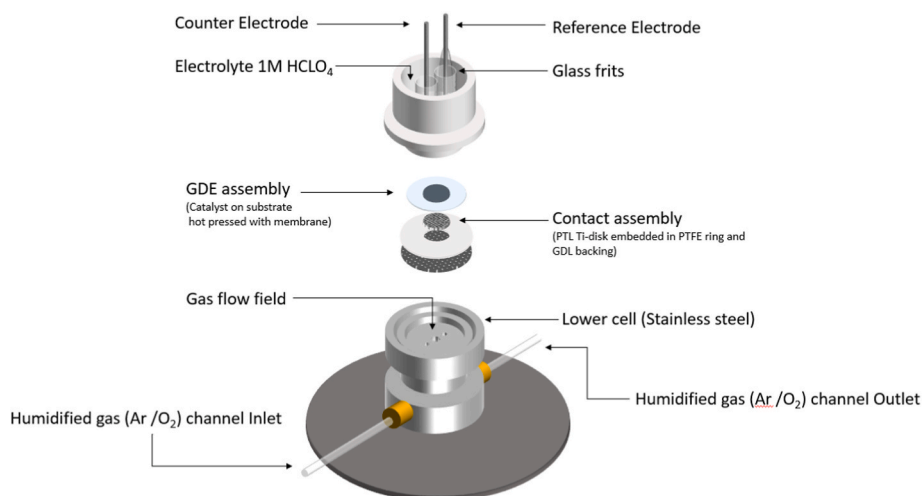


Fig. 1. GDE half-cell setup used in the study and assembly view of all elements.

Table 2
Electrochemical protocol for OER activity trials.

Acid leaching	Cyclic Voltammetry (CV)	Activation (Potentiostatic)	OER (Galvanostatic)	Steps	
30 cycles 100 sccm Ar 100 ml 1 M HClO ₄ 0.05–0.5 V _{RHE} 100 mVs ⁻¹ 5 kHz, 5 mV AC	30 cycles 100 sccm Ar 4 ml 1 M HClO ₄ 0.05–1.2 V _{RHE} 100 mVs ⁻¹ 5 kHz, 5 mV AC Post iR correction	20 min 100 sccm Ar 4 ml 1 M HClO ₄ 1.7 V _{RHE} Online iR-comp.	30/60 °C 100 sccm O ₂ 4 ml 1 M HClO ₄ 1 - 1000 Ag ⁻¹ 5 min/step Post iR correction	Step 0 Step 1 Step 2 Step 3	Leaching 1. CVs (ECSA) 2. OER 30 °C 3. CVs 1. CVs 2. Act. 3. CVs 4. OER 30 °C 5. CVs 1. OER 60 °C 2. CVs

a microporous layer (MPL) was placed directly over the flow field of the stainless-steel bottom cell. On top, a Ø 20 mm Teflon disk with a Ø 3 mm center hole was used as a sealant for the liquid and electrical insulator. Embedded inside, a Ø 3 mm PTL disk was positioned to allow the gas flow to contact the GDE on top and to serve as a current collector. Last, a Teflon upper cell was pressed against the assembly and secured tightly with a metal clamp. Both the Teflon upper cells and the CE and RE were cleaned before every use according to the following protocol. First, they were placed overnight in a tank with concentrated HNO₃ and concentrated H₂SO₄ solution 1:1 in volume. Afterwards, they were rinsed and boiled in distilled water for 1 h in at least 5 cycles. The unused materials were kept in a glass vial and boiled always one last time before use. Furthermore, the Pt wire was flame annealed every time it was used to remove any organic contaminations. After every trial, all the assembly components were discarded and replaced with new ones to decrease the influence of contaminations.

2.4. Electrochemical measurements

All the experiments were conducted with a Potentiostat (ECi-211, Nordic Electrochemistry ApS, Denmark). The Potentiostat also controlled the gas switching between humidified Ar and O₂ during the experiments. An overview of the experimental protocol is presented below in Table 2.

The GDE half-cell (Fig. 1) and a glass bubbler were placed inside an insulating glass chamber during the measurements (See Fig. S1 in SI). Precise temperature control (±0.1 °C) was achieved through a constant flow of distilled water recirculated in between the double glass walls with a water heating system (Lauda RC6 SC). The GDE half-cell was placed in the middle of the chamber, supported on an aluminium laboratory jack (Laborboy, Sigma Aldrich) and insulated with a PTFE plate in between. Before the start of the measurements, the system was allowed to equilibrate at a constant temperature for at least 30 min. All the temperature references correspond to the set point defined in the water heating system. To prevent any shifts in reference potential due to contaminations on the RHE electrode, the RE was protected in a glass frit manufactured by an in-house technical glassblower. In addition, the RHE electrode was calibrated before each measurement in a separate GDE cell against a Pt GDE with the same molarity and electrolyte as the testing GDE cell, i.e., 1 M HClO₄ electrolyte. The H₂ gas was supplied

through an in-house electrolyzer, connected to the gas flow through lines of the GDE cell. The RHE offset was measured by cyclic voltammetry in a potential interval between -0.005 and 0.005 V at 100 mV s⁻¹ for 200 cycles. The acceptable range for initial RHE values was defined as ± 0.003 V_{RHE}. In case of a larger deviation, the RHE was remade, and the calibration procedure was repeated to avoid large iR-correction errors. Before the measurements, Ar was purged through the flow field as a conditioning step and cyclic voltammograms were recorded at a scan rate of 100 mV s⁻¹ in a potential range between 0.025 and 1.2 V_{RHE} until a stable cyclic voltammogram could be observed (ca. 30 cycles). The ECSA of the catalyst (Table 3) was determined by integrating the H_{upd} area in the potential window of 0.025–0.25 V_{RHE} of the last CV acquired using a fixed conversion coefficient of 176 µC cm⁻² [11] according to the following formula:

$$ECSA [m^2 g^{-1}] = \frac{QH_{upd}}{L_{ir} \times 176 \mu C cm^{-2}} \quad (1)$$

The OER activity was determined through a galvanostatic step protocol with increasing currents based on Schröder et al. [25] and scaled accordingly to account for the loading difference. An AC signal (5 kHz, 5 mV) was applied during the current steps to obtain an online resistance measurement between the working and reference electrode (~10 Ω) which was used for an iR-correction of the measured potential values.

3. Results & discussion

3.1. Catalyst morphology and chemical composition

The morphology of the unleached catalyst layers, i.e., after the deposition process, was characterized using secondary electron imaging (SEM), see Fig. 2. As seen in Fig. 2a, b and c, all catalyst series featured a similarly packed globular structure. Similar morphologies have been previously observed in studies of catalyst films prepared on carbon paper substrates using comparable process conditions [33]. The size of the globular features was not substantially different between the respective series, ranging from 0.1 to 0.9 µm in diameter. However, the SEM micrographs indicate further development of nanoporous structures. That is, the surface of the globules exhibits a certain degree of roughness, which is especially distinct for the Co-rich series (Ir₂₈Co₇₂; in the following the notation refers to the elemental composition obtained

Table 3
Relevant electrochemical parameters for the catalyst series included in the study. Error measurements are expressed from the average of three trials per series.

Series By element wt. %	Tafel slope (mV dec ⁻¹) @30–100 Ag ⁻¹ _{ir}		Mean ECSA (m ² g ⁻¹) A _{geo} = 0.0707 cm ² C = 176 µCcm ⁻²	Mass Activity (Ag ⁻¹)		Specific Activity (Am ⁻²)	
	Activated 30 °C	60 °C		@1.50 V _{RHE} Activated 30 °C	@1.46 V _{RHE} 60 °C	@1.50 V _{RHE} Activated 30 °C	@1.46 V _{RHE} 60 °C
Ir ₂₈ Co ₇₂	62	49	52.6 ± 4.8	101.5	117.8	1.9	2.2
Ir ₄₅ Co ₅₅	64	52	33.7 ± 1.9	57.6	91.8	1.7	2.7
Ir ₇₅ Co ₂₅	68	58	21.4 ± 2.0	44.3	62.7	2.1	2.9
Alfa Aesar	53	47	–	12.14	10.18	–	–

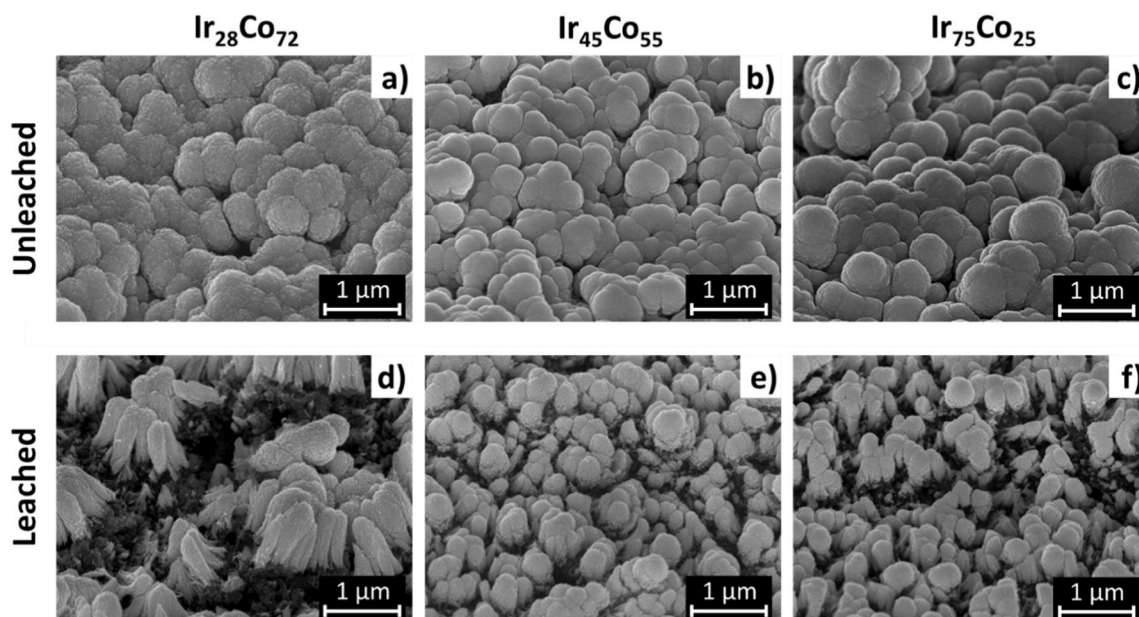


Fig. 2. SEM SE top measurements of IrCo catalysts on a carbon substrate taken with a 45° angle from the surface, at 15 kV and 10 k magnification. a) to c) correspond to the samples before the electrochemical dealloying in HClO₄ 1 M for 30 cycles between 0.05 and 0.5 V_{RHE} while d) to f) show the surface of the same samples after the process. A summary of EDX results normalized for Ir and Co is expressed in weight % (upper table) and atomic % (lower table). The results were obtained at 15 kV, averaged from 5 spots across the image area.

by EDX point analysis before the acid leaching), see Fig. 2a as well Fig. S2b for a closer look. Finally, yet importantly, EDX top-down mapping of different representative areas on the catalyst films, see Fig. S3, revealed that in all cases Ir and Co were homogeneously distributed across the film. As mentioned before in the Method section, Co was removed from the sputtered films in a process that is referred to as acid leaching. As the Pourbaix diagrams show for the respective catalyst film constituents, metallic Ir is stable under the leaching conditions while Co is oxidized to soluble Co²⁺ ions and does not form a passive film [45,46]. Hence, Co dissolution starts spontaneously when a sputtered sample is submerged in a de-aerated 1 M HClO₄ aqueous solution [11], giving the solution had a characteristic pink tone. The color of this solution has been described extensively as a result of the complexation of Co²⁺ complex in water to form [Co(H₂O)₆]²⁺. To confirm this, Cl⁻ ions were added to the solution from concentrated HCl and the temperature was raised. Both effects shift the equilibrium to [CoCl₄]²⁻ as a direct consequence of Le Chatelier principle [47], which shows a distinct blue color, see Fig. S4. To attain better control of the acid leaching process and to minimize Ir oxidation before ECSA determination of the metallic surface, the samples were submitted to an electrochemical cycling protocol (Table 2) between 0.05 V_{RHE} and 0.5 V_{RHE} with a scan rate of 100 mV s⁻¹ starting directly after the electrolyte was added to the upper cell compartment. The cycling continued until a stable CV was achieved. This was typically the case after 30 potential cycles. Along this process, the initial Co to Ir ratios were changed significantly. In every case, the relative amount of Co decreased to under 10% in weight according to the EDX. Using XPS for a more surface-sensitive analysis of the pre-leached and leached samples, see Fig. S5, we observed a trend in the decrease in the Co:Ir ratios after leaching following the series, albeit not proportional to the initial ratios (see Fig. S6). This discrepancy could perhaps be attributed to the drastic change in morphological differences and chemical gradients to form a more stable Ir shell with a Co core after the acid leaching [11,47,48]. The process of acid leaching has been well described for Pt-based alloys for the oxygen reduction reaction. It has been shown by low energy ion scattering (LEIS) that the exposition of PtM (M = Fe, Co, Ni, etc.) surfaces automatically leads to a full depletion of all non-noble atoms from the surface and the formation of “skeleton” or core shell surfaces [48]. In

the here reported work, sparse colonies of Ir-rich dendritical structures were formed of the GDL carbon substrate, which was also left exposed over large areas. The development of this porous structure differs substantially from the preparations on glassy carbon in a former study [11], see Fig. S2. The reason for this difference might be the three-dimensional structure of the gas diffusion electrode or the hydrophobicity. The initially Co-rich sample, Ir₂₈Co₇₂ presents the biggest size of the dendrites and area of the exposed substrate. Both features appeared to decrease together with the Co:Ir ratio when comparing Ir₂₈Co₇₂ with the Ir₄₅Co₅₅ and Ir₇₅Co₂₅ series (Fig. 2d, e and f respectively).

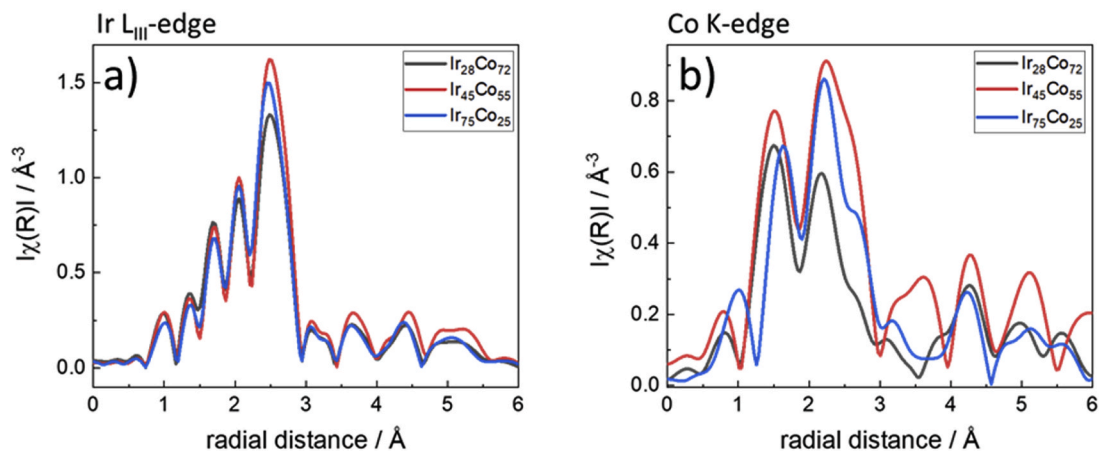
Series	wt.% norm.			
	Unleached		Leached	
	Ir	Co	Ir	Co
Ir ₂₈ Co ₇₂	27.7 ± 1.9	72.3 ± 1.9	95.0 ± 0.8	5.0 ± 0.8
Ir ₄₅ Co ₅₅	44.9 ± 0.7	55.1 ± 0.7	96.2 ± 1.5	3.8 ± 1.5
Ir ₇₅ Co ₂₅	75.3 ± 5.1	24.7 ± 5.1	91.9 ± 0.8	8.1 ± 0.8
Series	at.% norm.			
	Unleached		Leached	
	Ir	Co	Ir	Co
Ir ₂₈ Co ₇₂	10.5 ± 0.9	89.5 ± 0.9	85.4 ± 2.1	14.6 ± 2.1
Ir ₄₅ Co ₅₅	19.8 ± 0.7	80.2 ± 0.7	88.6 ± 4.1	11.4 ± 4.1
Ir ₇₅ Co ₂₅	48.8 ± 6.7	51.3 ± 6.7	77.8 ± 1.9	22.2 ± 1.9

The element distribution of representative leached areas can be found in the EDX mapping of Fig. S3 of the SI. An as-sputtered XRD analysis indicated that the elements are found in a heterogeneous film with a low degree of crystallinity, as it is normal for sputtered catalysts that do not experience a heat treatment [26,49,50]. While the overall structure remains amorphous, the shift to lower theta values and narrowing of the Ir (111) Bragg peak after leaching, see Fig. S7, suggests that it might experience a slight increase in crystallinity, which has also been reported in similar studies [11,34,51]. Since the first studies on AuAg nanoporous structure formations via selective leaching, several studies have emerged to explain the behaviour of homogeneous bimetallic alloys [52–57] as well as the change in electronic properties due to the formation of core-shell nanoparticles. However, a former study using a similar magnetron-sputtering and acid-leaching process to create a

self-supported Pt–CoO network revealed that no alloy was formed in the bimetallic deposition or leaching process [35]. A further look into the oxidation state and the small range structures of the Ir–Co series was conducted by ex-situ X-ray Absorption Spectroscopy (XAS) of the leached samples, see Fig. 3 and Figs. S8–10 of the SI. Data were collected at both, the Co and Ir edge, however, due to the low Co content the data quality is significantly lower for the Co edge than for the Ir edge. Therefore, we draw our conclusions mainly from the data obtained from the Ir L_{III} K-edge. The X-ray absorption fine structure (EXAFS) results reveal mixed metallic and oxide structures, see Fig. 3. The presence of Co–Co₁ and Ir–Ir₁ coordination indicates that a proportion of Co and Ir remains metallic after acid leaching and exposure to air. Furthermore, the presence of Ir–Co₁ coordination shows a partial alloy character with a similar trend as observed in the Co content of the leached samples by

EDX: Ir₇₅Co₂₅ > Ir₂₈Co₇₂ > Ir₄₅Co₅₅. In addition, Ir–O₁ and Co–O₁ coordination is seen indicating partial oxidation of the samples. Interestingly, the data from all series indicate a similar Ir–O₁ bond length, indicating that the Co content has no measurable effect on lattice strain.

Considering the mixed chemical nature of the material, we describe it as Ir_xCo_{1-x} nanoclusters rather than an IrCo alloy. In this context, the self-supported structure is achieved by the dissolution of a sacrificial templating metal in a selective acid leaching process under potential conditions, coupled with surface restructuring processes in the material due to diffusive forces. In an earlier study from the same authors concerning the leaching behaviour of co-sputtered noble and non-noble metals in a Pt–Cu system, a mechanism of acid leaching process leading to self-supported nanostructured catalysts was already discussed [34]. As the non-noble metal dissolves in acid, hydrogen gas evolution



Co-edge

Sample	bond	N	R / Å	$\sigma^2 / \text{Å}^2$	E ₀ / eV	R _f
Ir ₂₈ Co ₇₂	Co–O ₁	1.9 ± 0.7	1.94(5)	0.003	7712 ± 9	0.037
	Co–Co ₁	1.2 ± 1.0	2.58(5)	0.004(8)		
	Co–Ir ₁	3.2 ± 2.3	2.60(8)	0.012		
Ir ₄₅ Co ₅₅	Co–O ₁	2.1 ± 0.5	1.91(3)	0.003	7711 ± 6	0.018
	Co–Co ₁	1.1 ± 0.9	2.54(8)	0.004(6)		
	Co–Ir ₁	4.3 ± 0.9	2.64(2)	0.010		
Ir ₇₅ Co ₂₅	Co–O ₁	1.2 ± 0.6	1.98(4)	0.003	7718 ± 6	0.014
	Co–Co ₁	2.0 ± 1.3	2.66(6)	0.004(5)		
	Co–Ir ₁	3.4 ± 1.2	2.64(2)	0.010		

Ir-edge

Sample	bond	N	R / Å	$\sigma^2 / \text{Å}^2$	E ₀ / eV	R _f
Ir ₂₈ Co ₇₂	Ir–O ₁	1.3 ± 0.3	1.99(2)	0.003(3)	11224 ± 2	0.019
	Ir–Co ₁	1.4 ± 0.9	2.63(6)	0.012(9)		
	Ir–Ir ₁	6.7 ± 1.7	2.68(1)	0.005(1)		
Ir ₄₅ Co ₅₅	Ir–O ₁	1.0 ± 0.4	1.99(3)	0.003(1)	11223 ± 2	0.026
	Ir–Co ₁	0.7 ± 0.5	2.64(7)	0.010(4)		
	Ir–Ir ₁	8.2 ± 0.4	2.68(1)	0.005(1)		
Ir ₇₅ Co ₂₅	Ir–O ₁	1.0 ± 0.2	1.99(3)	0.003(3)	11225 ± 2	0.007
	Ir–Co ₁	1.9 ± 0.7	2.63(3)	0.010(5)		
	Ir–Ir ₁	6.7 ± 1.1	2.67(1)	0.005(1)		

Fig. 3. Fourier transformed magnitudes of the k^2 weighted extended X-ray absorption fine structure (EXAFS) data of the leached Ir_xCo_y samples, shown for the a) Ir L_{III} -edge and the b) Co K-edge.

starts spontaneously. Some of the gas can be trapped in interior cavities and mechanically push the material around to nucleate pores. At the same time, the catalyst-rich areas undergo a surface diffusion process due to the electrochemical and mechanical forces, which promote the redeposition of catalysts in neighbouring regions. The structures created in such a process depend on the irregularities of the morphology and porosity at the surface. Surface diffusion of catalyst particles is evidenced by an Ir enrichment and depletion of Co over the surface observed in the EDX maps (Fig. S3) and reinforced by the XPS results (Fig. S6). This process would be in agreement with the different morphologies observed in the series between the as-deposited and leached state for the different EDX Co:Ir ratios and the different initial distributions of Ir and Co-rich areas. A previous study of a very similar Ir-Co catalyst already demonstrated that Co dissolves from all areas in contact with the acid solution leaving a percolated Ir network with the same domain size as the initial deposition [11], which corresponds well with the results presented here.

3.2. GDE electrochemical characterization and activity measurements

After sputtering and acid leaching, each series of the catalyst layers was assembled into the GDE setup for electrochemical testing. The aim

of the electrochemical testing was twofold: first, the electrochemically active surface area (ECSA) of the leached Ir was determined. This was achieved by determining the H_{upd} area in cyclic voltammetry [58]. The leaching conditions were designed to dissolve the Co while preserving Ir in metallic state, as IrO_2 does not display any H_{upd} area. We assume that after leaching any oxidized Ir surface would be reduced and that there is a direct relationship between metallic Ir surface before activation and ECSA after activation. The second aim was to activate the catalyst layer and determine its activity for the OER.

The electrochemical characterization is exemplified in Fig. 4a which depicts the CV and OER activity of a leached Ir-rich ($\text{Ir}_{28}\text{Co}_{72}$) nanostructured IrCo film. It is seen that after leaching, the CV displays a pronounced H_{upd} area indicative of metallic Ir, allowing a straightforward ECSA determination of $52.6 \pm 4.8 \text{ m}^2\text{g}^{-1}$, Fig. 4a. After recording the CV, the gas was switched, and oxygen was flushed through the cell at 1 sccm for 20 min to guarantee a saturated oxygen atmosphere. The OER activity was determined before and after activation and benchmarked to published data from a commercial IrO_2 black powder (Alfa Aesar) [25]. It is worth mentioning that the commercial sample was prepared with a different loading (1 mg cm^{-2}) than the samples in this study. However, it is still considered to be a useful reference since the OER activities were measured using the same protocol and setup

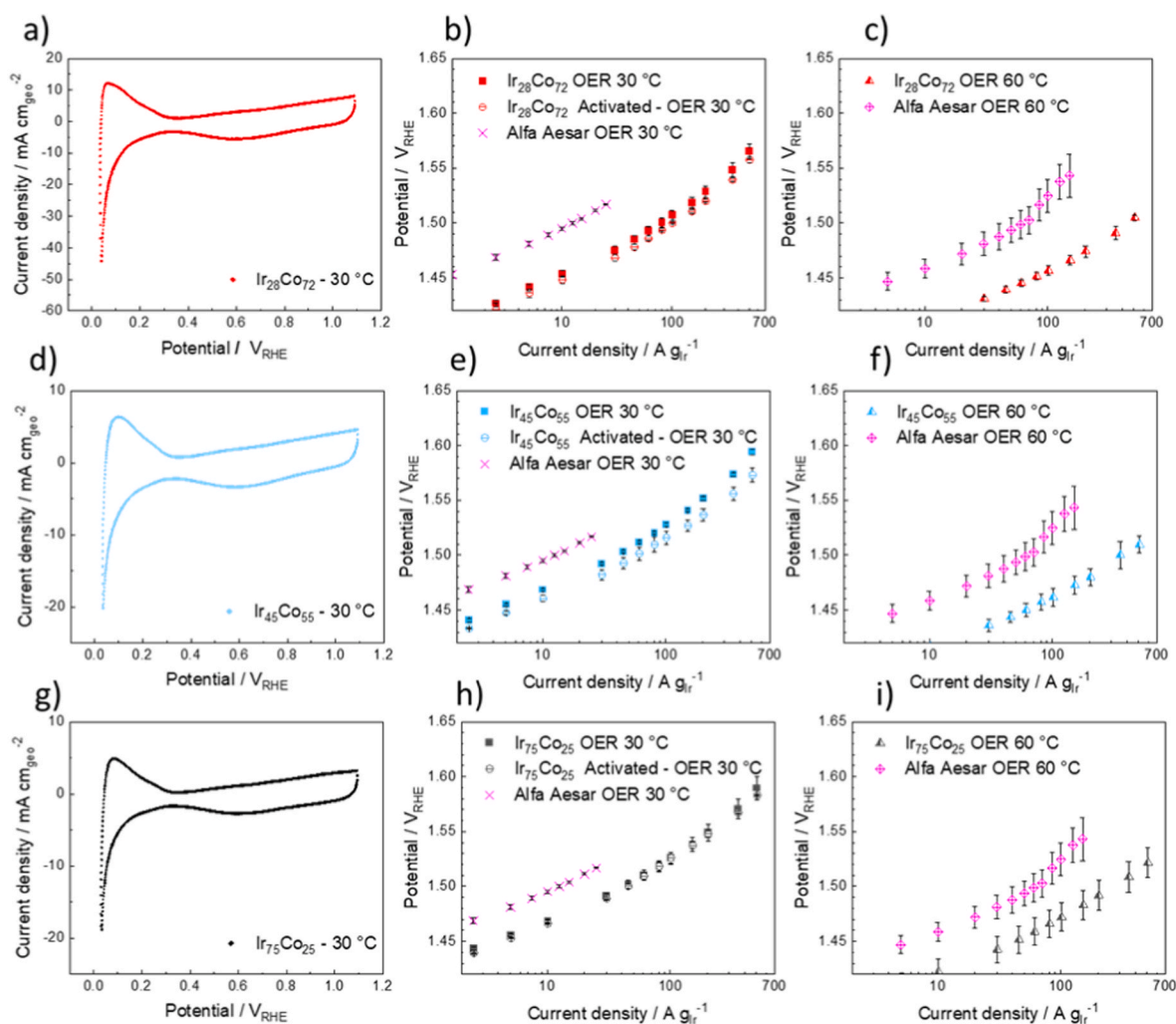


Fig. 4. Average of three cyclic voltammograms in Ar atmosphere measured at 30 °C, 100 mVs^{-1} in 1 M HClO_4 for the a) $\text{Ir}_{28}\text{Co}_{72}$, d) $\text{Ir}_{45}\text{Co}_{55}$ and g) $\text{Ir}_{75}\text{Co}_{25}$ series with a common iridium loading of $250 \mu\text{g}/\text{cm}^2$ before leaching (Table 1). iR-corrected OER mass activity in 100% humidified oxygen at 30 °C measured over the last 10 s of each 300-s current step from the commercial sample and b) $\text{Ir}_{28}\text{Co}_{72}$, e) $\text{Ir}_{45}\text{Co}_{55}$ and h) $\text{Ir}_{75}\text{Co}_{25}$ series in as-prepared (filled symbols) and activated (hollow symbols) states. iR-corrected OER mass activity in 100% humidified oxygen at 60 °C measured over the last 10 s of each 300-s current step for the commercial sample and c) $\text{Ir}_{28}\text{Co}_{72}$, f) $\text{Ir}_{45}\text{Co}_{55}$ and i) $\text{Ir}_{75}\text{Co}_{25}$ series. Each individual data point and error bars represents respectively the average and standard deviation of three different sample measurements.

configuration. The first set of OER activities revealed that the catalyst surface was not yet completely activated into IrO_x . Yet, the OER overpotential in this state was around 40 mV lower as compared to the benchmark. Recording another set of CVs in Ar atmosphere after the first OER measurements confirmed that remainders of metallic Ir were present from a decreased but still discernible H_{upd} area. In addition to the reduced H_{upd} area, the double-layer capacity was increased (Fig. S11b). To complete the oxidation of the metallic Ir, a potentiostatic activation step was applied at 1.70 V_{RHE} for 20 min in O_2 atmosphere (Fig. S12), after which a second set of OER activities was recorded. The fact that the overpotential was reduced by an additional 10 mV as compared to before activation indicates the further formation of the active IrO_2 phase. Nevertheless, recording another set of CVs in Ar atmosphere in step 2.3 of the protocol (Table 2) shows that a complete, irreversible oxidation of the surface has not yet been achieved and still some H_{upd} area is visible (Fig. S11c). Despite the incomplete activation, the OER mass activity at 1.50 V_{RHE} was 101.5 $\text{Ag}^{-1}_{\text{Ir}}$, roughly eight times higher than that of the commercial benchmark catalyst (Table 3). In the third and last step of the protocol the temperature was increased from 30 to 60 °C and OER activity was determined for one last time (Fig. 4c). The raise in temperature leads to a clear decrease in overpotential of ca. 40 mV even at the lowest (20 $\text{Ag}^{-1}_{\text{Ir}}$) current densities (Fig. S13). At this temperature, an OER activity of 117.8 $\text{Ag}^{-1}_{\text{Ir}}$ was determined at 1.46 V_{RHE} . Interestingly, in addition to a temperature-induced kinetic activation, the raise in temperature leads to an additional activation via further oxidation. This can be seen by the fact that the relative OER mass activity increases to a threefold value. In comparison, the benchmark catalyst is mostly oxidized in its initial state. A further description of the contributions to the decreased overpotential due to temperature and activation contributions can be found in the SI. In addition to the activation, it is seen that with the temperature rise the Tafel slope decreased slightly from 62 to 49 mV dec^{-1} . This is a small, but still, significant change, which can be explained by the temperature dependency of each rate constant for every step of the reaction according to Arrhenius' equation [59]. The electrochemical response of the $\text{Ir}_{45}\text{Co}_{55}$ series presented in Fig. 4d–f shows a similar development as the former discussed Co-rich series. From the initial CVs after acid leaching the measured H_{upd} region after acid leaching was determined to be $33.7 \pm 1.9 \text{ m}^2\text{g}^{-1}$. A possible explanation for the decreased surface area could be a smaller size of the features formed after the Co leaching (Fig. 2e) and less internal porosity. Since the measured surface area at the initial step (Fig. S11a) was only around half of the Co-rich series (Fig. 2a), the oxide formation after the activation in Step 2.3 (Table 2) also rendered a smaller oxide capacitive layer (Fig. S11d). However, at this point the $\text{Ir}_{45}\text{Co}_{55}$ samples still presented a comparable H_{upd} area to the $\text{Ir}_{28}\text{Co}_{72}$ series, indicating that the sample was not completely oxidized. Nevertheless, the overpotential still decreased by about 10 mV after activation as in the case of the Co-rich samples due to the oxidation of the metallic surface (Fig. 4e). As a result, the activity measured after activation at 30 °C and 1.50 V_{RHE} increased to 57.6 $\text{Ag}^{-1}_{\text{Ir}}$, four times greater than the value of the commercial sample (Table 3). Still, it was approximately two times lower than the Ir-rich ($\text{Ir}_{28}\text{Co}_{72}$) samples under the same conditions. OER activity measured at 60 °C was nearly doubled from the previous step, i.e., 91.8 $\text{Ag}^{-1}_{\text{Ir}}$ at 1.46 V_{RHE} . The sharp activity increase reinforces the hypothesis that the samples only experience full activation during the protocol at high temperatures. Even at the start of this step the overpotential already decreased by 45 mV compared to the activity recorded after activation (Fig. S13). Since the reversible reduction in the overpotential due to temperature increase is approximately 25 mV, the further decrease supports the argument of a dynamic activation process. Additionally, the Tafel slope also decreased from 64 to 52 mV dec^{-1} between the activation and high-temperature OER respectively. The Ir-rich $\text{Ir}_{75}\text{Co}_{25}$ series exhibited the lowest values for the surface area and activity throughout the OER measurements. After acid leaching, the ECSA was determined to be $21.4 \pm 2.0 \text{ m}^2\text{g}^{-1}$, see Table 3. This is in good agreement with the observed top-down

morphology from the leached sample at the SEM (Fig. 2f), which featured the smallest clusters in all three series. The reduction in overpotential after activation was also minimal, i.e., ca. 3 mV (Fig. S13). The OER activity after activation at 30 °C was 44.3 $\text{Ag}^{-1}_{\text{Ir}}$ at 1.50 V_{RHE} , which is approximately 30 mV lower than that of the commercial benchmark under the same conditions. As also observed for the other IrCo series, the mass activity improved at 60 °C, reaching 62.7 $\text{Ag}^{-1}_{\text{Ir}}$ at 1.46 V_{RHE} as compared to the 10.14 $\text{Ag}^{-1}_{\text{Ir}}$ of the commercial benchmark. Interestingly, even though the mass activity results were at the lowest of the series in absolute numbers, a similar reduction in overpotential at high temperatures was observed as compared to $\text{Ir}_{45}\text{Co}_{55}$. (Fig. S13). The Tafel slope was the highest of the series and only decreased from 68 to 58 mV dec^{-1} between activation and high-temperature OER respectively, which was the smallest change in all series (see Table 3). Along the series, the ECSA, the Tafel and the mass activity followed the trend defined by the initial as-deposited Co content $\text{Ir}_{28}\text{Co}_{72} > \text{Ir}_{45}\text{Co}_{55} > \text{Ir}_{75}\text{Co}_{25}$. When combined with the catalyst morphology, this trend strongly suggests that a high initial Co content increases the catalyst utilization by increasing the ECSA in a dynamic process as the catalyst is activated. On the other hand, the specific activity was found to correlate with the XAS results and the Co content after leaching from the EDX results, which hints at a positive influence from the remaining Co in the structure. A summary of the main electrochemical results can be found in Table 3 below.

Some additional factors need to be considered together with the electrochemical results. As mentioned in the methods section, the deposition time for the magnetron targets was defined between 1 s and 6 s for Co and kept constant at 3 s for Ir in each cycle. The Ir loading calibration was performed in a continuous deposition of 1200 s. In a preliminary test, it was confirmed for Ir that the loading for the continuous deposition matched the loading for the cycled deposition by mass gravimetry. However, when measuring the expected ratios by EDX they were found to be different from the nominal. While EDX is a versatile tool to determine the spatial resolution of the thin catalyst layer and the element distribution on the substrate, it is known that absolute quantification using automatic standardless EDX profiles is generally poor [60]. We found that using 15 kV for the analysis was a compromise between good surface sensitivity and exciting the higher energy lines for better elemental analysis (Co $K_{\alpha} = 6.924 \text{ keV}$, Ir $L_{\alpha} = 9.147 \text{ keV}$) to maximize the number of counts. However, in the acid-leaching process, the catalyst loading is further reduced which leads to larger errors in the elemental quantification. Hence, we assumed the initial loading was unchanged for the electrochemical mass activity results, while it is likely that both the surface area and the mass activity might be larger than what was measured. The quantification of the changes in the Ir loading during electrochemical measurements is not trivial. Unlike other PGM catalysts (Pt, Pd), iridium is known to fully dissolve only in extremely aggressive conditions requiring high temperatures, pressures, and strong acids [61,62]. Therefore, the preparation of the samples for conventional ex-situ techniques such as Inductively Coupled Plasma Mass Spectrometry (ICP-MS) that relies on the analysis of the dissolved species is non-standard and complex. However, in recent years, some approaches have been taken to quantify the Ir loading or loss during the electrochemical measurements. One of the most relevant methods is the Scanning Flow Cell (SFC) coupled with an ICP-MS system, which allows to perform time-resolved measurements of the material loss during an electrochemical protocol. Unfortunately, it also does not provide information about the remaining catalyst in the deposited layer [63]. Furthermore, there is not yet a compatible design to combine the high-current capabilities of the GDE method with the access to analytics of the SFC ICP-MS. Additionally, most techniques have been optimized so far for the study of supported catalysts with Ir nanoparticles which are known to present higher degradation rates compared to self-supported catalysts [11,34,35]. Since the purpose of this study was to assess the performance of different Ir-based catalysts under the same conditions and using a comparative approach, a quantitative study of the Ir loading

loss or the formation of transient species was not performed. In addition, speculations about specific activity changes in correlation to XAS data were made with data measured at 30 °C in combination with the ECSA measurement in metallic state by Hupd. However, the increase in the double layer capacity of the CVs due to the oxidation to IrOx after the OER at higher temperatures (see Fig. 2f) would have resulted in different surface areas and thus different specific activities. Therefore the specific activity reported at 60 °C has to be taken with caution. Other in-situ methods such as the mercury underpotential deposition could have also been considered [64]. However, this was not possible, as the membrane would need to be removed to avoid poisoning, impeding further electrochemistry. For the same reason, most material characterization methods in this study have been limited to the after-leaching state. Further insight into the dynamic catalyst activation at high temperatures and its link to the morphology may be achieved with *in-operando* XAS methods as soon as they are developed. Nevertheless, these limitations were considered as boundary conditions to help the discussion and understanding of our results.

4. Conclusion

In this study, we applied the GDE method to perform activity measurements of PVD-produced catalysts for the OER. First, three series of Ir-Co catalysts with equal 250 µg/cm² Ir loading were sputtered on carbon substrate using different Co:Ir weight ratios (Ir₂₈Co₇₂, Ir₄₅Co₅₅, Ir₇₅Co₂₅). To create a self-supported nanoporous structure with increased ECSA, Co was removed in an acid-leaching step. This is rendering a distinct dendritical surface morphology with Ir-rich clusters and slight changes in crystallinity. During the process, a mixed metallic and oxide structure with local Ir-Co coordination is formed. A higher initial Co content leads to larger surface areas after leaching, outperforming the OER activity of a commercial IrOx catalyst benchmarked at 30 °C and 60 °C. Overall, the performance followed the Co:Ir series Ir₂₈Co₇₂ > Ir₄₅Co₅₅ > Ir₇₅Co₂₅ > IrOx, where the best-performing catalyst at 60 °C reached more than a tenth-fold increase in mass activity over the commercial sample. The performance increase as compared to the benchmark catalyst, accounting for loading and preparation differences, can be due to higher dispersion in addition to a ligand effect. The latter is supported by the specific activity trend correlation with the remaining Co after acid leaching and XAS coordination data. A strain effect, by comparison, was not supported by the XAS data. The temperature increase and dynamic surface activation due to oxidation of metallic Ir, both observed by CV and the OER activity, had a positive influence on the catalyst activity. The authors acknowledge that the complex mechanisms behind the influence of the Co content and the electrochemical performance may not be fully explained from the measurement results, but also remain beyond the scope of this study. On the other hand, it was demonstrated that the flexible and reproducible characteristics achievable from the nanostructured PVD-produced catalysts in combination with the three-electrode GDE setup can reveal further insights into the electrode evolution under more realistic conditions than traditional methods such as RDE, helping to fast-track OER catalyst experimental research.

CRedit authorship contribution statement

Pablo Collantes Jiménez: Methodology, Investigation, Writing – original draft. **Gustav Sievers:** Writing – review & editing, Supervision, Conceptualization. **Antje Quade:** Investigation, Methodology. **Volker Brüser:** Supervision, Methodology. **Rebecca Katharina Pittkowski:** Investigation, Methodology. **Matthias Arenz:** Writing – review & editing, Supervision, Conceptualization, All authors checked and approved the final version of the manuscript.

Declaration of competing interest

The authors declare the following financial interests/personal relationships which may be considered as potential competing interests: Gustav Sievers has patent #DE102016013185B4.

Data availability

Data will be made available on request.

Acknowledgements

The authors gratefully acknowledge the financial support by the German Federal Ministry of Education and Research (BMBF) in the framework of the VIP + Projekt. 03VP06451 (3DNanoMe). The authors thank Adam Clark from the SuperXAS beamline X10DA at the Paul Scherrer Institute (PSI) for measuring the XAS data via mail-in service. MA and RKP acknowledge funding from the Swiss National Science Foundation (SNSF) via project No. 200021 184742 and the Danish National Research Foundation Center for High Entropy Alloys Catalysis (CHEAC) DNR1-149.

Appendix A. Supplementary data

Supplementary data to this article can be found online at <https://doi.org/10.1016/j.jpowsour.2023.232990>.

References

- [1] R. Ma, B. Cui, D. Hu, S.M. El-Bahy, Y. Wang, I.H.E. Azab, A.Y. Elnaggar, H. Gu, G.A. M. Mersal, M. Huang, V. Murugadoss, Enhanced energy storage of lead-free mixed oxide core double-shell barium strontium zirconate titanate@magnesium aluminate@zinc oxide-boron trioxide-silica ceramic nanocomposites, *Adv. Compos. Hybrid Mater.* 5 (2022) 1477–1489, <https://doi.org/10.1007/s42114-022-00509-z>.
- [2] Y. Zhao, F. Liu, K. Zhu, S. Maganti, Z. Zhao, P. Bai, Three-dimensional printing of the copper sulfate hybrid composites for supercapacitor electrodes with ultra-high areal and volumetric capacitances, *Adv. Compos. Hybrid Mater.* 5 (2022) 1537–1547, <https://doi.org/10.1007/s42114-022-00430-5>.
- [3] Y. Zhang, L. Liu, L. Zhao, C. Hou, M. Huang, H. Algadi, D. Li, Q. Xia, J. Wang, Z. Zhou, X. Han, Y. Long, Y. Li, Z. Zhang, Y. Liu, Sandwich-like CoMoP₂/MoP heterostructures coupling N, P co-doped carbon nanosheets as advanced anodes for high-performance lithium-ion batteries, *Adv. Compos. Hybrid Mater.* 5 (2022) 2601–2610, <https://doi.org/10.1007/s42114-022-00535-x>.
- [4] Y. Ma, X. Xie, W. Yang, Z. Yu, X. Sun, Y. Zhang, X. Yang, H. Kimura, C. Hou, Z. Guo, W. Du, Recent advances in transition metal oxides with different dimensions as electrodes for high-performance supercapacitors, *Adv. Compos. Hybrid Mater.* 4 (2021) 906–924, <https://doi.org/10.1007/s42114-021-00358-2>.
- [5] C. Dang, Q. Mu, X. Xie, X. Sun, X. Yang, Y. Zhang, S. Maganti, M. Huang, Q. Jiang, I. Seok, W. Du, C. Hou, Recent progress in cathode catalyst for nonaqueous lithium oxygen batteries: a review, *Adv. Compos. Hybrid Mater.* 5 (2022) 606–626, <https://doi.org/10.1007/s42114-022-00500-8>.
- [6] S.C. D'Angelo, S. Cobo, V. Tulus, A. Nabera, A.J. Martín, J. Pérez-Ramírez, G. Guillén-Gosálbez, Planetary boundaries analysis of low-carbon ammonia production routes, *ACS Sustain. Chem. Eng.* 9 (2021) 9740–9749, <https://doi.org/10.1021/acssuschemeng.1c01915>.
- [7] Net Zero by 2050 - A Roadmap for the Global Energy Sector, IEA, IEA, Paris, 2021. <https://www.iea.org/reports/net-zero-by-2050>.
- [8] IRENA, Green Hydrogen Cost Reduction, 2020 publications/2020/Dec/Green-hydrogen-cost-reduction%0Ahttps://www.irena.org/-/media/Files/IRENA/Agency/Publication/2020/Dec/IRENA_Green_hydrogen_cost_2020.pdf.
- [9] S.M. Saba, M. Müller, M. Robinus, D. Stolten, The investment costs of electrolysis – a comparison of cost studies from the past 30 years, *Int. J. Hydrogen Energy* 43 (2018) 1209–1223, <https://doi.org/10.1016/j.ijhydene.2017.11.115>.
- [10] M. Carmo, D.L. Fritz, J. Mergel, D. Stolten, A comprehensive review on PEM water electrolysis, *Int. J. Hydrogen Energy* 38 (2013) 4901–4934, <https://doi.org/10.1016/j.ijhydene.2013.01.151>.
- [11] A.W. Jensen, G.W. Sievers, K.D. Jensen, J. Quinson, J.A. Arminio-Ravelo, V. Brüser, M. Arenz, M. Escudero-Escribano, Self-supported nanostructured iridium-based networks as highly active electrocatalysts for oxygen evolution in acidic media, *J Mater Chem A Mater* 8 (2020) 1066–1071, <https://doi.org/10.1039/c9ta12796h>.
- [12] C. Wei, R.R. Rao, J. Peng, B. Huang, I.E.L. Stephens, M. Risch, Z.J. Xu, Y. Shao-Horn, Recommended practices and benchmark activity for hydrogen and oxygen electrocatalysis in water splitting and fuel cells, *Adv. Mater.* 31 (2019), 1806296, <https://doi.org/10.1002/adma.201806296>.

- [13] Johnson Matthey 2022, No Title, PGM Management, 2022. June 28, 2022), <https://matthey.com/products-and-markets/pgms-and-circularity/pgm-management>
- [14] M. Eqi, C. Shi, J. Xie, F. Kang, H. Qi, X. Tan, Z. Huang, J. Liu, J. Guo, Synergetic effect of Ni-Au bimetal nanoparticles on urchin-like TiO₂ for hydrogen and arabinose co-production by glucose photoreforming, *Adv. Compos. Hybrid Mater.* 6 (2023) 1–14, <https://doi.org/10.1007/s42114-022-00580-6>.
- [15] A.L. Strickler, R.A. Flores, L.A. King, J.K. Norskov, M. Bajdich, T.F. Jaramillo, Systematic investigation of iridium-based bimetallic thin film catalysts for the oxygen evolution reaction in acidic media, *ACS Appl. Mater. Interfaces* 11 (2019) 34059–34066, <https://doi.org/10.1021/acsami.9b13697>.
- [16] X. Chen, M. Xu, S. Li, C. Li, X. Sun, S. Mu, J. Yu, Ultrafine IrNi bimetallics encapsulated in zeolitic imidazolate frameworks-derived porous N-doped carbon for boosting oxygen evolution in both alkaline and acidic electrolytes, *Adv. Mater. Interfac.* 7 (2020) 1–8, <https://doi.org/10.1002/admi.202001145>.
- [17] S.L. Hamukwaya, Z. Zhao, H. Hao, H.M. Abo-Dief, K.M. Abualnaja, A.K. Alanazi, M.M. Mashigaidze, S.M. El-Bahy, M. Huang, Z. Guo, Enhanced photocatalytic performance for hydrogen production and carbon dioxide reduction by a mesoporous single-crystal-like TiO₂ composite catalyst, *Adv. Compos. Hybrid Mater.* 5 (2022) 2620–2630, <https://doi.org/10.1007/s42114-022-00545-9>.
- [18] B.M. Tackett, W. Sheng, S. Kattel, S. Yao, B. Yan, K.A. Kuttiyiel, Q. Wu, J.G. Chen, Reducing iridium loading in oxygen evolution reaction electrocatalysts using core-shell particles with nitride cores, *ACS Catal.* 8 (2018) 2615–2621, <https://doi.org/10.1021/acscatal.7b04410>.
- [19] Y.T. Kim, P.P. Lopes, S.A. Park, A.Y. Lee, J. Lim, H. Lee, S. Back, Y. Jung, N. Danilovic, V. Stamenkovic, J. Erlebacher, J. Snyder, N.M. Markovic, Balancing activity, stability and conductivity of nanoporous core-shell iridium/iridium oxide oxygen evolution catalysts, *Nat. Commun.* 8 (2017) 1–8, <https://doi.org/10.1038/s41467-017-01734-7>.
- [20] C. van Pham, M. Bühler, J. Knöppel, M. Bierling, D. Seeberger, D. Escalera-López, K.J.L. Mayrhofer, S. Cherevko, S. Thiele, IrO₂ coated TiO₂ core-shell microparticles advance performance of low loading proton exchange membrane water electrolyzers, *Appl. Catal., B* 269 (2020), <https://doi.org/10.1016/j.apcatb.2020.118762>.
- [21] A. Ahmed, S. Seth, J. Purewal, A.G. Wong-Foy, M. Veenstra, A.J. Matzger, D. J. Siegel, Exceptional hydrogen storage achieved by screening nearly half a million metal-organic frameworks, *Nat. Commun.* 10 (2019), <https://doi.org/10.1038/s41467-019-09365-w>.
- [22] J. Gao, H. Tao, B. Liu, Progress of nonprecious-metal-based electrocatalysts for oxygen evolution in acidic media, *Adv. Mater.* 33 (2021) 1–18, <https://doi.org/10.1002/adma.202003786>.
- [23] E. Chamanehpour, M.H. Sayadi, M. Hajiani, A hierarchical graphitic carbon nitride supported by metal-organic framework and copper nanocomposite as a novel bifunctional catalyst with long-term stability for enhanced carbon dioxide photoreduction under solar light irradiation, *Adv. Compos. Hybrid Mater.* 5 (2022) 2461–2477, <https://doi.org/10.1007/s42114-022-00459-6>.
- [24] J. Zhao, K. Bao, M. Xie, D. Wei, K. Yang, X. Zhang, C. Zhang, Z. Wang, X. Yang, Two-dimensional ultrathin networked CoP derived from Co(OH)₂ as efficient electrocatalyst for hydrogen evolution, *Adv. Compos. Hybrid Mater.* 5 (2022) 2421–2428, <https://doi.org/10.1007/s42114-022-00455-w>.
- [25] J. Schröder, V.A. Mints, A. Bornet, E. Berner, M.F. Tovini, J. Quinson, G.K. H. Wiberg, F. Bizzotto, H.A. El-Sayed, M. Arenz, The gas diffusion electrode setup as straightforward testing device for proton exchange membrane water electrolyzer catalysts, *JACS Au* 1 (2021) 247–251, <https://doi.org/10.1021/JACS Au.1C00015>.
- [26] G.W. Sievers, A.W. Jensen, V. Brüser, M. Arenz, M. Escudero-Escribano, Sputtered platinum thin-films for oxygen reduction in gas diffusion electrodes: a model system for studies under realistic reaction conditions, *Surfaces* 2 (2019) 336–348, <https://doi.org/10.3390/surfaces2020025>.
- [27] J. Du, J. Quinson, A. Zana, M. Arenz, Elucidating Pt-based nanocomposite catalysts for the oxygen reduction reaction in rotating disk electrode and gas diffusion electrode measurements, *ACS Catal.* 11 (2021) 7584–7594, <https://doi.org/10.1021/acscatal.1c01496>.
- [28] T. Tian, Y. Cheng, Z. Sun, K. Huang, M. Lei, H. Tang, Carbon nanotubes supported oxygen reduction reaction catalysts: role of inner tubes, *Adv. Compos. Hybrid Mater.* 6 (2023) 1–10, <https://doi.org/10.1007/s42114-022-00592-2>.
- [29] R. Wang, Z. Zhang, P. Du, Z. Fu, K. Huang, K. Xu, Y. Du, D. Fan, R. Zhang, M. Lei, Efficient synthesis of sulfur-modified cobalt hydroxide self-supported electrocatalysts for enhanced oxygen evolution, *Adv. Compos. Hybrid Mater.* 5 (2022) 2491–2499, <https://doi.org/10.1007/s42114-022-00495-2>.
- [30] Z. Zhao, Y. Lin, J. Wu, J. Li, M. Lei, Mixed-phase cobalt-based nanosheets prepared by rapid thermal annealing for oxygen evolution catalysis, *Adv. Compos. Hybrid Mater.* 5 (2022) 2589–2600, <https://doi.org/10.1007/s42114-022-00537-9>.
- [31] J. Liang, H. Shen, J. Kong, Steel mesh reinforced Ni(OH)₂ nanosheets with enhanced oxygen evolution reaction performance, *ES Materials and Manufacturing* 14 (2021) 79–86, <https://doi.org/10.30919/esmm5f454>.
- [32] D. Xue, J. Cheng, P. Yuan, B.A. Lu, H. Xia, C.C. Yang, C.L. Dong, H. Zhang, F. Shi, S. C. Mu, J.S. Hu, S.G. Sun, J.N. Zhang, Boron-tethering and regulative electronic states around iridium species for hydrogen evolution, *Adv. Funct. Mater.* 32 (2022) 1–9, <https://doi.org/10.1002/adfm.202113191>.
- [33] S.I. Nefedkin, M.A. Klimova, A.V. Ryabukhin, A.V. Chizhov, I.I. Levin, Fabrication of catalytic compositions for electrodes of fuel cells and water electrolyzers with proton-exchange membrane by magnetron sputtering of composite targets, *Nanobiotechnology Reports* 16 (2021) 516–524, <https://doi.org/10.1134/S2635167621040078>.
- [34] G.W. Sievers, J.R. Bowen, V. Brüser, M. Arenz, Support-free nanostructured Pt–Cu electrocatalyst for the oxygen reduction reaction prepared by alternating magnetron sputtering, *J. Power Sources* 413 (2019) 432–440, <https://doi.org/10.1016/j.jpowsour.2018.12.044>.
- [35] G.W. Sievers, A.W. Jensen, J. Quinson, A. Zana, F. Bizzotto, M. Oezaslan, A. Dworzak, J.K.K. Kirkensgaard, T.E.L. Smitshuysen, S. Kakhkhozadadeh, M. Juelsholt, K.M.Ø. Jensen, K. Anklam, H. Wan, J. Schäfer, K. Cépe, M. Escudero-Escribano, J. Rossmeisl, A. Quade, V. Brüser, M. Arenz, Self-supported Pt–CoO networks combining high specific activity with high surface area for oxygen reduction, *Nat. Mater.* 20 (2021) 208–213, <https://doi.org/10.1038/s41563-020-0775-8>.
- [36] B. Han, C.E. Carlton, A. Kongkanand, R.S. Kukreja, B.R. Theobald, L. Gan, R. O'Malley, P. Strasser, F.T. Wagner, Y. Shao-Horn, Record activity and stability of dealloyed bimetallic catalysts for proton exchange membrane fuel cells, *Energy Environ. Sci.* 8 (2014) 258–266, <https://doi.org/10.1039/C4EE02144D>.
- [37] J. Knöppel, M. Möckl, D. Escalera-López, K. Stojanovski, M. Bierling, T. Böhm, S. Thiele, M. Rzepka, S. Cherevko, On the limitations in assessing stability of oxygen evolution catalysts using aqueous model electrochemical cells, *Nat. Commun.* 12 (2021), <https://doi.org/10.1038/s41467-021-22296-9>.
- [38] S. Geiger, O. Kasian, M. Ledendecker, E. Pizzutilo, A.M. Mingers, W.T. Fu, O. Diaz-Morales, Z. Li, T. Oellers, L. Fruchter, A. Ludwig, K.J.J. Mayrhofer, M.T.M. Koper, S. Cherevko, The stability number as a metric for electrocatalyst stability benchmarking, *Nat Catal* 1 (2018) 508–515, <https://doi.org/10.1038/s41929-018-0085-6>.
- [39] T. Lazaridis, B.M. Stühmeier, H.A. Gasteiger, H.A. El-Sayed, Capabilities and limitations of rotating disk electrodes versus membrane electrode assemblies in the investigation of electrocatalysts, *Nat Catal* 5 (2022), <https://doi.org/10.1038/s41929-022-00776-5>.
- [40] H.A. El-Sayed, A. Weiß, L.F. Olbrich, G.P. Putro, H.A. Gasteiger, OER catalyst stability investigation using RDE technique: a stability measure or an artifact? *J. Electrochem. Soc.* 166 (2019) F458–F464, <https://doi.org/10.1149/2.0301908jes>.
- [41] M. Inaba, A.W. Jensen, G.W. Sievers, M. Escudero-Escribano, A. Zana, M. Arenz, Benchmarking high surface area electrocatalysts in a gas diffusion electrode: measurement of oxygen reduction activities under realistic conditions, *Energy Environ. Sci.* 11 (2018) 988–994, <https://doi.org/10.1039/c8ee00019k>.
- [42] K. Ehelebe, D. Seeberger, M.T.Y. Paul, S. Thiele, K.J.J. Mayrhofer, S. Cherevko, Evaluating electrocatalysts at relevant currents in a half-cell: the impact of Pt loading on oxygen reduction reaction, *J. Electrochem. Soc.* 166 (2019) F1259–F1268, <https://doi.org/10.1149/2.091191jes>.
- [43] S. Nösberger, J. Du, J. Quinson, E. Berner, A. Zana, G.K.H. Wiberg, M. Arenz, The gas diffusion electrode setup as a testing platform for evaluating fuel cell catalysts: a comparative RDE-GDE study, *Electrochemical Science Advances* (2022) 1–12, <https://doi.org/10.1002/elsa.202100190>.
- [44] K. Ehelebe, N. Schmitt, G. Sievers, A.W. Jensen, A. Hrnjić, P. Collantes Jiménez, P. Kaiser, M. Geuß, Y.P. Ku, P. Jovanović, K.J.J. Mayrhofer, B. Etzold, N. Hodnik, M. Escudero-Escribano, M. Arenz, S. Cherevko, Benchmarking fuel cell electrocatalysts using gas diffusion electrodes: inter-lab comparison and best practices, *ACS Energy Lett.* 7 (2022) 816–826, <https://doi.org/10.1021/acscenergylett.1c02659>.
- [45] S.M. Alia, B. Rasimick, C. Ngo, K.C. Neyerlin, S.S. Kocha, S. Pylypenko, H. Xu, B. S. Pivovar, Activity and durability of iridium nanoparticles in the oxygen evolution reaction, *J. Electrochem. Soc.* 163 (2016), <https://doi.org/10.1149/2.015161jes>. F3105–F3112.
- [46] J.B. Gerken, J.G. McAlpin, J.Y.C. Chen, M.L. Rigsby, W.H. Casey, R.D. Britt, S. S. Stahl, Electrochemical water oxidation with cobalt-based electrocatalysts from pH 0–14: the thermodynamic basis for catalyst structure, stability, and activity, *J. Am. Chem. Soc.* 133 (2011) 14431–14442, <https://doi.org/10.1021/ja205647m>.
- [47] A.W. Grant, Cobalt complexes and le Chatelier, *J. Chem. Educ.* 61 (1984) 466, <https://doi.org/10.1021/ed061p466>.
- [48] V.R. Stamenkovic, B.S. Mun, M. Arenz, K.J.J. Mayrhofer, C.A. Lucas, G. Wang, P. N. Ross, N.M. Markovic, Trends in electrocatalysis on extended and nanoscale Pt-bimetallic alloy surfaces, *Nat. Mater.* 6 (2007) 241–247, <https://doi.org/10.1038/nmat1840>.
- [49] E. Slavcheva, I. Radev, S. Bliznakov, G. Topalov, P. Andreev, E. Budevski, Sputtered iridium oxide films as electrocatalysts for water splitting via PEM electrolysis, *Electrochim. Acta* 52 (2007) 3889–3894, <https://doi.org/10.1016/j.electacta.2006.11.005>.
- [50] P. Kús, A. Ostroverkh, I. Khalakhan, R. Fiala, Y. Kosto, B. Šmíd, Y. Lobko, Y. Yakovlev, J. Nováková, I. Matolínová, V. Matolín, Magnetron sputtered thin-film vertically segmented Pt–Ir catalyst supported on TiC for anode side of proton exchange membrane unitized regenerative fuel cells, *Int. J. Hydrogen Energy* 44 (2019) 16087–16098, <https://doi.org/10.1016/j.ijhydene.2019.04.216>.
- [51] W. Hu, H. Zhong, W. Liang, S. Chen, Ir-surface enriched porous Ir–Co oxide hierarchical architecture for high performance water oxidation in acidic media, *ACS Appl. Mater. Interfaces* 6 (2014) 12729–12736, <https://doi.org/10.1021/am502719z>.
- [52] S. Chatterjee, S. Intikhab, L. Proffitt, Y. Li, V. Natu, R. Gawas, J. Snyder, Nanoporous multimetallic Ir alloys as efficient and stable electrocatalysts for acidic oxygen evolution reactions, *J. Catal.* 393 (2021) 303–312, <https://doi.org/10.30890/phe.1.2017.21>.
- [53] J. Erlebacher, M.J. Aziz, A. Karma, N. Dimitrov, K. Sieradzki, Evolution of nanoporosity in dealloying, *Nature* 410 (2001) 450–453, <https://doi.org/10.1038/35068529>.
- [54] S. Parida, D. Kramer, C.A. Volkert, H. Rösner, J. Erlebacher, J. Weissmüller, Volume change during the formation of nanoporous gold by dealloying, *Phys. Rev. Lett.* 97 (2006) 4–7, <https://doi.org/10.1103/PhysRevLett.97.035504>.

- [55] S. Koh, P. Strasser, Electrocatalysis on bimetallic surfaces: modifying catalytic reactivity for oxygen reduction by voltammetric surface dealloying, *J. Am. Chem. Soc.* 129 (2007) 12624–12625, <https://doi.org/10.1021/ja0742784>.
- [56] B. Han, C.E. Carlton, A. Kongkanand, R.S. Kukreja, B.R. Theobald, L. Gan, R. O'Malley, P. Strasser, F.T. Wagner, Y. Shao-Horn, Record activity and stability of dealloyed bimetallic catalysts for proton exchange membrane fuel cells, *Energy Environ. Sci.* 8 (2015) 258–266, <https://doi.org/10.1039/C4EE02144D>.
- [57] M. Göbeler, E. Hengge, M. Bogar, M. Albu, D. Knez, H. Amenitsch, R. Würschum, In situ study of nanoporosity evolution during dealloying AgAu and CoPd by grazing-incidence small-angle X-ray scattering, *J. Phys. Chem. C* 126 (2022) 4037–4047, <https://doi.org/10.1021/acs.jpcc.1c09592>.
- [58] C. Wei, S. Sun, D. Mandler, X. Wang, S.Z. Qiao, Z.J. Xu, Approaches for measuring the surface areas of metal oxide electrocatalysts for determining their intrinsic electrocatalytic activity, *Chem. Soc. Rev.* 48 (2019) 2518–2534, <https://doi.org/10.1039/c8cs00848e>.
- [59] T. Shinagawa, A.T. Garcia-Esparza, K. Takanebe, Insight on Tafel slopes from a microkinetic analysis of aqueous electrocatalysis for energy conversion, *Sci. Rep.* 5 (2015) 1–21, <https://doi.org/10.1038/srep13801>.
- [60] D.E. Newbury, N.W.M. Ritchie, Is scanning electron microscopy/energy dispersive X-ray spectrometry (SEM/EDS) quantitative? *Scanning* 35 (2013) 141–168, <https://doi.org/10.1002/SCA.21041>.
- [61] A.P.J. Hodgson, K.E. Jarvis, R.W. Grimes, O.J. Marsden, Development of an iridium dissolution method for the evaluation of potential radiological device materials, *J. Radioanal. Nucl. Chem.* 307 (2015) 2181–2186, <https://doi.org/10.1007/S10967-015-4381-1>, 3. 307 (2015).
- [62] M.M. Todand, I. Jarvis, K.E. Jarvis, Microwave digestion and alkali fusion procedures for the determination of the platinum-group elements and gold in geological materials by ICP-MS, *Chem. Geol.* 124 (1995) 21–36, [https://doi.org/10.1016/0009-2541\(95\)00021-D](https://doi.org/10.1016/0009-2541(95)00021-D).
- [63] J.P. Grote, A.R. Zeradjanin, S. Cherevko, K.J.J. Mayrhofer, Coupling of a scanning flow cell with online electrochemical mass spectrometry for screening of reaction selectivity, *Rev. Sci. Instrum.* 85 (2014), <https://doi.org/10.1063/1.4896755>.
- [64] S. Duran, M. Elmaalouf, M. Odziomek, J.Y. Piquemal, M. Faustini, M. Giraud, J. Peron, C. Tard, Electrochemical active surface area determination of iridium-based mixed oxides by mercury underpotential deposition, *Chemelectrochem* 8 (2021) 3519–3524, <https://doi.org/10.1002/celec.202100649>.

Supporting Information: Gas Diffusion Electrode activity measurements of Iridium-based support-free catalysts produced by alternated physical vapor deposition.

Pablo Collantes Jiménez ^a, Gustav Sievers ^{a*}, Antje Quade ^a, Volker Brüser ^a, Rebecca Katharina Pittkowski ^{b*}, Matthias Arenz ^{c*}

^a Leibniz Institute for Plasma Science and Technology, Felix-Hausdorff-Strasse 2, 17489 Greifswald, Germany

^b Department of Chemistry, University of Copenhagen, Universitetsparken, Copenhagen, Denmark

^c Department of Chemistry, Biochemistry and Pharmaceutical Sciences, University of Bern, Freiestrasse 3, CH-3012 Bern, Switzerland

Sample preparation

The most prominent feature of the catalyst manufacturing to testing pathway proposed in this study is its flexibility and industrial-readiness. The process is characterized by a series of repetitive steps, which could easily be scaled and automatized. Figure S1 below depicts a composite of images that illustrate the details of this process. The process starts at the PVD reactor (Figure S1a), which can be described geometrically by three operating modules: two chambers and one swiveling arm to transport the samples between them. The smaller chamber is the load lock, which is accessible through a circular aperture to mount the samples on the swiveling arm. A turbopump evacuates this chamber in less than 2 minutes to a pressure of 1e-3 mbar, which help to maintain a constant pressure of 1e-6 mbar in the process chamber. The latter is situated within the gray enclosure. It

hubs one ion beam and other three magnetron sources, where the targets can be installed in custom geometries. In this case, rectangular targets were installed with their long side in a perpendicular position to the axis of the swiveling arm, which travels under them (Figure S1b). The chamber interior is also visible through a circular opening equipped with a radiation-resistant blinder. It is also possible to access this chamber for example to maintain or switch the targets. After one deposition, the sample is collected from the load lock and brought to the self-designed acid leaching station (Figure S1c). The Teflon chamber has a 55 x 55 mm opening with a carbon plate “floor” that serves as counter electrode which ideally creates a constant electric field. The catalyst film is positioned facing down in a pool of 1 M HClO₄ electrolyte, closed and connected electrically with a carbon rod. By introducing Ar and controlling the potential in this floating 3-electrode half-cell setup, it is possible to create the conditions for the Co dissolution in acid electrolyte without oxidizing the Ir. A great part of the success of testing the GDE depends on the assembly configuration and hot-pressing conditions. It was necessary to design a simple setup to produce half membrane-electrode assemblies in a reproducible manner. After several approaches and iterations in this process, it was deemed that a modified soldering iron coupled with a small arbor-type press was sufficient for the purpose (Figure S1d). The temperature control was performed through a thermocouple connected to the middle of the hot iron piece, which achieved a stable temperature (+/- 2 °C) after approximately 15 min. After a catalyst disk was punched out of the acid-leached film and placed on the hot iron surface, the membrane would be situated directly on top (Figure S1e) and the pressure would be applied by adding manually a series of weights to the top. At this point, the GDE assembly would be ready to be mounted into the cell (Figure S1f), as it is depicted in Figure 1. The electrolyte would be added, the RHE made and the connections checked. Finally, already at the test bench (Figure S1g), the cell would be connected to the gas lines and placed in the glass enclosure seen behind the cell in the image.

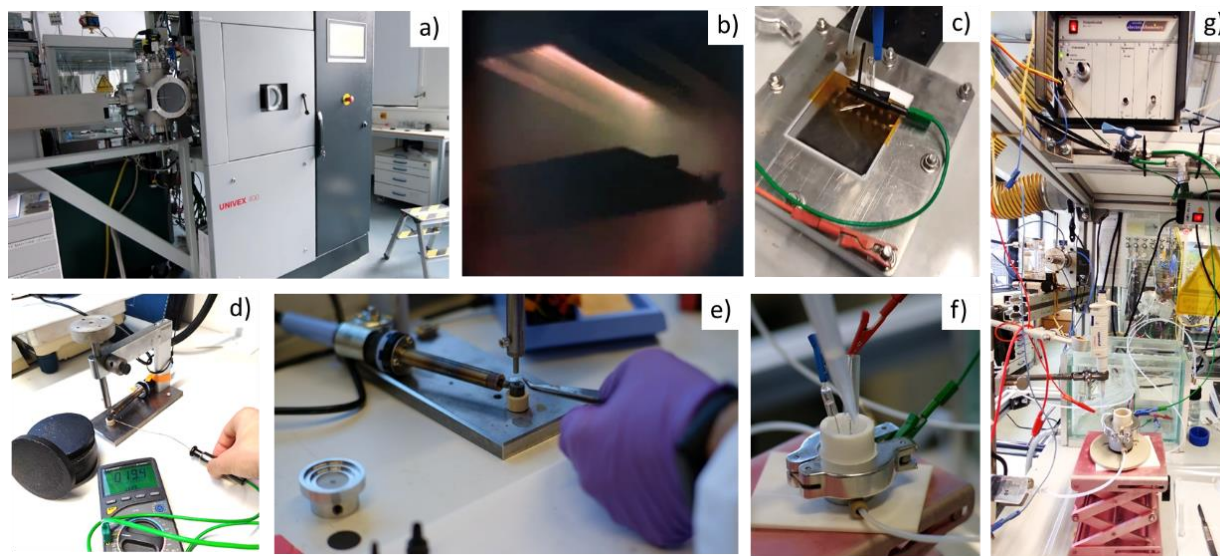


Figure S1. Material manufacturing to testing process described graphically a) PVD alternate magnetron sputtering b) Acid leaching of the Co in a self-designed three-electrode floating cell in a controlled gas atmosphere. c) Hot-pressing of the catalyst with the membrane to create the GDE at 84 bar and 125 °C for 30 s. d) Test bench with the Potentiostat (upper part), the GDE half-cell (lower section) and the isolated double glass cell, behind the GDE setup Electrochemical analysis.

Electrochemical characterization

The development of the oxidation states of the catalyst series was observed by CV. After the Co acid leaching under non-oxidizing conditions ($0.05 - 0.5 V_{RHE}$), Ir was still found in metallic state (Figure S2a). As proposed by Jensen et al. [1], the H_{upd} area was used to quantify the ECSA. In theory, this measured surface would be approximate to the available area where IrO_x could be formed in a further Activation step (Figure S3). Surprisingly, despite the Activation procedure and the several OER steps, the H_{upd} revealed persisting Ir metal features through the protocol (Figure S2a-f). On the other hand, the double layer capacity increased steadily, especially in the higher potential window. Our hypothesis is that the electrochemically formed oxide is porous, which leaves more internal layers of Ir exposed leading to a very slowly oxidation process progress under the conditions studied. As new active areas are created during the process, the initial calculated ECSA has to be interpreted carefully.

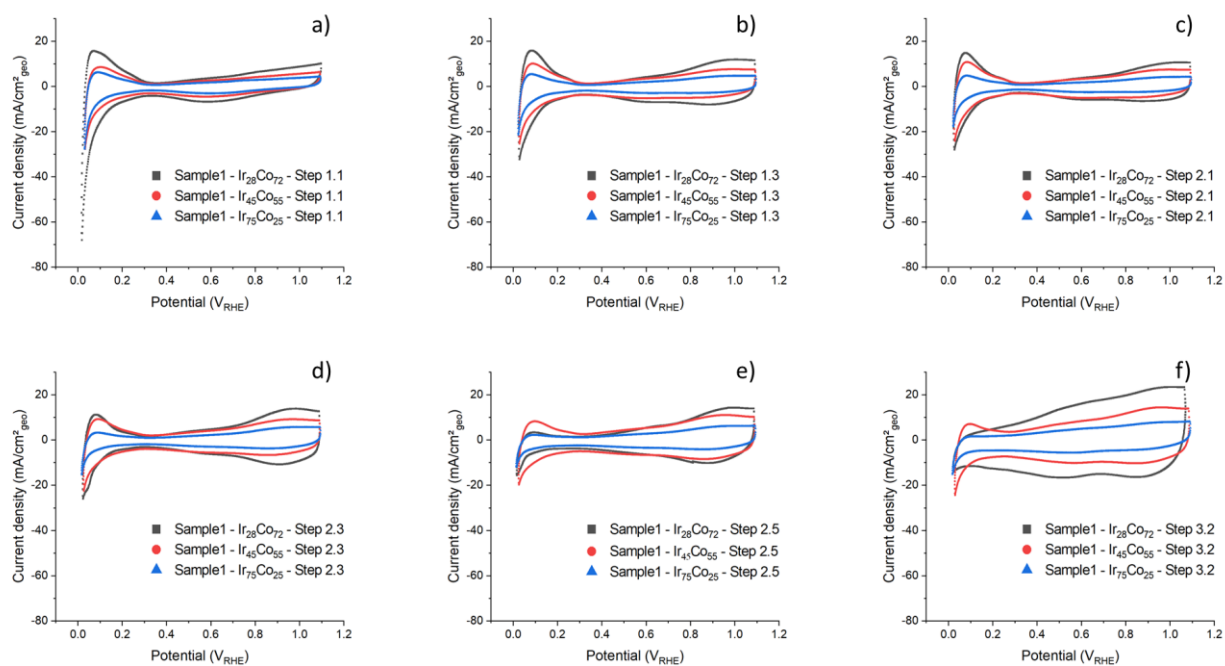


Figure S2. CVs obtained for one of the samples of each series from the different steps along the electrochemical protocol referred in Table 2: a) After cell assembly b) After the first OER at 30 °C c) Before activation d) After Activation e) After the second OER at 30 °C f) After the OER at 60 °C

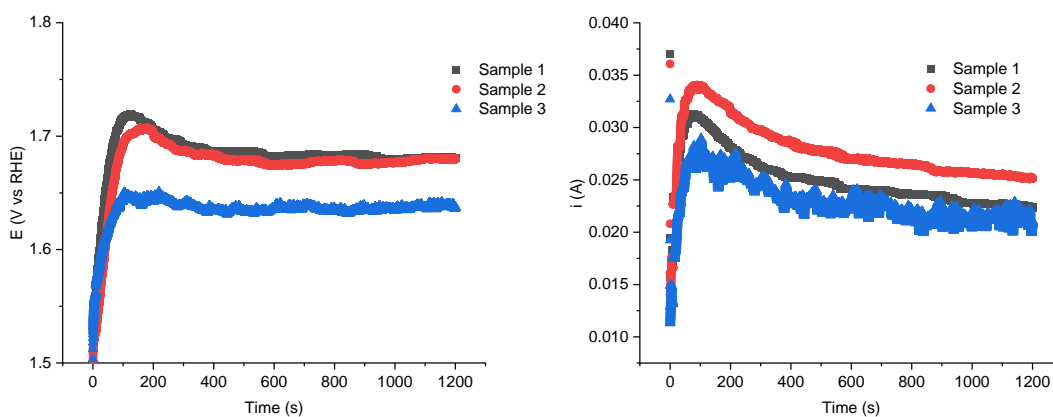


Figure S3. Activation step in Ar atmosphere at 1.70 V vs RHE for 20 min. with iR-compensation set to 95%. a) iR-corrected voltage applied on three samples from the Ir₂₈Co₇₂ series. b) Current response.

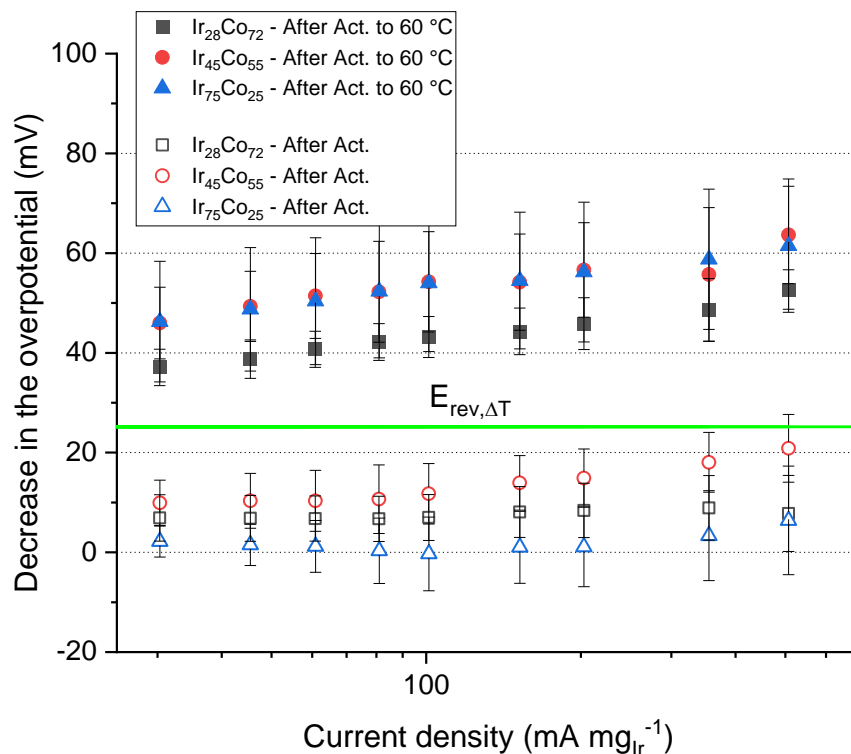


Figure S4. Reduction of the overpotential in each series during the OER activity measurements compared between different stages of the electrochemical protocol. The lower group of data series with hollow symbols describes the increase in overpotential between the first run of the OER at 30 °C and the one after activation. The upper group, with filled symbols, compares the decrease between OER after the activation step and at 60 °C. The green line has been plotted for reference of the reversible OER potential due to the temperature increase.

The dynamic oxidation process described before as well as the raise in temperature directly influenced the measured OER activity (Figure S4) by reducing the overpotential, increasing the ECSA and the kinetic transfer of species respectively. This improvement was situated in between 0 - 20 mV for the OER trials at 30 °C, before and after the activation, where only the oxidation part could have taken effect. Despite the large error bars, it is possible to see a trend for larger decreases in the overpotential towards the high current densities. This trend was further increased when comparing the decrease between the OER at 30 °C and 60°C. In this case, both the temperature and the surface oxidation contributed simultaneously to this effect. The equation below, formulated by Parthasarathy et al. [2] for the oxygen reversible potential can be used to determine the expected increase in activity in relation to the temperature change.

$$E_{rev,T} = -\frac{\Delta G^0}{nF} = \frac{295600 + 33.5 T \ln(T) - 388.4 T}{nF} \quad (2)$$

Where $n = 2$ transferred electrons, and F represents the Faraday constant. It can be also written as:

$$\Delta E_{rev,T} = \frac{33.5 [T_2 \ln(T_2) - T_1 \ln(T_1)] - 388.4 (T_2 - T_1)}{nF} \quad (2)$$

Accordingly, an increase in temperature from 30 ° to 60 °C would decrease the oxygen reversible potential by ~25 mV. The expected decrease of the overpotential due to temperature ($E_{rev\Delta T}$) is constant and consistently lower than the overall contribution, which we attributed to the samples experiencing a further activation during the protocol as an increased oxide capacity and sharp decrease of metallic features was also observed by CVs after the OER run at high temperature, see Figure S2f.

Composition and chemical analysis

The phase crystallinity of the as-prepared and acid-leached IrCo catalyst was investigated with a Bruker D8 Advance Diffractometer, equipped with a Cu K α X-ray source. The measurements were performed in Bragg-Brentano geometry over a 2 Theta range from 30° to 80°, step width 0.5° and 5 s per step. TOPAS software was used for the evaluation of the diffractograms via Diffract Eva (access to databases ICSD and PDF) and Rietveld refinement.

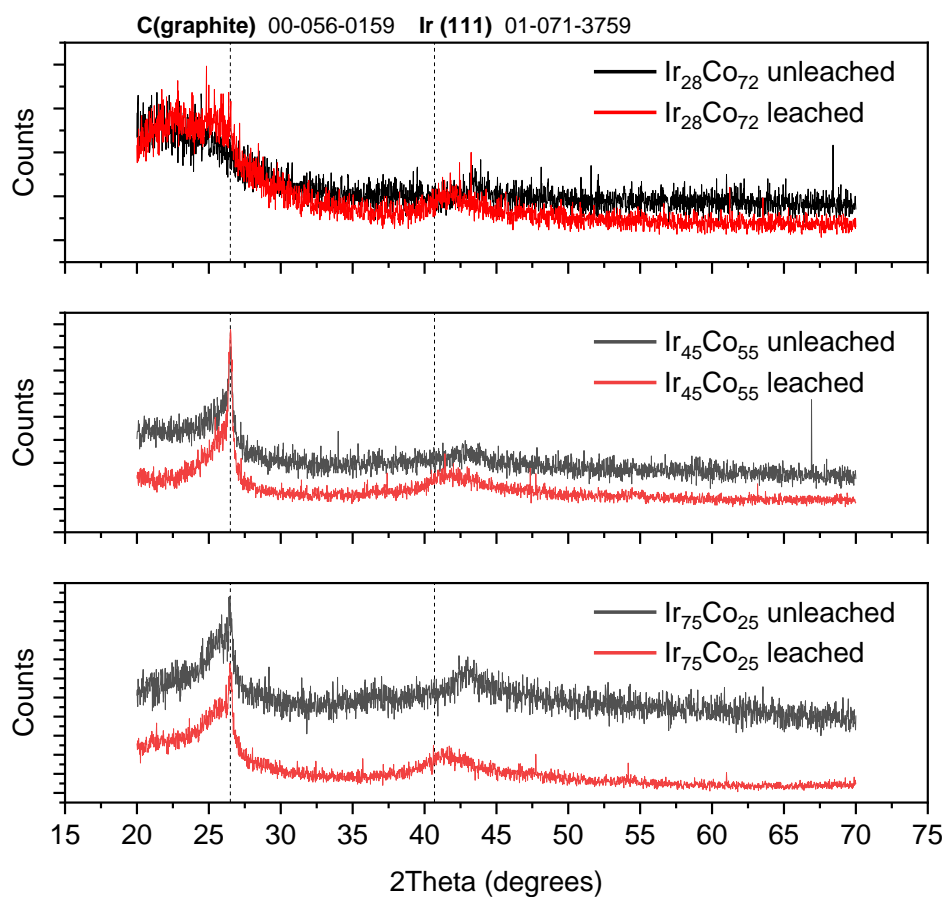


Figure S5. XRD results from the IrCo series, as-sputtered (black line) and acid leached (red line) for a)Ir₂₈Co₇₂, b)Ir₄₅Co₅₅ and c)Ir₇₅Co₂₅ series.

XPS analyses were performed with a Kratos Axis Supra spectrometer using a monochromatic AlK α source (1.486 eV) at a pressure of $6.8 \cdot 10^3$ Pa and an X-ray power of 150 W for survey and elemental scans, and 225 W for highly resolved measured spectra, respectively. Charge neutralization was used for all samples. Survey scan analyses were performed with an analysis area of 300 x 700 microns and a pass energy of 160 eV. Core level spectra of all identified elements were acquired at a pass energy of 80 eV, and the highly resolved measured peaks were collected at a pass energy of 10 eV. For these analyses, the instrument was set to the medium magnification lens mode (FOV 2) and by selecting the slot mode providing an analysis area of $\sim 300 \mu\text{m}$. Spectra were corrected to the main line of the carbon-1s (adventitious carbon) spectrum, which was set to 284.8 eV. Data analysis was performed using CasaXPS (2.3.15) using a Shirley background. Peak fits were

achieved using Functional Lorentzian (LF) for the 4f-Peaks and Gaussian-Lorentzian (GL) lineshapes for the satellites as supposed by Freakley et al. [3]

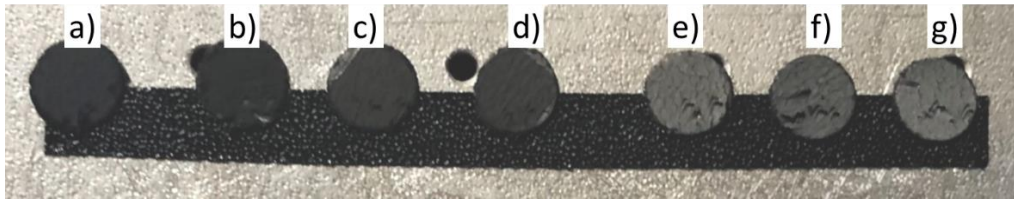


Figure S6. Sample strip fixed to a double-side carbon tape of the XPS sample holder. All samples had a disk geometry of 3 mm in diameter and less than 1 mm in height. From left to right: a) IrOx reference (sputtered IrOx with 250 $\mu\text{g}/\text{cm}^2$), b) acid-leached $\text{Ir}_{28}\text{Co}_{72}$, c) acid-leached $\text{Ir}_{45}\text{Co}_{55}$, d) acid-leached $\text{Ir}_{75}\text{Co}_{25}$, e) unleached $\text{Ir}_{28}\text{Co}_{72}$, f) unleached $\text{Ir}_{45}\text{Co}_{55}$, g) unleached $\text{Ir}_{75}\text{Co}_{25}$

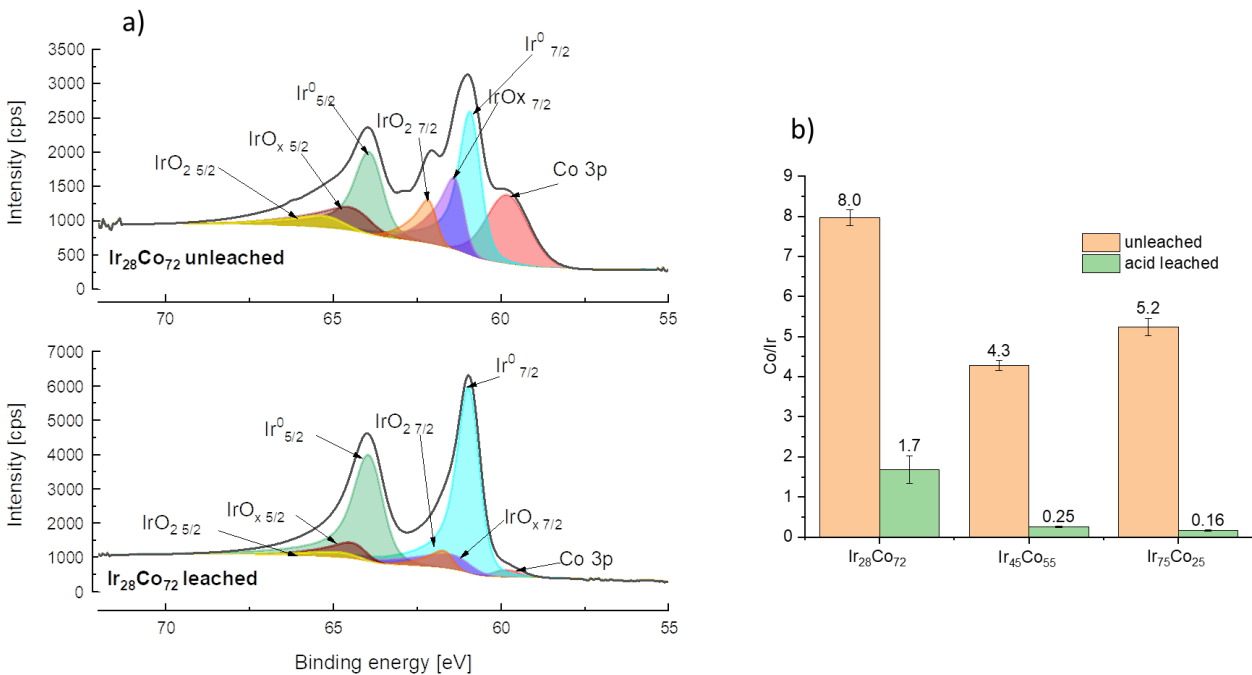


Figure S7. a) 4f peak fitting of sample $\text{Ir}_{28}\text{Co}_{72}$ b) Change in the Co:Ir ratios before and after acid leaching through the IrCo series

SEM-EDX measurements were performed with a JSM-7500F instrument (JEOL), equipped with a cold FEG suitable for high-resolution imaging up to 1 M magnification in a range of 0.1 – 30 kV and with a lateral resolution of 1 nm. The samples were mounted at a 45° angle to enhance the 3D visualization of the surface morphology, and inspected at 15 kV. The in-lens SE mode was used to obtain the micrographs between 10k – 100k magnifications. For the EDX spot chemical analysis,

5 positions separated several microns apart were selected, and averaged. The spectra was quantified for Ir and Co lines in automatic mode within the BRUKER software, correcting for the sample tilting of 45° . The chemical distribution was gathered by mapping of Ir, Co and substrate elements such as C and O in areas of 50 by 75 microns. Figure S7a illustrates the decrease in the Co 3p peak after leaching and the increased signal from the metallic $\text{Ir}^{0}_{5/2}$ and $_{7/2}$. IrO_x and IrO_2 found in the unleached state could have been formed from the exposure to air, since it is still found also in the same proportion after leaching (mind the count intensity scale).

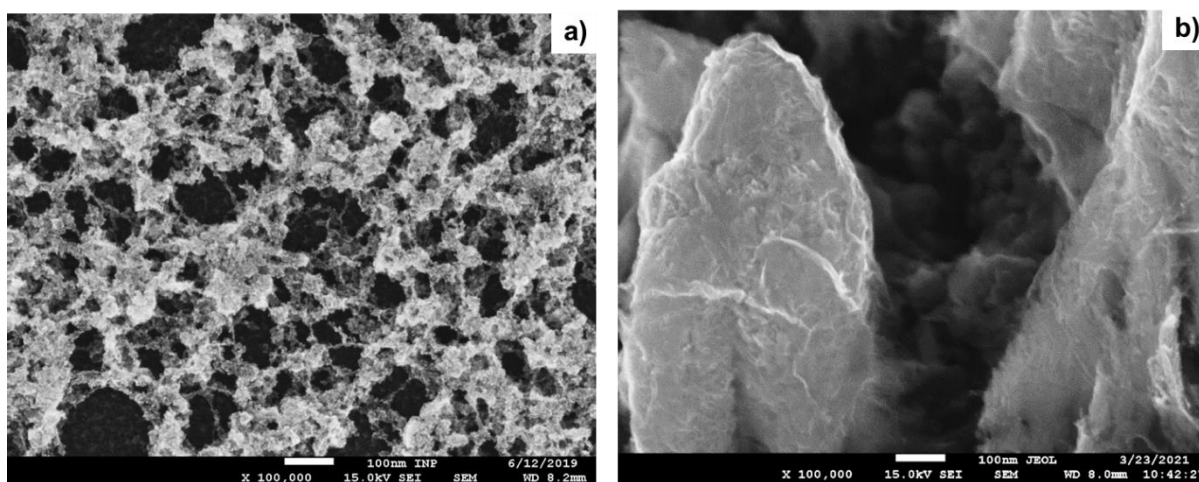


Figure S8. Detailed SEM micrographs of differences in post-leached porous morphology of IrCo sputtered on a) glassy carbon and b) GDL

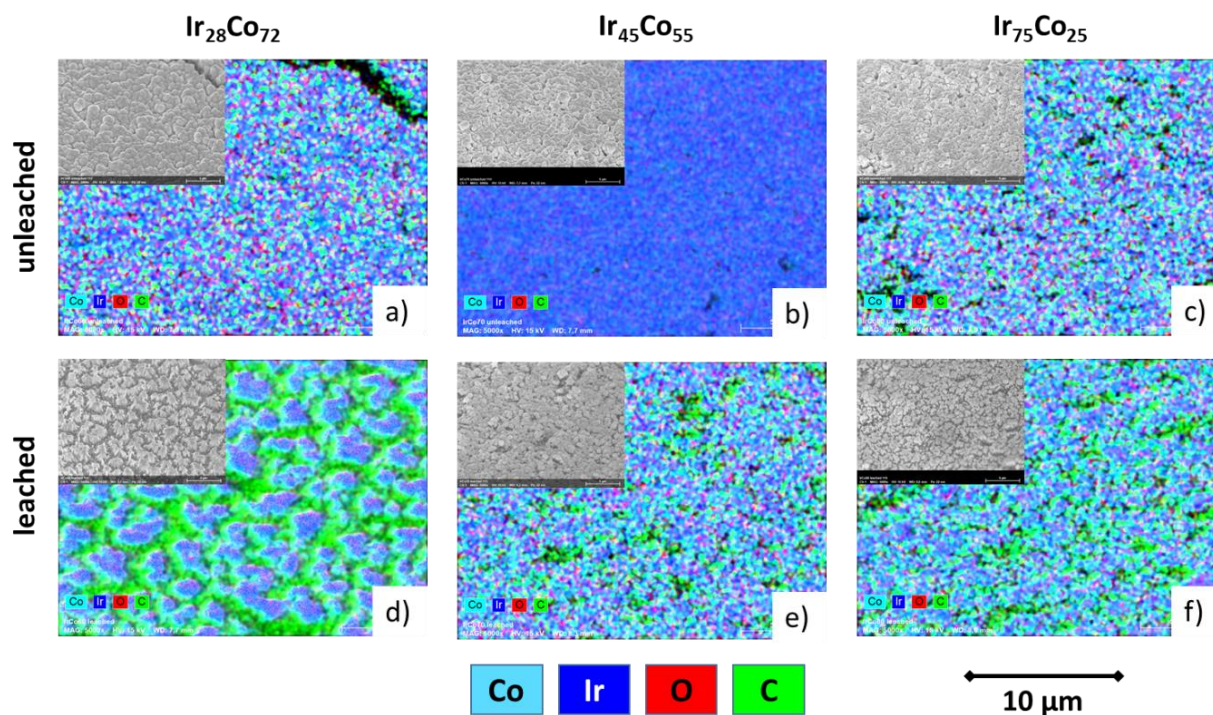


Figure S9. EDX images of the chemical distribution across the surface in the IrCo series before the acid leaching a) to c) and after d) to f). A miniature image from the same area captured using the in-lens detector is presented as a visual aid and reference to the morphology.

Ex-situ XANES and EXAFS measurements were carried out at the SuperXAS - X10DA beamline of the Swiss Light Source (SLS) at PSI, Switzerland (2.9T superbend source, storage ring current of 400 mA) via a send in service. The leached samples were protected with Kapton-film and directly mounted to a sample holder. The incident beam was collimated by a collimating mirror at 2.9 mrad (Rh-coated for Ir L_{III}) and monochromatized with a liquid nitrogen cooled channel-cut Si(111) monochromator in qexafs mode[4]. The beam size on the sample was 1.5mm x 0.4 mm (h_{xv}). Energy calibration was performed with a Co reference foil to the Co K-edge position and with a Pt reference foil to the Ir L_{III}-edge. Ion chambers with 2 bar of N₂ were used for XAS detection in transmission mode at the Ir L_{III}-edge. Co K-edge spectra were collected in quick fluorescence mode with a PIPS detector[5]. The data were processed using ProQEXAFS for calibration, interpolation, normalisation and averaging (300 s of measurement on each sample)[6]. The averaged XAS spectra were analyzed by using the DEMETER software package. The raw spectra were energy aligned to a metal reference foil, background corrected and normalized by the edge step. After conversion of the energy units (eV) into photoelectron wave number k units (Å⁻¹), the resulting $\chi(k)$ functions of the XAS spectra were weighted with k² and

then Fourier transformed to obtain pseudo-radial structure functions. The fits to the EXAFS spectra were performed in ARTEMIS of the DEMETER software package based on IFFEFIT [7]. XAS spectra of the pure metal foils were used as references to estimate the amplitude reduction factors (S_0^2). The Ir L_{III}-edge data were fitted in R-space, with fitting weights of k^2 and k^3 . The k-range for the Fourier transform was from 3-15 Å⁻¹ with a fit window in an R-range of 1.2-3.0 Å. The Co K-edge data were fitted in R-space, with a fitting weight of k^3 . The k-range for the Fourier transform was from 3-11 Å⁻¹ with a fit window in an R-range of 1.15-3 Å. The metal-oxygen scattering path has an ideal six-fold (octahedral) coordination, while the metal-metal scattering paths are based on a 12-fold coordination. To reduce the number of variables used in the fits of the Co K-edge EXAFS, the estimated values from the respective fits of the Ir L_{III}-edge data were used and kept constant for the M-O and Co-Ir scattering paths.

Fits for Ir₇₅Co₂₅

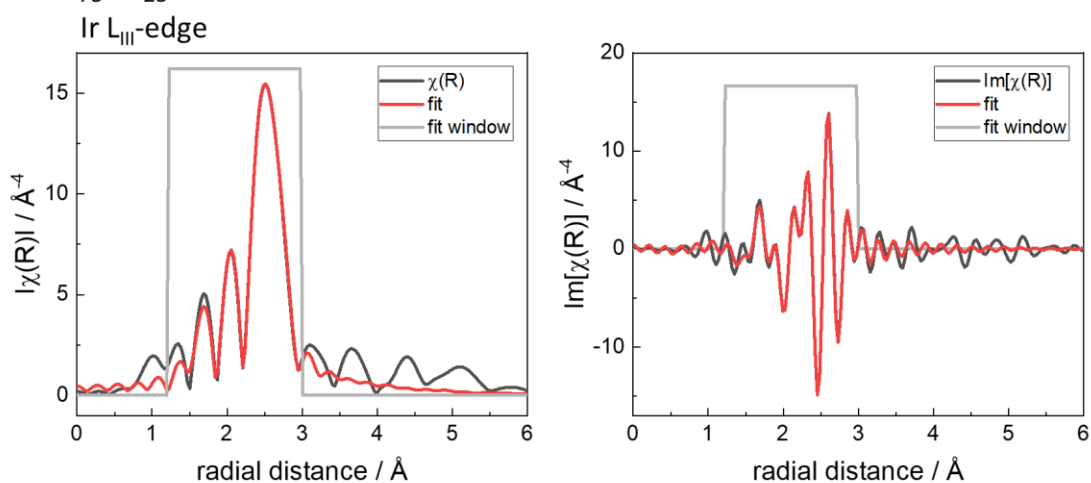


Figure S10. Ir L_{III}-edge Fourier Transform (FT) magnitudes of the k^2 -weighted extended X-ray absorption fine structure (EXAFS) data (right) and the imaginary part (left) of the FT for the leached Ir₇₅Co₂₅ sample. The k-range for the Fourier-transformed spectra at the Ir L_{III} K-edge was from 3 to 14 Å⁻¹, while the R-range for the fit was from 1.2 to 3.0 Å

Fits for Ir₇₅Co₂₅

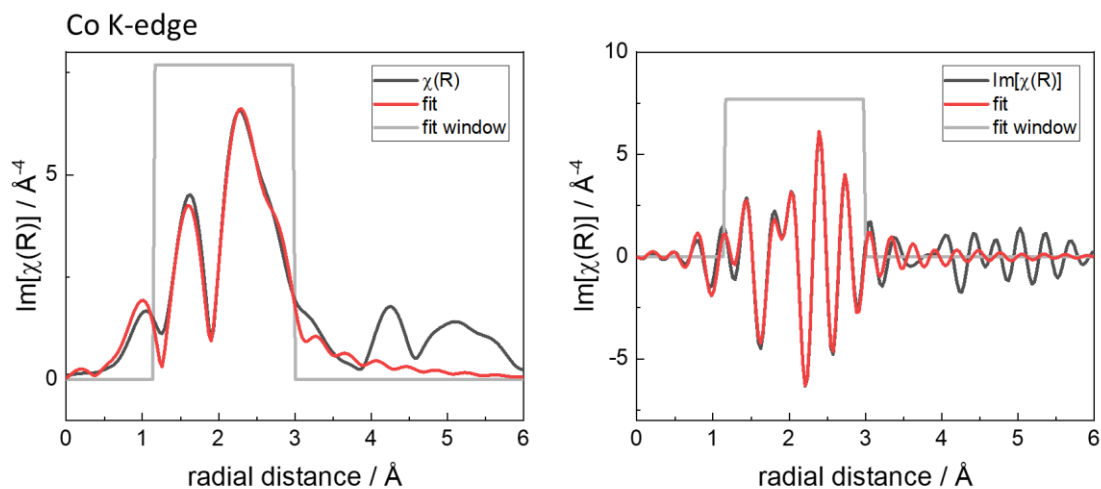


Figure S11. Co K-edge Fourier Transform (FT) magnitudes of the k^2 -weighted extended X-ray absorption fine structure (EXAFS) data (right) and the imaginary part (left) of the FT for the leached Ir₇₅Co₂₅ sample. The k -range for the Fourier-transformed spectra at the Co K-edge was from 3 to 11 \AA^{-1} , while the R -range for the fit was from 1.15 to 3.0 \AA .

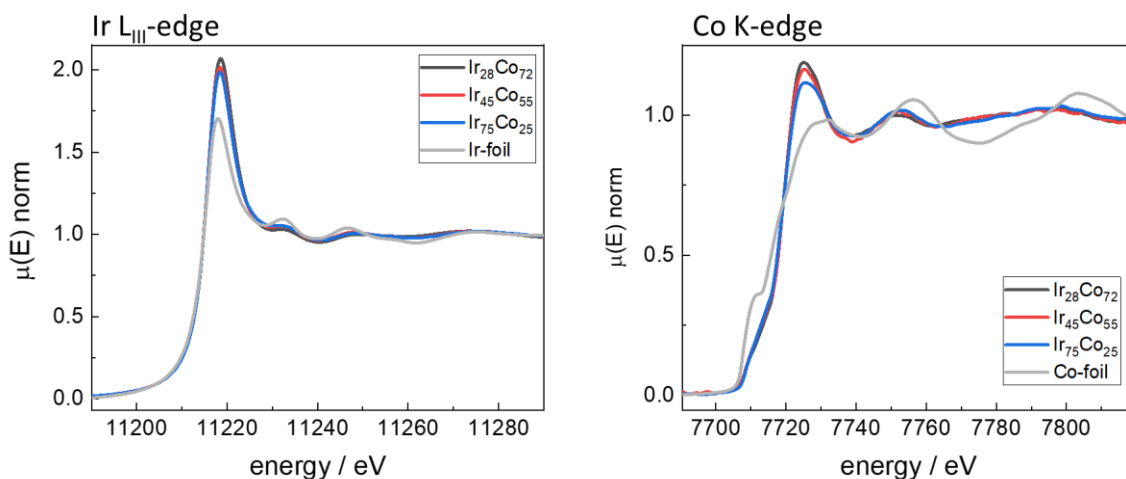


Figure S12. X-ray absorption near edge structure (XANES) of the leached Ir_xCo_y samples, measured at the Ir L_{III}-edge (left) and the Co K-edge (right). The samples are very similar in oxidation state and mostly metallic, with a small oxide contribution. The metallic character increases with increasing Ir-content of the as-prepared sample series.

References

- [1] A. W. Jensen *et al.*, “Self-supported nanostructured iridium-based networks as highly active electrocatalysts for oxygen evolution in acidic media,” *J Mater Chem A Mater*, vol. 8, no. 3, pp. 1066–1071, 2020, doi: 10.1039/c9ta12796h.
- [2] A. Parthasarathy, S. Srinivasan, A. J. Appleby, and C. R. Martin, “Temperature Dependence of the Electrode Kinetics of Oxygen Reduction at the Platinum/Nafion® Interface—A Microelectrode Investigation,” *J Electrochem Soc*, vol. 139, no. 9, pp. 2530–2537, Sep. 1992, doi: 10.1149/1.2221258/XML.
- [3] S. J. Freakley, J. Ruiz-Esquiús, and D. J. Morgan, “The X-ray photoelectron spectra of Ir, IrO₂ and IrCl₃ revisited,” *Surface and Interface Analysis*, vol. 49, no. 8, pp. 794–799, Aug. 2017, doi: 10.1002/SIA.6225.
- [4] O. Müller, M. Nachtegaal, J. Just, D. Lützenkirchen-Hecht, and R. Frahm, “Quick-EXAFS setup at the SuperXAS beamline for in situ X-ray absorption spectroscopy with 10 ms time resolution,” *urn:issn:1600-5775*, vol. 23, no. 1, pp. 260–266, Jan. 2016, doi: 10.1107/S1600577515018007.
- [5] A. H. Clark *et al.*, “Fluorescence-detected quick-scanning X-ray absorption spectroscopy,” *urn:issn:1600-5775*, vol. 27, no. 3, pp. 681–688, Apr. 2020, doi: 10.1107/S1600577520002350.
- [6] A. H. Clark, J. Imbao, R. Frahm, and M. Nachtegaal, “ProQEXAFS: a highly optimized parallelized rapid processing software for QEXAFS data,” *urn:issn:1600-5775*, vol. 27, no. 2, pp. 551–557, Feb. 2020, doi: 10.1107/S1600577519017053.
- [7] B. Ravel and M. Newville, “ATHENA, ARTEMIS, HEPHAESTUS: data analysis for X-ray absorption spectroscopy using IFEFFIT,” *urn:issn:0909-0495*, vol. 12, no. 4, pp. 537–541, Jun. 2005, doi: 10.1107/S0909049505012719.

7.3 Manuscript III:

P. Collantes Jiménez, G.K.H. Wiberg, G. Sievers, V. Brüser, M. Arenz.

Bridging the gap between basic research and application: a half-cell setup for high current density measurements of Ir-based oxygen evolution reaction catalysts on porous transport electrodes.

The published paper is reproduced from *J. Mater. Chem. A.* **2023**, 11, 20129-20138 with permission from the Royal Society of Chemistry.

J. Mater. Chem. A. **2023**, 11, 20129-20138

<https://doi.org/10.1039/D3TA04136K> (Open Access)

Cite this: *J. Mater. Chem. A*, 2023, 11, 20129

Bridging the gap between basic research and application: a half-cell setup for high current density measurements of Ir-based oxygen evolution reaction catalysts on porous transport electrodes†

Pablo Collantes Jiménez, ^a Gustav K. H. Wiberg, ^b Gustav W. Sievers, ^a Volker Brüser^a and Matthias Arenz ^{*b}

Electrochemical benchmarking in three-electrode setups at a laboratory scale can greatly accelerate the development of catalysts for the oxygen evolution reaction in proton exchange membrane water electrolyzers. However, current systems such as the rotating disk electrode suffer from measurement artifacts, low current densities, and limited extrinsic validity. In this study, we introduce a novel three-electrode setup referred to as the PTE setup, specifically designed to investigate OER catalysts on realistic porous transport electrodes (PTEs) used in the anode side of water electrolyzers at high current densities. We evaluated the effectiveness of the PTE setup using self-supported iridium oxide (IrO_x) and Ir–Co catalysts produced *via* physical vapor deposition on a porous Ti porous transport layer (PTL) and pressed to a Nafion membrane. Our results demonstrate that the PTE setup is capable of measuring the activity and stability of self-supported catalysts creating conditions found in the anode cell compartment of a single-cell electrolyzer at current densities up to 2 A cm_{geo}^{−2}. This setup represents a promising alternative to traditional benchmarking techniques, offering a practical and efficient approach for evaluating catalyst performance in relevant electrochemical environments.

Received 13th July 2023
Accepted 6th September 2023

DOI: 10.1039/d3ta04136k

rsc.li/materials-a

1. Introduction

Optimizing efficiency and reducing the consumption of critical raw materials in electrocatalysts is of paramount importance to achieve a significant increase in hydrogen production.^{1,2} Hence, bridging catalyst research into their application is of prime interest. With respect to proton exchange membrane water electrolyzers (PEMWEs), for their large-scale commercialization, testing oxygen evolution reaction (OER) catalysts at high current densities is essential. Such testing should not be limited to activity measurements but also needs to include accelerated stress tests. To date, most activity and degradation studies start with half-cell studies in rotating disk electrodes which are later verified in membrane electrode assembly techniques, which effectively work as single cells.^{3–12} In this regard, the gap between model studies and application is large. In single-cell

tests, focusing on the anode catalyst degradation behavior can be challenging due to the overlapping effects with other cell elements. At the very least, full-scale trials are material and time-intensive processes, which rely on a series of instruments and stack engineering not available to every research group. On the other hand, while the rotating disk electrode technique is very useful for fundamental studies of intrinsic catalyst activities, it falls short of representing relevant electrode morphologies and their mass transport behavior under realistic operating conditions.^{7,9,13,14} Furthermore, the lack of mass transport in liquid electrolyte compared to membrane assemblies limits the achievable current densities to less than 100 mA cm_{geo}^{−2}.¹⁵ For accelerated stress test studies and catalyst dissolution rate measurements, flow cells are the state-of-the-art laboratory setups for online spectrometry such as in-coupled spectroscopy studies.^{16,17} However, the direct contact of the electrolyte with the catalyst surface also leads to a substantial overestimation of the catalyst dissolution rates as compared to accelerated stress tests in membrane electrode assemblies¹⁸ Hence, stability data obtained from aqueous systems have to be interpreted carefully. Alternatively, the recently developed gas diffusion electrode (GDE) half-cell setup offers a more accurate physical representation of the individual electrode reactions due to its three-electrode configuration

^aLeibniz Institute for Plasma Science and Technology, Felix-Hausdorff-Strasse 2, 17489, Greifswald, Germany. E-mail: sievers@inp-greifswald.de; matthias.arenz@unibe.ch

^bDepartment of Chemistry, Biochemistry and Pharmaceutical Sciences, University of Bern, Freiestrasse 3, CH-3012 Bern, Switzerland

† Electronic supplementary information (ESI) available. See DOI: <https://doi.org/10.1039/d3ta04136k>



while preserving the fast screening and flexibility that is desired for laboratory techniques. In particular, a key feature of the GDE setup is the ability to perform realistic electrode preparation processes, which unlike in rotating disk electrode measurements, permits the study of the triple phase boundary of catalyst layers. By hot-pressing the coated substrate with a proton exchange membrane, the catalyst performance can be studied at high-current densities without limitations in gas solubility and bubble formation in liquid electrolyte.⁶ While the GDE technique has been featured primarily in ORR studies using carbon gas diffusion layers,^{19–22} recent efforts have been made to allow their application in OER studies for Ir-supported catalysts to match previous rotating disk electrode studies.^{23,24} However, the high positive potentials required for the OER accelerate carbon corrosion,²⁵ which can lead to flooding due to changes in the gas diffusion layer hydrophobicity. Under these conditions, the current is unevenly distributed, resulting in early failure due to emerging “hot spots” in the membrane causing uneven swelling and detachment from the catalyst. For this reason, catalyst formulations based on carbon-supported Ir nanoparticles typically struggle with early corrosion onsets resulting in catalyst agglomeration^{26,27} and loss of surface area.

On the other hand, an increased OER activity up to 10-fold higher compared to commercial catalysts has already been obtained in the former GDE setup for a new type of Ir-based self-supported catalysts with a large electrochemical surface area. This is obtained by a combined alternated magnetron sputtering and acid leaching step, eliminating the need for carbon in their composition and potentially increasing their stability.²⁸ Even though these catalysts demonstrated higher activity, their performance and stability measurements were initially limited due to the constraints of the GDE setup, particularly when working with carbon-based Gas Diffusion Layer (GDL) substrates. Consequently, it became essential to improve the measurement technique to perform catalyst stability measurements using Porous Transport Electrodes (PTEs) using the more chemically robust titanium (Ti) porous transport layer (PTL) substrates.

In this work, we develop the GDE setup to enable testing at industrially relevant electrolysis conditions. To this end, we optimized the electrode assembly on Ti PTLs with a magnetron-sputtered IrO_x catalyst with an 0.250 mg_{Ir} cm_{geo}⁻² loading to minimize the influence of material-related processing steps needed for the Ir–Co catalysts. Following the first positive results in the cell configuration achieving current densities >2 A cm_{geo}⁻² in an OER current-step protocol, we conducted a 20 h steady-state stability protocol at room temperature. The beginning-of-life and end-of-life OER activity and stability measurements, completed with cyclic voltammetry data, suggest that the new method can be used to extract meaningful information about the catalyst stability and perform degradation studies. Furthermore, the OER activity and stability of the Ir–Co self-supported catalyst sputtered on a Ti PTL with the same Ir loading and a nominal Co:Ir ratio of 4 was benchmarked and compared to the standard IrO_x in the new PTE setup. Ultimately, this study showcases the possibilities of this technique to the new generations of self-supported catalysts

and the high flexibility to adapt the setup to specific conditions by performing minor changes in its configuration.²⁹

2. Experimental

2.1 Materials, chemicals, gases

De-ionized (DI) ultrapure water (resistivity >18.2 MΩ cm, total organic carbon (TOC) < 5 ppb) from an Aquinity P-10² system (Membrapure, Germany) was used for electrolyte preparation, the cleaning of the upper cell parts and reactant in the PTE setup. Carbon gas diffusion layers with a microporous layer (Sigracet 29BC, 325 μm thick, Fuel Cell Store) served as a substrate for the sputtering of the catalyst film for the GDE preparation. Conversely, a Ti porous transport layer (PTL) (ANKURO Int. GmbH, 0.3 mm thickness, 50% open porosity) was used to create the PTEs. Polytetrafluoroethylene (PTFE) disks (Bola, 0.12 and 0.25 mm thicknesses), a gas diffusion layer without a microporous layer (Freudenberg H23, 210 μm thick, Fuel Cell Store), uncoated PTLs and Nafion membrane (Nafion 117, 183 μm thick, Chemours, Wilmington, DE, USA) were used for the cell assembly in GDE (Fig. S1†) and PTE (Fig. S2†) configurations. As a counter electrode, a platinum wire of 0.5 mm diameter (99.99%, Junker Edelmetalle GmbH) was used, which was folded several times at one side to increase the active surface area. Perchloric acid (70% HClO₄, Suprapur, Merck) was used for electrolyte preparation. O₂ (99.999%, Air Liquide) and Ar (99.999%, Air Liquide) were used for magnetron sputtering, acid leaching, and electrochemical measurements.

2.2 Catalyst synthesis and electrode preparation

To prepare the self-supported IrO_x catalyst film on the carbon gas diffusion layer substrates and Ti PTL substrates, a linear sputtering magnetron reactor (Univex 400, Leybold GmbH, Germany) was used. The process chamber was evacuated to a pressure of 1.7×10^{-5} Pa. The substrate was first cleaned in acetone and isopropanol, and placed on a holder in a load lock at atmospheric pressure. Then, the chamber was evacuated to a base pressure of at least 10^{-4} Pa. From there, a swiveling arm allowed the holder to enter the process chamber with minimal interruption. To create the plasma during the deposition, an Ar and O₂ mixture with a 2:3 ratio was ignited at the magnetron electrode at a working pressure of 5 Pa and flushed through the individual magnetron sources at a flow rate of 100 sccm. For the IrO_x deposition, a magnetron was equipped with a planar target of Ir (99.95%, MaTeck, Germany) of $177 \times 25 \times 1.5$ mm located at the upper part of the chamber. The RF generator (Cito 136, COMET) operated at a driving frequency of 13.56 MHz. A mask of a 5 cm × 5 cm window on the substrate holder limited the sputtered area during the deposition. The RF power was 158 W for the Ir source. The sputtering process was performed in a continuous deposition during 748 s until the desired Ir loading of 0.250 mg cm_{geo}⁻² was reached. The Ir–Co catalyst was prepared with the same Ir loading and a nominal Co:Ir ratio of 4 as described by Collantes *et al.*,²⁸ except a Ti PTL substrate was used instead of a carbon gas diffusion layer. Following the deposition, the Ir–Co electrode was leached



Table 1 Electrochemical protocol used for OER and stability determination of the IrO_x catalyst in GDE and PTE setup, indicating differences in bold

Step	Electrochemical technique	Parameters
Reference electrode calibration (both setups)	Open circuit potential (OCP)	Gas purge (flow rate) H ₂ (250 ml min ⁻¹) Time ~5 min
Electrochemical cleaning (both setups)	Cyclic voltammograms (CV)	Gas purge (flow rate) Ar (100 ml min ⁻¹), humidified Potential limits 0.05–1.2 V _{RHE} Scan rate 100 mV s ⁻¹ Number of cycles ~30 (until CV is stable)
OER activity	Galvanostatic steps coupled with online high-frequency resistance determination	Reactant supply GDE setup: Ar (100 ml min ⁻¹), humidified, PTE setup: H ₂ O (40 ml min ⁻¹) Current steps (hold in s) 1–2000 mA cm _{geo} ⁻² , 10 s per step, integrated potential over the last s per step (30 s per step for IrCo, integrated potential over the last 10 s per step) <i>iR</i> -correction 5 kHz, variable amplitude (100% post-correction)
Stability trial (PTE setup)	Galvanostatic steps coupled with online high-frequency resistance determination	Current steps (18 000 s hold) ~2 A cm _{geo} ⁻² , 4 block sequence <i>iR</i> -correction 5 kHz, 5 mV (100% post-correction)

chemically in 1 M HClO₄ for 30 min and then cleaned with DI water to wash any acid before pressing with the membrane. The hot-pressed procedure and assemblies for the respective GDEs and PTEs are described in detail in the ESI, see Fig. S1 and S2.†

2.3 Electrochemical measurements

All the experiments were conducted with a Potentiostat (ECi-211, Nordic Electrochemistry ApS, Denmark). An overview of the experimental protocol is presented below in Table 1.

The OER activity was determined through a quasi-steady state galvanostatic step protocol with increasing currents based on Schröder *et al.*²³ and scaled accordingly to account for the loading difference. An AC signal (5000 Hz, amplitude 1–5% of applied current) was applied during the current steps to obtain an online high-frequency resistance (HFR) measurement between the working and reference electrode, which was used for an *iR*-correction of the measured potential values.

3. Results and discussion

3.1 Setup development: from GDE to PTE

The GDE half-cell setup described by Schröder *et al.*²³ constituted a good starting point to work with carbon gas diffusion layer substrates, which were initially pressed at room temperature, *i.e.*, cold-pressed. The introduction of the hot-pressing step was a key element to stabilize the membrane assembly at higher current densities and avoid detachment due to bubble formation,³⁰ see Fig. 1.

While the hot pressing of the GDE was an important element in extending the kinetic-dominated potential region, mass transport limitations were still present at current densities greater than 100 mA cm_{geo}⁻².²⁸ There were further limitations due to the setup configuration, as it was previously reported by

Wiberg *et al.*²⁹ that the position of the reference electrode and the counter electrode in the single chamber design could vary during the measurements, therefore leading to substantial differences in the *iR* correction especially at high current densities.

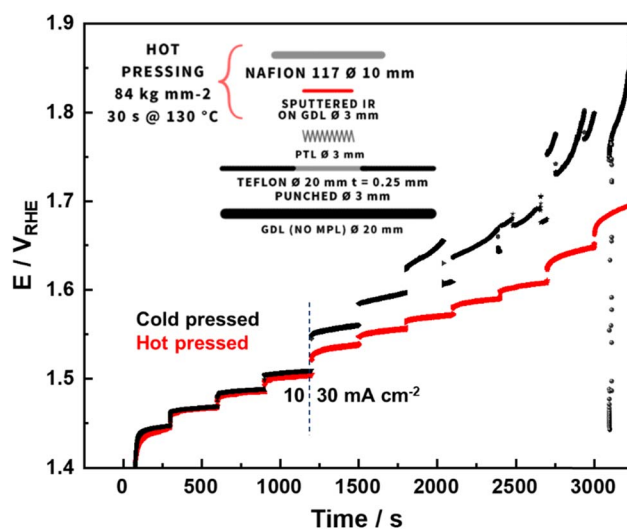


Fig. 1 Influence of hot pressing on the observed potential of a metallic Ir sputtered catalyst layer with a 1 mg cm_{geo}⁻² loading measured in the GDE setup. The test was conducted in a galvanostatic step protocol with current densities increasing from 1, 2.5, 5, 10, 30, 45, 60, 80, 100, 150 to 200 mA cm_{geo}⁻² in steps of 5 minutes per current density. The measurements were performed at room temperature. The black line corresponds to a cold-pressed sample, exhibiting contact problems beyond 30 mA cm_{geo}⁻². A hot-pressed sample, in the red line, achieved an extended current density range without showing contact problems. The inset shows a cross-section of the inner cell assembly with details of the hot pressing process.



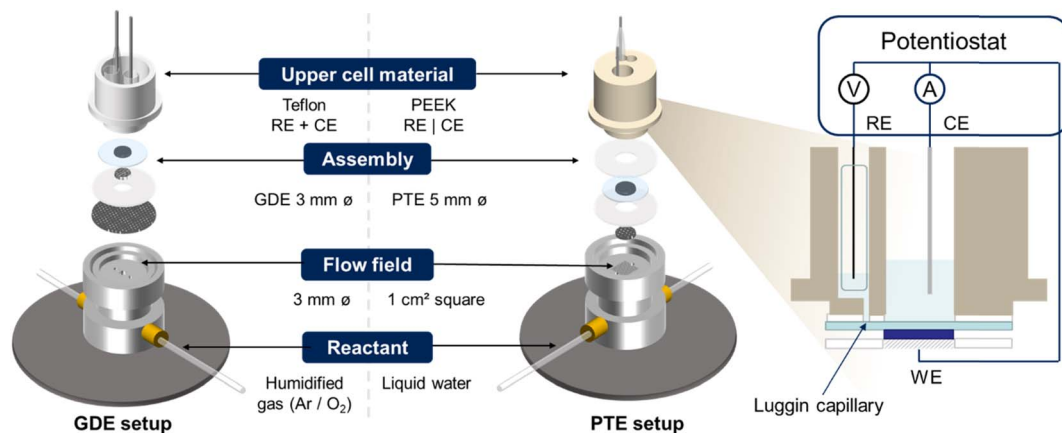


Fig. 2 Schematics of the design evolution from the GDE setup (left) to the PTE setup (center) and a detail of the cross-section of the top cell (right) showing the position of the Luggin capillary to the reference electrode (RE) compartment, the position of the working electrode (WE) and the independent chamber for the counter electrode (CE).

At the same time, given the small area of the working electrode (WE), the edge imperfections and inhomogeneities led to a larger spread in the obtained results. High current densities lead to intense bubble formation at the CE, which is easily stuck in the PTFE upper cell due to its aerophilic nature.^{31,32} This can lead to a blocking of the 3 \varnothing mm aperture of the PTFE cell rendering the covered areas inactive and leading to very high local currents in the adjacent areas or even a complete loss of potential control at the WE. All these effects can cause pronounced degradation effects.

Based on these observations, a new top cell was designed to test Ti PTLs. PEEK was used instead of PTFE since its comparatively lower hydrophobicity reduced the bubble adhesion. The single chamber design of the cell top part was also substituted by two independent electrolyte compartments. The main compartment centered over the assembly was reserved for the CE. Adjacent to this, another chamber was designed for the reference electrode with a Luggin capillary. At first, the Luggin capillary ended directly over the aperture of the main compartment, but it was experimentally observed that with the two reservoirs of electrolyte in contact, the iR was not less than 4–5 Ohm even at low current densities where no excessive bubble formation that could affect the Luggin capillary channel is expected. Most importantly, altering the position of the counter electrode affected the measured iR drop. Since there should not be an electric field inside the Luggin capillary (no current through the RE), these observed variations can be attributed to a distorted electric field due to the non-ideal geometry of the working and counter electrode. Hence, in the final version of the cell, a Luggin capillary with an independent electrolyte reservoir was designed to directly probe the membrane. With this design, the iR drop was minimized to 0.1–0.3 Ohm and remained independent of the counter electrode position as long as the electrolyte was not transferred between the two chambers.

The contact assembly also had to be redesigned to accommodate the thicker (0.3 mm) Ti PTL, which was increased to 5 mm in diameter to offset the edge imperfections caused by the

sample extraction process. Furthermore, a liquid water feed by a peristaltic pump replaced the humidified gas, and the carbon gas diffusion layer backing was discarded, thus eliminating all sources of carbon degradation. Instead, two Teflon disks were used to ensure tight sealing. To achieve a more even water flow and to minimize the plastic deformation of the membrane through the top cell apertures due to the upward pressure from the water supply and gas evolution, a bottom cell with a rectangular flow field pattern was used. The combination of all these improvements on the former GDE setup resulted in the PTE setup displayed in Fig. 2.

3.2 Parametric study in the PTE setup

A comparative series of OER activity measurements was performed in the PTE setup using carbon gas diffusion electrodes (GDEs) and Ti porous transport electrodes (PTEs) with an IrO_x catalyst with $0.250 \text{ mg}_{\text{Ir}} \text{ cm}_{\text{geo}}^{-2}$, see Fig. 3A. After deposition, a homogeneous catalyst layer was found even on the highly porous Ti PTL fibers, see the cross-section in Fig. 3B and C. Using IrO_x as a benchmark allowed us to concentrate the characterization efforts on evaluating the impact of substrate type, reactant supply, and hot-pressing configurations. This approach eliminates the requirement for additional processing steps such as acid leaching or activation necessary for Ir–Co catalysts.

Considering the data series hot pressed at 84 bar (red) in Fig. 3A, using liquid water in GDE assemblies (filled red circles) resulted in a slightly poorer performance already at low current densities as compared to the GDEs supplied with humidified gas (hollow red circles), indicating flooding problems.

The latter was still better than PTE assemblies under the same conditions (hollow red triangles), which could be expected from the larger pore structure at the surface in the PTEs, not optimized to maximize the number of active sites. Regardless, the trend in all series was to experience very high with very noticeable after $100 \text{ mA cm}_{\text{geo}}^{-2}$ due to diffusion limitations from the humidified gas together with the instability of carbon



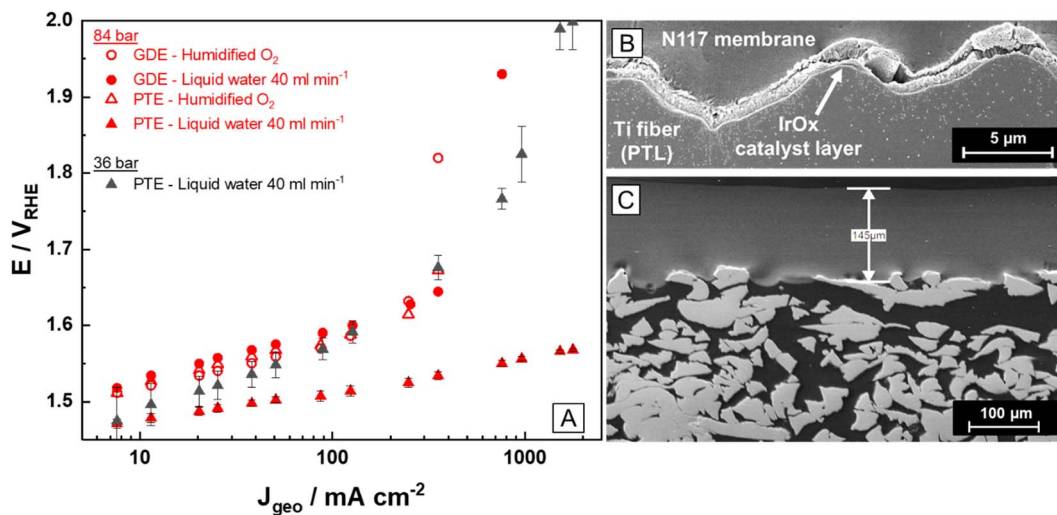


Fig. 3 (A) Influence of the configuration of the substrate (GDEs vs. PTEs), the supply of reactant (humidified O₂ vs. liquid water), and the hot-pressing (36 vs. 84 bar) in the OER activity of a sputtered IrO_x 0.250 mg cm_{geo}⁻² catalyst measured in the PTE setup. The best setup, substrate, and reactant supply combination produced an OER activity of $\sim 1.57 V_{RHE}$ at 2 A cm_{geo}⁻². (B) Cross-section micrograph obtained by scanning electron microscopy of the PTE before OER showing a homogeneous IrO_x layer thickness. (C) A wider view of the cross-section of the electrode where the interfaces in contact with the fibers and membrane, internal porosity as well as membrane thickness are visible.

degradation particularly in the GDE assemblies. On the other hand, a radically different behavior was observed when combining PTEs with liquid water, reaching current densities up to 2 A cm_{geo}⁻² (filled red triangles) at 1.55 V_{RHE}. This is a noticeable improvement as compared to the previous study designs, where the current was limited to around one order in magnitude lower values.²³ Next, the influence of the pressure applied during hot pressing of the PTEs over the OER activity was studied as several studies have reported that high pressures applied to the stiff Ti PTL fibers can accelerate pinhole formation in the membrane and reduce the catalyst efficiency due to gas crossover or cause short circuits.^{33,34} This was a relevant concern in the context of this study where a larger weight was needed to maintain the pressure conditions with 5 Ø mm samples. Hence, the OER performance using liquid water was measured for another three PTEs hot-pressed at a lower pressure of 7 kgf (~ 36 bar) and compared to the nominal 16.6 kgf (~ 84 bar). The low-pressure settings (filled black triangles) circles consistently lead to increased overpotentials already at relatively low current densities and large concomitant Tafel

slopes (80–100 mV dec⁻¹) when going to medium current densities and beyond, see Fig. 3A. In contrast, the PTEs hot-pressed at 84 bar (filled red triangles), exhibited substantially improved and more reproducible activity results to the point where the error bars are barely visible over the averaged data. Within this series of measurements, a Tafel slope of 37 mV dec⁻¹ was calculated in the 10–50 mA cm_{geo}⁻² region, see Table 2. Interestingly, with *iR* correction, a linear Tafel of 42 mV dec⁻¹ could still be extracted when increasing the upper fitting threshold to 2 A cm_{geo}⁻² currents, indicating minor or no diffusion limitations. In summary, the GDE setup shows no substantial differences between the use of humidified gas and water for either substrate, while in the PTE setup, the current density using humidified gas or low pressing conditions remains low. Hence, it can be concluded from these experiments that the only way to enable high current densities is by using PTEs with liquid water in the high hot-pressure setting in combination with the PTE setup. A summary of the relevant electrochemical findings can be seen in Table 2.

Table 2 Summary of the influence of different study parameters in the Tafel behavior and OER current density measured at 1.55 V_{RHE} of an IrO_x 0.250 mg cm_{geo}⁻² catalyst sputtered both on carbon gas diffusion layers (GDLs) and Ti porous transport layers (PTLs)

Setup configuration	Substrate type	Reactant type	Hot pressing pressure (bar)	Tafel slope@10–50 mA cm _{geo} ⁻² (mV dec ⁻¹)	Current density (mA cm _{geo} ⁻²)@1.55 V _{RHE}
GDE setup ^a	Carbon GDL	Humidified gas (O ₂)	84	70	21.4
PTE setup	Carbon GDL	Humidified gas (O ₂)	84	57	36.5
		Liquid water (40 ml min ⁻¹)	84	68	20.6
	Ti PTL	Humidified gas (O ₂)	84	67	27.0
		Liquid water (40 ml min ⁻¹)	84	37	758.7
			36	93	50.8

^a Represented in Fig. S2 in the ESI, section “Setup reproducibility”.



3.3 Stability tests

After successfully reaching high current densities without noticeable mass transfer limitations in the polarization curves performed in the PTE setup, a longer stability test was designed to resemble operation conditions seen in membrane electrode assemblies. Previous studies report that the most demanding conditions for anode catalyst stability are met at continuous high-current density tests with an extended duration.^{5,8,15,35} Using the IrO_x catalyst as a benchmark for the proposed protocol, a constant current density of 2 A cm_{geo}⁻² was applied for 20 h, separated into 4 sequenced blocks of 5 h. The HFR was measured online using an AC signal at 5 kHz and 5 mV amplitude, which allowed the continuous measurement of the cell resistance while minimally disturbing the measurement. During the first five hours of the stability measurement, the *i*R-free electrode potential, represented in black in Fig. 4A, remained stable with only local fluctuations during the conditioning in the first hour as well as an upward jump at the end of the period. Small disturbances in the range of a few tenths of mV were always present due to temporary gas bubble formation at the Pt CE. The readout time of the protocol macro in the Potentiostat produced a 1 or 2 second-long OCP period between the blocks where the activity of the catalyst was recovered in a downward jump, an effect also seen in membrane electrode assembly configurations.^{35,36} The HFR, see Fig. 4B, was initially very low at approx. 100 mOhm, and only experienced a slight increase up to approx. 150 mOhm during the first 5 hour period. In later blocks, high potential intervals appeared during short times.

These interferences, which are also visible in the HFR resistance measurement, correspond to temporary blockages of the Luggin capillary. Even though the blocked reference electrode prevented the direct interpretation of the degradation from the potential trend, the measurement remained valid as

the current was still applied continuously, see the right axis in Fig. 4A.

As the measurement progressed, the cell resistance plotted in black in Fig. 4C showed a steep increase during the measurement until a cell potential of 10 V was reached. A further inspection of the cell chambers after the test revealed that the main chamber was almost fully empty of electrolyte. During the measurement, the fast evolution of H₂ bubbles on the Pt wire at the counter electrode could have caused the electrolyte to evaporate faster, lowering the area in contact with the electrode and continuously increasing the cell resistance. In the last 5 hour period, the 10 V compliance voltage of the Potentiostat was reached altering the correct recording of the HFR-free voltage data, see the red dotted line in Fig. 4B. After the test, the cell was refilled with electrolyte and the reversible hydrogen electrode was remade to eliminate any offsets.

In the next step, the stability of an Ir-Co catalyst sputtered on a Ti PTL substrate was compared to that of the IrO_x in a short 5 hour measurement stability measurement at 2 A cm⁻² and 60 °C, see inset in Fig. 4A. The graph shows a reduced number of data points for a more clear comparison. Aside from an expected decrease of *ca.* 25 mV in the reversible electrode potential from the temperature difference, the further reduction would support the effects of an activation process observed in this type of catalyst.²⁸ Notably, it was also possible to record a stable potential with this material even at 60 °C where a lower stability could have been expected in comparison to the IrO_x benchmark measured at RT. The catalyst degradation produced in the stability measurement was assessed by performing cyclic voltammetry and OER activity measurements in beginning-of-life and end-of-life states, see Fig. 5.

For the IrO_x catalyst, the degradation can be interpreted from the decrease (6 mV dec⁻¹) in the Tafel slope between beginning-of-life and end-of-life OER activity, see Fig. 5A. Additionally, two 30 minute potential intervals from the

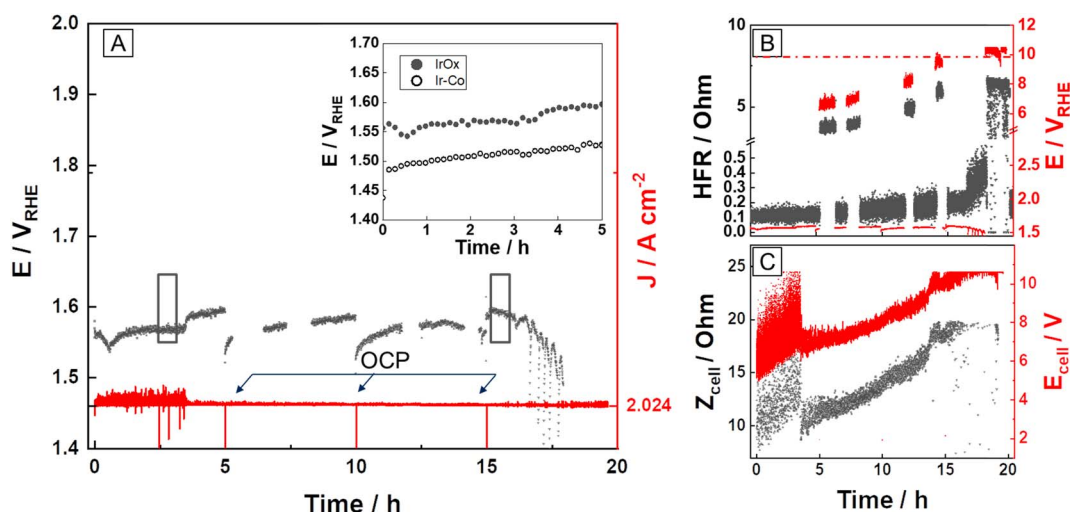


Fig. 4 (A) Stability measured at room temperature on the PTE setup of a 0.250 mg_{Ir} cm_{geo}⁻² IrO_x catalyst sputtered on Ti PTL. For comparison, the inset in the graph shows the stability of the 0.250 mg_{Ir} cm_{geo}⁻² Ir-Co catalyst measured at 60 °C in a 5 h period. (B and C) Show a cross-examination of measurement signals to determine the origin of the high potential regions during the stability IrO_x catalyst. (B) HFR (left axis) and HFR-free voltage (right axis) vs. time. The dotted line indicates the compliance voltage limit. (C) Cell resistance (left axis) and cell potential (right axis) vs. time.



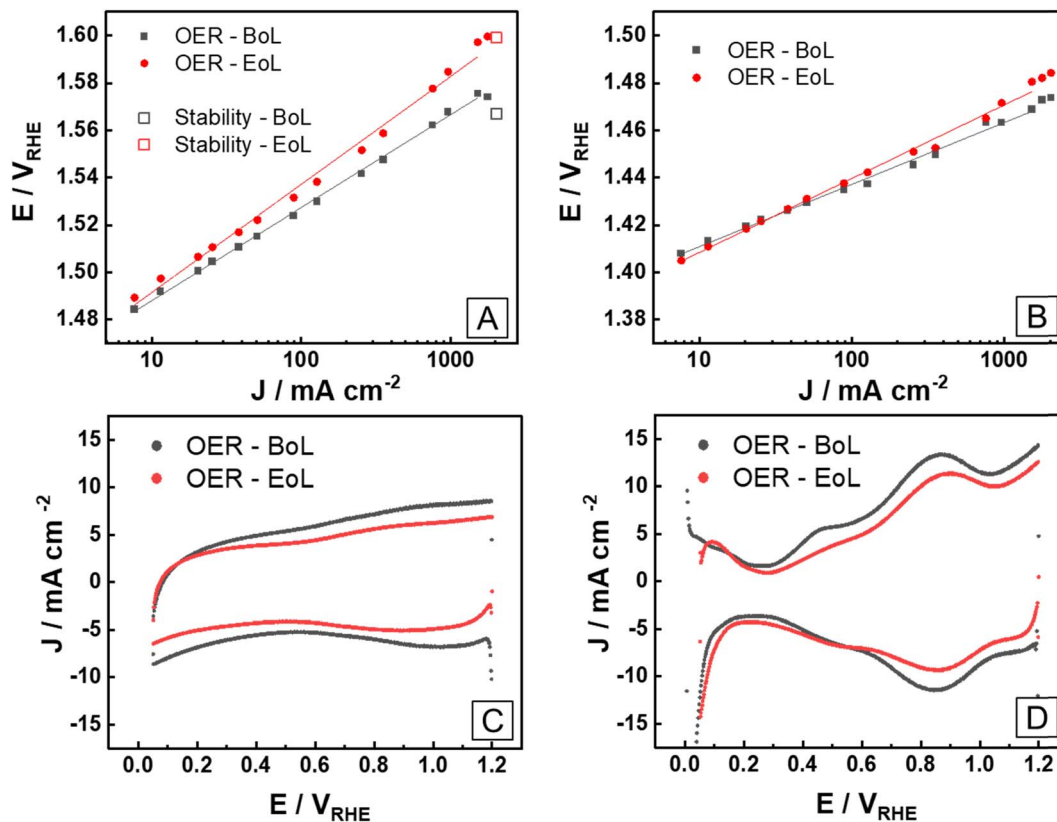


Fig. 5 OER activity and cyclic voltammetry recorded before (black) and after (red) the stability test for the IrO_x (A and C) and IrCo (B and D) self-supported catalysts. The OER step protocol, in filled symbols, was performed at room temperature for the IrO_x, and at 60 °C for the IrCo. In (A) the hollow symbols show 30 min of integrated measurements from the beginning (black) and end (red) of the stability test, see areas marked in Fig. 4A. In (C) and (D), the cyclic voltammograms were recorded at 100 mV s⁻¹ between 0.05–1.2 V_{RHE} before the beginning-of-life (BoL) and after the end-of-life (EoL) OER activity measurements.

beginning and end of the stability measurement, see Fig. 4A, were integrated and plotted in hollow symbols together with the OER data in Fig. 5A. These recorded potentials closely match the trend of the OER protocol, showing that the stability measurements in the PTE setup are also capable of displaying the real performance of the catalyst in artifact-free data intervals. Furthermore, comparing the cyclic voltammogram features before and after the stability test, see Fig. 5C, the decrease in the double layer capacity strongly suggests a loss of surface area from the catalyst degradation process during the stability, which could have also been a contributing factor to the gradual increase in HFR during the stability measurement.

Despite the larger surface area of the Ir-Co catalyst in comparison to IrO_x, as seen in the cyclic voltammogram features in Fig. 5D, an analogous reduction in double-layer capacity was observed between beginning-of-life and end-of-life states following the stability test. While the Ir-Co catalyst did experience a Tafel slope reduction of 13 mV dec⁻¹ between the beginning-of-life and end-of-life states, along with a decrease in activity at high current densities, it surprisingly exhibited an enhancement in its OER activity within the low current density range, as depicted in Fig. 5B. An explanation for this behavior could be the kinetic activation process of the microporous catalyst layer, which exhibits a mixed metallic and oxide nature.^{28,37,38} This interpretation is further supported by

Table 3 Summary of OER activity in the beginning-of-life (BoL) and end-of-life (EoL) states of the IrO_x and Ir-Co catalyst in the PTE setup from the galvanostatic steps and integrated 30 minute intervals from the stability test of the IrO_x (indicated in black rectangles in Fig. 4A)

Measurement state	Data source	Tafel slope (mV dec ⁻¹)		Potential (V _{RHE} @2 A cm _{geo} ⁻²)	
		IrO _x	Ir-Co	IrO _x	Ir-Co
BoL	Step OER	39	27	1.57	1.47
	2 A cm _{geo} ⁻² stability (30 min)	—	—	1.56	—
EoL	Step OER	45	36	1.59	1.48
	2 A cm _{geo} ⁻² stability (30 min)	—	—	1.59	—



the cyclic voltammogram features, see Fig. 5D, where distinct H_{upd} regions indicate remaining metallic Ir while the large capacitances are found in higher potentials suggesting the formation of oxides. Most interestingly, the remarkable performances observed using the self-supported catalyst preparation on PTEs have also been recently reported using a similar method in a membrane electrode assembly configuration.³⁹ The main electrochemical results are summarized in Table 3 below.

4. Conclusions

With this study, we have demonstrated the possibility of measuring OER potentials at relevant current densities $>2 \text{ A cm}^{-2}$ and temperatures with an improved configuration of the original GDE three-electrode half-cell that extends the range of application to conditions found in membrane electrode assemblies. By combining the PTE setup with PVD-based catalyst production, we demonstrate that it is possible to simplify and fast-track catalyst research closer to the industry standards at a lab scale. Although the results of the stability test should not necessarily provide a quantitative measure of catalyst degradation, they show the potential of the PTE setup to perform electrochemical tests under realistic high-current density conditions. Comparing the behavior of a IrO_x to a Ir-Co catalyst, the importance of employing measurement setups capable of attaining relevant current densities becomes particularly evident when considering the nonlinear evolution of the OER activity in nanostructured bimetallic catalysts.¹⁹ Further development of the PTE setup in combination with parallel developments of this cell design²⁹ will unlock further capabilities such as pressurized and high-temperature measurements and coupling with online spectrometric analytics (ICP-MS, OES) to make quantitative degradation studies possible.

Author contributions

Pablo Collantes Jiménez: methodology, investigation, writing – original draft. Gustav K. H. Wiberg: conceptualization, methodology. Gustav Sievers: writing – review & editing, supervision, conceptualization. Volker Brüser: supervision, methodology. Matthias Arenz: writing – review & editing, supervision, conceptualization, all authors checked and approved the final version of the manuscript.

Conflicts of interest

Gustav Sievers has patent DE102016013185B4 issued to himself and Gustav Sievers and Pablo Collantes have PCT/EP2022/082 349 and EP 4 184 618 A1 issued to INP Greifswald.

Acknowledgements

The authors gratefully acknowledge the financial support by the German Federal Ministry of Education and Research (BMBF) in the framework of the VIP + Projekt. 03VP06451 (3DNanoMe).

References

- W. T. Hong, M. Risch, K. A. Stoerzinger, A. Grimaud, J. Suntivich and Y. Shao-Horn, Toward the rational design of non-precious transition metal oxides for oxygen electrocatalysis, *Energy Environ. Sci.*, 2015, **8**, 1404–1427, DOI: [10.1039/c4ee03869j](https://doi.org/10.1039/c4ee03869j).
- R. R. Rao, M. J. Kolb, N. B. Halck, A. F. Pedersen, A. Mehta, H. You, K. A. Stoerzinger, Z. Feng, H. A. Hansen, H. Zhou, L. Giordano, J. Rossmeisl, T. Vegge, I. Chorkendorff, I. E. L. Stephens and Y. Shao-Horn, Towards identifying the active sites on RuO₂(110) in catalyzing oxygen evolution, *Energy Environ. Sci.*, 2017, **10**, 2626–2637, DOI: [10.1039/c7ee02307c](https://doi.org/10.1039/c7ee02307c).
- C. Spöri, C. Brand, M. Kroschel and P. Strasser, Accelerated Degradation Protocols for Iridium-Based Oxygen Evolving Catalysts in Water Splitting Devices, *J. Electrochem. Soc.*, 2021, **168**, 034508, DOI: [10.1149/1945-7111/abeb61](https://doi.org/10.1149/1945-7111/abeb61).
- M. Bernt, A. Siebel and H. A. Gasteiger, Analysis of Voltage Losses in PEM Water Electrolyzers with Low Platinum Group Metal Loadings, *J. Electrochem. Soc.*, 2018, **165**, F305–F314, DOI: [10.1149/2.0641805jes](https://doi.org/10.1149/2.0641805jes).
- A. Weiß, A. Siebel, M. Bernt, T.-H. Shen, V. Tileli and H. A. Gasteiger, Impact of Intermittent Operation on Lifetime and Performance of a PEM Water Electrolyzer, *J. Electrochem. Soc.*, 2019, **166**, F487–F497, DOI: [10.1149/2.0421908jes](https://doi.org/10.1149/2.0421908jes).
- H. A. El-Sayed, A. Weiß, L. F. Olbrich, G. P. Putro and H. A. Gasteiger, OER Catalyst Stability Investigation Using RDE Technique: A Stability Measure or an Artifact?, *J. Electrochem. Soc.*, 2019, **166**, F458–F464, DOI: [10.1149/2.0301908jes](https://doi.org/10.1149/2.0301908jes).
- A. Hartig-Weiss, M. F. Tovini, H. A. Gasteiger and H. A. El-Sayed, OER Catalyst Durability Tests Using the Rotating Disk Electrode Technique: The Reason Why This Leads to Erroneous Conclusions, *ACS Appl. Energy Mater.*, 2020, **3**, 10323–10327, DOI: [10.1021/acsaem.0c01944](https://doi.org/10.1021/acsaem.0c01944).
- P. Aßmann, A. S. Gago, P. Gazdzicki, K. A. Friedrich and M. Wark, Toward developing accelerated stress tests for proton exchange membrane electrolyzers, *Curr. Opin. Electrochem.*, 2020, **21**, 225–233, DOI: [10.1016/j.coelec.2020.02.024](https://doi.org/10.1016/j.coelec.2020.02.024).
- M. Fathi Tovini, A. Hartig-Weiß, H. A. Gasteiger and H. A. El-Sayed, The Discrepancy in Oxygen Evolution Reaction Catalyst Lifetime Explained: RDE vs MEA - Dynamicity within the Catalyst Layer Matters, *J. Electrochem. Soc.*, 2021, **168**, 014512, DOI: [10.1149/1945-7111/abdcc9](https://doi.org/10.1149/1945-7111/abdcc9).
- K.-R. Yeo, K.-S. Lee, H. Kim, J. Lee and S.-K. Kim, A highly active and stable 3D dandelion spore-structured self-supporting Ir-based electrocatalyst for proton exchange membrane water electrolysis fabricated using structural reconstruction, *Energy Environ. Sci.*, 2022, **15**, 3449–3461, DOI: [10.1039/D2EE01042A](https://doi.org/10.1039/D2EE01042A).
- Z.-Y. Wu, F.-Y. Chen, B. Li, S.-W. Yu, Y. Z. Finfrock, D. M. Meira, Q.-Q. Yan, P. Zhu, M.-X. Chen, T.-W. Song, Z. Yin, H.-W. Liang, S. Zhang, G. Wang and H. Wang, Non-



- iridium-based electrocatalyst for durable acidic oxygen evolution reaction in proton exchange membrane water electrolysis, *Nat. Mater.*, 2023, **22**, 100–108, DOI: [10.1038/s41563-022-01380-5](https://doi.org/10.1038/s41563-022-01380-5).
- 12 J. W. D. Ng, M. Tang and T. F. Jaramillo, A carbon-free, precious-metal-free, high-performance O₂ electrode for regenerative fuel cells and metal-air batteries, *Energy Environ. Sci.*, 2014, **7**, 2017–2024, DOI: [10.1039/c3ee44059a](https://doi.org/10.1039/c3ee44059a).
- 13 S. Nösberger, J. Du, J. Quinson, E. Berner, A. Zana, G. K. H. Wiberg and M. Arenz, The gas diffusion electrode setup as a testing platform for evaluating fuel cell catalysts: A comparative RDE-GDE study, *Electrochem. Sci. Adv.*, 2023, **3**, 1–12, DOI: [10.1002/elsa.202100190](https://doi.org/10.1002/elsa.202100190).
- 14 T. Lazaridis, B. M. Stühmeier, H. A. Gasteiger and H. A. El-Sayed, Capabilities and limitations of rotating disk electrodes versus membrane electrode assemblies in the investigation of electrocatalysts, *Nat. Catal.*, 2022, **5**, 363–373, DOI: [10.1038/s41929-022-00776-5](https://doi.org/10.1038/s41929-022-00776-5).
- 15 S. Geiger, O. Kasian, M. Ledendecker, E. Pizzutilo, A. M. Mingers, W. T. Fu, O. Diaz-Morales, Z. Li, T. Oellers, L. Fruchter, A. Ludwig, K. J. J. Mayrhofer, M. T. M. Koper and S. Cherevko, The stability number as a metric for electrocatalyst stability benchmarking, *Nat. Catal.*, 2018, **1**, 508–515, DOI: [10.1038/s41929-018-0085-6](https://doi.org/10.1038/s41929-018-0085-6).
- 16 O. Kasian, S. Geiger, K. J. J. Mayrhofer and S. Cherevko, Electrochemical On-line ICP-MS in Electrocatalysis Research, *Chem. Rec.*, 2019, **19**, 2130–2142, DOI: [10.1002/tcr.201800162](https://doi.org/10.1002/tcr.201800162).
- 17 J. Knöppel, S. Zhang, F. D. Speck, K. J. J. Mayrhofer, C. Scheu and S. Cherevko, Time-resolved analysis of dissolution phenomena in photoelectrochemistry – A case study of WO₃ photocorrosion, *Electrochem. Commun.*, 2018, **96**, 53–56, DOI: [10.1016/j.elecom.2018.09.008](https://doi.org/10.1016/j.elecom.2018.09.008).
- 18 J. Knöppel, M. Möckl, D. Escalera-López, K. Stojanovski, M. Bierling, T. Böhm, S. Thiele, M. Rzepka and S. Cherevko, On the limitations in assessing stability of oxygen evolution catalysts using aqueous model electrochemical cells, *Nat. Commun.*, 2021, **12**, 2231, DOI: [10.1038/s41467-021-22296-9](https://doi.org/10.1038/s41467-021-22296-9).
- 19 K. Ehelebe, N. Schmitt, G. Sievers, A. W. Jensen, A. Hrnjić, P. Collantes Jiménez, P. Kaiser, M. Geuß, Y. P. Ku, P. Jovanović, K. J. J. Mayrhofer, B. Etzold, N. Hodnik, M. Escudero-Escribano, M. Arenz and S. Cherevko, Benchmarking Fuel Cell Electrocatalysts Using Gas Diffusion Electrodes: Inter-lab Comparison and Best Practices, *ACS Energy Lett.*, 2022, **7**, 816–826, DOI: [10.1021/acscenergylett.1c02659](https://doi.org/10.1021/acscenergylett.1c02659).
- 20 G. W. Sievers, A. W. Jensen, V. Brüser, M. Arenz and M. Escudero-Escribano, Sputtered Platinum Thin-films for Oxygen Reduction in Gas Diffusion Electrodes: A Model System for Studies under Realistic Reaction Conditions, *Surfaces*, 2019, **2**, 336–348, DOI: [10.3390/surfaces2020025](https://doi.org/10.3390/surfaces2020025).
- 21 M. Inaba, A. W. Jensen, G. W. Sievers, M. Escudero-Escribano, A. Zana and M. Arenz, Benchmarking high surface area electrocatalysts in a gas diffusion electrode: Measurement of oxygen reduction activities under realistic conditions, *Energy Environ. Sci.*, 2018, **11**, 988–994, DOI: [10.1039/c8ee00019k](https://doi.org/10.1039/c8ee00019k).
- 22 K. Ehelebe, D. Seeberger, M. T. Y. Paul, S. Thiele, K. J. J. Mayrhofer and S. Cherevko, Evaluating Electrocatalysts at Relevant Currents in a Half-Cell: The Impact of Pt Loading on Oxygen Reduction Reaction, *J. Electrochem. Soc.*, 2019, **166**, F1259–F1268, DOI: [10.1149/2.0911915jes](https://doi.org/10.1149/2.0911915jes).
- 23 J. Schröder, V. A. Mints, A. Bornet, E. Berner, M. Fathi Tovini, J. Quinson, G. K. H. Wiberg, F. Bizzotto, H. A. El-Sayed and M. Arenz, The Gas Diffusion Electrode Setup as Straightforward Testing Device for Proton Exchange Membrane Water Electrolyzer Catalysts, *JACS Au*, 2021, **1**, 247–251, DOI: [10.1021/jacsau.1c00015](https://doi.org/10.1021/jacsau.1c00015).
- 24 A. Bornet, R. Pittkowski, T. M. Nielsen, E. Berner, A. Maletzko, J. Schröder, J. Quinson, J. Melke, K. M. Ø. Jensen and M. Arenz, Influence of Temperature on the Performance of Carbon- and ATO-supported Oxygen Evolution Reaction Catalysts in a Gas Diffusion Electrode Setup, *ACS Catal.*, 2023, **13**, 7568–7577, DOI: [10.1021/acscatal.3c01193](https://doi.org/10.1021/acscatal.3c01193).
- 25 T. Reier, M. Oezaslan and P. Strasser, Electrocatalytic oxygen evolution reaction (OER) on Ru, Ir, and Pt catalysts: A comparative study of nanoparticles and bulk materials, *ACS Catal.*, 2012, **2**, 1765–1772, DOI: [10.1021/cs3003098](https://doi.org/10.1021/cs3003098).
- 26 S. Chatterjee, S. Intikhab, L. Profitt, Y. Li, V. Natsu, R. Gawas and J. Snyder, Nanoporous Multimetallic Ir Alloys As Efficient And Stable Electrocatalysts For Acidic Oxygen Evolution Reactions, *J. Catal.*, 2021, **393**, 303–312, DOI: [10.30809/phe.1.2017.21](https://doi.org/10.30809/phe.1.2017.21).
- 27 P. Jovanović, N. Hodnik, F. Ruiz-Zepeda, I. Arčon, B. Jozinović, M. Zorko, M. Bele, M. Šala, V. S. Šelih, S. Hočvar and M. Gaberšček, Electrochemical Dissolution of Iridium and Iridium Oxide Particles in Acidic Media: Transmission Electron Microscopy, Electrochemical Flow Cell Coupled to Inductively Coupled Plasma Mass Spectrometry, and X-ray Absorption Spectroscopy Study, *J. Am. Chem. Soc.*, 2017, **139**, 12837–12846, DOI: [10.1021/jacs.7b08071](https://doi.org/10.1021/jacs.7b08071).
- 28 P. Collantes Jiménez, G. Sievers, A. Quade, V. Brüser, R. K. Pittkowski and M. Arenz, Gas diffusion electrode activity measurements of iridium-based self-supported catalysts produced by alternated physical vapour deposition, *J. Power Sources*, 2023, **569**, 232990, DOI: [10.1016/j.jpowsour.2023.232990](https://doi.org/10.1016/j.jpowsour.2023.232990).
- 29 G. K. H. Wiberg, S. Nösberger and M. Arenz, Evolution of a GDE setup: Beyond ambient conditions, *Curr. Opin. Electrochem.*, 2022, **36**, 101129, DOI: [10.1016/j.coelec.2022.101129](https://doi.org/10.1016/j.coelec.2022.101129).
- 30 H.-Y. Jung and J. W. Kim, Role of the glass transition temperature of Nafion 117 membrane in the preparation of the membrane electrode assembly in a direct methanol fuel cell (DMFC), *Int. J. Hydrogen Energy*, 2012, **37**, 12580–12585, DOI: [10.1016/j.ijhydene.2012.05.121](https://doi.org/10.1016/j.ijhydene.2012.05.121).
- 31 H. Mirsandi, W. J. Smit, G. Kong, M. W. Baltussen, E. A. J. F. Peters and J. A. M. Kuipers, Influence of wetting



- conditions on bubble formation from a submerged orifice, *Exp. Fluids*, 2020, **61**, 83, DOI: [10.1007/s00348-020-2919-7](https://doi.org/10.1007/s00348-020-2919-7).
- 32 C. Yu, P. Zhang, J. Wang and L. Jiang, Superwettability of Gas Bubbles and Its Application: From Bioinspiration to Advanced Materials, *Adv. Mater.*, 2017, **29**, 1703053, DOI: [10.1002/adma.201703053](https://doi.org/10.1002/adma.201703053).
- 33 Q. Feng, X. Z. Yuan, G. Liu, B. Wei, Z. Zhang, H. Li and H. Wang, A review of proton exchange membrane water electrolysis on degradation mechanisms and mitigation strategies, *J. Power Sources*, 2017, **366**, 33–55, DOI: [10.1016/j.jpowsour.2017.09.006](https://doi.org/10.1016/j.jpowsour.2017.09.006).
- 34 C. Liu, K. Wippermann, M. Rasinski, Y. Suo, M. Shviro, M. Carmo and W. Lehnert, Constructing a Multifunctional Interface between Membrane and Porous Transport Layer for Water Electrolyzers, *ACS Appl. Mater. Interfaces*, 2021, **13**, 16182–16196, DOI: [10.1021/acsami.0c20690](https://doi.org/10.1021/acsami.0c20690).
- 35 C. Rakousky, G. P. Keeley, K. Wippermann, M. Carmo and D. Stolten, The stability challenge on the pathway to high-current-density polymer electrolyte membrane water electrolyzers, *Electrochim. Acta*, 2018, **278**, 324–331, DOI: [10.1016/j.electacta.2018.04.154](https://doi.org/10.1016/j.electacta.2018.04.154).
- 36 C. Rakousky, U. Reimer, K. Wippermann, M. Carmo, W. Lueke and D. Stolten, An analysis of degradation phenomena in polymer electrolyte membrane water electrolysis, *J. Power Sources*, 2016, **326**, 120–128, DOI: [10.1016/j.jpowsour.2016.06.082](https://doi.org/10.1016/j.jpowsour.2016.06.082).
- 37 A. Grimaud, A. Demortiere, M. Saubanere, W. Dachraoui, M. Duchamp, M. L. Doublet and J. M. Tarascon, Activation of surface oxygen sites on an iridium-based model catalyst for the oxygen evolution reaction, *Nat. Energy*, 2017, **2**, 17002, DOI: [10.1038/nenergy.2017.2](https://doi.org/10.1038/nenergy.2017.2).
- 38 M. Suermann, T. J. Schmidt and F. N. Büchi, Comparing the kinetic activation energy of the oxygen evolution and reduction reactions, *Electrochim. Acta*, 2018, **281**, 466–471, DOI: [10.1016/j.electacta.2018.05.150](https://doi.org/10.1016/j.electacta.2018.05.150).
- 39 J. K. Lee, G. Anderson, A. W. Tricker, F. Babbe, A. Madan, D. A. Cullen, J. D. Arregui-Mena, N. Danilovic, R. Mukundan, A. Z. Weber and X. Peng, Ionomer-free and recyclable porous-transport electrode for high-performing proton-exchange-membrane water electrolysis, *Nat. Commun.*, 2023, **14**, 4592, DOI: [10.1038/s41467-023-40375-x](https://doi.org/10.1038/s41467-023-40375-x).



Supporting information

Bridging the gap between basic research and application: A half-cell setup for high current density measurements of Ir-based oxygen evolution reaction catalysts on porous transport electrodes.

Pablo Collantes Jiménez ¹, Gustav K.H. Wiberg ², Gustav W. Sievers ¹, Volker Brüser ¹, Matthias Arenz ²

¹ Leibniz Institute for Plasma Science and Technology, Felix-Hausdorff-Strasse 2, 17489 Greifswald, Germany

² Department of Chemistry and Biochemistry, University of Bern, Freiestrasse 3, CH-3012 Bern, Switzerland

* Corresponding authors: sievers@inp-greifswald.de , matthias.arenz@unibe.ch

Hot pressing and cell assembly in the GDE and PTE setup configurations

Our laboratory-developed hot pressing station was constructed using a modified soldering iron installed in a small vertical lever press, see Figure S1A. The unit was set to a temperature of 130 °C, as measured with a type J thermocouple inserted in the hot tip. The sample was positioned on the hot end for 15 min before pressing to adjust it to the target temperature. In this study, the Nafion membrane (Nafion 117, 183 µm thick, Fuel Cell Store) was activated before pressing as described by Schröder et al. [1]. Then, the samples were pressed at 84 bar for 60 s. to achieve good interfacial contact between the coated substrates and the membrane

In the GDE setup configuration, see Figure S1B, the GDEs were prepared as described by Collantes et al. [2]. In this compartment, the CE and RE shared the same pool of electrolyte (HClO_4) and were separated only by independent porous glass frits, see Figure S1C. In the GDE setup measurements, the reactant was supplied through a humidified gas bubbler (Ar/O_2) and set to a constant flow rate of 100 sccm, see Figure S1D. The assembly details of the GDE setup appear below in Figure S1E.

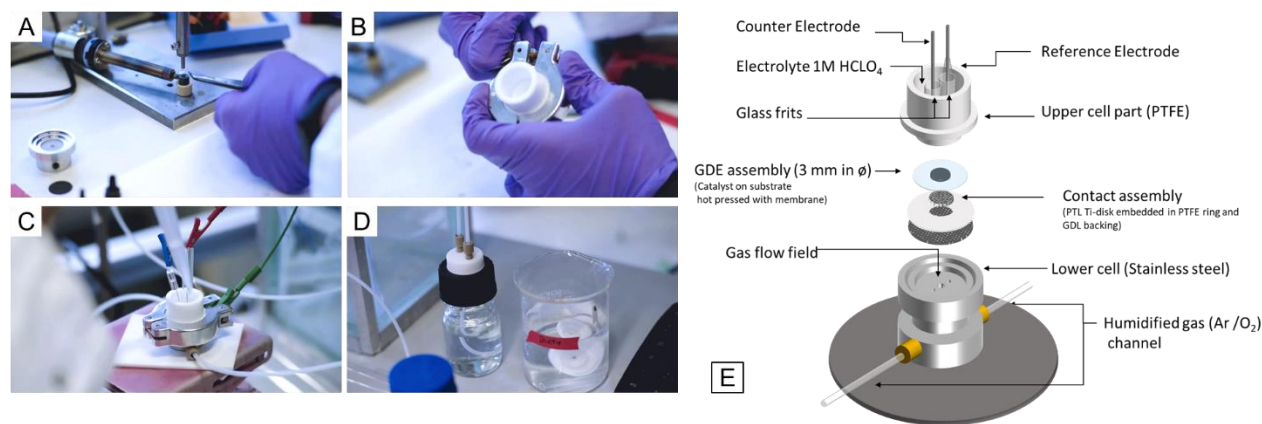


Figure S1. Snapshots of the sample manufacturing process and inner assembly of the GDE setup. A. Hot pressing procedure. B. Tightening of the top cell part after inserting the cell assembly. C. Electrodes connected and ready to test. D. Water bubbler for humidified gas. E. Schematic of the cell parts and the assembly used for GDL substrates.

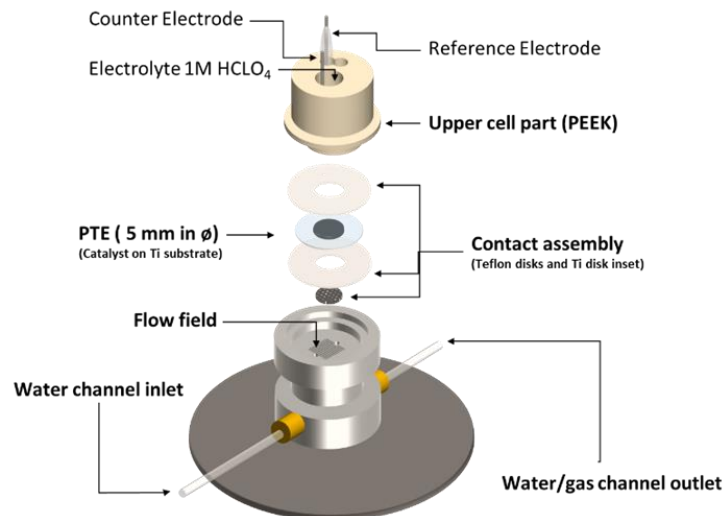


Figure S2: Schematic of the PTE cell setup and assembly used for Ti PTL substrates.

In the PTE setup, a disk of $\text{\O} 5 \text{ mm}$ was punched from the sputtered Ti PTL - the PTE - and hot pressed with a $\text{\O} 16 \text{ mm}$ Nafion membrane at $130 \text{ }^\circ\text{C}$ for 60 s. The resulting half-cell assembly, see Figure S2, was immediately immersed in DI water for one minute to rehydrate the membrane and avoid detachment due to differential strain in the interface with the substrate, and then dried before assembly. For the assembly, $\text{\O} 20 \text{ mm}$ disks with concentric holes were punched using a concentric circular steel punch (BOEHM, Germany) from a 0.25 mm and 0.50 mm Teflon sheet respectively, and also from a $\text{\O} 5 \text{ mm}$ PTL blank. The thinner Teflon disk was positioned directly over the flow field, with the PTL blank as an inset. Then, the half-cell assembly was dried lightly on a lab tissue (Rotizell, Roth) and sandwiched with the thicker Teflon disk. The latter disk also featured a small eccentric $\text{\O} 1.5 \text{ mm}$ hole centered 5 mm aside from the main aperture to communicate the tip of the Luggin capillary in the RE chamber directly to the membrane. After mounting the PTE and the contact assembly into the lower stainless steel cell, the PEEK part was carefully positioned on top, ensuring an unobstructed path for the Luggin capillary to the membrane. The two parts were manually clamped, and water tightness was checked filling the Luggin the capillary while checking that the main chamber was dry.

Setup reproducibility:

Starting from a sputtered IrOx $0.250 \text{ mg cm}^{-2}_{\text{geo}}$ catalyst deposition on a carbon substrate, two GDE catalyst assemblies were hot pressed at 84 bar and the OER activity was measured using humidified oxygen gas in the GDE setup (hollow black circles) and the PTE setup (hollow red circles), see Figure S3. The assembly measured in the PTE setup showed an improvement of $15 \text{ mA cm}^{-2}_{\text{geo}}$ measured at $1.55 \text{ V}_{\text{RHE}}$ and consistently larger improvements at higher potentials over the GDE setup, which indicates a better iR correction from the Luggin capillary design ending on the membrane. Additionally, the lower Tafel slopes up to higher current densities show that more favorable mass transport conditions are achieved in the PTE setup, see Table 2. However, it is also seen that both setups exhibit limitations at $100 \text{ mA cm}^{-2}_{\text{geo}}$, which as it was mentioned earlier indicates the degradation onset in carbon substrates operating with potentials exceeding $1.6 \text{ V}_{\text{RHE}}$.

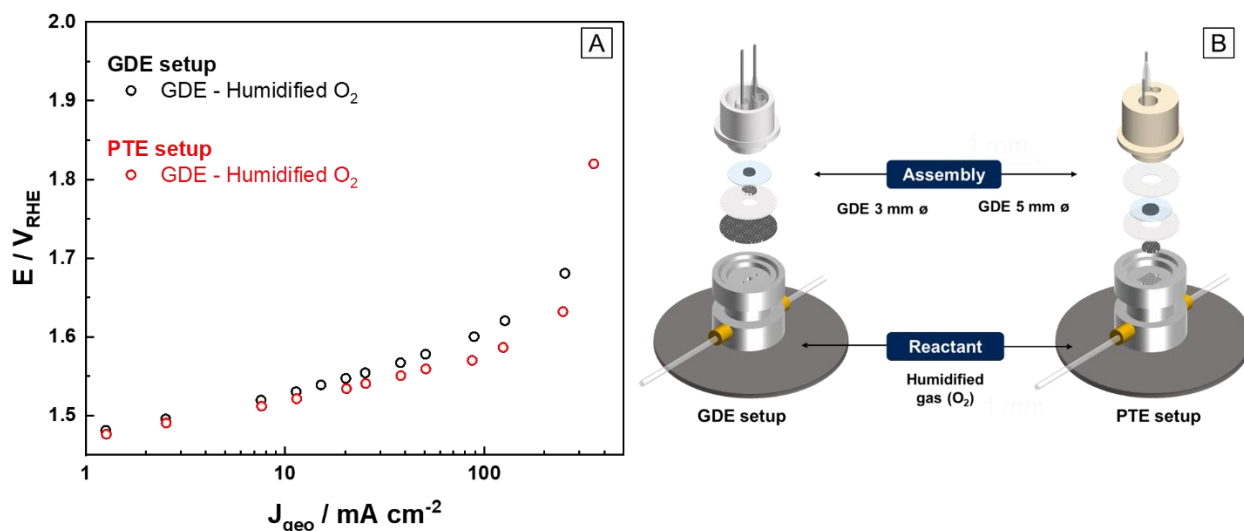


Figure S3. A. Influence of the setup configuration (GDE vs PTE) in the OER activity of a sputtered IrOx $0.250 \text{ mg cm}^{-2}_{\text{geo}}$ catalyst measured in punched samples of 5 mm in diameter on GDL substrates. B. Schematic figure of the assembly and experimental conditions in both setup configurations.

References

- [1] J. Schröder, V.A. Mints, A. Bornet, E. Berner, M. Fathi Tovini, J. Quinson, G.K.H. Wiberg, F. Bizzotto, H.A. El-Sayed, M. Arenz, M.F. Tovini, J. Quinson, G.K.H. Wiberg, F. Bizzotto, H.A. El-Sayed, M. Arenz, Supporting Information - The Gas Diffusion Electrode Setup as Straightforward Testing Device for Proton Exchange Membrane Water Electrolyzer Catalysts, *JACS Au*. 1 (2021) 247–251. <https://doi.org/10.1021/jacsau.1c00015>.
- [2] P. Collantes Jiménez, G. Sievers, A. Quade, V. Brüser, R.K. Pittkowski, M. Arenz, Gas diffusion electrode activity measurements of iridium-based self-supported catalysts produced by alternated physical vapour deposition, *J Power Sources*. 569 (2023). <https://doi.org/10.1016/j.jpowsour.2023.232990>.

Declaration of consent

on the basis of Article 18 of the PromR Phil.-nat. 19

Name/First Name:

Registration Number:

Study program:

Bachelor Master Dissertation

Title of the thesis:

Supervisor:

I declare herewith that this thesis is my own work and that I have not used any sources other than those stated. I have indicated the adoption of quotations as well as thoughts taken from other authors as such in the thesis. I am aware that the Senate pursuant to Article 36 paragraph 1 litera r of the University Act of September 5th, 1996 and Article 69 of the University Statute of June 7th, 2011 is authorized to revoke the doctoral degree awarded on the basis of this thesis.

For the purposes of evaluation and verification of compliance with the declaration of originality and the regulations governing plagiarism, I hereby grant the University of Bern the right to process my personal data and to perform the acts of use this requires, in particular, to reproduce the written thesis and to store it permanently in a database, and to use said database, or to make said database available, to enable comparison with theses submitted by others.

Place/Date

Signature